# CONTROL AND QUALIFICATION OF TITANIUM WELDS

A thesis submitted for the degree of Doctor of Philosophy

by

**YUNG Kam-Chuen, Winco**

**Department of Materials Engineering**
**Brunel University**

**December 1997**

# Declaration

No part of the work described in this thesis was performed in collaboration with anyone else. Although advice and help was sought and received from a number of people, all the work described herein is my own. Acknowledgements have been given to the people whose advice and aid was sought.

The work has not been submitted before for any other award to this or any other university, or any other institution of learning.

**Acknowledgements**

First and foremost, I like to give my whole-hearted thanks to my supervisor Professor Brian Ralph for his unfailing support, his patience, his helpful supervision and the understanding he tendered, without which my research study would not have been successful.

Also, my sincere thanks go to Dr. Robert Fenn, also my supervisor. His advice, help and guidance in my work was very helpful in the preparation of this thesis. His encouragement also counted towards the success of my study.

I am also grateful to Professor W.B. Lee, head of the Department of Manufacturing Engineering of PolyU for providing the resources and facilities for me to undertake this work within the department.

I would like to thank Timet UK Limited (formerly named IMI) and their staff who kindly supplied material for my experimental work. Financial support from the British Council and Hong Kong Polytechnic University is gratefully acknowledged.

Thanks are also due to Ms. Gail Forey and Mr. Chris Katzko for helping me in polishing my English in the text.

Last but not least, my utmost thanks go to my dearest wife, Angle and my two lovely daughters, Vivian and Veronica, for their love, care, encouragement and understanding. Without them, I would not even have started or continued this research.

I dedicate this thesis to the memory of my Father.

# Abstract

The study was aimed at controlling the weld geometry of thin-plate titanium and one of its alloys (Ti-6Al-4V) by ultrasonic means and qualifying the metals in the as-welded condition in terms of their grain sizes and mechanical properties.

The alignment and symmetry of the weld pools were successfully tested by using ultrasonic shear waves. The grain sizes at the weld fusion zone were found to be related to their ultrasonic attenuation by a mathematical relationship. The temperature effect in locating weld pool radii in titanium was found at temperatures up to 600 °C. The ultrasonic velocity decreased as the temperature increased and the square of temperature affected the rate of change of the ultrasonic velocity. After compensation for the temperature effect, the maximum location error of the weld pool radius was 17 % which was comparable to previous measurement using different techniques.

A positive relationship was seen between weld geometry (penetration depth and weld width) and heat input. A welding spectrum for titanium and its alloys of different thicknesses was obtained. Back shielding gas was beneficial in obtaining good welds. Both heat input rate and cooling rate were found to affect the grain size of the weld, with the cooling rate being the dominant factor. The grain size exhibited a Hall-Petch effect on mechanical properties, such as the tensile properties and fracture toughness of the weld. The phase transformation positively contributed to better mechanical properties in most cases, whilst the presence of interstitials worsened tensile properties.

A system was developed in this study to utilise the above information and data for possible real-time and closed-loop control of the TIG welding process to give a desirable weld. Specifically, a process control data base was built up using software and a knowledge-based system for acceptable welding parameters, which were determined by acceptable penetration depth, grain size and mechanical properties. An algorithm was successfully written which relates the ultrasonic signal to the penetration depth of the weld. A hardware control circuit was built which took in the ultrasonic signal and converted it to a driving signal to change the welding speed and thereby change cooling rate.

APPENDICES

A - The set up and the use of calibration blocks

B - Detail part drawings of the welding and clamping fixture

C - Representative screens available in "Computer Data Book"

D - Program listing of the weld depth control program and its flow chart

E - Copy of refereed journal papers published during the PhD programme

**Nomenclature**

$I$ = Peak welding current, A

$I_i$ = Initial welding current, A

$V$ = Welding voltage, V

$V_L$ = Load voltage, V

$q$ = Heat input, J

$v$ = Welding speed, $mms^{-1}$

$\eta$ = Heat transfer efficiency during welding

$H$ = Heat input rate, $Jmm^{-1}$

$H_{net}$ = Net heat input rate, $Jmm^{-1}$

$T_p$ = The peak temperature at a distance from the weld fusion boundary, K

$T_m$ = Melting temperature, K

$T_o$ = Initial uniform temperature of the sheet or plate, K

$T$ = The temperature of interest, K

$\alpha$ = Diffusivity of heat, $m^2s^{-1}$

$\rho$ = Density of material, $kgm^{-3}$

$C$ = Specific heat of solid metal, $Jkg^{-1}\,^{o}C$

$\rho C$ = Volumetric specific heat, $Jmm^{-3}\,^{o}C$

$t$ = Thickness of sheet or plate, mm

$Y$ = Width of heat-affected zone, mm

$\tau$ = Relative thickness of the plate

$R$ = The cooling rate at a point on the weld centre line, $Ks^{-1}$, at temperature T

$G$ = The temperature gradient in the weld pool

$S_R$ = Rate of advance of the solidification front

$k$ = Thermal conductivity of the metal, $Wm^{-1}K^{-1}$

$S_t$ = Solidification time, the time lapse from beginning to end of solidification at a fixed point in the weld metal, s

$F$ = Heat of fusion, $Jmm^{-3}$

$L$ = Beta grain size, μm

$e$ = Elongation, mm

$r_c$ = Radius of curvature at the inside surface of the bend specimen, mm

$H_v$ = Vickers hardness number

$U$ = Elastic energy stored in a structure under fracture, J

$\gamma$ = Surface energy, $Jm^{-2}$

$\gamma_I$ = Surface energy pertaining to the initiation of fracture, $Jm^{-2}$

$\gamma_F$ = The work of fracture averaged over the whole fracture process, $Jm^{-2}$

$\alpha$ = Attenuation

$f$ = Frequency, Hz

$\lambda$ = Wavelength, μm

$D$ = Mean grain diameter, μm

$d_w$ = Depth of weld pool, mm

$\delta t$ = Time difference between two ultrasonic echo, μs

$V_L$ = Longitudinal velocity of the ultrasound, $ms^{-1}$

$r$ = True weld pool radius, mm

$r_a$ = Apparent weld pool radius, mm

$W$ = Gauge width of the specimen used in tensile test, mm

$T_G$ = Thickness of specimen at gauge width in tensile test, mm

$T_b$ = Average thickness of specimen in tensile test, mm

## 1.0 INTRODUCTION

Titanium and its alloys represent an important class of materials due to their high specific strength (i.e. strength-to-density ratio) and toughness, excellent elevated-temperature properties (up to approximately 650 °C) and superior corrosion resistance. Titanium is a low-density element (approximately 60% of the density of steel) which can be highly strengthened by alloying and deformation processing. Titanium is non-magnetic and has good heat-transfer properties. Its coefficient of thermal expansion is somewhat lower than that of steel and less than half that of aluminium. Titanium and its alloys have melting points higher than those of steel. Titanium is non-toxic and is therefore generally biologically compatible with human tissues and bones.

Titanium has a hexagonal close packed crystal structure (HCP) at room temperature, this structure is called alpha ($\alpha$). The structure transforms at 883 $^{o}$C to a body-centred-cubic crystal structure (BCC), called beta ($\beta$). Alloying elements favour one or the other of the two structures. The addition of an alloying element causes a division of the single temperature for equilibrium transformation into two temperatures - the $\alpha$ transus, below which the alloy is all-$\alpha$, and the $\beta$ transus, above which the alloy is all-$\beta$. Between these temperatures, both $\alpha$ and $\beta$ are present. The transformation temperature, known as the $\beta$ transus, is strongly influenced by the presence of interstitial elements.

Unalloyed titanium

Unalloyed or commercially pure (CP) titanium usually has excellent resistance to corrosion, with maximum interstitial impurities but minimum mechanical properties. As can be seen from Table 1.1, there are several grades of unalloyed titanium. The primary difference between the grades is oxygen and other interstitial elements and iron content. Grades of higher purity (lower interstitial content) are both lower in strength, hardness and transformation temperature than those with higher interstitial content. The high solubility of the interstitial elements oxygen and nitrogen creates problems which is not a concern for most other metals. For example, heating titanium in air at high temperature results not only in oxidation, but also in solid-solution hardening of the surface as a result of inward diffusion of oxygen. Nevertheless, these CP titanium grades comprise about 30% of production and are widely used in the industry. Typically CP titanium is used to manufacture chemicals, marine and aircraft parts, and in applications where high strength is not required.

$\alpha/\beta$ alloys

$\alpha/\beta$ alloys contain mixtures of $\alpha$ and $\beta$ phases in their microstructures. They can be strengthened by solution treating and ageing heat treatments. Some $\alpha/\beta$ alloys are also used in the annealed condition. They have excellent fracture toughness when annealed, and outstanding strength-to-density ratios in heat-treated conditions. Examples from this group are Ti-6Al-4V (IMI 318) and Ti-6Al-2Sn-4Zr-6Mo. IMI 318 is unique in that it combines attractive properties with inherent workability. It can be produced in both large and small sizes in all types of mill products.

IMI 318 is the basic alloy currently used for high - performance applications. In fact, it is the most widely used titanium alloy. It can be processed to provide mill-annealed or $\beta$-annealed structures. The alloy is sometimes solution treated and aged for other purposes. IMI 318 has four main forms of use :

- It is used for aircraft gas turbine disks and blades;
- It is extensively used in all mill product forms;
- It is used for airframe structural components and in other applications requiring strength at temperatures up to 588 K;
- It is used for high-strength prosthetic implants and chemical-processing equipment.

When selecting a titanium alloy for a specific application, IMI 318 has become the standard alloy against which other alloys must be compared. Table 1.1 presents the chemical composition of typical titanium and its alloys. Table 1.2 gives the physical properties of CP titanium (IMI 115 to IMI 160) and IMI 318.

Scope and methodology of the study

This dissertation investigates the controlling factors and parameters when welding CP titanium and titanium alloy -- IMI 318. The study was undertaken with reference to welding physics and metallurgy. Particular interest was given to the control of the weld geometry (e.g. penetration depth) through ultrasonic means and the qualification of the alloy in the as-welded condition, in terms of its grain size and mechanical properties. The

findings from the study has resulted in a better understanding of the performance of the alloy in the as-welded condition.

The methodology of the study is as following : The study aimed to find the relationship between the weld geometry and the welding parameters (sections 5.1 and 6.1). The weld penetration and weld pool radius were then detected by ultrasonic means (sections 4.1 and 4.2). The ultrasonic signals were related to the welding parameters (section 3.4) which were subsequently changed by hardware (section 3.2) if necessary, to attain the required weld penetration and weld pool radius. The result is a set of welding parameters that produced welds with acceptable weld pool geometry--set A parameters.

In addition, the relationship between mechanical properties and the welding parameters (sections 5.2, 6.2 and 6.3) and that between grain size and welding parameters (section 6.1) was studied. The grain sizes were then determined by ultrasonic attenuation (section 4.1), the signal from this was used to change adaptively the welding parameters (section 3.4) through the use of hardware (section 3.2). The result of this adaptive control was another set of welding parameters that produced welds with desirable grain size and also mechanical properties--set B parameters.

Through the introduction of software and a knowledge-based system in section 3.3 and with the inputs of set A and set B parameters described above, the set of welding parameters that would fabricate welds with both desirable weld geometry, grain size and mechanical properties in the as-weld condition could be obtained. Thus, through the control and qualification processes mentioned above, it is envisaged that acceptable IMI 318 thin-plate welds could be produced in the as-welded condition.

To prepare for the investigation, experiments on the qualification of CP grade titanium were conducted because CP grade titanium exhibits good weldability amongst all other titanium alloys. Also, thin plates were selected for the study since previous work (Fenn & Stroud, 1982; Stroud, 1983; Johnson *et al.*, 1986; Stroud, 1989) were carried out on thicker (over 10 mm) plates. Furthermore, the study will be of a more practical nature if the ultrasonic control can be made in a real time mode during the welding process. Thus, due to a lack of previous research in this area, a study of the ultrasonic response in the alloy at elevated temperatures was carried out in this study (section 4.2).

Table 1.1 Chemical composition of typical titanium alloys (Donachie, 1985)

| | ←Maximum impurity limits → | | | | | ←Nominal composition, wt %→ | | | | |
|---|---|---|---|---|---|---|---|---|---|---|
| Designation | N | C | H | Fe | O | Al | Sn | Zr | Mo | Others |
| Unalloyed grades | | | | | | | | | | |
| ASTM Grade 1 | 0.03 | 0.10 | 0.015 | 0.20 | 0.18 | | | | | |
| ASTM Grade 2 | 0.03 | 0.10 | 0.015 | 0.30 | 0.25 | | | | | |
| ASTM Grade 3 | 0.05 | 0.10 | 0.015 | 0.30 | 0.35 | | | | | |
| $\alpha$ / near $\alpha$ alloys | | | | | | | | | | |
| Ti-5Al-2.5Zn-ELI | 0.07 | 0.08 | 0.0125 | 0.25 | 0.12 | 5.0 | 2.5 | | | |
| Ti-8Al-1Mo-1V | 0.05 | 0.08 | 0.015 | 0.30 | 0.12 | 8.0 | | | 1.0 | 1.0V |
| Ti-6Al-2Sn-4Zr-2Mo | 0.05 | 0.05 | 0.0125 | 0.25 | 0.15 | 6.0 | 2.0 | 4.0 | 2.0 | |
| Ti-5Al-5Sn-2Zr-2Mo | 0.03 | 0.05 | 0.0125 | 0.15 | 0.13 | 5.0 | 5.0 | 2.0 | 2.0 | 0.25 Si |
| $\alpha$-$\beta$ alloys | | | | | | | | | | |
| IMI 318 | 0.05 | 0.10 | 0.0125 | 0.30 | 0.20 | 6.0 | | | | 4.0 V |
| Ti-7Al-4Mo | 0.05 | 0.10 | 0.013 | 0.30 | 0.20 | 7.0 | | | 4.0 | |
| Ti-6Al-2Sn-4Zr-6Mo | 0.04 | 0.04 | 0.0125 | 0.15 | 0.15 | 6.0 | 2.0 | 4.0 | 6.0 | |
| Ti-5Al-2Sn-2Zr-4Mo-4Cr | 0.04 | 0.05 | 0.0125 | 0.30 | 0.13 | 5.0 | 2.0 | 2.0 | 4.0 | 4.0 Cr |
| $\beta$ alloys | | | | | | | | | | |
| Ti-8Mo-8V-2Fe-3Al | 0.05 | 0.05 | 0.015 | 2.5 | 0.17 | 3.0 | | | 8.0 | 8.0V |
| Ti-13V-11Cr-3Al | 0.05 | 0.05 | 0.025 | 0.35 | 0.17 | 3.0 | | | | 11Cr,13V |

Table 1.2 : Physical properties of IMI 115, 125, 130, 155, 160 and IMI 318 (Duncan & Hanson, 1980)

| Alloy (IMI #) | Density | Coefficient of expansion (20-100°C) | Thermal conductivity | Resisitivity | Temperature coefficient of resistivity (20-100°C) | Specific heat | Magnetic susceptibility | Elastic modulus |
|---|---|---|---|---|---|---|---|---|
| | $kgm^{-3}$ | $x\ 10^{-6}\ K^{-1}$ | $W^{-1}\ m^{-1}\ K^{-1}$ | $\mu\Omega m$ | | $Jkg^{-1}\ K^{-1}$ | $x\ 10^{-6}$ | $GN\ m^{-2}$ |
| 115-160 | 4.51 | 7.6 | 16 | 0.48 | 0.0036 | 528 | +3.4 | 110 |
| 318 | 4.42 | 8.0 | 5.8 | 1.8 | 0.0004 | 610 | +3.3 | 110-125 |

# 2.0 LITERATURE SURVEY

## 2.1 Titanium and its alloys

### 2.1.1 Microstructures of titanium alloys (Mills, 1985)

Microstructural control is basic to successful processing of titanium alloys. Undesirable structures can interfere with optimum property development. In some cases, similar microstructures may not produce the same levels of mechanical properties.

(i) α phase

*Equiaxed α grains*, as shown in Figure 2.1, are usually developed by annealing cold worked alloys above the recrystallisation temperature.

*Elongated α grains*, as shown in Figure 2.2, result from unidirectional working of the metal and are commonly found in longitudinal sections of rolled or extruded alloys.

(ii) β phase

In α/β and β alloys, some equilibrium β is present at room temperature. A non equilibrium, or metastable, β phase can be produced in α/β alloys which contain enough β-stabilising elements to retain the β phase at room temperature during rapid cooling from the α + β phase field. The composition of the alloy must be such that the temperature for the start of martensite formation has decreased to below room temperature.

(iii) Transformed β phase

Generally, two types of α are present -- primary α and secondary α. The primary α is present before heat treatment. The secondary α is produced by transformation from β. This transformation may occur upon cooling from above the β transus or high within the α + β phase field (Figure 2.3). The α in these area have different structures known as serrated, acicular, platelike, Widmanstatten and α prime (martensite). The term "transformed β" is used to describe these various α structures plus any β that may remain at room temperature.

*Acicular α* is the most common product transformed from β during the cooling process. It is produced by nucleation and growth along one set of preferred crystallographic planes of the prior β matrix (Figure 2.4) or along several sets of planes (Figure 2.5). In the latter

case, the $\alpha$ has a basketweave appearance characteristic of a Widmanstatten structure. 'acicular $\alpha$' and 'Widmanstatten $\alpha$' are generally interchangeable terms.

Under some conditions, the long grains of $\alpha$ produced along preferred planes in the $\beta$ matrix take on a wide, platelike appearance, as shown in Figure 2.6. Under other conditions, grains of irregular size and with jagged boundaries, called 'serrated $\alpha$', are produced (Figure 2.7).

*Martensite ($\alpha$ prime),* is a non-equilibrium supersaturated $\alpha$ structure produced by diffusionless transformation of $\beta$. The needle-like structure is often difficult to distinguish from that of acicular $\alpha$, although acicular $\alpha$ is usually less well-defined and has curved rather than straight sides. Figure 2.8 shows an example of martensite formed by quenching.

### 2.1.2 Microstructural changes during or after heat treatment (Smith, 1993)

This section will discuss the microstructural changes of $\alpha/\beta$ titanium alloy IMI 318. The microstructural changes caused by thermal treatment of IMI 318 can best be understood by considering the pseudo-binary phase diagram shown in Figure 2.9.

(i) Cooling from above the $\beta$ transus (1066 °C)

*Air cooling* : Air cooling the solution-treated IMI 318 alloy from 1066 °C, which is about 50 °C above the $\beta$ transus (Figure 2.9), produces a structure consisting of acicular $\alpha$ that is transformed from the $\beta$ phase by nucleation and growth. This type of structure produced by intermediate cooling rates from high temperatures, is shown in Figure 2.10.

*Water quenching* : Heating a bar of IMI 318 to 1066 °C, and holding it for 30 minutes, produces an all $\beta$-phase structure. Upon water quenching from 1066 °C, a structure consisting of all titanium martensite is produced (Figure 2.11).

(ii) Cooling from 954°C (approximately 50 °C below the $\beta$ transus ).

*Air cooling* : Air cooling a solution-treated IMI 318 bar from 954°C produces a structure of primary $\alpha$ in a matrix of transformed $\beta$, some of which is acicular $\alpha$ (Figure 2.12).

*Water quenching* : When solution heating a bar of IMI 318 to 954 °C, some primary α will coexist with the β phase. After quenching to room temperature, the β phase is transformed immediately to titanium martensite. Thus, a structure consisting of primary α embedded in titanium martensite is produced (Figure 2.11).

(iii) Cooling from 843 °C ( just below the Ms temperature at which the martensite starts)
Water quenching a IMI 318 bar from 843 °C, which is just below the Ms, produces a structure consisting of primary α and untransformed or retained β (Figure 2.13). The retained β is metastable, but it may undergo a subsequent strain-induced transformation.

### 2.1.3 Mechanical properties and heat treatment of CP titanium and $\alpha/\beta$ alloys
(Donachie, 1985)

(i) CP titanium
Due to a result of variations in the interstitial and impurity levels, yield strengths of unalloyed or CP grades (see Table 2.1) vary from 215 MPa to 475 MPa. In these grades, oxygen and iron are the main impurities and strength increases with increasing oxygen and iron contents.

(ii) α-$\beta$ alloys
α-$\beta$ alloys can be strengthened by solution treating and ageing. Solution treating is usually carried out at a high temperature in the two-phases $\alpha$-$\beta$ field, and is followed by quenching in water, oil or other suitable quenchant. As a result of quenching, the $\beta$ phase present at the solution treating temperature may be retained or may be partly transformed during cooling by either martensitic transformation or nucleation and growth. The specific response depends on alloy composition, solution treating temperature ($\beta$-phase composition at the solution temperature) and cooling rate. Solution treatment is followed by ageing, normally at 480 °C to 650 °C, to precipitate $\alpha$ and produce a fine mixture of $\alpha$ and $\beta$ in the retained or transformed $\beta$ phase.

Solution treating and ageing can increase the strength of $\alpha/\beta$ alloys 30 to 50 %, or more, over the annealed or over-aged condition. Alloys relatively low in $\beta$ stabilisers (IMI 318, for example) have poor hardenability and must be quenched rapidly to achieve significant strengthening. For IMI 318, the cooling rate during a water quench is not rapid enough to significantly harden sections thicker than about 25 mm.

Table 2.2 presents the mechanical properties of four common titanium alloys in their wrought bar form and in their annealed condition. While different forms of product of the same alloy may possibly exhibit different mechanical properties, plate and sheet commonly exhibit the same tensile properties in both the transverse and longitudinal directions relative to the final rolling direction. With a precise control systems now available, proper texturing and directionality can be obtained in $\alpha/\beta$ sheet by unidirectional rolling. These characteristics favourably affect tensile properties of IMI 318 sheet in various gauges. Other properties, such as fatigue resistance, are also improved by this type of rolling. Directionality in properties is observed only as a slight drop in transverse ductility of plate greater than 25 mm.

### 2.1.4 **Weldability of CP titanium and $\alpha/\beta$ alloys** (Duncan and Hanson, 1980; Donachie, 1985; Polmear, 1995)

Welding has the greatest potential for affecting material properties. Titanium alloys in an inert atmosphere can be welded by gas tungsten-arc welding. In all types of welds, contamination by interstitial impurities such as oxygen and nitrogen must be closely controlled to maintain useful ductility in the weldment. The final properties of welded joints are importantly determined by alloy composition, welding procedure, the weld geometry and the thermal cycle in the subsequent heat treatment.

During fusion welding, solid grains of $\beta$ titanium exist immediately next to the molten metal. In the cooler regions farther from the weld, the solid titanium is all $\beta$ phase, mixtures of $\alpha$ and $\beta$ phases, or all single-phase $\alpha$, depending on the alloy composition. The progressive solidification of the weld is accompanied by growth of solid $\beta$ grains in the direction of solidification.

Mechanical properties for representative alloys and types of welds can be summarised as: welding generally increases strength and hardness but decreases tensile and bend ductility. Some mechanical properties of the as-welded CP titanium and IMI 318 are listed in Table 2.1.

(i) CP titanium

It has good weldability but, if the iron content is above 0.05%, a preferential corrosive attack of weld metal can occur in nitric acid solutions. Welds in unalloyed titanium grades 1, 2 and 3 do not require postweld treatment unless the material is highly stressed in an intense reducing atmosphere. If the material is highly stressed, stress relieving or annealing may prove useful. The welds are particularly vulnerable because of the acicular nature of any of the retained $\beta$ phase that is stabilised by the iron. However, this is not true for the base metal (BM) where retained $\beta$ is finely divided and discontinuous. In this instance, filler metal with low iron content should be used and all sources of iron contamination during preparation and welding should be avoided.

(ii) $\alpha/\beta$ alloys

As a result of the thermal cycle to which the alloy is exposed during the welding of these alloys, there may be a significant changes in their strength, ductility, and toughness characteristics. Welds may have a high tendency to fracture with little or no plastic straining, this happens for example in Ti-6Al-6V-2Sn. Weld ductility can be improved by postweld heat treatment which consists of a slow cooling process from the high annealing temperature.

The low ductility of most $\alpha/\beta$ alloy welds is caused by phase transformations in the fusion zone (FZ) or the heat-affected zone (HAZ), or both. These alloys can be welded with unalloyed titanium or $\alpha$-titanium alloy filler metal which produces a weld metal that is low in $\beta$ phase. This also improves the weld ductility. However, this procedure does not overcome the low ductility of the HAZ in alloys which contain large amounts of $\beta$ stabilisers.

$\alpha/\beta$ alloys that are highly $\beta$ stabilised have limited weldability. They crack when welded under high restraint or when minor defects are present in the weld zone. The resistance to cracking may be improved by preheating the alloys in the range of 150$^{o}$ to 175 $^{o}$C, and then apply stress-relief immediately after welding.

The increased amounts of $\beta$ stabilising elements (e.g. molybdenum, iron, vanadium, and others) in advanced titanium alloys has tended to reduce weldability. For example, Ti-6Al-2Sn-4Zr-2Mo alloy exhibits inconsistent arc weld mechanical properties due to a

small variations in the weld cooling rates (Mitchell & Tucker, 1969). Unsatisfactory ductility has been encountered in fusion weldments in the metastable $\beta$ Ti-8Mo-8V-2Fe-3Al alloy (Hatch, 1973).

These studies have shown that it can be difficult to achieve satisfactory properties when welding these high strength titanium alloys. It is necessary therefore to develop unique welding and heat treatment procedures to control the $\alpha$-$\beta$ phase transformations and precipitation reactions. These transformations and reactions are responsible for the deleterious weld properties in these materials. For instance, it has been shown that control of weld heating and cooling rates by preheating could improve the toughness of Ti-6Al-6V-2Sn welds (Lewis & Wu, 1963). Also, another study demonstrates that the tungsten-inert-gas weldment ductilities in the Ti-5Al-6V-2Sn and Ti-8Mo-8V-2Fe-3Al alloys were significantly improved by unique postweld heat treatments (Simpson & Wu, 1974; Greenfield & Pierce, 1973). These heat treatments produced $\alpha$ phase morphologies in HAZ which are considerably more fracture resistant than the microstructures obtained in the as-welded or conventionally post-weld heat treated conditions.

## 2.2 Welding physics and metallurgy

### 2.2.1 Heat flow in tungsten-inert-gas (TIG) welding

Tungsten-inert-gas (TIG) welding is a process in which a very intense, moving heat source is applied to the workpiece. It is very useful to predict the form of the temperature gradients surrounding this heat source, in order to understand the effect of a given heat input on the microstructural changes in the HAZ zone and the residual stresses. An understanding of all these conditions is necessary if predictions concerning cracking problems are to be possible.

It is difficult to measure the temperature distribution within the weld pool. Theoretical analyses of the weld thermal cycle have also been attempted. The first efforts in quantifying weld thermal cycles started in the early 1940s (Rosenthal, 1941). As a result of quantitative temperature measurements in the HAZ of arc welds, a series of differential equations were developed (Hess *et al.*, 1943; Nippes *et al.*, 1949). These equations express the temperature distribution in the neighbourhood of an arc weld as a function of time, distance from weld centreline, and welding variables. The heat flow equations also show rather satisfactory agreement between the measured and theoretical temperature profiles in the HAZ.

The thermal conditions of welding include heat input, distribution of peak temperature, cooling rates and solidification rate. These conditions all affect the metallurgical situations of the HAZ and the weld metal.

### 2.2.2 Heat input rate

The heat input rate for the welding process is given by:

$$Heat-input-rate\ (H) = \frac{Current\ x\ voltage(Heat-input)}{Traveling\ speed\ of\ arc} = (IxV)/v = q/v \qquad (2.1)$$

$$Net\ heat-input-rate\ (H_{net}) = Heat-input-rate\ x\ Heat\ transfer\ efficiency = \eta\,(q/v) \qquad (2.2)$$

As the welding voltage is dependent on the welding current (refer to later section 2.3.5), heat input basically is determined by welding current. With a fixed welding current and therefore heat input, the heat input rate is determined by the welding speed as revealed in Equation 2.1 above.

The heat input rate governs : heating rates, cooling rates and weld pool size. The higher the heat input rate, the lower the cooling rate and the larger the welding pool. In addition, there is an inverse relationship between the weld pool size and the cooling rate. Also, a higher heat input rate gives a longer thermal cycle and tends to generate a coarser structure. Therefore, it is necessary to seek a heat input rate that gives the optimum combination of the grain size and cooling rate.

### 2.2.3 Peak temperature

Interpreting metallurgical transformations at a point in the solid metal near a weld requires some knowledge of the peak temperature reached at a specific location. To enable the computation of peak temperature, different heat flow models and their solutions have been developed.

The solution to the heat flow equations of a moving point heat source was given by Rosenthal (1946) and was later reviewed by other investigators. The limitations of the simplifying assumptions in the earlier efforts have consequently led to attempts by many others to modify the analytical solutions to account for various assumptions (Jhaveri *et al.*, 1962; Swifthook & Gick, 1973; Uwer & Degenkolbe, 1977).

However, due to the complex nature of the heat flow problem, the modified analytical solutions, or even computer simulated models, so far have had rather limited success in characterising the thermal cycles in the weld pool (Kou, 1981). But, in the HAZ region, the modified analytical solutions can characterise the thermal cycles with adequate accuracy for practical implementation (Kou, 1981; Goldak *et al.*, 1986).

For TIG welding, a heat flow model was developed in 1991 (Vishnu *et al.*, 1991). The heat flow model amends two of Rosenthal's (1946) assumptions, the two assumptions amended are as follows : Firstly, instead of a point or line source, a distributed source is

assumed. The point source solutions are simple, but this gives rise to a singularity at the source origin and causes the temperature predictions in the area surrounding the source to be invalid. The distributed source model avoids the problem of singularity and is more accurate. Secondly, the assumption of a quasi-stationary state is invalid for pulsed welding and has been amended because heat flow model of pulsed welding must take into account the transients associated with periodic change in power from peak to background level. The present heat model for pulsed TIG welding is discussed by Vishnu and co-workers (1991).

For a single pass, full penetration butt weld in a sheet, the distribution of peak temperatures in the base metal (BM) adjacent to the weld is given by Adams (1958):

$$\frac{1}{T_p - T_0} = \frac{4.13\rho C t Y}{H_{net}} + \frac{1}{T_m - T_0} \tag{2.3}$$

Y is the distance from FZ/ HAZ boundary to HAZ/ BM boundary; i.e. the width of HAZ may be used as Y. Following a study by Greenfield and Duvall (1975), they suggested that the HAZ regions farthest from the FZ of an alloy (Ti-6Al-2Sn-4Zr-6Mo) were exposed to a temperature slightly below the $\beta$ transus. Therefore, the $\alpha/\beta$ transformation temperature may be used here as the peak temperatures ($T_p$) in the boundary between HAZ and BM region.

The peak temperature equation (2.3) can be used to determine the peak temperatures at specific locations in the HAZ. It can also be used to estimate the width of the HAZ. However, when calculating the width accurately, the outer extremity of the HAZ must be clearly identified with a specific peak temperature. This calculation in turn is associated with some characteristics of change in the structure or properties. Lastly, the effect of preheating step on the width of the HAZ can also be evaluated using the same equation.

### 2.2.4 Cooling rate and solidification rate

After the point in or near the weld has reached its peak temperature, the rate at which it cools may have a significant effect on : the metallurgical structure, the properties, or the soundness of the weld metal. To compute the cooling rate in the FZ, the conventional

solution from Adams (1958) is adopted. When the plate is thin (heat flow is 2-dimensional), the cooling rate, R, as shown below:

$$R = 2\pi k\rho C(\frac{t}{H_{net}})^2(T - T_0)^3 \tag{2.4}$$

When the plate is thick (heat flow is 3-dimensional), R equals:

$$R = \frac{2\pi k(T - T_0)^2}{H_{net}} \tag{2.5}$$

The relative thickness of the plate is defined as (Nippes, 1983):

$\tau < 0.75$ for thin plate

$\tau > 0.75$ for thick plate

the relative plate thickness $\tau$ is given by:

$$\tau = t\sqrt{\frac{\rho C(T - T_0)}{H_{net}}} \tag{2.6}$$

In addition, for each titanium composition, there exists a critical cooling rate. If the actual cooling rate in the weld metal exceeds this critical value, there is a great risk of cracking in the presence of hydrogen under the influence of thermal stresses. The presence of hydrogen may introduce porosity defects during solidification and the pores serve as stress raisers and thus reduce the fatigue properties of the weld.

Equations 2.4 to 2.6 apply to cooling rate at the FZ. For the cooling rate at any point at the rear of a weld pool, the analytical solutions of the heat-diffusion equation assuming a point or line heat source can be used (Lancaster, 1993). These solutions are valuable in developing an overall picture of the character of heat flow in welding and the nature of the thermal cycle.

The equation for the diffusion of heat is linear, and analytical solutions are available for many boundary conditions. Those most relevant to fusion welding, in rectangular co-ordinates (x, y, z) and relative to the heat source as origin, are as follows.

1. A point heat source with heat input $q$ on the surface of a semi-infinite body that is moving with velocity $v$:

$$T = \frac{q}{2\pi kr} e^{-v(r-x)/2\alpha} \tag{2.7}$$

where $r^2 = x^2 + y^2 + x^2$

2. A line source with heat input per unit length penetrating an infinite plate that is moving with velocity $v$:

$$T = \frac{q}{2\pi k} e^{vx/2\alpha} K_o\left(\frac{vr}{2\alpha}\right) \tag{2.8}$$

where $r^2 = x^2 + y^2$, $K_0$ is constant.

Solution 1 (Equation 2.7) represents an approximation to the conditions in multi-pass welding on thick plate; solution 2 (Equation 2.8) approximates to single-pass welding of thin sheet (of thickness less than 5mm) or welding with a penetrating heat source such as an electron beam or a laser beam.

The point and line source solutions are those relevant to the temperature distribution in fusion welding. The thermal cycle is obtained by plotting $T$ as a function of $t$ (equal to $x/v$) for a fixed distance from the centreline where $y = 0$.

The theoretical cooling rate for any point (x, y, z) relative to the source as origin may be obtained by a differentiation of Equations 2.7 and 2.8. For a three-dimensional case, it is given by:

$$\frac{\partial T}{\partial t} = \frac{vT}{r}\left[\frac{x}{r} - \frac{vr}{2\alpha}\left(1 - \frac{x}{r}\right)\right] \tag{2.9}$$

and for a two-dimensional case, it is given by:

$$\frac{\partial T}{\partial t} = \frac{v^2 T}{2\alpha}\left(\frac{(x/r)K_1(vr/2\alpha)}{K_o(vr/2\alpha)} - 1\right) \tag{2.10}$$

where $K_1$ is constant.

For simplicity, consider a point along the central axis of the weld at the rear boundary of the weld pool where $r = x = x_1$ and $T = T_m$ the melting temperature. Then for three-dimensional flow,

$$\frac{\partial T}{\partial t} = -\frac{v T_m}{x_1} \tag{2.11}$$

while for two-dimensional flow,

$$\frac{\partial T}{\partial t} = -\frac{2\pi k T_m^{\,2}}{q / v} \tag{2.12}$$

Equations 2.11 & 2.12 predict that the cooling rate at the downstream edge of the weld pool will increase as the welding speed increases, and similar welding speeds will be higher for smaller weld pools.

Moreover, for two-dimensional flow, the cooling rate along the axis at the rear of the weld pool is inversely proportional to the parameter $q/v$ which is the heat input rate. Equations 2.11 and 2.12 may be used as a means of comparing the heat-flow conditions of the weld. Both the weld pool size and the heat input rate are readily observable indicators of the cooling rate.

The cooling rate can affect the mechanical behaviour of the welds significantly. For instance, the cause of the hard, brittle condition of a weld may be due to the formation and rapid auto-ageing of orthorhombic martensite in the weld and the HAZ on cooling from welding (Greenfield & Duvall, 1975).

The rate at which the weld metal solidifies can have a profound effect on its metallurgical structure and properties. The solidification time of the weld metal depends on the net heat

input rate. A mathematical model of solidification time ($S_t$) is given by (Nippes, 1983):

$$S_t = \frac{FH_{net}}{2\pi \quad k\rho \quad C(T_m - T_0)^2} \tag{2.13}$$

Equation 2.13 shows that the solidification time is proportional to net heat input rate. The solidification time directly affects the structure of the weld metal. The dendrite spacing is proportional to the square root of the solidification time. With most metals, strength, ductility, and toughness can all be improved with finer dendrite spacing.

### 2.2.5 Welding metallurgy in fusion zone

(i) Effect of cooling rate

The work of Watanabe and co-workers (1995) shows that the grain size is influenced by the welding speed. The grain size decreases when the welding speed increases. According to Kou (1987), under the same heat input, the cooling rate increases with an increase in the welding speed. Therefore, the increase of the cooling rate when welding will result in a decrease of the grain size. Besides, the higher the cooling rate, the finer the cell spacing of the structure. In other words, the subgrain structure becomes finer as the welding speed and cooling rate increase. Furthermore, a finer cell spacing leads to higher ductility and yield strength of the weld and a more effective postweld heat treatment. On the other hand, it has been observed in several metals that the higher the heat input rate of the weld, the coarser the dendrite arm spacing.

For the commercially pure titanium alloy, a slow cooling rate results in the size of the saw-tooth-like α structure or the needle-like α structure becoming larger. For the α/β system alloys, the prior β grains are coarser and precipitates of coarser needle-like α phase form during slow cooling. Where the cooling rate is high, the diameter of prior β grains become smaller and the α phase of the grain boundary does not precipitate and resulting in the grains becoming single phase martensite.

(ii) Weld pool solidification

According to Easterling (1992), the crystals that are formed during solidification of the weld pool are nucleated by the solid crystals located at the solid-liquid interface and are

epitaxial. The primary grain size is determined by the grain size of the solid metal at the fusion boundary. A fusion weld has a primary grain structure, and individual grains have a substructure which is a result of microsegregation. The type of substructure that appears in the weld metal depends on the form of the solidification front. This in turn is influenced by the solute content of the liquid weld metal and by a solidification parameter equal to the temperature gradient (G) in the direction of solidification divided by the rate of advance ($S_R$) of the solidification front. The latter is abbreviated to the $G/S_R$ ratio.

The grain structure of the weld also depends on the composition (solute content) and the shape of the weld pool. The grain structures and weld pool shapes are shown in Figure 2.14. Furthermore, some important points for consideration are the effects of welding parameters on heterogeneous nucleation. As the heat input is increased, the temperature gradient in the weld pool, G is decreased. Furthermore, as the welding speed is increased, $S_R$ is increased.

According to Kou (1987), the weld subgrain structure changes from cellular to dendritic when the welding current increases. At the same welding speed, the higher the current and therefore heat input, the lower the temperature gradient G and hence the lower $G/S_R$ ratio. The lower $G/S_R$ ratio favours dendritic solidification. On the other hand, at low heat inputs, the $G/S_R$ ratio is high which favours cellular solidification.

(iii) Structure and mechanical properties

The structure and mechanical properties of fusion welds in titanium alloys, and the degree to which they differ from that of the BM, are influenced by metallurgical phenomena which occur during weld solidification and in the solid-state during continuous-cooling from peak temperatures during post weld heat treatment. From the viewpoint of the weld solidification, four characteristics are significant, these are : the morphology of the $\beta$ grain solidification structure, macrosegregation, microsegregation and solidification defect formation. During the past decade, numerous investigations have been carried out to understand more thoroughly, and in certain cases control, these characteristics so that the weld integrity and mechanical properties can be optimised.

*$\beta$ grain structure*- Fusion welds in titanium alloys are generally characterised by coarse, columnar-shaped $\beta$ grains in the FZ. The $\beta$ grains in the FZ nucleate epitaxially from coarsened $\beta$ grains in the weld HAZ and grow competitively into the weld pools. The FZ $\beta$ grain structure is dependent on several factors, including : (1) the weld thermal cycle as

it influences the size of the nucleating $\beta$ grains in the near-HAZ and the cooling rate during FZ solidification and (2) the shape of the weld pool due to its influences on the competitive $\beta$ grain growth process. In most titanium welding applications, $\beta$ grain size is determined principally by the weld heat input, with a higher heat input promoting a coarser grain size. The $\beta$ grain size may be reduced somewhat by altering the welding parameters (Baeslack & Banas, 1981).

However, the potential for reducing the $\beta$ grain size by producing a weldment with an increased number of smaller passes (i.e. lower heat input) is generally not effective due to the successive epitaxial nucleation of $\beta$ grains as each weld layer is deposited, resulting in the formation of vertically oriented columnar $\beta$ grains. This effect was clearly demonstrated by Misra and co-workers (1982) for multi-pass TIG welds in IMI 318. It is also important to note that the higher cooling rates associated with a reduced heat input can promote the formation of a brittle martensitic transformed-$\beta$ microstructure.

Based on the strong desire to provide a refined $\beta$ grain size while avoiding rapid cooling rates and undesirable brittle martensitic microstructures, numerous attempts have been made over the years to refine the FZ grain size using traditional grain refinement techniques (e.g. ultrasonic and mechanical vibration, convective cooling, electromagnetic stirring). The success of these initial studies was generally variable and limited. During the past decade, further effort has been directed into the grain refinement of titanium alloy welds.

*Solidification segregation effects*- Both macrosegregation (which extend over distances of several $\beta$ grain diameters) and microsegregation (which occurs on an inter-cellular or inter-dendritic scale) can occur during the solidification of titanium alloy arc weldments. However, the degradation of the weld integrity, structure or properties, due to such compositional segregation, is generally not significant in titanium alloys. This is due to the limited extent of segregation of common alloying elements and the appreciable diffusional homogenisation of alloying elements during the weld cooling through the $\beta$ phase field. This significant effect of alloying element homogenisation on cooling through the $\beta$ phase field has been demonstrated by Inoue and Ogawa (1989) for TIG welds in IMI 318.

*Solidification-related weld defects*- Many other structural alloys, such as aluminium alloys and many austenitic stainless steels, titanium alloys are generally not considered

susceptible to FZ solidification cracking. Studies by Baeslack (1982) have demonstrated, however, that under severe conditions of restraint solidification, cracking along columnar $\beta$ grain boundaries can occur. Work by Prokhorov (1986) has further evaluated the solidification cracking of IMI 318 using a weldability test in which a TIG weld is strained during the welding operation. He reported the formation of solidification cracks oriented along the welding direction and a quantitative susceptibility comparable to some steels. However, this observation generally conflicts with the well known excellent cracking resistance of this alloy, and suggest that his test imposed an excessive strain condition not representative of that experienced during conventional arc welding.

Hydrogen-included porosity represents another solidification-related defect in titanium alloy welds, this can generally be eliminated through proper cleaning of the base and filler metals prior to welding. The reduction in fatigue properties and ductility due to the presence of pores in the weld metal has been well acknowledged.

(iv) Solid state phase transformations

The solidification-related phenomena discussed above can markedly influence the integrity and mechanical properties of titanium alloy welds. However, the room-temperature microstructures and mechanical properties of titanium alloy weldments are dependent on an even greater extent on the solid-state phase transformations which occur in the weld FZ and HAZ on weld cooling from the solidus to room temperature.

For example, Ti-6Al-2Sn-4Zr-2Mo-0.1Si (wt. %) is a near-$\alpha$ titanium alloy used widely by the gas-turbine engine industry for modest temperature service. Figure 2.15 shows a continuous cooling transformation (CCT) diagram developed for this alloy (Mitchell & Tucker, 1969). Figure 2.16 shows light and TEM micrographs of TIG welds produced in thin sheets using welding parameters which provided three different cooling rates (which are superimposed on the CCT diagram in Figure 2.15). As shown in Figure 2.16, a decrease in cooling rate generally promotes an increase in the quantity of colony-type $\alpha$+ retained $\beta$ microstructure versus an acicular, twinned martensite structure. A similar trend is observed in most near-$\alpha$ and $\alpha/\beta$ titanium alloys.

*Subsolidus weld cracking*- It was reported when cooling from temperatures above the $\beta$ transus that there is an occurrence of a severe ductility loss at a temperature of about 750 to 850 °C. In response to this phenomena, Lewis and co-workers (1985) utilised a typical TIG weld thermal cycle to evaluate the sensitivity of several near-$\alpha$ and $\alpha/\beta$ titanium

alloys. The results of their analysis, shown in Figure 2.17, support this phenomena. Also, metallographic and fractographic analysis of the failed hot-ductility specimens revealed the occurrence of low-ductility fracture along prior-$\beta$ grain boundaries (Figure 2.18).

### 2.2.6 Welding metallurgy in heat-affected zone

The HAZ may be divided into two regions, a high temperature region, in which major structural changes such as grain growth take place; and the lower temperature region, in which a secondary effect such as precipitation may occur (Kou, 1987). In the grain growth region, the final grain size for any given alloy will depend mainly on the peak temperature which it is exposed to and the time of heating and cooling.

For CP titanium, the HAZ contains the same structure as the weld metal, that is the coarse saw-tooth-like $\alpha$ structure or needle-like $\alpha$ structure and the grain size becomes large when the heat input increases. For the $\alpha/\beta$ system alloys, the HAZ has the coarse prior $\beta$ grains and in the grains, either needle-like $\alpha$ phase and $\beta$ phase or needle-like martensite structure. In addition, when heating in the $\beta$ region at over 1200 °C, prior $\beta$ grains become coarser and precipitate coarse needle-like $\alpha$ phase during the following stages of cooling.

On the other hand, when heating in the $\alpha+\beta$ region, a part of the pro-eutectoid $\alpha$ phase transforms to $\beta$ phase and, during the following stage of cooling, needle-like $\alpha$ phase is precipitated from the $\beta$ phase. Therefore, the HAZ is made up of the pro-eutectoid $\alpha$ phase, the needle-like $\alpha$ phase and the $\beta$ phase. When the cooling rate is higher, the size of prior $\beta$ grains become smaller and the $\alpha$ phase at the grain boundary does not precipitate and so the grains become a single martensite phase, owing to the high speed in heating and cooling. The martensitic transformation occurs before the $\alpha \rightarrow \beta$ transformation completes and so the lath length of the martensite phase becomes short.

The effect of work hardening is completely lost in the FZ owing to melting and solidification and is partially lost in the HAZ owing to recrystallisation and grain growth. In addition, the loss of strength in the HAZ become more severe as the heat input rate of the weld is increased. Therefore, due to the higher heat input and lower cooling rate of TIG welding, recrystallisation and even grain growth are often observed in the HAZ.

## 2.3 Controlling factors and parameters in welding titanium thin plate

### 2.3.1 DC TIG welding of thin plate

The tungsten inert gas (TIG) welding process is widely used for welding titanium and its alloys. In TIG welding, the arc is formed between a pointed tungsten electrode and the workpiece in an atmosphere of argon or helium. In DC welding, the electrode usually has negative (or straight) polarity (DCEN) - its thermionic electron emission properties reduce the risk of overheating which may otherwise occur with positive electrode polarity (Giedt *et al.*, 1989). Thus, with thin materials, TIG welding with DCEN permits a much higher welding speed to be used. The ionised gas or plasma stream which has been formed can attain a temperature of several thousand degrees centigrade, at least in the central core of the arc near to the electrode (Metcalfe & Quigley, 1977). Consequently, within the normal range of welding currents from a fraction of an ampere to several hundred amperes (selected according to the thickness of the material), rapid melting can be effected.

In butt welding of material within the thickness range 0.5 - 3 mm, welding is normally carried out autogenously, i.e. without the addition of filler material. Some of the important welding parameters of TIG which have a considerable effect on the depth of penetration, bead shape and weld soundness are: cleanliness, shielding gas, flow rate, welding current, arc voltage and power source, welding speed, welding torch, geometric parameters, electrode-to-work distance (arc length). These will be briefly discussed in the following sections.

### 2.3.2 Cautions and preparations to be taken before welding

Titanium at high temperature has a great chemical affinity for numerous elements including those present during the welding operation. These elements like oxygen, nitrogen, hydrogen and carbon, react with the metal and have harmful effects on the alloy properties. In particular oxygen and nitrogen can embrittle welds. The joint edge of titanium should be brushed using stainless steel brushes and wiped with acetone just prior to welding (McCue & Irving, 1991). Pickled mill surfaces usually require cleaning with acetone. All rough surfaces or gouges that retain cutting oxides or dirt must be ground out, as they are likely to cause porosity. It should also be mentioned that a weld

preheating is not required for CP titanium or for titanium alloys. Furthermore, it is desirable to scratch brush the joint after each weld pass to remove any oxide film formed during welding.

### 2.3.3 Shielding gas and its flow rate

Because of the inherent risk of porosity and embrittlement due to surface oxidation and contamination in TIG welding, the importance of efficient gas shielding cannot be stressed too highly (Woolcock & Ruck, 1980). Hydrogen embrittlement (Barrett, 1954), which decreases the ductility of the weldments by hardening the metals, is the most common welding defect found in the welding of titanium and its alloys. It may be caused by the improper value of gas flow rate (Levy & Wickham, 1955), impurities in the shielding gas, or lack of the shielding gas during solidification, i.e. removing the shielding gas during solidification.

In fact, there exists a critical value of shielding gas flow rate for each thickness of material being welded. A gas flow rate higher or lower than this value may cause contamination which in turn affects the weld's ductility and fracture toughness. For example, in a study by Mitchell (1965), porosity in titanium welds increased with increases in the welding torch gas flow rate (primary shielding) but decreased with increases in the back-shielding gas flow rate.

The primary concern with welding in the open air is adequate inert gas shielding of (i) the molten weld pool and adjacent BM (primary shielding), (ii) the hot, solidified weld metal and HAZ (secondary shielding), and (iii) the back side of the weld joint (back shielding).

Levy and Wickham (1955) showed that the gas pressure setting is fairly critical and that it varies with the metal thickness and machine settings. The higher the current and the greater the thickness, the higher the gas flow rate. Too high a pressure causes the fused joint to have concave areas along its face due to the argon pressure (Sewell, 1989), and creates a gas flow pattern that tends to roll contaminating air into the joint. Reduction of this pressure to a critical value results in an optimum protection of the joint.

In addition, gas pressure on the root side of the weld is the key to a weld with no filler metal added. It is the dual function of the back-up gas to protect the weld from air

contamination and to create a pressure that will prevent the fused weld metal from dropping through forming a convex protrusion on the underside of the weld and a concave depression along the top surface.

A typical argon gas shielding condition for 2.6 mm IMI 318 sheet suggested by Thomas and co-workers (1992) is: Torch inert gas, 83-111 $x10^3$ $mm^3s^{-1}$; Trailer inert gas, $56x10^3$ $mm^3s^{-1}$; Backup inert gas, 42 $x10^3$ $mm^3s^{-1}$.

### 2.3.4 Pulsed welding current

The welding current was found to have a significant effect on increasing the depth of penetration and the peak temperature of a thermal cycle (sections 2.2.2 and 2.2.3) and thus the mechanical properties (Vishnu *et al.*, 1991). However, when the welding current was increased beyond a certain value, the surface conditions of the weld bead became unsatisfactory. For a given sheet thickness, there exists a maximum limiting current that gives the deepest penetration with a good bead surface.

The pulsed technique has been found to be particularly beneficial in controlling penetration of the weld bead (Grist, 1975), even with extreme variation in heat sink. Such variations are experienced either through the component design, thick-to-thin sections, or from normal production variations in component dimensions, fit-up, clamping and heat build-up. In conventional continuous current welding, where a balance must always be achieved between the heat input from the arc, the melting to form the weld pool and the heat sink represented by the material or component being welded, penetration is greatly influenced by these variations. However, in pulsed operation, rapid penetration of the weld pool during the high current pulse and solidification of the weld pool between pulses markedly reduces the sensitivity to process variation through the effects of heat build-up and/or disparity in heat sink. (Muncaster, 1991)

Welding thick sections at too low a pulsed current can result in loss of most of the advantages of pulsing (controlled depth of penetration and tolerance to variation in heat sink) as the weld pool takes a long time to penetrate the material and thermal diffusion occurs ahead of the fusion front. In welding thinner sections with too high a pulsed current, the excessive arc forces may cause cutting and splashing of the weld pool, resulting in a poor bead profile and electrode contamination.

### 2.3.5 Welding power source and voltage

The power source necessary to maintain the TIG arc has a drooping voltage-current characteristic which provides an essentially constant current output even when the arc length is varied over several millimetres. Hence, the natural variations in arc length which occur in manual welding have little effect on welding current level.

Although the arc voltage (alternatively named load voltage) does not remain constant as it increases or falls during welding due to arc characteristics and varies with the current and arc length (Bromage, 1968), there is a standard reference which establishes a characteristic of the 'theoretical' standard arc and is defined by Equation 2.14 below:

$$V_L = 10 + 0.04\, I_i \qquad (\text{for } I_i < 600A), \tag{2.14}$$

where $V_L$ is the load voltage and $I_i$ is the initial current

An increase in arc voltage produces a more intense application of heat (Cornu, 1988) with the advantages like: better penetration; pre-heating is rarely required; possibility of welding more quickly or with fewer passes; lower viscosity of the weld pool; improved gas evolution and thus improved weld consistency.

### 2.3.6 Welding speed

The higher arc energy associated with argon gas allows higher operating speeds. This effect is particularly marked when TIG welding with direct current, electrode negative (DCEN). In addition, small changes in the welding speed can affect the geometry of the weld bead, i.e. its depth of penetration and its width (Wareing, 1988), although the effect of welding speed on the depth of penetration is relatively less as compared to the welding current. If the speed is high and the effective current low, the HAZ and the FZ are small, which prevents the overheating of the BM. However, at high welding speeds, undercut can appear at the weld edges.

### 2.3.7 Geometric torch parameters

Selection of electrode composition and size is not completely independent and must be considered in relation to the operating mode and the current level. Electrodes for DC welding are pure tungsten or tungsten with 1, 2 or 4% thoria, the thoria being added to improve electron emission which facilitates arc ignition (Muncaster, 1991).

The electrode diameter is determined by the range of currents used (Cornu, 1988). Up to 250A, an electrode of 3 mm diameter is sufficient (Charlotte, 1981). A cone angle of the electrode of 35° is the best for lower currents and 60° for higher currents. The height of the arc of 1.5 ± 0.5 mm has been determined experimentally to be the optimum height.

### 2.3.8 Heat transfer efficiency

The heat transfer efficiency describes the welding process in two ways, namely arc efficiency and melting efficiency. Arc efficiency gives a quantitative measurement of the fraction of total arc energy delivered to the substrate, and the melting efficiency is the fraction of the energy delivered to the FZ. In order to utilise accurately heat flow models of a weld, it is important to know the arc efficiency. The arc efficiency must also be taken into consideration in order to measure the experimental melting efficiency. The arc efficiency is only slightly affected by welding parameters. Bromage (1968) has shown that increasing the arc gap decreases the arc efficiency. Therefore, in order to minimise the energy lost to the environment, it is necessary to control the length of the arc gap.

Melting efficiency depends strongly on the arc power and welding speed (Wells, 1952; Okada, 1977; Fuerschbach & Knorovsky, 1991). Careful adjustment of welding parameters can minimise wasted process energy and reduce the size of the HAZ. The optimum welding parameters can be predicted in terms of melting efficiency from the relationship between the arc power, welding speed and the melting efficiency. Although the heat transfer efficiency is varied by the welding parameters, experiments carried out in recent years (Giedt *et al.*, 1989; Fuerschbach & Knorovsky, 1991) show that the heat transfer efficiency of TIG welding is about 0.8. However, 0.6 is practical in most laboratory set-up and is adopted in this dissertation.

### 2.3.9 Typical defects and penetration depth in TIG welding

The defect types which may occur in TIG welding are similar to those appearing in other welding processes, e.g. lack of root penetration, lack of side-wall fusion, undercut, porosity, weld metal cracks, etc. One of the main problems in TIG welding is maintaining a uniform degree of penetration. Difficulties occur if adequate attention is not paid to minimise variations which may arise, such as: process parameters like component dimensions and joint fit-up; welding parameters; and material.

Special mention must be made of variations in penetration which are caused by minor differences in material composition (Pollard, 1988). These are generally known as cast-to-cast variation, two lots of material conforming to the same nominal specification may produce vastly differing weld bead shapes when welded with exactly the same welding procedure (Heiple & Roper, 1982; Wareing, 1988). This problem has been attributed to the small differences in the level of impurity elements in the material. Two process techniques, which are capable of improving the tolerance of the TIG operation to variations in material composition, are low frequency current pulsing (Grist, 1975) and the selection of the shielding gas composition, both have been mentioned earlier in the chapter.

## 2.4 Qualification of titanium welds through inspection and mechanical testing

The investigation presented in this dissertation was conducted to gain a better understanding of the effect of heating and cooling rates on the mechanical properties of the advanced α/β titanium alloy IMI 318 as well as CP grade titanium. The former was selected for study since it is the most commonly used titanium alloy and enhanced behaviour would further extend its use. The microstructural and mechanical properties of IMI 318 TIG arc welds were examined in the as-welded condition.

### 2.4.1 Visual inspection

A good weld normally should exhibit a uniform width and an even, smoothly rippled surface with no pin holes, cracks, or gaps, and no holes burned through the material. The reaction between titanium and oxygen and nitrogen becomes significant at approximately 500 °C. Consequently, thin layers of oxide form on the surface of titanium, which cause interference colours to be generated. These colours are related to the oxide thickness and are conventionally used to give an indication of the degree of contamination which has occurred, as indicated in Table 2.3 (Yonesawa, 1987; Gittos & Scott, 1993).

### 2.4.2 Mechanical properties

A number of studies (Lewis & Wu, 1963; Schwenk *et al.*, 1967; Mitchell & Tucker, 1969; Hatch, 1973; Simpson & Wu, 1974) have shown that it can be difficult to achieve satisfactory properties when welding some high strength α/β titanium alloys. It has become necessary to develop unique welding procedures and techniques to control the *α-β* phase transformations and precipitation reactions responsible for the deleterious weld properties in these materials. For instance, it has been demonstrated that control of weld heating and cooling rates by preheating could improve the toughness of Ti-6Al-6V-2Sn (Ti-662) welds (Lewis & Wu, 1963).

Factors affecting mechanical properties of α/β alloys

*(i) Cooling rate*

It was found in previous studies (Wu, 1961; Wu, 1965) that the mechanical properties of *α/β* titanium alloys are cooling-rate sensitive. High cooling rates produce more α and thinner α platelets, which lower toughness and reduce weldability. Slow cooling rates promote the growth of α plates that enrich the β phase with β stabilisers. The enriched phase has a lower *β*-transus ($M_s$) temperature and, hence, a lower tendency to transform to α, preferring to remain as retained β at room temperature. Large and tough α plates produced by slow cooling rates divert crack propagation paths and possibly reduce crack propagation by blunting the crack tip. On the other hand, thin martensitic α plates will provide a poorer medium for energy absorption and limit resistance to crack propagation. These mechanisms, of course, are directly related to the strength, ductility and fracture toughness of these alloys. Therefore, once the effect of cooling rate is determined, control techniques for improving mechanical properties can be explored, if needed, in a systematic manner.

In addition to the cooling rate which is affected by welding parameters, mechanical properties of *α/β* titanium alloys, such as IMI 318, also strongly depend on their interstitial element content, prior *β* grain size and homogeneous microstructures (Greenfield *et al.*, 1972; Chesnutt *et al.*, 1976; Lin *et al.*, 1984; Enjo *et al.*, 1988). These influences are detailed in the following subsections.

*(ii) Grain size*

It is a well-established fact that grain boundaries affect the strength of the metallic materials at low temperatures. Since slip cannot go directly from one grain to another, grain boundaries act as barriers during dislocation glide. The result is that the energy required for slip or cracks to propagate in metallic materials with finer grains is higher compared to that in metallic materials with coarser grains. Grain boundaries have proved to be significant obstacles to the growth of cracks (Zhang, 1989). Moreover, dislocations would pile-up at grain boundaries and hinder further dislocation motion. Becker and co-workers (1992) showed that for titanium alloy Ti-5Al-5Sn-2Zr-4Mo, the ultimate tensile strength decreased moderately and the elongation decreased significantly with increasing grain size, which follows the Hall-Petch relationship. Therefore, grain refinement

processes which result in more grain boundaries may improve the strength and ductility of material.

It is generally agreed that the slower the solidification rate and cooling rate, the coarser the grains are. Broderick and co-workers (1985), using a rapid solidification (RS) technique, found that the microstructure of as-solidified IMI 318 was martensitic, with the martensite size decreasing with $\beta$ grain size, L, (μm), which in turn decreased with increasing cooling rate, R ($Ks^{-1}$). Furthermore, it was found that $L = 3.1 \times 10^6 R^{-0.93\pm0.12}$. This mathematical relationship suggests that the grain size of the $\beta$ phase and also the grain size of the martensite phase, increases with a decrease in the cooling rate. This is because the embryos, which are smaller than a critical size for grain growth, are easy to re -dissolve into the molten metal pool when the temperature is high. Only a few embryos can grow into nuclei successfully with a slower solidification rate, therefore the grains are few and coarse. The results of applying RS to other alloy systems suggested that fine grain size could be produced in rapidly solidified IMI 318, leading to enhanced mechanical properties similar to those reported in an Ti-Mo-Al alloy produced at high cooling rates (Belov & Polkin, 1982).

Similar results suggested that a lower cooling rate resulted in significantly greater $\alpha$ plate coarseness (Becker *et al.*, 1992). This resulted in a lower strength. On the other hand, it was found that reducing the $\alpha$ plate thickness will increase both tensile strength and ductility (Chen & Devletian, 1990). Thus, it is believed that the strength of the weld metal with high solidification rates and cooling rates may be higher than that with low rates, if the grain size effect is the only factor affecting the strength and ductility of the weld.

*(iii) Martensite formation*

Martensite would be formed in $\alpha/\beta$ titanium as in carbon steel by fast cooling. When an α/β titanium alloy cools from the α+β transformation temperature, $\alpha$ phase and $\beta$ stabilisers are precipitated. A slow cooling rate promotes precipitation of the $\alpha$ phase and $\beta$ stabilisers. The ejected $\beta$ stabilisers enrich the untransformed $\beta$ phase, and so, improve its stability. The enriched phase has a lower $M_s$ temperature and, hence, a lower tendency to transform to martensite. It was shown that for Ti-662 (Wu, 1981), the relative percentage of $\alpha$ phase and martensite $\alpha$ phase (α'), and the fineness of the α plates, all of which can be altered by different cooling rates, affected the mechanical properties of the alloy, including the tensile strength of the weldment FZ.

Furthermore, Becker and co-workers (1992) suggested that martensite began to age immediately after it was formed during cooling and when the martensite aged, the fine $\alpha$ which precipitated from it would increase its strength. It is expected that the faster the cooling rate, the finer the $\alpha$ precipitation and the higher the strength. On the other hand, it may also be suspected that the $\beta$ stabilising elements may distort the unit cell of titanium at room temperature if the cooling rate is too fast and that it may also affect the strength of the alloy. However, this distorted structure only strengthens the material a little.

For $\alpha$ alloys, it is believed that the cooling rate has no significant effect on their strength or ductility (Voldrich, 1953). These properties are governed only by the solid solution effect which is discussed next. This is because $\alpha$ alloys transform completely to $\alpha$ even under rapid cooling.

*(iv) The solid solubility of interstitials and their effect in titanium*

Observations and studies of titanium welds porosity has led researchers to look into the solid solubility of interstitials, particularly O, N and H. The rejection of a gas from a cooling molten pool because of decreasing solubility is the essence of the classical explanation for porosity in welds. A number of researchers (Gurevich *et al.*, 1968; Erokhin & Oboturov, 1971) suggested that the formation of pores is due to diffused hydrogen, nitrogen rejected from solution and oxide formed by oxidation or surface contaminants. Besides porosity, the attainable mechanical properties of CP titanium depend to a large extent on the level of interstitial elements present in solid solution with the metal, either as impurities or deliberate additions.

It is generally accepted that in principle residual elements, O, N, C and iron included, account for the increases in the strength observed in CP titanium and that this is achieved through solid solution strengthening and to some extent microstructure control. Interstitially dissolved oxygen strengthens the lattice while preserving the corrosion resistance of the $\alpha$ phase. Oxygen acts to refine the microstructures of the $\alpha$ phase (Jaffee & Campbell, 1949) unlike nitrogen, which promotes acicular grain morphology. The high solubility of oxygen and nitrogen in titanium, however, has been historically considered more of a detriment than an asset. In the early days of titanium production, interstitials were blamed for premature failure and erratic material performance (Kessler *et al.*, 1955; Kotfila & Burte, 1955). Moreover, inclusions such as refractory oxides can act as crack

initiation sites, while thick oxide layers reduce mechanical properties such as fatigue strength, thus their removal is advisable (Donachie, 1988).

Titanium is used in many applications where hydrogen is present and, although the surface oxide layer is virtually impermeable to hydrogen, titanium alloys are not immune to hydrogen attack (Fromm, 1986). Hydrogen may enter the lattice during pickling or welding. It has been linked to reduced impact strength, reduced notch tensile strength, and delayed crack phenomena (Williams & Jaffee, 1960; Beevers *et al.*, 1968). Hydrogen ingress can occur under highly reducing conditions, and absorption is generally enhanced by temperatures above 353K (Williams *et al.*, 1969; Covington, 1979). Surface contamination increases the amount of absorbed hydrogen, and when the surface oxide is unstable or has eroded away, embrittlement can be severe (Covington, 1979).

There are several ways in which hydrogen can affect a material. First, hydrogen can react with the metal to form a discrete hydride phase when hydrogen concentrations exceed 200 ppm (Kotfila & Burte, 1955). Second, hydrogen can interact with dislocations and internal cracks, affecting the plastic behaviour, such as dislocation generation and mobility as well as crack formation and growth. Finally, it can diffuse monatomically to pores or cracks in the lattice and recombine to form bubbles and gas pockets. Hydrogen may also affect mechanical properties even at 'safe' levels below 125 ppm in both $\alpha$ and $\alpha+\beta$ titanium alloys (Meyn, 1974; Wasz *et al.*, 1993). Transmission electron microscopy (TEM) studies have shown that both interstitial hydrogen and hydrides have a strong effect on dislocation formation and generation (Shih *et al.*, 1988).

*(v) The role of interstitials in the mechanical properties of titanium alloy welds*

Titanium and its alloys exhibit high reactivity with other elements, with a notable affinity for oxygen, nitrogen, hydrogen, and carbon. As shown in Table 2.4, the solubility of these interstitial elements in titanium and aluminium are greater by several orders of magnitude than other commonly used metals. The higher the interstitial content, the higher the strength, hardness and $\beta$-transformation temperature. The heavy interstitial elements, such as oxygen, nitrogen, and carbon, are $\alpha$ stabilisers, whereas iron and hydrogen stabilise the $\beta$ phase and lower the $\beta$ to $\alpha$ transformation temperature (Donachie, 1988).

Nitrogen, oxygen and carbon

Amounts of these interstitial elements affect the strength, ductility, fracture, and hardness of titanium. Small amounts of carbon, oxygen or nitrogen absorption during welding can strengthen the weldment, with carbon having the strongest effect and nitrogen the weakest (Conrad, 1966). This is because the carbon, oxygen or nitrogen atoms in titanium obstruct dislocation motion. Voldrich's study (1953) revealed that when the amounts of nitrogen and oxygen were less than 0.1% and 0.15% respectively in the weld, they increased the strength of weld metal significantly by an increasing amount. However, when the amount of nitrogen and oxygen increased to more than 0.1% and 0.15% respectively, the strengthening effect was poor because of embrittlement. Micro-cracks were then observed. At low temperatures, fracture in titanium alloys containing oxygen equivalents of less than 1.5% (e.g. in which case CP titanium and IMI 318 are examples) occurs by ductile shearing, preceded by necking and failure by microvoid coalescence at temperatures as low as 78K. The ductility of the oxygen bearing alloys is substantial less than that of CP titanium. Fracture strains decrease with increasing oxygen content (Conrad *et al.*, 1978). Elongation decreases with increasing oxygen content, and the rate of the decrease is largest at the lowest oxygen concentrations. Dependence of the fracture stress on the grain size in CP titanium follows the Hall-Petch equation (Sargent *et al.*, 1976). A hardness increase proportional to the square root of concentration for oxygen, nitrogen, and carbon was also noted (Okazaki & Conrad, 1973).

Hydrogen

In most $\alpha/\beta$ alloys, hydrogen significantly modifies the tensile properties (Beachem, 1977). Small amounts of hydrogen cause embrittlement of titanium. Hydrogen is readily absorbed by titanium and is detrimental because a number of alloys are susceptible to hydrogen embrittlement, particularly in aqueous environments. Although the precise mechanism for embrittlement is uncertain, it seems likely to arise either from the formation of brittle plates of a titanium hydride, or from the directed diffusion of hydrogen to highly stressed regions such as crack tips, thereby assisting crack propagation. Respectively, it should also be noted that hydride formation occurs most readily in alloys containing aluminium (Polmear, 1995) and that the presence of oxygen may enhance hydrogen embrittlement by reducing the lattice solubility of hydrogen, thereby increasing the amount of precipitated hydride.

On the other hand, the effects of hydrogen on un-notched tensile properties in CP titanium are limited at room temperature and moderate strain rates (Wasz *et al.*, 1989).

For hydrogen concentrations below 200 ppm, only small reductions in ductility are observed and there is no evidence of solution hardening, and furthermore, hydrogen concentrations up to 4% had no effect on the hardness (Lenning *et al.*, 1954). However, a study by Clarke and co-workers (1994) showed that grade 2 CP titanium failed by a ductile mode at hydrogen levels up to 500 ppm, but changed to hydride embrittlement when the hydrogen concentration was raised further. In addition, it was believed that if the $\alpha$ grain size increases, the hydrogen tolerance of $\alpha/\beta$ titanium will decrease. This means that the material is easier to embrittle by hydrogen if the $\alpha$ grain size increases.

Fracture strengths decreased for hydrogen concentrations between 0 and 30 ppm, but changed very little from 30 to 85 ppm. Alloys containing the same hydrogen concentrations failed by void growth when tested between room temperature and 573K (Beevers *et al.*, 1968). At temperatures between 77 and 195K and at hydrogen concentrations between 30 and 85 ppm, CP titanium was found to form internal cracks. In recent fracture tests, hydrogen concentrations of 70-90 ppm slightly increased the fracture toughness (Wasz *et al.*, 1990). These results suggest that hydrogen has a greater effect on crack propagation than on crack initiation. This is consistent with TEM observations of enhanced dislocation mobility in the presence of free hydrogen (Shih *et al.*, 1988). However, a later investigation of CP titanium indicated that the slow crack growth rate was not replaced by fast brittle failure until hydrogen concentrations exceeded 600 ppm (Clarke *et al.*, 1994).

Interstitials and welding parameters

Excessively high heat input or poor shielding gas protection in TIG welding, results in severe absorption of oxygen / nitrogen / hydrogen or other elements in the welds. Hence, they cause embrittlement and even reduce the strength of the weld metal due to defect creation like porosity. The degree of porosity can be influenced by welding speed and associated cooling rate. At lower speeds and therefore lower cooling rates, pores have time to grow and escape from the weld pool, while at very high speeds nucleation may be suppressed. On this basis, there is an undesirable and intermediate speed range where there is enough time for pores to nucleate, but insufficient time for all of them to be released (Woolcock, 1982).

*(vi) Degree of homogenisation of microstructures*

While the weldment is being cooled, diffusion of solute elements occurs. The degree of homogenisation depends on (Becker *et al.*, 1992):

a) The initial extent of microsegregation (section 2.2.5);

b) The diffusivity of alloying elements in the particular alloy (section 2.2.5);

c) The length of time experienced at super-transus temperatures.

Item (c) suggests that low cooling rates promote the degree of homogenisation of the microstructures which results in more even properties.

### 2.4.3 Tensile strength of CP titanium and IMI 318 welds

The results of Levy and Wickham (1955) showed that the weld metal of CP titanium is stronger than the base metal (BM). Furthermore, it was found that weldments generated without filler rods were of higher quality than those where filler rods were used. While the results of Thomas and co-workers (1993) showed that the ultimate tensile strength of the weld metal of IMI 318 is lower than that of the BM (1006.2 and 1039.5 MPa respectively), the results of Wu (1981) revealed that the strength of Ti-6Al-6V-2Sn weldment increased with cooling rate and was higher than that of its BM. These weldments were found to fracture in the BM.

The strength across an arc weld is determined by the strength of the weakest "link" in the composite weld region, which consists of the fusion zone (FZ), near-heat-affected-zone (HAZ) where the peak temperature exceeded the $\beta$ transus temperature, and far-HAZ where peak temperatures were below the $\beta$ transus, and the BM. If arc welds are produced in solution-annealed base material, joints commonly fracture in the BM due to a slightly higher strength in the weld metal owing to oxygen pickup or the initiation of second phase precipitation if cooling rates are sufficiently slow. Following postweld heat treatment, the presence of a coarse $\beta$ grain structure in the FZ combined with the formation of $\alpha$ preferentially along these grain boundaries (in addition to its precipitation homogeneously within the $\beta$ grains) can promote fracture in the FZ at lower ductility. The reference data from Nippes (1983) shows that the weldments at FZs and HAZs of both CP and IMI 318 have higher strength than the BM.

In the computation of the tensile strength of a specimen, following formulae are used :

$$\text{Tensile strength (if failed at FZ)} = \text{Maximum loading} / (W \times T_G) \quad (2.15\ a)$$

$$\text{Tensile strength (if failed at base metal)} = \text{Maximum loading} / (W \times T_b) \quad (2.15\ b)$$

where W is the gauge width of the specimen, $T_G$ is the specimen thickness at the gauge width and $T_b$ is the average specimen thickness. In sections 6.3 and 7.5.4 of this dissertation, the factors affecting the strength of these alloys will be presented and discussed.

### 2.4.4 Ductility of CP titanium and IMI 318 welds

Ductility is a measure of a material's ability to undergo appreciable plastic deformation before a fracture. It may be expressed as percent elongation (%EL) or percent area reduction (%AR) from a tensile test. Alternatively, the ductility of a weld can be represented by the bend test results. Some published data show that welding generally decreases ductility as measured by bend tests (Lampman, 1990; Baeslack *et al.*, 1993).

Ductility evaluations from bend tests are expressed in various terms such as: percent elongation of outer fibres; minimum bend radius prior to failure; go or no-go (passage or failure) for specific test conditions; and angle of bend prior to failure. Elongation is considered to provide the most reliable and reproducible ductility data. Elongation (e) occurring in the surface fibres, at the outer radius of the bend, is determined from gauge marks that are scribed, inked, or photo-etched on the specimens prior to testing. In addition, elongation may be estimated from the radius of curvature ($r_c$) on the inside surface of the bend, and the initial plate thickness (t), (Smith, 1981) :

$$e = t / (2r_c + t) \times 100 \qquad (2.15c)$$

Welding without filler metal

The loss of ductility in the weld joint is due, in part, to the absorption of gases such as oxygen, hydrogen and nitrogen into the weld metal from the air. These gases become interstitial alloying elements which decrease the ductility of the resulting joint. The use of filler metal extends a path for the air to penetrate the argon shielding blanket around the weld puddle and contaminate the weld. In addition, the oxide layer on the filler metal itself, which is another source of weld contamination, also lowers the ductility. Thus, the reduction in contamination from the surrounding atmosphere is critical in the improvement of the weld ductility. It has been shown that in unalloyed titanium sheets, a significant improvement in the ductility of a weld was observed in terms of transverse and longitudinal bend tests, when it was made without filler rod added (Levy & Wickham, 1955).

Ductility of weld of CP titanium and IMI 318

CP titanium has very good weldability in terms of ductility. With proper attention to the basic welding rules, welded joints in this grade of titanium have a ductility almost as good as the unwelded metal. The $\alpha$ type alloys with only the $\alpha$-stabilising elements, do

not harden when cooled through the transformation range, and consequently the heat effects of welding do not make the weld joint brittle.

The $\alpha/\beta$ alloys however, are susceptible to embrittlement as a result of transformation effects, and the heating and cooling cycle of welding often produces such embrittlement. The single phase $\beta$-alloys, some of which have an exceptionally good combination of strength and ductility, are stable enough to withstand the heat effect of welding without embrittlement.

### 2.4.5 Hardness of IMI 318 welds

Hardness is a measure of a material's resistance to localised plastic deformation (e.g. a small dent or a scratch). Both tensile strength and hardness are indicators of a metal's resistance to plastic deformation. Consequently, they are roughly proportional to each other in the case of cast iron, steel and brass. However, the same proportionality relationship does not hold for all metals.

A number of studies (Schwenk *et al.*, 1967; Mitchell & Tucker, 1969; Hatch, 1973) have shown that it may be difficult to achieve satisfactory properties including hardness, when welding high strength $\alpha/\beta$ titanium alloys. In general, the welds in these alloys exhibit increased strength and hardness but a decreased ductility and fracture toughness compared to the BM. Also, it is well established that the microhardness values of titanium alloys increase with increasing interstitial element content and decreasing $\alpha$ plate thickness (Brooks, 1982).

The increase in weld hardness (and decrease in weld ductility) increases with increasing quantities of $\beta$ stabilising elements. This undesirable phenomenon can be overcome, at least partially, by altering the welding parameters and cooling rates and by using chemically dissimilar filler wires (Stark *et al.*, 1962; Mitchell & Feige, 1967; Obata *et al.*, 1984), the former is particularly effective. Furthermore, experience in arc welding IMI 318 (Banas, 1974) and Ti-662 (Simpson & Wu, 1974) showed that the variety of microstructural changes induced by welding and postweld heat treatment would favourably affect the hardness of these alloys.

However, in a study of TIG welding of Ti-6Al-2Sn-4Sn-6Mo titanium alloy (Greenfield & Duvall, 1975), when measuring hardness across the weldments in the as-welded condition and some postweld heat treatment conditions, the weld zone and near-HAZ in the as-welded condition were extremely hard compared to the BM (460 $H_v$ vs 360 $H_v$). Moreover, the direct age/stress relief not only failed to lower these harnesses but extended this region farther into the HAZ. Only after a full solution and age heat treatment did the hardness value level out across the weld. A later intermediate postweld heat treatment proved successful in improving the weldability of the alloy. Thus, it is believed that different guidelines for improving weldability may be needed for different titanium alloys, even if they are of the same class.

Also, as pointed out in the above investigations, these studies were mostly limited to post-weld treatments. Thomas and co-workers (1993) attempted to study the effect of pre-weld treatment (solution treated + welded + aged) in improving the electron beam welded IMI 318 alloy. A series of microhardness transverses across the weld joint showed that the hardness across the FZ was relatively higher than the BM (averaged 420 $H_v$). The hardness measurements across the FZ of samples with pre-weld treatment showed a comparatively higher hardness than those of as-welded samples.

Notwithstanding the aforesaid findings, little effort has been spent on the effect of the thermal cycle (i.e. heating and cooling rates) during TIG welding on the hardness of IMI 318. This was investigated in the present study and will be discussed in a later section (section 7.5.3) of this dissertation.

### 2.4.6 Work of fracture and fracture toughness of CP titanium and IMI 318 welds

Crack growth and Griffith's theory of fracture

The effective surface energy to a large extent is a property of fundamental importance in determining the mechanical properties of brittle materials and also ductile materials. It is defined as the work done to create the unit area of new fracture face. During the crack extension process, new free surfaces are created at the face of a crack, which gives rise to an increase in the surface energy of the system.

The Griffith's energy balance criterion for crack growth and propagation is developed using an energy balance approach. The criterion is given as follows:

$$-\frac{\partial U}{\partial A} = \gamma \qquad (2.16a)$$

Where U is the elastic energy stored in the structure, A is the area of the fracture face, and $\gamma$ is the surface energy per unit area. There may come a point during the propagation of the crack when $-\delta U/\delta A$ becomes less than $\gamma$, and external work must be done to keep the crack moving. In such a case, the growth of the crack can be controlled, and it is possible to measure the energy required to make it grow (Berry, 1960). For a given material, $\gamma$ is not necessarily the same for all stages in the fracture process. Two values of $\gamma$ are of particular interest : $\gamma_I$, pertaining to the initiation of fracture, and $\gamma_F$ , the work of fracture, the value averaged over the whole fracture process.

Use of pre-cracked specimens in study of fracture mechanics of titanium alloys

It is, in general, believed that the reason why titanium alloys were considered to be immune from cracking (e.g. stress-corrosion cracking) in mild environments and at low temperatures, is due to the difficulty in initiating cracks. Many titanium alloys including IMI 318, are highly resistant to pitting corrosion whereas in many other materials the pits provide the stress concentration necessary to initiate stress-corrosion cracking. Although this characteristic of titanium alloys is very desirable, it is now standard practice to use notched or pre-cracked specimens (e.g. as used in the Crack-Tip Opening Displacement test), and to apply fracture mechanics techniques when evaluating and comparing the stress-corrosion resistance of different titanium alloys. This result is due to the use of titanium alloys in a number of critical aerospace applications.

Crack-Tip Opening Displacement(CTOD) test (with a 3-point bend load)

In practice, one can limit the amount of elastic energy stored in the specimen at the moment of fracture initiation, i.e. to minimise $\gamma_I$. A reduction in this stored energy can be achieved by shaping the specimen so that only a small load is required to initiate crack growth. The stored elastic energy is proportional to the square of the load, thus it is particularly advantageous to shape the specimen so that fracture begins at a small load. The specimen shape most commonly used in this series of experiments is shown in Figure 2.19. Pre-crack notches are sawn at the centre of the bars to depths c.

The load is applied through three rollers, two of which are fixed directly to the table of the load cell, and the third to the underside of the cross-head. When a load is applied, a stress-concentration of sufficient magnitude exists resulting in a crack initiated before a sufficient elastic energy is available which would break the specimen completely. Furthermore, crack-growth takes place in a "controlled" manner, if the potential energy of the system is increased by deflecting the specimen with a movement of the cross-head. In this set-up, the energy involved is basically the work of fracture growth (i.e. $\gamma_F$ ).

Work of fracture

When a sufficiently deep notch is present, the specimen is weakened to the extent that the total stored energy becomes smaller compared with the surface energy required to break the specimen. In this instance a controlled fracture follows as in Figure 2.20. The work of fracture for a specimen with breath b, depth d and notch depth c, is given (Tattersall & Tappin, 1966) as follows:

$$\gamma_F = \frac{U}{2b(d-c)} \qquad (2.16b)$$

It is suggested that increasing control of crack growth (i.e. decreasing crack velocity) can be achieved by increasing the notch depth (Nakayama, 1965). Specimens with small notches will have a larger proportion of material under high stress compared to specimens with large notches, and thus a higher probability of energy loss. This suggests that the $\gamma_F$ values obtained for deep notch depths will be closer to the true effective surface energy. Davidge and Tappin (1968) found that specimens with $c/d \geq 0.3$ showed controlled fracture for aluminium.

Fracture toughness and $K_{IC}$ value

Fracture toughness is a measure of a material's resistance to brittle fracture when a crack is present. Fracture occurs when the applied stress level exceeds some critical value. Since the stresses in the vicinity of a crack tip can be defined in terms of the stress intensity factor, a critical value of this parameter exists, which may be used to specify the conditions for brittle fracture. This critical value is termed the fracture toughness $K_c$, and $K_{Ic}$ is the plane strain fracture toughness.

Although the three-point bend technique, which is a CTOD test, may not provide a valid $K_{IC}$ measurement, work by Kaufman (1967) and Ahmady (1987) has shown that there is an approximate correlation between the work of fracture and valid $K_{IC}$ data.

Microstructures and grain size effect on fracture toughness

Previous investigations (Soboyejo *et al.*, 1991; James & Bowen, 1992; Davidson & Campbell, 1993; James *et al.*, 1993; Soboyejo & Mercer, 1994) have shown that microstructure strongly affects the fracture toughness of Ti-Al based alloys. A microstructure with a fine grain size gives a lower fracture toughness and a coarse grain size provides a better fracture toughness. It was also confirmed (Yue *et al.*, 1995) that coarse microstructures, by imposing tortuous crack paths, exhibit higher crack resistance than those microstructures where the crack path is more closely confined to the general crack plane. Furthermore, it is known that the microstructure has a very strong effect on fracture toughness and fracture resistance curves (Kumpfert *et al.*, 1995; Pu *et al.*, 1995).

The effect of grain size, volume fraction of $\alpha$ phase, $\beta$ phase of an $\alpha/\beta$ titanium alloy can be represented by the following Equation 2.17 (Fan & Miodownik, 1993):

$$K_{IC}^{C} = \left(K_{IC,\alpha} + k_{F,\alpha} d_{\alpha}^{-1}\right) f_{\alpha c} + \left(K_{IC,\beta} + k_{F}^{\beta} d_{\beta}^{-1}\right) f_{\beta c} + \left(K_{IC,\alpha\beta} + k_{F,\alpha\beta} \overline{d_{\alpha\beta}^{-1}}\right) F_{s} \quad (2.17)$$

Where $K_{IC}^{C}$ is the fracture toughness of an α/β titanium alloy; $d_{\alpha}$, $d_{\beta}$ are the average grain sizes of α grains and β grains respectively, $d_{\alpha\beta}$ is the volume-fraction-weighted-average grain diameter; $f_{\alpha c}$ and $f_{\beta c}$ are the volume fractions of the α and β phases respectively, all other parameters are constant. If all other parameters are kept constant, it is clear that the fracture toughness is dependent on the average grain size. This was later verified in a study on CP titanium (chapter 5.2).

## 2.5 Penetration control of titanium welds through ultrasonic measurement

### 2.5.1 Different modes of ultrasonic waves (Duffill *et al.*, 1989)

There are four modes of ultrasonic waves, these are:

a) Longitudinal or compressive waves
b) Shear or transverse waves
c) Rayleigh or surface waves
d) Lamb or plate waves.

Longitudinal or compressive waves are similar to audible sound waves as they are also compressive in nature. For instance, longitudinal waves are generated by the alternate expansion and contraction of a piezoelectric crystal. Particle displacements are in the direction of wave propagation. Only longitudinal waves can travel through a liquid.

In shear or transverse waves, the particle vibrations are transverse (at right angles) to the direction of wave propagation and they can only exist in materials possessing "shear elasticity", that is, only in solids. Shear waves are generated by passing the ultrasonic beam through the material at an angle and the velocity of shear waves is approximately half of the velocity of longitudinal waves.

Rayleigh or surface waves are similar to transverse waves but differ in that they do not penetrate below the surface by more than one wavelength. This is because the oscillation amplitude decreases rapidly as the wave penetrates below the surface of the material. This velocity is about 8% less than that of transverse waves and they can only propagate in solids. The particle motions of surface waves are a combination of longitudinal and transverse waves and thus follow an elliptical particle motion.

Lamb or plate waves are produced by an angular compression wave launched into a plate. These waves can exit in any mode of particle motion, however, there are two most common modes of vibration motion, symmetrical and asymmetrical. The velocity of the Lamb wave is dependent on type of material, material thickness and wave frequency.

### 2.5.2 Behaviour of ultrasonic waves

Ultrasonic vibrations are reflected at the interface of two different materials when a mismatch occurs in acoustic impedance. Acoustic mismatches are likely to occur in: a water-metal interface, metal-flaw surface interface, or metal-metal interface where the material properties are quite different. When the incident beam strikes the interface, the beam is reflected in both longitudinal and shear modes. The amount reflected is determined by the specific acoustic impedance of the two media. Refraction occurs when the ultrasonic wave changes direction and velocity as it crosses a boundary between different materials. The ultrasonic energy will separate into two modes, one is a longitudinal mode and the other is a shear mode.

As the angle of incidence reaches a certain angle, the refracted beam of the longitudinal component reaches 90° and total reflection takes place. Only shear waves propagate from medium 1 into medium 2. This angle of incidence is called the 1st critical angle. As the angle of incidence reaches a certain angle, all the shear wave energies in medium 2 are converted into surface waves. This incidence angle is called the 2nd critical angle. Thus, between the 1st and 2nd critical angles, only shear waves exist.

The attenuation of an ultrasonic beam is the reduction of the intensity of a beam with increasing distance, which results from scattering and absorption. Scattering results from the fact that the material is not strictly homogeneous. It contains grain boundaries on which the acoustic impedance changes abruptly due to different density, sound velocity and elastic properties. Even when only one type of crystal is present, the material may still be inhomogeneous for ultrasonic waves if the grains are oriented at random. If there is a change in sound velocity in different directions, this property is known as anisotropy, and causes the scattering of energy in different directions. Attenuation due to the grains scattering can be divided into three regions:

1. Rayleigh region

$$\alpha = B_1 D^3 A^2 f^4 \quad for\ \lambda > 2\pi D \tag{2.18}$$

2. Stochastic region

$$\alpha = B_2 D A^2 f^2 \quad for\ \lambda < 2\pi D \tag{2.19}$$

3. Diffusion region

$$\alpha = \frac{B_3}{D} \qquad for\ \lambda << 2\pi D \tag{2.20}$$

where $\alpha$ = attenuation

$B_1, B_2, B_3$ = coefficients involving the longitudinal and shear wave velocities

A = elastic anisotropy of a single grain

f = frequency

$\lambda$ = wavelength

D = mean grain diameter

Absorption is a result of the elastic reaction of the material particles which resist propagation of sound energy producing friction and heat which is finally dissipated. Thus, a rapid oscillation of the particles will lose more energy than slow oscillation; absorption increases as frequency increases.

### 2.5.3 Ultrasonic testing methods

Generally, there are two ultrasonic testing methods, they are the through-transmission and pulse-echo methods. The pulse-echo method will receive major attention in this survey.

Pulse-echo technique (Parker *et al.*, 1985)

The pulse-echo method gives short bursts of ultrasonic energy (pulses) which are introduced into a test piece at regular time intervals. In relation to the size of the incident ultrasonic beam, if the pulses encounter a reflecting surface, some or all of the energy which is reflected is highly dependent on the size of the reflecting surface. The direction of the reflected beam (echo) with respect to the incident beam depends on the orientation of the reflecting surface. The reflected energy is monitored by both the amount of energy reflected in a specific direction and the time delay measured between transmission of the initial pulse and receipt of the echo.

Angle-beam technique

This is commonly used in the pulse-echo technique. The incident sound pulse enters the test piece at an oblique angle instead of at right angles. This approach eliminates echoes from the front and back surfaces and only displays reflections from the discontinuities

that are normal to the incident beam. Only rarely will a back surface be oriented properly to give a reflection indication. The sound beam enters the test material at an angle and propagates by successive zigzag reflections from the specimen boundaries until it is interrupted by a discontinuity or boundary where the beam reverses direction and is reflected back to the transducer.

Angle beam techniques are also useful in flaw location where there is a loss of back reflection. In flaw location , the time base (horizontal scale) on the oscilloscope must be carefully calibrated because in angle-beam testing there is no back reflection echo to provide a reference for depth estimates of the flaw. Usually, an extended time base is used so that flaws are located within one or two skip distances from the search unit.

A shear wave from an angle-beam transducer progresses through a flat test piece by reflecting from the surface at points called "nodes". The linear distance between two successive nodes on the same surface is called the "skip distance". This is important in defining the path over which the transducer should be moved for reliable and efficient scanning.

Moving the search unit back and forth between one-half skip distance and one skip distance from an area of interest can be used not only for the purpose of defining the location, depth, and size of a flaw, but also for the general purpose of initially detecting flaws.

Calibration

Calibration of the device ensures that the appliance is working under normal conditions and providing an accurate value during application. When calibrating the ultrasonic equipment, more interest is given to the beam angle of the probe, time base, linearity, resolution, etc.. There are standard calibration blocks for ultrasonic equipment. The set-up and their use is described in Appendix A.

Before selecting the standard reference blocks, several variables should be considered such as: the nature of the test piece, alloy type, grain size, effects of thermal or mechanical processing, distance-amplitude effects (attenuation), flaw size and direction of the ultrasonic beam. All of these will affect the characteristics of the ultrasonic beam in a test piece.

### 2.5.4 Ultrasonic testing at high temperatures

In an automatic production of high quality weld joints, there is a requirement for a means of measuring weld quality in real time and a feedback control strategy for regulating that quality. Penetration is a good first order indicator of weld integrity, and a lot of effort at weld quality control has concentrated on penetration. The weld penetration is defined by the solid/liquid interface of the weld pool during welding. To interrogate the solid/liquid interface, many researchers have developed models or experiments.

Ultrasonic detection of molten/solid interface

Lott and co-workers (1984), in their study of the problem of ultrasonically detecting, locating and determining the dimensions of molten weld zones in steel, demonstrated that molten weld pools can be detected using longitudinal ultrasonic waves. Information about weld pool depth or penetration, for a simple weld configuration, can be obtained during welding which might be used for closed-loop process control. The weld pool depth is understood in terms of the time difference between two echoes in the A-scan of the forming weld pool. As the pool started to form, the single ultrasound reflected a signal split into two reflected pulses (or echoes) which separated further in time as the pool grew in depth. The first signal came from the solid/air interface, the second from the molten metal/air interface. The time difference between the other two echoes is approximately proportional to the pool depth, as shown in the equation below:

$$d_w = 3.95\delta t \tag{2.21}$$

where $d_w$ = depth of weld pool.

$\delta t$ = time difference between two echoes.

However, further research is needed in several areas and these are discussed below. The high temperature environment near a weld zone presents the problem of coupling ultrasonic energy into a hot test piece. This can be solved by using cooled ultrasonic sensor heads or by momentary contact techniques. Also, with respect to welding geometries which are more complex than the stationary flat plate, a more detailed knowledge of the effects of temperature gradients on wave propagation is necessary. Realistic weld configurations are also likely to require the use of ultrasonic shear waves entering from the top surface of the structure being welded, and an investigation of weld

zone detection by shear waves is necessary. Furthermore, the fact that the ultrasonic signals reflected from liquid/solid interfaces of molten weld pools are quite small is likely to require the use of sophisticated signal processing techniques for detection and analysis of the data.

Change of ultrasonic velocity with temperature

It is commonly known that an increase in temperature will cause an increase in attenuation and a reduction in ultrasonic velocity. The increase in attenuation is thought to be attributable to mechanisms involving the interaction of the waves:

a. with variations of the magnetic state of the material
b. with the crystal structure during any solid state transformations
c. with the growth of the grains

Because of the change in ultrasonic velocity, the weld pool location and dimensions become more difficult to estimate. Thus, the relationship between ultrasonic velocity and temperature is an important parameter when determining the weld pool location.

To investigate this point, Fenn and Wooton (1986) conducted an experiment on a steel rod. The result obtained the relationship between longitudinal velocity of the ultrasound and temperature. This is shown in the following equation:

$$V_L = \frac{8l_{SH}}{t_{(FP-SP)}} \tag{2.22}$$

where $V_L$ = longitudinal velocity
$l_{SH}$ = shoulder length
$t_{(FP-SP)}$ = time interval between first and second primary echoes

It is clear that the velocity gradual decreases by increasing the temperature of the test piece. However, as yet no similar work with concluding results has been carried out on titanium and its alloys.

Grain scattering of ultrasonic waves at high temperatures

At high temperatures, not only is there a decrease in ultrasonic velocity, but also the scattering of the ultrasound produces backscattered noise, called 'grass'. This 'grass' can

easily obscure the back wall echo, thus making it difficult to 'see' the back wall echo. To overcome this problem, signal averaging is applied.

*Signal Averaging*

The back scattered signal is the result of the reflections of all the grain boundaries in the sound beam, and this has a frequency spectrum quite similar to the transmitted pulse and is coherent with the signal obtained by reflection from the back wall. To render this noise signal incoherent, it is necessary to vary the interference path lengths that produce the resulting back scattered signal, whilst at the same time keeping the flaw or back wall echo relatively constant in amplitude and delay time.

Variation of the probe position by about one grain diameter leads to a substantial variation in the scattering signal amplitude, this also leaves the defect or back wall signal largely unchanged. Thus, signal averaging does not and cannot reduce the attenuation due to scattering; but what it can do is to reduce the ability of the back scattered waves to obscure the desired wall or interface signal.

*'Mushy Zone'*

On welding, beside grain scattering, there is a dendritic structure called the 'mushy zone' which is formed in between the solid and liquid phases. This occurs because solidification of the molten metal happens first in this region. The 'mushy zone' causes a poor reflection of the ultrasonic waves.

Ultrasonic response in titanium at elevated temperatures

To control in real-time the penetration depth information about the location of the liquid/solid interface between the molten weld pool and the surrounding solid BM is critical. Ultrasonic techniques can detect and locate the edge of a molten weld pool by virtue of the unique ability of ultrasonic waves to penetrate thick metal structures and be reflected at discontinuities in acoustic impedance such as those that occur at solid/liquid interfaces. For instance, measurement of the ultrasonic wave velocity in 304 stainless steel samples by Lott (1984), using accurate timing of pulses reflected from a weld-pool interface, confirmed that a weld-pool size can be obtained from ultrasonic data.

However, to determine the size of the weld pool correctly from the transit time of the echoes returned from the pool, corrections on weld pool size due to the temperature gradients must be included. Fenn (1989) and Lott and co-workers (1984) commented that

to apply all of these in a real-time basis, it is necessary to take into account the temperature gradient effect, bearing in mind that the weld, during on-line monitoring experiences a temperature as high as the material's melting temperature.

Parker and co-workers (1985) reviewed the relationship between the velocity of ultrasound wave and the temperature of a number of common metals, including their melting points. In other words, a quantitative understanding of the propagation of ultrasonic waves at elevated temperatures near molten weld pools was acquired. Seeing such importance, Fenn and Wooten (1986) successfully confirmed the changes of longitudinal wave velocities and attenuation on steel with temperatures up to 1374 °C.

However, to date no such data and investigation on titanium has been reported. Like other metals, the ultrasonic velocity in titanium is expected to change drastically with temperature; this data is of fundamental importance for the development of any ultrasonic-sensor-based expert control systems. Without such data to correct the ultrasonic beam path length (due to change in velocity), it would be impossible to measure accurately to allow for real-time control and monitoring of the weld quality. Thus, there is a definite and fundamental need to produce the necessary ultrasonic data for titanium at elevated temperatures.

### 2.5.5 Ultrasonic detection and depth measurement for thin-plate welds

Ultrasonic techniques offer very useful and versatile ways to investigate microstructure and geometry of welds in materials. Basically, a transducer operating in the pulse-echo mode converts electrical signals into high-frequency sound waves that travel to the area of the weld pool. When the sound wave hits the metal/molten metal interface, a portion of the energy in the wave is reflected. This ultrasonic echo provides information about the location of the interface.

Various mechanisms exist through which energy can be lost from ultrasonic waves propagating through real materials. Measurement of this ultrasonic attenuation can yield valuable information about the weld geometry (Parker, 1982; Duffill *et al.*, 1989) and internal microstructures (Green, 1981), particularly around the weld bead. Among the inhomogeneities which can cause ultrasonic attenuation, those at grain boundaries and interphase boundaries are more interesting as far as welding control is concerned.

Previous work (Stroud, 1983) examined the compression wave techniques in thicker material up to 100 mm, utilising probes positioned either normal to the welding direction or "head-on" to the welding head. As an automatic welding technique was being utilised, the results were more meaningful with distinct beam path perturbations occurring during welding. However, from the control point-of-view the technique was not usable.

Shear wave techniques were then re-examined over the same material thickness. Much thicker material, than used previously, enabled the technique to be used in a 1/2 to 1 skip mode, an experimental arrangement which immediately produced valuable results. It was found that the apparent beam path lengths were reflections from the liquid/solid interface and not from within the weld pool (George, 1965). The greatest source of inaccuracy in the whole measurement system was due to the frequency of the ultrasound employed. Generally speaking, the higher the frequency of the ultrasound, the higher the accuracy.

Having demonstrated that skip shear waves detected the weld pool accurately, a control algorithm was determined (Fenn & Stroud, 1983). This algorithm can be represented as: "*increased beam path length, decreased penetration; thus, increases current until beam path length decreases to the desired value and vice versa*". A microcomputer was easily capable of controlling the system with sensing from each probe in pulse-echo mode, and current changes of 1000 times per second. A 1000A transistorised power source was available which can pulse from 0 to 100% output at 3 kHz; thus, response rates can be controlled by plate melt rates and should reach an operating maximum. At the present stage of existing hardware, an ultrasonic penetration depth monitor exists which works quite satisfactorily on automatic machines.

Thin-plate welds

The feasibility work for detecting the molten pool started in 1977 (Lott *et al.*, 1983; Lott, 1984). Since then much research has invested in the application of ultrasonic sensors in a real-time basis. However, most work has been done on thick materials (Fenn & Stroud, 1982; Johnson *et al.*, 1986; Stroud, 1989), that is, materials of thickness over 10 mm and very little on thinner materials. One of the possible reasons may be the need to use surface or Lamb waves for "better" ultrasonic detection, which in itself are more complicated to generate and interpret than conventional ultrasonic compression and/or shear waves.

However, even with surface or Lamb waves, these techniques work better for thicker material. Also, though both of these waves offer some advantages in revealing the quality of thin plate welds (Cook & Valkenburg, 1954; Kubiak & Rowand, 1970), they also suffer from constraints. For example, when working with surface waves, the surface of the solid under investigation has to be very smooth (Cook & Valkenburg, 1954). This cannot be easily achieved in practice. Any scratch or defect on or just below the surface will cause an acoustic reflection. However, this may not be desirable if the prime concern of the investigation is on side-wall penetration, as it will give rise to many unwanted signals.

When working with Lamb waves, the generation of pure mode waves require a tight control on the bandwidth and beam spread of the signals produced from the ultrasonic transducer (Alleyne & Cawley, 1992), this involves very complicated procedures and control. Thus, it is worthwhile investigating the possibility of detecting and testing thin-plate welds by conventional shear waves or longitudinal waves.

Table 2.1 : Mechanical properties of some CP grade titanium and IMI 318 (Duncan & Hanson, 1980; Donachie, 1985; Polmear, 1995)

| Material and condition | Tensile strength MPa | 0.2%Yield strength MPa | Elongation % | Minimum bend radius t[a] | Hardness (Vickers) $H_V$ |
|---|---|---|---|---|---|
| Grade 1 | | | | | |
| Unwelded sheet | 315 | 215 | 50.4 | 0.7t | 140 |
| Single-bead weld | 345 | 255 | 37.5 | 1.0 | 140 |
| Transverse weld | 325[c] | - | - | - | - |
| Grade 2 | | | | | |
| Unwelded sheet | 460 | 325 | 26.2 | 2.9 | 165 |
| Single-bead weld | 505 | 380 | 18.3 | 2.9 | 175 |
| Transverse weld | 475[c] | - | - | - | - |
| Grade 3 | | | | | |
| Unwelded sheet | 545 | 395 | 25.9 | 1.9 | 175 |
| Single-bead weld | 605 | 475 | 15.5 | 4.7 | 220 |
| Transverse weld | 560[c] | - | - | - | - |
| IMI 318 | | | | | |
| Unwelded sheet | 1000 | 945 | 11.0 | 2.6 | 320 |
| Single-bead weld | 1060 | 920 | 3.5 | 10.5 | 350 |
| Transverse weld | 1015[c] | - | - | - | - |

[a] t = Sheet thickness [c] Fracture occurred in base metal

Table 2.2 Major mechanical properties of four common titanium alloys (Donachie, 1985)

| Product | Tensile strength | 0.2% Yield strength | Elongation | Reduction in area | Impact strength | Fracture toughness |
|---|---|---|---|---|---|---|
| | MPa | MPa | % | % | J | MPa $m^{1/2}$ |
| Unalloyed Ti | 550 | 480 | 18 | 33 | 35 | -- |
| Ti-5Al-2.5Sn-ELI | 815 | 710 | 19 | 34 | -- | -- |
| IMI 318 | 1000 | 925 | 16 | 34 | 22 | 52 |
| Ti-13V-11Cr-3Al | 1220 | 1172 | 8 | -- | -- | -- |

Note : Products are of wrought bar form and at annealed condition

Table 2.3 : Relationship between degree of discoloration at weld and its characteristics (Yonesawa, 1987; Gittos & Scott, 1993)

| Degree of colouration at titanium weld | Characteristics of weld | Verified result |
|---|---|---|
| Silver | Good weld with no contamination | Pass |
| Gold or barley colour | Weld with hardly any contamination | Pass |
| Purple or blue | There is a small effect on the ductility of weld surface. However, it can be judged that there is generally little effect on weld characteristics. | Pass |
| Light blue | Some degree of contamination | Unacceptable |
| Pale blue or grey | There is a considerable degree of contamination. Ductility deteriorates considerably at the weld of thin plate | Failure |
| White or pale yellow | Very heavy contamination, weld becomes brittle | Failure |

Table 2.4 : Solubility of O, N, C and H in titanium and aluminium at room temperature (Morton, 1976)

| | Interstitial element | | | |
|---|---|---|---|---|
| Metal | Oxygen | Nitrogen | Carbon | Hydrogen |
| Titanium | 14.5 wt % | 20 wt % | 0.5 wt % | 100 ppm |
| Aluminium | < 1 ppm | < 1 ppm | < 1 ppm | < 1 ppm |

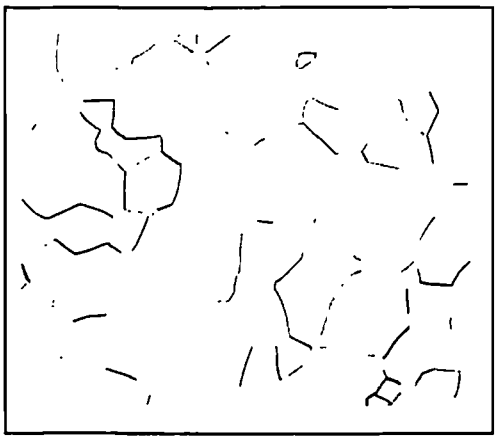

40 µm

Figure 2.1
High-purity (iodide-process) unalloyed titanium sheet, cold rolled, and annealed 1 hr at 700 °C. Equiaxed, recrystallised grains of α. Kroll's reagent (ASTM192).
*(Metals Handbook, Ninth ed., vol. 9, American Society for Metals, Metal Park, Ohio, 1978, p.462.)*

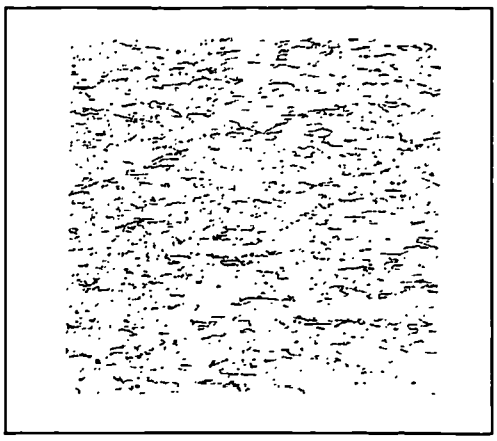

40 µm

Figure 2.2
Commercially-pure (99.0%) unalloyed titanium sheet, as rolled to 1.0 mm thick at 760 °C. Grain of α, which have been elongated by cold working. Kroll's reagent (ASTM192).
*(Metals Handbook, Ninth ed., vol. 9, American Society for Metals, Metal Park, Ohio, 1978, p.462.)*

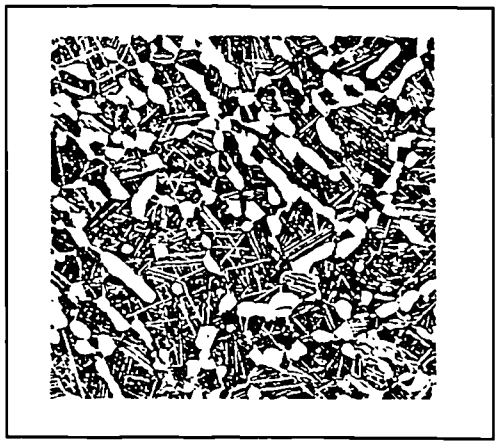

20 µm

Figure 2.3
Ti-6Al-2Sn-4Zr-6Mo, forged at 870 °C, solution treated 2 hr at 915 °C, which reduced the amount of "primary" α grains in the α + β matrix. Kroll's reagent (ASTM 192).
*(Metals Handbook, Ninth ed., vol. 9, American Society for Metals, Metal Park, Ohio, 1978, p.471.)*

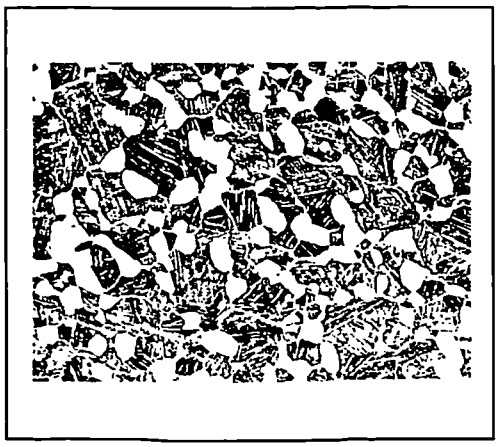

40 µm

Figure 2.4
Ti-8Al-1Mo-1V, forged with a starting temperature of 1005 °C, which is within the normal temperature range for forging this alloy and air cooled. The resulting structure is equiaxed α grains (light) in a matrix of transformed β (dark) containing fine acicular α. Kroll's reagent (ASTM192).
*(Metals Handbook, Ninth ed., vol. 9, American Society for Metals, Metal Park, Ohio, 1978, p.464.)*

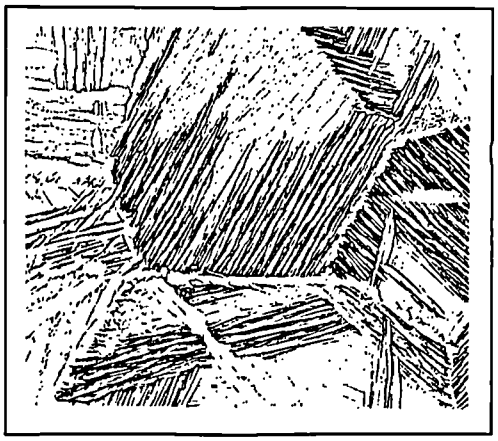

100 µm

Figure 2.5
Ti-5Al-2.5Sn, hot worked below the α transus, annealed 30 min at 1175 °C, then air cooled instead of furnace cooled. The faster cooling rate produced acicular α that is finer than the platelike α in Figure 2.6. Prior-β grains are outlined by the α that was first to transform. Kroll's reagent (ASTM192). *(Metals Handbook, Ninth ed., vol. 9, American Society for Metals, Metal Park, Ohio, 1978, p.463.)*

100 µm

Figure 2.6
Ti-5Al-2.5Sn, hot worked below the α transus, annealed 30 min at 1175 °C, which is above the β transus, furnace cooled to 790 °C in 6 hr, and furnace cooled to room temperature in 2 hr. Coarse, platelike α is seen. Kroll's reagent (ASTM192). *(Metals Handbook, Ninth ed., vol. 9, American Society for Metals, Metal Park, Ohio, 1978, p.463.)*

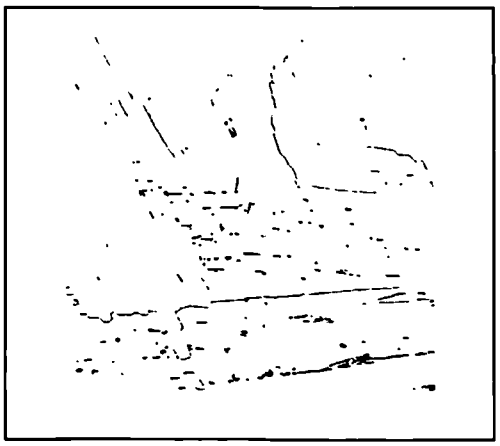

40 µm

Figure 2.7
Same as Figure 2.2, but annealed 2 hr at 1000 °C, and air cooled. Colonies of serrated α plates; particles of TiH and retained β (both black) between plates of α. Kroll's reagent (ASTM 192) *(Metals Handbook, Ninth ed., vol. 9, American Society for Metals, Metal Park, Ohio, 1978, p.462.)*

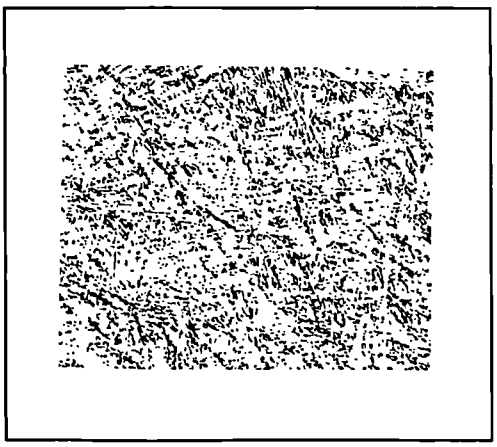

100 µm

Figure 2.8
Ti-6Al-2Sn-4Zr-2Mo forgings, finish forged starting at 970 °C, air cooled, machined to 13 mm diameter test bars, reheated to 995 °C for 1 hr, and then air cooled. The microstructure consists entirely of martensite. Kroll's reagent (ASTM192). *(Metals Handbook, Ninth ed., vol. 9, American Society for Metals, Metal Park, Ohio, 1978, p.465.)*

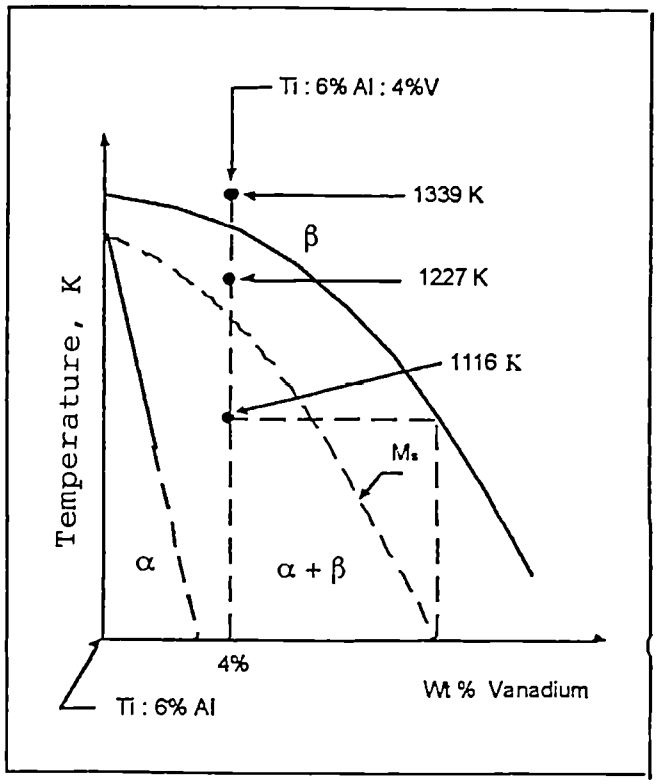


Figure 2.9
Schematic pseudo-binary phase diagram for Ti - 6Al alloy with additions of vanadium. ($M_s$ = martensite start temperature )
*( Willian F. Smith, Second Edition. (1993). Strucutre and Properties of Engineering Alloys. McGraw-Hill, Inc..)*

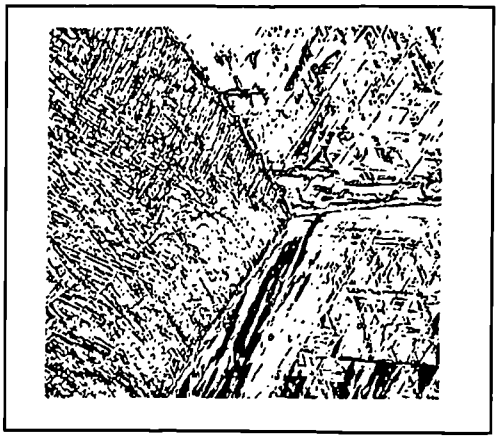


Figure 2.10
Ti-6Al-4V alloy solution-heated at 1066 °C about 50 °C above the β transus and air cooled; the structure consisting of acicular α that is transformed from the β phase; prior beta grain boundaries appear. (10% HF, 5% $HNO_3$, 85% $H_2O$)
*(Metals Handbook, Ninth ed., vol. 9, American Society for Metals, Metal Park, Ohio, 1978, p.467.)*

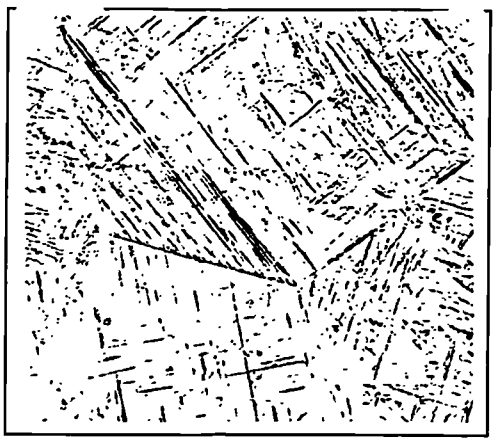


Figure 2.11
Ti-6Al-4V bar solution-heat-treated at 1066 °C for 30 min and water quenched. Structure consists of alpha prime formed by martensite type shear process. Prior beta grain boundaries are evident. (Etchant : 10% HF, 5% $HNO_3$,)
*(William F. Smith, Second Ed. 1993. Structure and Properties of Engineering alloys. McGraw-Hill, Inc. P 463. )*

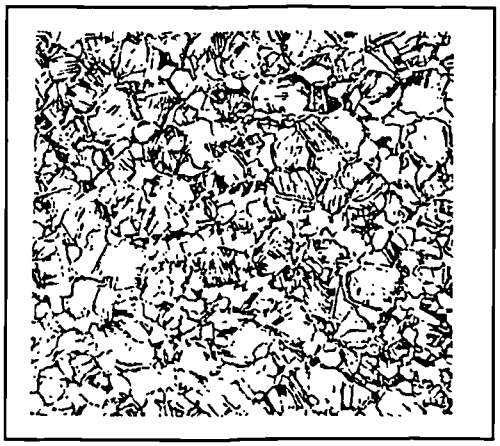


Figure 2.12
Ti-6Al-4V alloy solution heated at 954 °C (about 50 °C below the beta transus) and air-cooled. Structure shows grains of primary alpha (light) in a matrix of transformed beta containing acicular alpha. (10% HF, 5% $HNO_3$, 85% $H_2O$)
*(Metals Handbook, Ninth ed., vol. 9, American Society for Metals, Metal Park, Ohio, 1978, p.467.)*

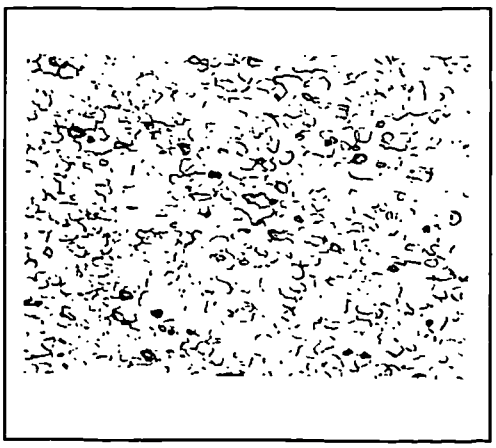


Figure 2.13
Ti-6Al-4V alloy solution heated at 843 °C for 1 hr and water quenched. Structure consists of retained β in an α matrix. (10% HF, 5% $HNO_3$)
*(William F. Smith, Second Ed. 1993. Structure and Properties of Engineering alloys. McGraw-Hill, Inc. P 468. )*

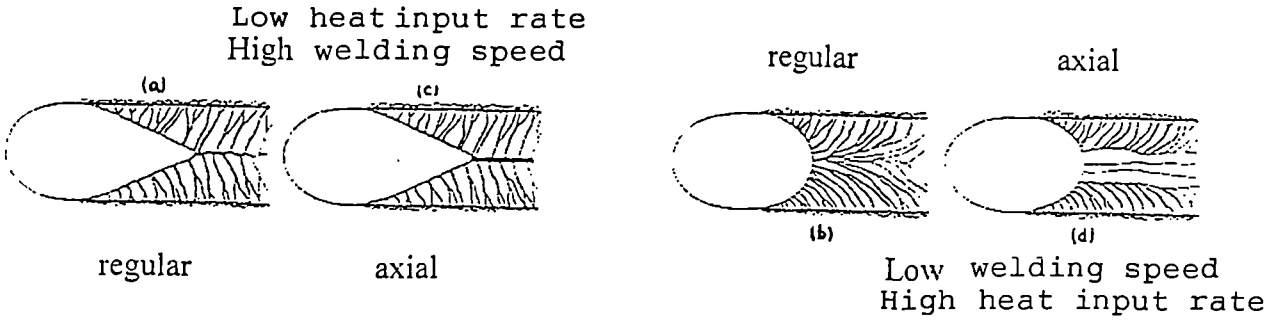


Figure 2.14 The structure and shape of a typical weld pool

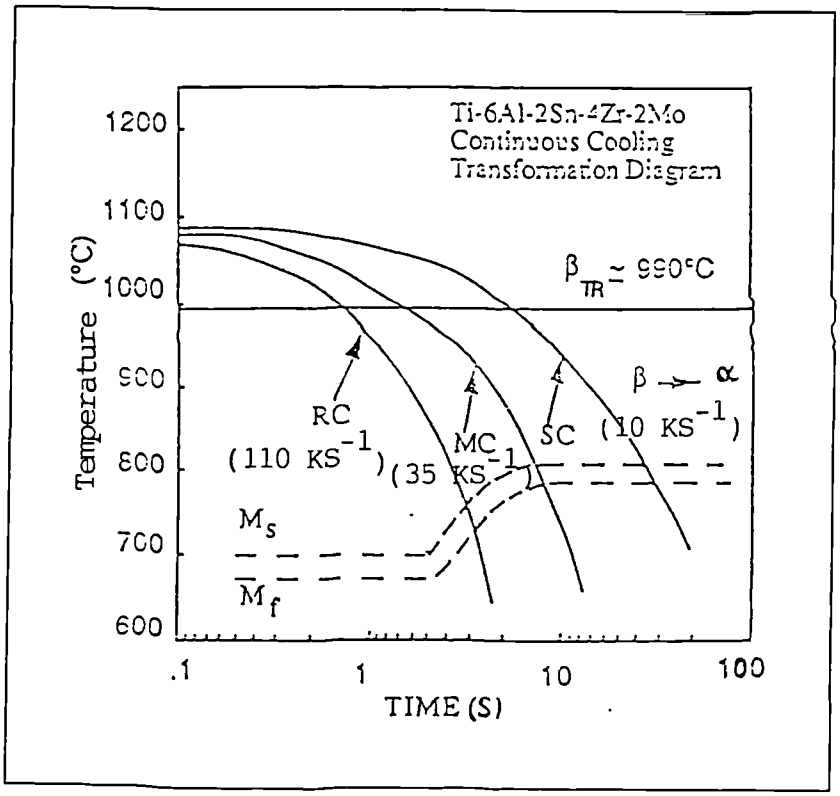


Figure 2.15 CCT diagram for Ti-6Al-2Sn-4Zr-2Mo
(Source : Mitchell & Tucker, 1969)

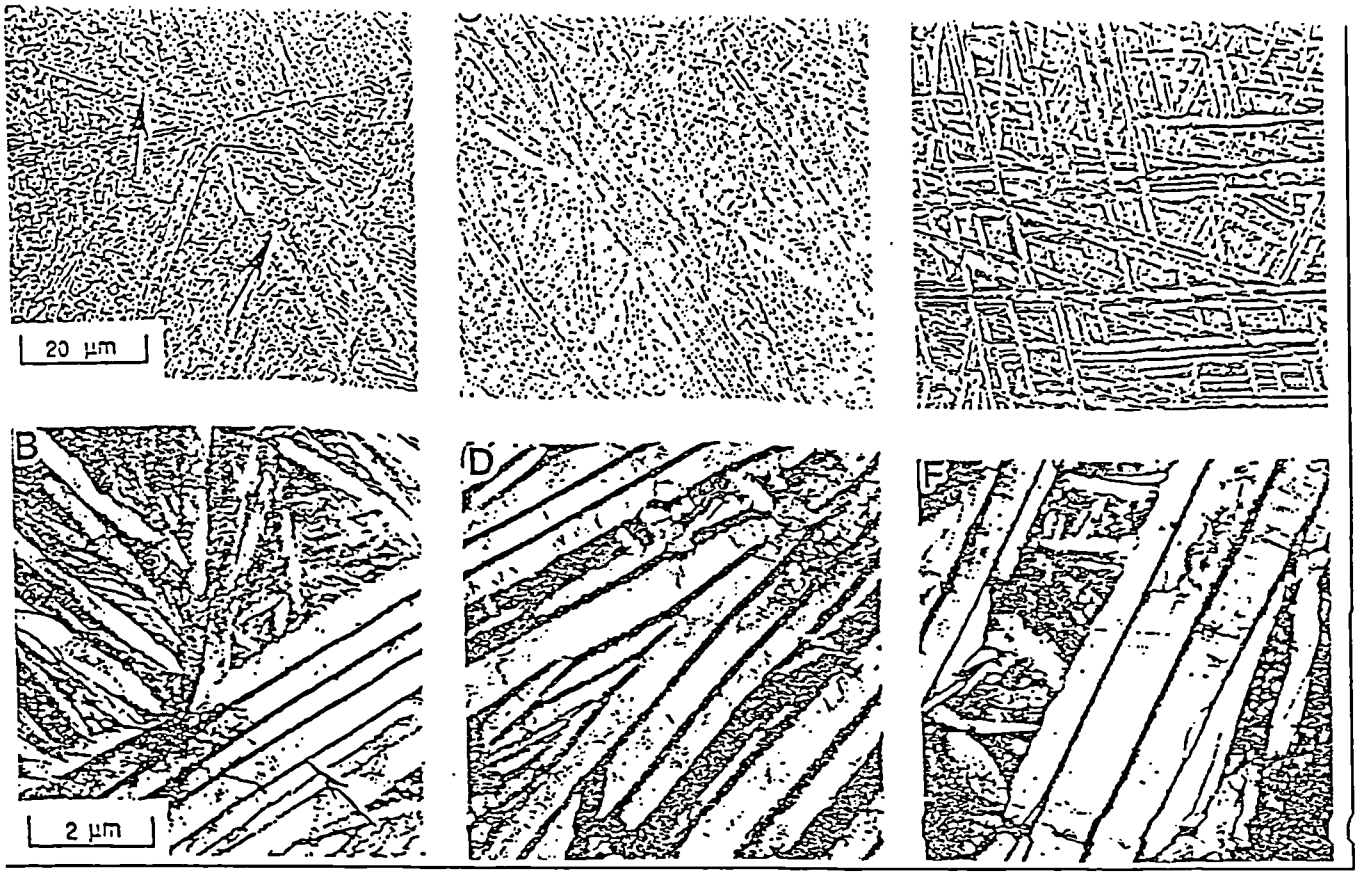


Figure 2.16 : Light and TEM micrographs of TIG weld FZ structures cooled at 110 $Ks^{-1}$ (A,B); 35 $Ks^{-1}$ (C,D); 10 $Ks^{-1}$ (E,F). (Source : Mitchell & Tucker, 1969)

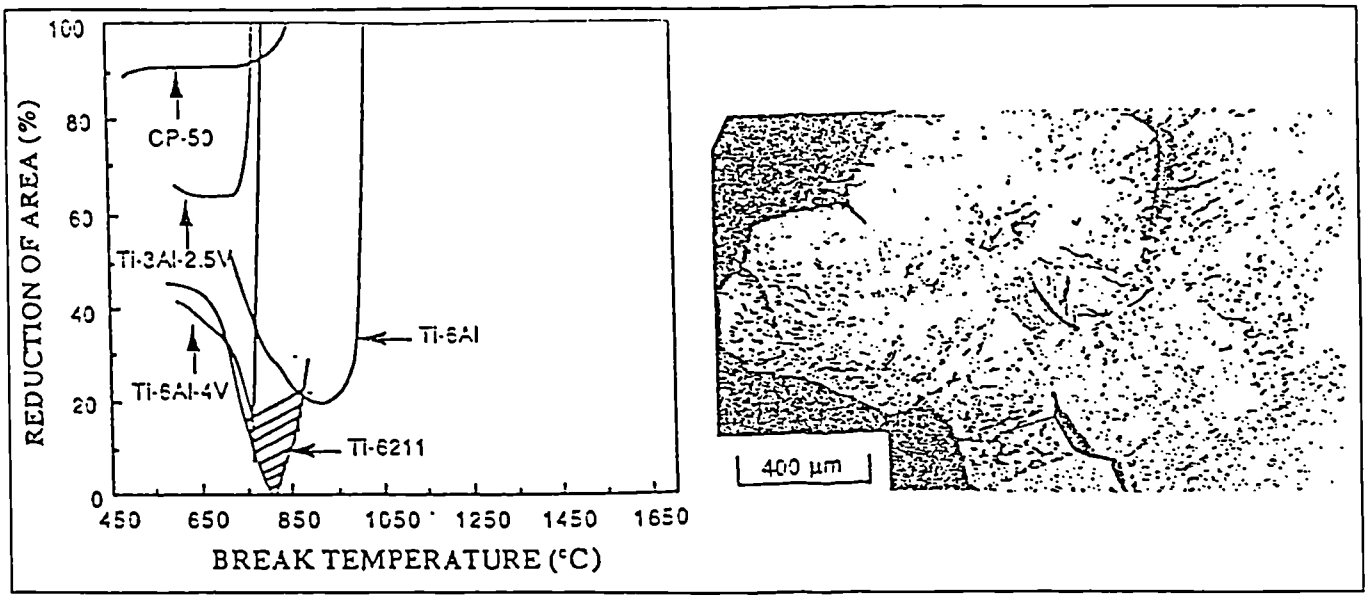


Figure 2.17 : Hot ductility (%RA) verses fracture temperature on cooling form super-transus temperature for near-alpha and alpha-beta titanium alloys (Source : Lewis et al. 1985)

Figure 2.18: Light micrograph of Ti-6Al-2Cb-1Ta-0.8Mo hot ductility speciments fractured at temperature in ductility-dip region showing fracture along prior-beta grain boundaries (Source : Lewis et al. 1985)

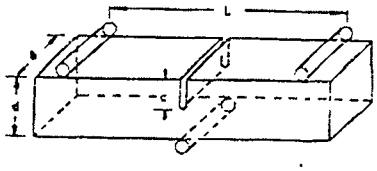


Figure 2.19 Schematic of specimen shape used in the three point bend test

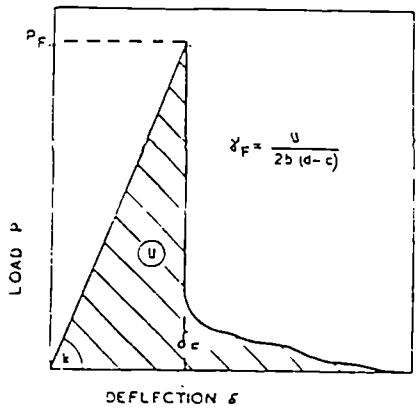


Figure 2.20 Sketch of typical load-deflection curve resulted from a three point bend test

# 3.0 CONTROL OF WELDING SPEED & DEPTH OF PENETRATION

## 3.1 Experimental set-up of welding fixture [@] and clamping fixture

For successful welding of titanium and titanium alloys, complete shielding of the weld was necessary because of the high affinity of titanium to oxygen and nitrogen at its melting temperature (refer to section 2.3.3). Moreover, in order to produce welded joints of a consistent quality, a welding fixture was fabricated to hold titanium sheet of various thicknesses. This device also reduced distortions by maintaining the parts in a rigid position and by removing the absorbed arc heat. The fixture for TIG welding was complied in line with the following conditions :

- Correct presentation of the edges for welding, clamping and levelling.
- Ability to present the joint at a fixed distance in relation to the electrode and limit the distortion due to weld shrinkage. The latter was particularly important in welding thin titanium plates.
- Ability to support the weld pool when full penetration was required.
- Ability to protect the back side of the weld pool against oxidation with inert gas.
- The upper clamps, located near the electrode, should be made of non-magnetic metal to avoid arc instability resulting from magnetic fields.
- Very rigid and robust.
- Ability to withstand clamp pressures of 3 $kNm^{-2}$ on the sheet without noticeable distortion.
- Inclusion of a gap adjustment control for the clamps. This gap should always be reduced to a minimum, especially for very thin sheets.
- Ability to provide a backing support appropriate for the component being welded.

The outline of the fixture is shown as Figure 3.1. The detailed part drawings are contained in Appendix B. The fixture was mounted on one side of a brass base plate. Brass was selected mainly due to the fact that brass has good hot working properties and has better strength than copper. Furthermore, as brass is a non-magnetic material, no arc blow would take place during the welding process.

The fixture composed of five main parts :

i) Base

This was a plate which is made of brass. In the centre of the plate, there was a rectangular pocket, 30 W x 80 L x 10 D (mm) and a 5 mm hole was drilled in the side of the base plate (Figure 3.2). Through this hole, the shielding gas (Argon) could go into the pocket. With a titanium sheet covering the pocket, the pocket served as a pool which was filled with argon gas for back shielding. A gap was designed between the fixture and titanium sheet to allow for a continual flow of shielding gas. Moreover, there was a groove with a depth of 0.5 mm for guiding the titanium sheet to ensure there is no misalignment. On each corner of the base plate, there was a hole for locating the guide pin and spring.

ii) Clamping bars

The clamping bars were also made of brass (Figure 3.3). Each clamping bar had a hole in it through which the guide pins could pass and the clamping bars could move upward or downward along the guide pins. Furthermore, there was a "T-shape" groove on the bottom of the clamping bars in order to clamp the titanium sheet.

Additionally, to achieve secondary front shielding, one side of each clamping bar was drilled with a deep hole and there were a few holes drilled from the bottom of the clamping bar at an inclined angle. The location of holes on the two clamping bars were positioned alternately (Figure 3.4) so as to provide a better coverage of the sheet for shielding gas flow.

iii) Guide pin

There were four guide pins which were 10 mm in diameter and were made of mild steel. The pins were fixed at the corners of the base plate by screws of 4 mm diameter. The purpose of the guide pins was to guide the clamping bars. There was a spring around each guide pin, to allow the clamping bars to rise automatically when the clamps were released.

iv) Clamps

Four clamps were used during a welding process (Figure 3.5). They were located at the side of the clamping bars and were fixed to the base plate. The heads of the clamps were made of rubber which allowed minor variation of titanium thickness in a single plate. The clamps also provided quick release when required. Using these four clamps, the titanium sheet could be held firmly in position and this resulted in minimum distortion during and after welding.

v) Flow control device

As the flow rate of shielding gas could affect the quality of the weld, special attention was given to the design of this part of the fixture (Figure 3.6). To provide adequate and a smooth gas flow to both clamping bars (the source of front shielding) and the pocket (back shielding), valve 'b' controlled the flow rate of the shielding gas which flowed to the bars while valve 'a' controlled the flow rate of the gas to the pocket (Figure 3.7).

vi) Overall specification of the welding fixture

(a) Dimension of the fixture : 200 W x 220 L x 68 H (mm)

(b) Clamping method : Four quick release clamps

(c) Shielding method : Secondary front and back shielding

(d) Maximum size of specimen sheet : Width -- 80 mm
Length -- 500 mm
Thickness -- 10 mm

[a] The welding fixture included a Hitachi inverter-controlled welder (model NPII 300) which was used as a pulsed welding power supply. The equipment could be operated in DC or AC mode with variable pulsing frequency.

## 3.2 Hardware to control welding speed

In TIG welding, the control and uniformity of speed of heat input (welding torch or workpiece) was of particular importance. Since it was almost impossible to control and maintain a constant speed in a manual welding operation, an automatic speed control unit was designed and fabricated. The control unit comprised some hardware and electronic components and was controlled by software.

(i) Slideway

A slideway unit was used to control the direction of welding of titanium which consisted of vertical and horizontal slides (Figure 3.8). The basic components of each slide was:

- one set of lead screws and a lead screw nut
- two supporting rods
- a pair of bracket plates
- bearings

The horizontal slide was used to control the welding feed rate and enabled a straight welding path. A stepping motor was connected to the lead screw which was controlled by a personal computer (PC/AT 80286). The vertical slide was used to adjust the gap between the weld torch and workpiece. The design of this slide was the same as the horizontal slide, and the movement was controlled by a stepping motor.

The two slides were mounted together to form a compound slideway. The pitch of the lead screw was very important for controlling the accuracy of the feed rate. The major diameter of the lead screw was 12.5 mm with 0.4 pitch per millimetre. It gave a linear movement with a feed rate of 0.5 $mms^{-1}$ when the stepping motor rotated at 120 revolutions per minute.

(ii) Stepping motor and control circuit

The stepping motor used had an accuracy of 1.8 degrees per step and was controlled by a two-phases excitation operation where two phases of the motor windings were always excited at any one time. The advantage of two-phases excitation over single and half phases was the generation of higher holding torque and lower vibration effects.

The excitation mentioned above was provided by a special integrated circuit chip PMM8713 (Figure 3.9). This could generate different sequence signals according to the signal it received from a PC via an interface card. Transistors TIP122 were used to amplify the signal to drive the stepping motor.

(iii) Pulse generator

To enable computerised control over the speed of the welding torch (heat input), a pulse generator was designed to give the necessary pulses to the control circuit 8713. This pulse generator was made up of a PC computer and a 8255 8 bit interface card. The whole block diagram is presented in Figure 3.10.

(iv) Modification of control circuit due to electrical noise and interference

The disadvantage of high frequency (HF) spark devices was the radio-electric disturbances introduced despite its low wattage power. The control unit which consisted of mostly electronic circuits, and particularly the personal computer, were operationally halted once the arc was initiated.

The other source of disturbance was found to come from the mains. Further investigation established that electrical noise from the mains "killed" the electronic circuitry of the automatic control unit while the welding process was in process. Quite a number of integrated circuits (ICs) were replaced during the test trials.

To enable the control circuits above to work as desired, the noise introduced from various sources (e.g. noise from mains) had to be taken into consideration. Thus, some electronics were added to address this problem. Figure 3.11 details the electronics added. This package comprised:

a) A DC voltage converter section which could verify the AC/DC conversion and also "purify" the power source.
b) The 7805 power section which gave a stable 5V source from the power supply to the IC PMM8713.
c) The Darlington transistor TIP122 which amplified the signal controlling the stepping motor.

d) The rest was a filter section which was intended as a filter for any noise that might be carried in the welding current signal. Thus, a much cleaner signal to the control IC (PMM8713) was obtained. This was substantiated by the fact that no PMM8713 was damaged (8 PMM8713s were damaged before) since the installation of the filter section.

In addition, further shielding, grounding, screening and filtering techniques and/or devices were used. These included the following:

a) All cables used in the TIG power supply and automatic control unit were twisted.
b) A filtering circuit was added inside the TIG power supply circuitry to screen the HF noise.
c) Separate power sources were used for the TIG power supply and the automatic control unit.
d) The signal cables were further shielded with thin metal foils.
e) Metallic (Faraday) cage encapsulation was used to limit the HF radiation.

## 3.3 Software and knowledge-based system for acceptable welding parameters

The computer program controlling the welding speed was written in Turbo C which is a highly structured programming language with plenty of built-in libraries for program simplification. In addition, it offered the advantage of being highly readable by other programmers, who could easily make amendments to the existing program when required. The program listing is available from the author. Also, a user-friendly program--"Computer Data Book" (CDB), was designed for the gathering and retrieving of the welding data with the results logged using Lotus Freelance Graphics operating under the Microsoft Windows Version 3.1 operating system. The welding parameter spectrum (e.g. welding current, voltage, welding speed, pulse frequency, etc.) for different material thicknesses, found in previous successful experiments, ultrasonic measurements and physical tests, were inputted into this knowledge-based system. These data were used to activate the welding operation.

The CDB was designed particularly to help new users who want to perform TIG welding on titanium without any background knowledge concerning the parameters which should be selected. In addition, the users could access a lot of welding information about the TIG welding techniques and properties of titanium and its alloys. Representative screens of information available in the CDB are in Appendix C.

The CDB had the capability to include another data base which provided diagnostic information of all possible welding faults and recommendations of their immediate and/or long term rectification and solution. Thus, it served as a useful tool for unskilled operators/users to rectify any welding problem without the supervision of engineering/technical personnel on site.

## 3.4 Adaptive control of penetration depth detected by ultrasonic means

The aim here was to prepare for the automatic running of a welding machine with its depth of weld automatically controlled by the welding speed and current. The depth of weld was measured by an ultrasonicscope and the voltage signal produced by the ultrasonicscope was transmitted to a personal computer for signal processing. A program written in C-Language was used to digitise the analogue signal from the ultrasonicscope. This program calculated the actual depth of the weld and then produced an analogue signal to regulate the welding current and speed of the welding machine (or even pulse frequency) so as to achieve the required depth of penetration adaptively.

The control program as written was the heart of this adaptive control. The program could be divided into three parts. This included the sampling of the analogue signal, the calculation of optimum welding current and speed, and the resulting signal output for regulating the machine input. The C-program started with a collection of signal samples from the ultrasonicscope output terminal by using a 12-bit Analogue-to-Digital / Digital-to-Analogue (AD/DA) converter card.

Then the resulting digital signal was used to find the average value of the penetration depth, this was then compared with the theoretical value in the subsequent operation in the C-program. The resulting difference was used to calculate the actual current or speed value as required. The algorithm of the calculation was based on a previously known relationship between the welding parameter to be controlled (e.g. welding current or welding voltage) and the depth of the weld, keeping the other welding parameters constant.

The program listing of the closed-loop weld-depth control program and its flow chart are attached in Appendix D, whereas the user guide is available from the author.

## 3.5 Standard welding condition and sample preparation for CP titanium and IMI 318

All the titanium sheets were sheared to 85 x 50 mm small plates. The specimens were then cleaned with a steel brush, pickled in $H_2O/HNO_3/HF$ solution, and then degreased with acetone prior to welding. Different welding currents and speeds were used to fabricate autogenous welds on the plates. Unless otherwise specified, other welding conditions employed throughout this study were as following :

| | |
|---|---|
| Configuration : | No filler metal used, autogenous weld bead on plate |
| Electrode : | 1.6 mm diameter, pure tungsten |
| Polarity : | Direct current electrode negative (DCEN) |
| Type of weld : | Single pass with pulsed current |
| Arc length : | 2.0 mm |
| Crater current: | 30 A |
| Initial current : | 70 A |
| Welding voltage : | 12.8 V (computed by using Equation 2.7) |
| Torch inert gas: | $1.0 \times 10^5$ $mm^3s^{-1}$ |
| Back shielding gas: | $1.0 \times 10^5$ $mm^3s^{-1}$ |
| Room temperature: | 20 $^oC$ |
| Heat transfer efficiency, $\eta$ : | 0.6 (refer to section 2.3.8) |

All welds were studied in terms of their surface appearance and integrity of penetration for acceptance. Apart from the special investigation in some of the experimental work, acceptable weldments were the weldments which 'passed' visual inspection where :

i) the colouration of the weld was bright silverly or straw,
ii) no crack / undercut / porosity / tungsten inclusion was observed,
iii) the weldment had complete penetration.

Where a particular size of welded specimens was needed, they were cut by electrical discharge wire-cut machine (EDM). Where microsectioning was conducted, each of the specimens was sectioned perpendicular to the weld. The microsectioned specimens were first ground, polished and etched.

Unless otherwise specified, notations 51xx are the specimen numbers of the welded specimens in section 5.1, 63xx are the welded specimens in section 6.3 etc.

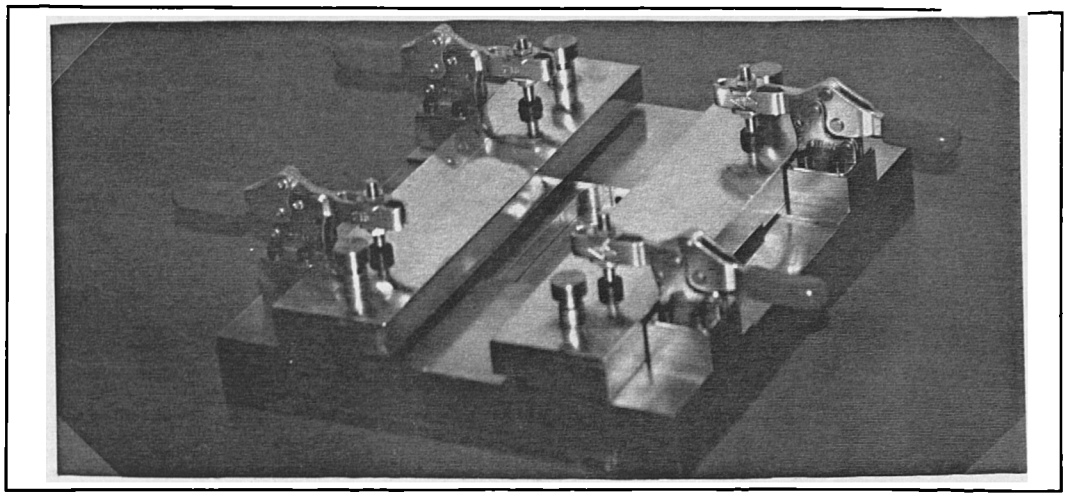

Figure 3.1 Outline of welding fixture

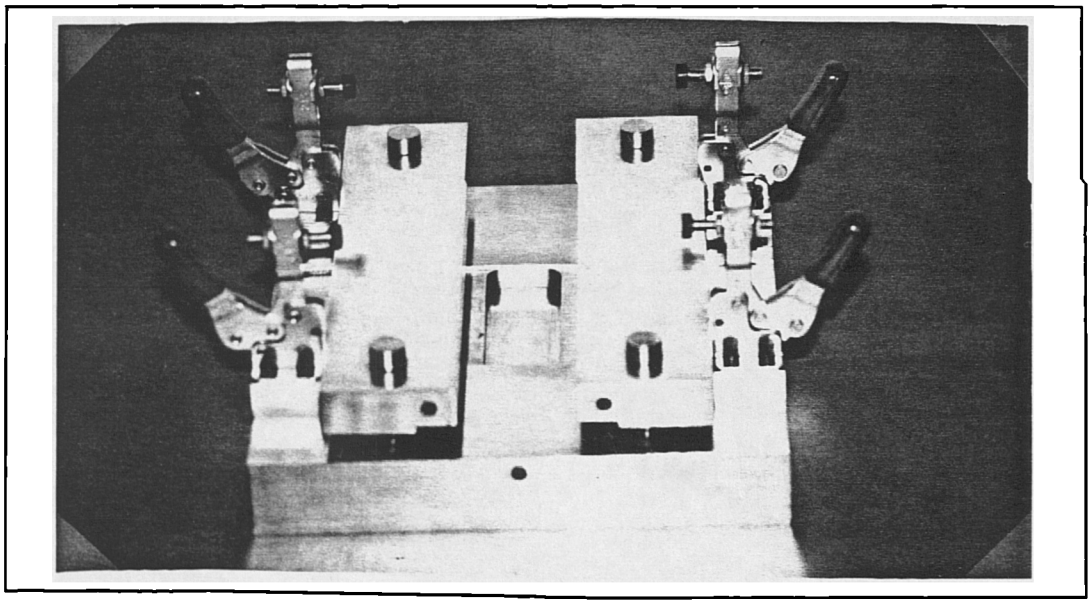

Figure 3.2 Rectangular pocket of the fixture

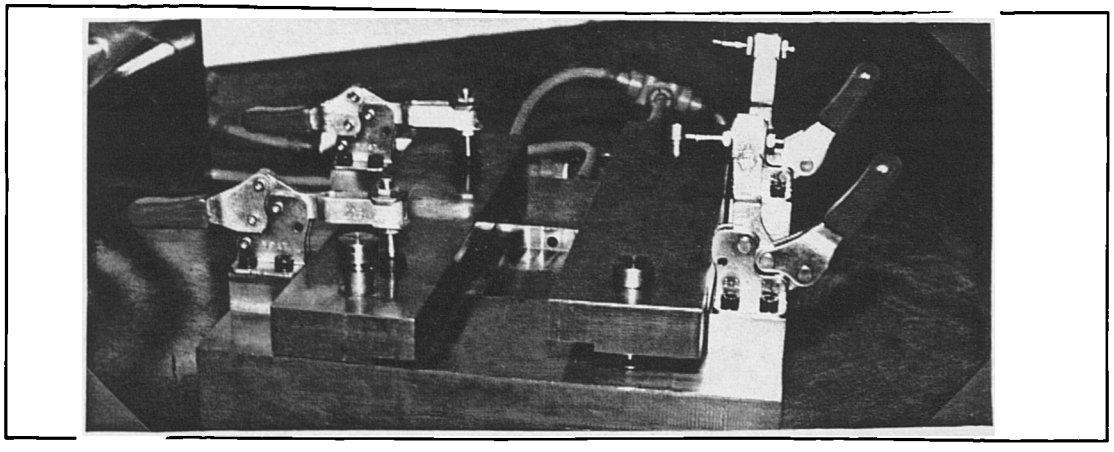

Figure 3.3 Outline of the clamping bars

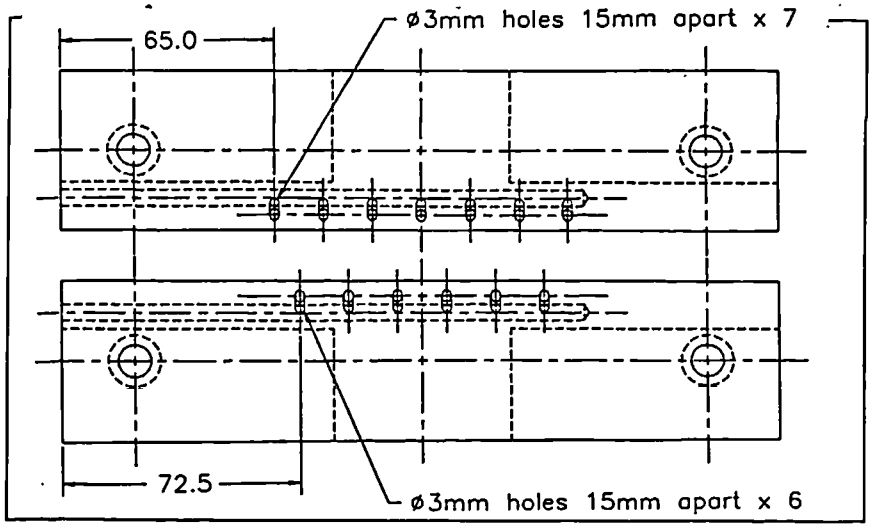


Figure 3.4 Positions of holes in the clamping bars

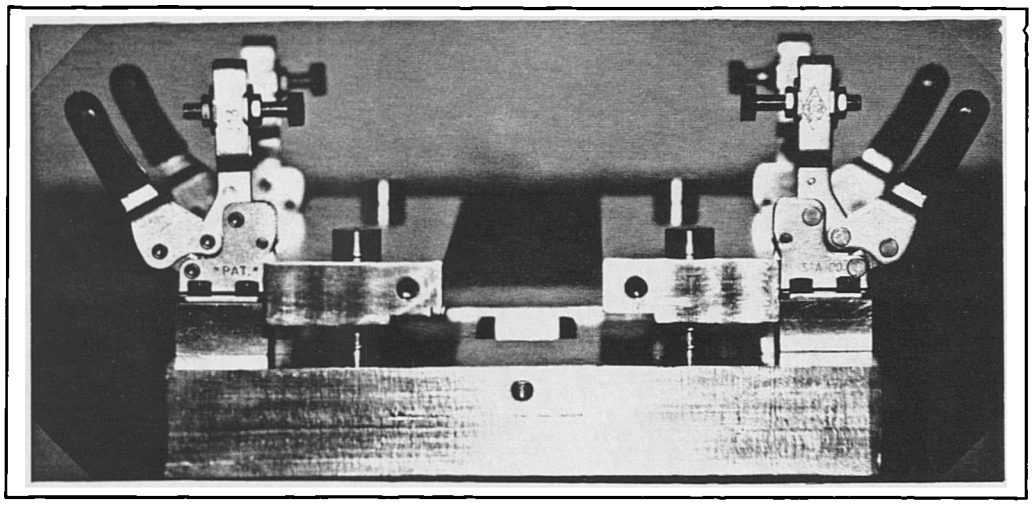

Figure 3.5 Outline of the quick release clamps

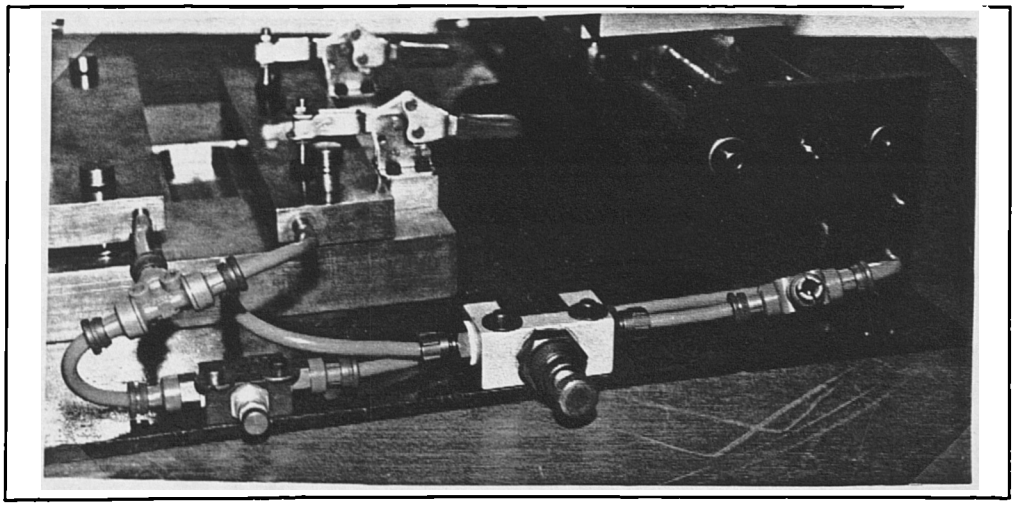

Figure 3.6 Outline of flow control device

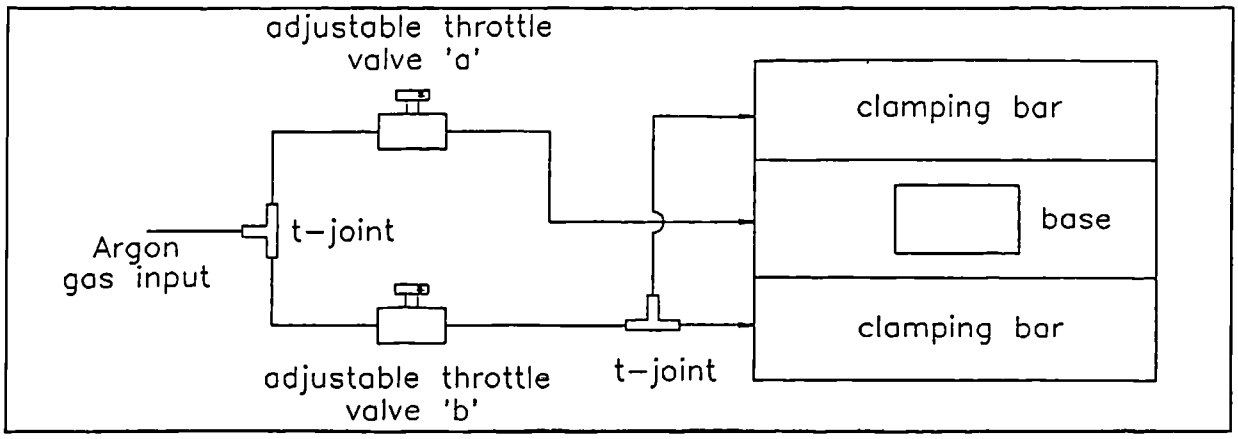


Figure 3.7 Layout of flow control device

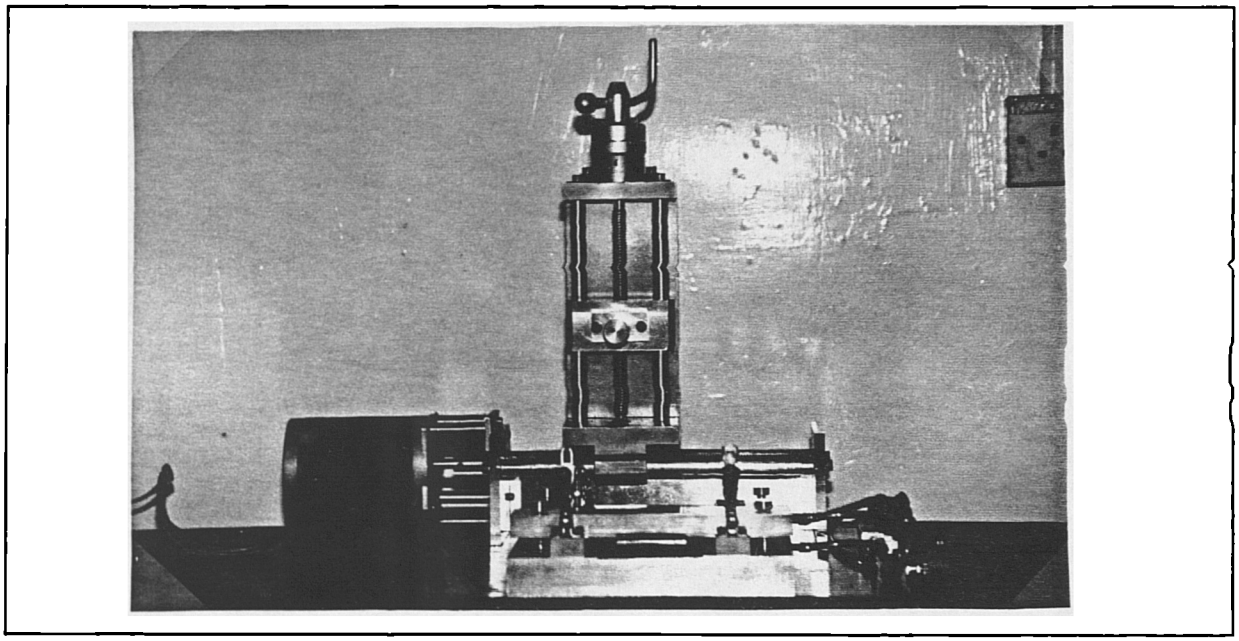

Figure 3.8 Computerised slideway

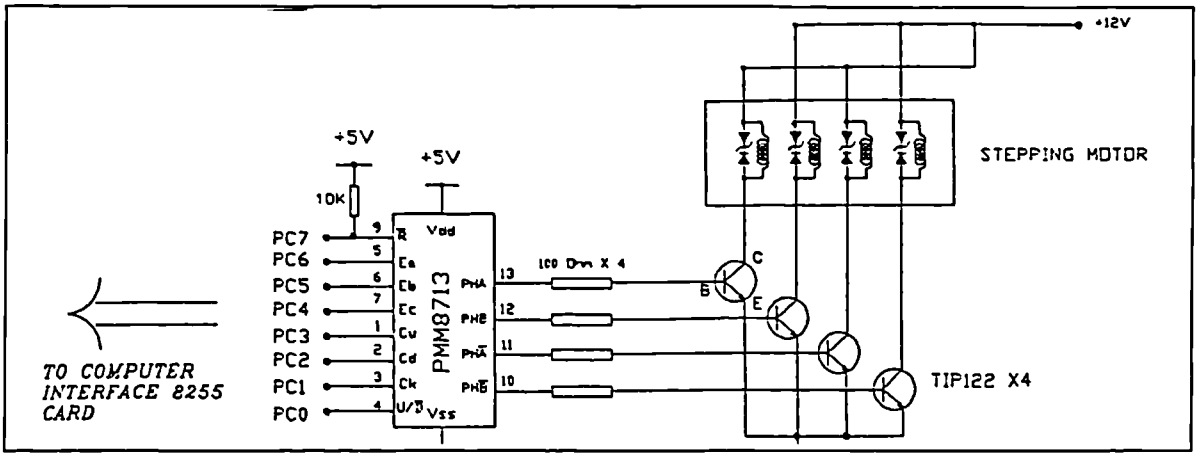


Figure 3.9 Stepping motor control circuit

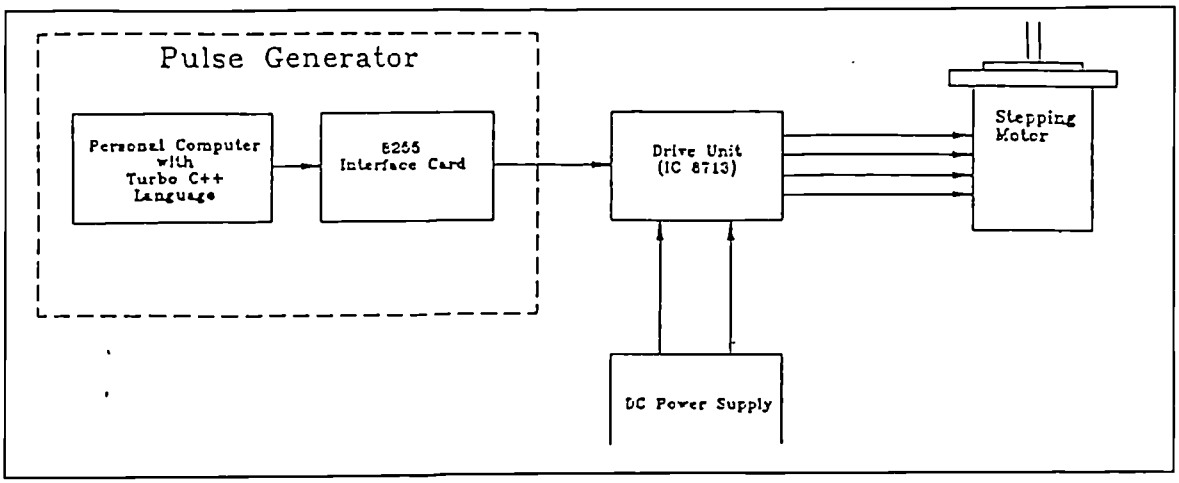


Figure 3.10 Block diagram of stepping motor control system

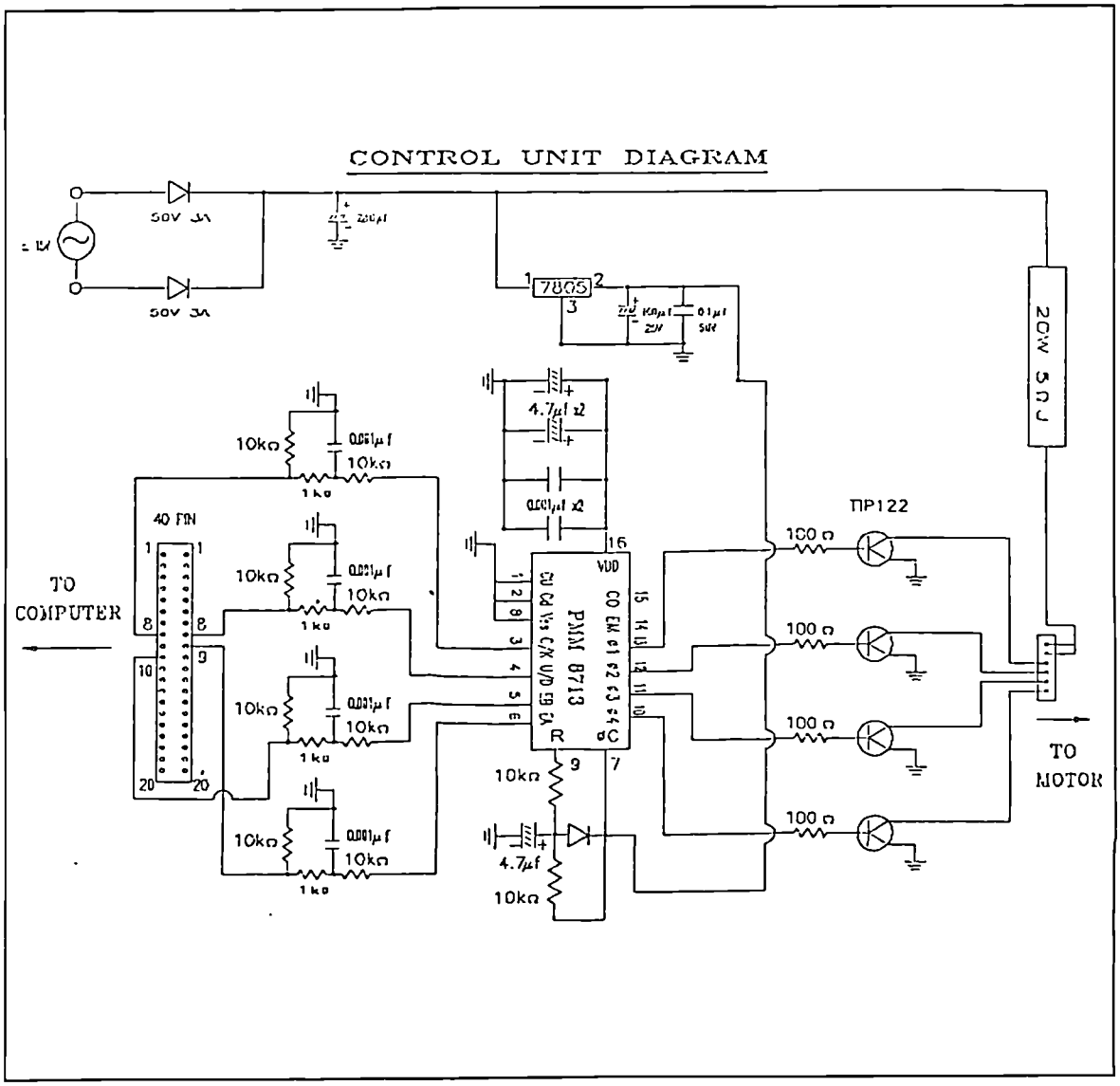


Figure 3.11 Modification of control circuit

# 4.0 ULTRASONIC DETECTION OF GEOMETRY AND GRAIN SIZE OF WELDS IN THIN PLATES

## 4.1 Detection of geometry and grain size in weld by ultrasonic shear waves -- A feasibility study on stainless steel

### 4.1.1 Experimental details and findings

All the weldments were made using a TIG (tungsten inert gas) welder. The material used was 6 mm ANSI 304 stainless steel plate with ANSI 308 filler metal of 3.2 mm diameter. The compositions of these materials are referred to in Table 4.1. Stainless steel was used instead of titanium alloy (IMI 318) because the prime purpose here was to study the feasibility of using ultrasonic shear waves to determine relationship, if any, between the grain size within and around the weld and the ultrasonic response. From this relationship, some information on the quality of the weld was expected to be gained. The absolute information from the ultrasonic response was not targeted in this study. Stainless steel was readily available and was chosen for this reason.

The standard welding conditions and sample preparation as detailed in section 3.5 were used in these experiments. The welding parameters selected included welding currents of between 135 A and 200 A, welding speeds of from 1.7 $mms^{-1}$ to 2.1 $mms^{-1}$ and a welding voltage of 12.8 V. The weldments were taken for analysis by an ultrasonic unit from Parametric Inc. (model Epoch II), with available peak power equivalent to amplitude gain of 120 dB.

A 4 MHz dual angle-TR-probe was employed to generate 45 degree shear waves, with oil as the sonic coupling medium. Using a 45 degree shear wave allowed for enhanced detection of the weld boundary because the reflection coefficient was greater than that for 60 degree shear waves. Before carrying out the ultrasonic measurements, the system was calibrated using a standard A2 IIW calibration block. The experiments were conducted in the pulse-echo mode; the echo amplitude height and travelling time (time-of-flight) were measured and analysed.

The time base of the ultrasonic unit was calibrated using a plate of the same thickness and material as that of the test pieces. The ultrasonic probe was put on both sides of the joint to detect and measure the echo signal from the weld boundary (the reflector). The received echo signals were recorded as A-scans in the ultrasonic unit, photographs of which are presented in Figure 4.1. The distance from the probe to the reflector, R, was calculated from its calibrated

linear relationship with the time base. Hence, the distance between the reflector and the nominal centre line of the weldment, D, was found by the difference of Y-R (Figure 4.2). The distance was measured from side a and side b of the centre line and were denoted as $D_a$ and $D_b$ correspondingly.

Micrographs of the weld in cross-section were taken and are presented in Figure 4.3. The results of $D_a$ and $D_b$, together with the measured weld pool width (by microscope), are tabulated in Table 4.2. The amplitude of the signals received and the welding parameters of the corresponding weldments are tabulated in Table 4.3. Graphs of amplitude data were plotted against welding current (I) and heat input rate (Q) from Table 4.3 and are presented in Figures 4.4 and 4.5.

## 4.2 Ultrasonic detection of size of titanium weld at elevated temperatures

### 4.2.1 Experimental set-up

To carry out this investigation, two critical problems were identified and dealt with before starting the experiments. The first problem was that the transducer would be damaged if it came into contact with high temperatures. Another problem was to maintain the temperature of the titanium sheet during the tests. Also, to maintain a relatively stable temperature near the ultrasonic transducer, and to avoid excessive temperature gradients (Cole, 1978), a cooling system near the transducer was used. The cooling system was developed by modifying the cover of a carbolite furnace which was used to provide the source of heat.

Design of furnace cover

Figure 4.6 shows a section view of the cover. This cover allowed the titanium sheet to pass through, such that part of the sheet was in the furnace environment at high temperature and part was exposed to the atmospheric environment where the titanium sheet was maintained at room temperature; the ultrasonic transducer was positioned at this point for the tests. The ultrasound was transmitted into the titanium sheet and went into the high temperature zone to achieve the purposes of the test. In between the hot and cold zones, a cooling channel and brickwork were used as insulation between the zones.

Material and weld

The material used was 2.3 mm thick titanium alloy sheet (IMI 318). Both plain sheet and weld bead on sheet were used as samples. The plain sheet sample was used as a reference in the experiments. A weld bead was formed on a number of sheets using a welding current of 120 A and a welding speed of 4.2 $mms^{-1}$. These parameters were used as they gave visually acceptable welds. Other welding conditions followed the details in section 3.5. A representative sample was carefully selected from all the welded samples for subsequent measurements. The diameter of the weld pool of this sample was measured at 5.0 mm.

Ultrasonic testing

An ultrasonic unit from Parametric Inc.(model Epoch II) with available peak power equivalent to amplitude gain of 120 dB was used in this section. The time-base of the ultrasonic unit was first calibrated to correspond to a travel distance (D) of the ultrasonic waves. Angled shear waves were used in the ultrasonic measurement since they make monitoring more easily attainable. The best shear wave angle was found to be related to plate thickness (Fenn &

Wooton, 1986) but generally 45° transducer was used. Coupling between the 5 MHz, 45° (equivalent to 43° for titanium in this study, by taking shear wave velocity of steel as 3.24 $mm\mu s^{-1}$ and that of titanium as 3.12 $mm\mu s^{-1}$ (Mark and Gauthier, 1993)) ultrasonic shear wave crystal and the sample end was achieved by an acoustic oil. A transducer was placed at a fixed distance, $D_c$, (80 mm) from the weld bead centre line. The temperature of the furnace was then raised and the positions of the returned echo signal from the sheet edge and from the weld pool were recorded in terms of calibrated time base from the ultrasonic unit, and were plotted for every hundred degree Celsius.

### 4.2.2 Data and computations

The actually measured quantity was the travel time t(T) of the ultrasonic signal at temperature T; $V_r$ and V(T) were the ultrasound velocities at room temperature (RT) and temperature T respectively. D(T) denoted the apparent distance travelled for the plain sheet sample, and $D_w(T)$ denoted that for the weld bead on plate sample. As mentioned above, $D_c$ was constant = 80 mm. Figure 4.7 is a graph of D(T) vs T, Figure 4.8 is a graph of $D_w(T)$ vs T, and Figure 4.9 reveals the apparent weld pool radius $r_a = D_c - D_w(T)$. Table 4.4 displays $D(T) - D_w(T)$ which was the compensated weld pool radius r, and Figure 4.10 is a graph of r vs temperature. A detailed analysis and discussion are presented in section 7.3.

Table 4.1 : Compositions of ANSI 304 and 308 stainless steels (Redmond, 1985)

| Type\Compositions (%) | C | Mn | Si | Cr | Ni | P | S | Others |
|---|---|---|---|---|---|---|---|---|
| 304 | 0.08 | 2.00 | 1.00 | 19.0 | 9.0 | 0.045 | 0.03 | 0.10 N |
| 308 | 0.08 | 2.00 | 1.00 | 20.0 | 11.0 | 0.045 | 0.03 | |

Table 4.2 : Distance between reflector and the nominal centre line of the weldment and weld pool width for welded specimens 4101 to 4106

| Specimen no. | 4101 | 4102 | 4103 | 4104 | 4105 | 4106 |
|---|---|---|---|---|---|---|
| Measured weld pool width (mm) | 8.5 | 8.3 | 13.7 | 8.7 | 8.0 | 7.5 |
| Half weld pool width (mm) | 4.3 | 4.2 | 6.8 | 4.4 | 4.0 | 3.8 |
| $D_a$ / $D_b$ (mm) | 3.0/3.3 | 5.5/-1.2 | 6.5/1.5 | 3.0/2.0 | -1.5/4.0 | 4.2/1.5 |
| Mean D (mm) | 3.2 | 2.2 | 4.0 | 2.5 | 1.3 | 2.9 |

Table 4.3 : Amplitude of the reflected signal and the welding parameters for welded specimens 4101 to 4106

| | | Welding parameters | | |
|---|---|---|---|---|
| Specimen no. | Amplitude A; $A^{2/3}$ (unit) | Current, I (A) | Speed, v ($mms^{-1}$) | Heat input rate, Q ($Jmm^{-1}$) |
| 4101 | 4.0; 2.5 | 160 | 2.1 | 730 |
| 4102 | 5.0; 2.9 | 135 | 1.7 | 770 |
| 4103 | 46.1; 13.0 | 200 | 2.1 | 910 |
| 4104 | 11.2; 5.1 | 140 | 1.7 | 800 |
| 4105 | 14.1; 5.9 | 150 | 1.7 | 850 |
| 4106 | 14.2; 5.9 | 153 | 2.1 | 680 |

Table 4.4 : Compensated weld pool radius at various temperatures

| Temperature (°C) | 20 | 44 | 100 | 200 | 300 | 400 | 500 | 560 | 600 |
|---|---|---|---|---|---|---|---|---|---|
| Radius of weld pool (mm), r | 1.5 | 1.5 | 1.4 | 1.2 | 1.0 | 1.2 | 1.3 | 1.1 | 1.1 |

Amplitude (unit)

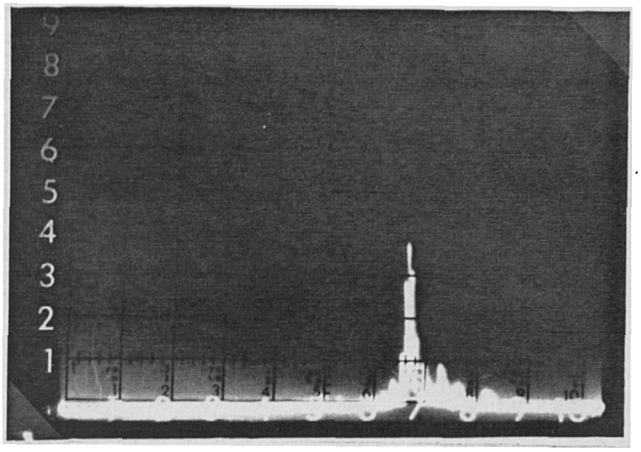

Ultrasonic transit time (μs)- 4101

Amplitude (unit)

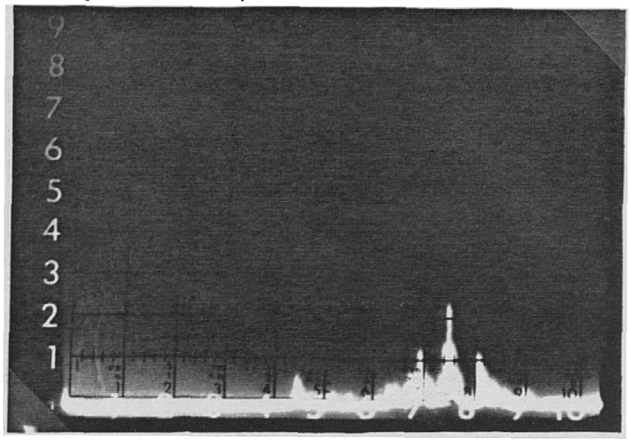

Ultrasonic transit time (μs)- 4102

Amplitude (unit)

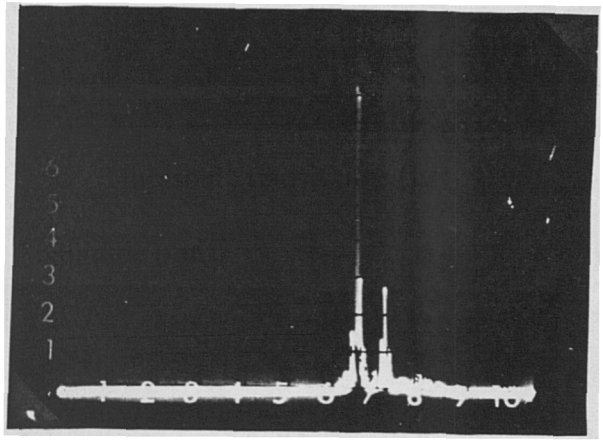

Ultrasonic transit time (μs)- 4103

Amplitude (unit)

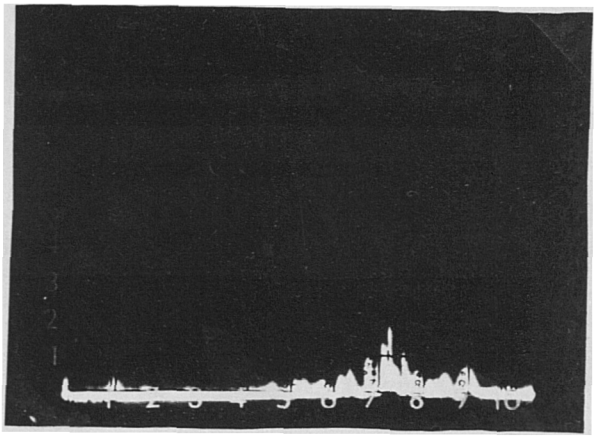

Ultrasonic transit time (μs)- 4104

Amplitude (unit)

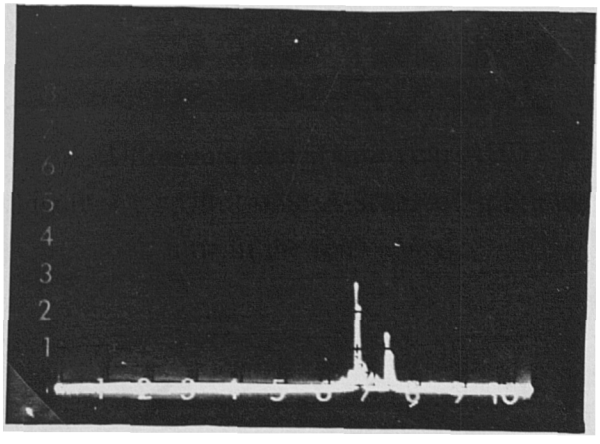

Ultrasonic transit time (μs)- 4105

Amplitude (unit)

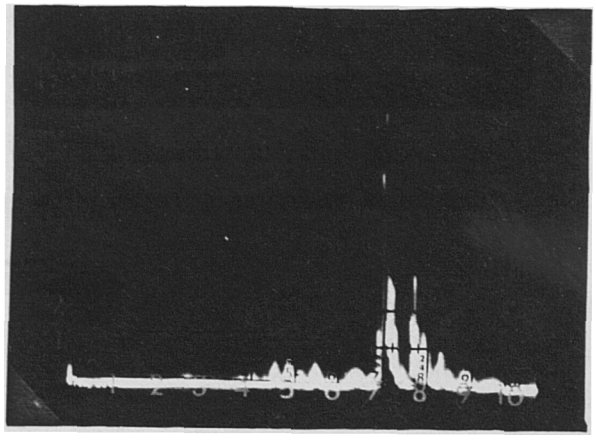

Ultrasonic transit time (μs)- 4106

Figure 4.1 : Ultrasonic A-scans of specimens 4101 to 4106 showing amplitude and transit time of the echo signal

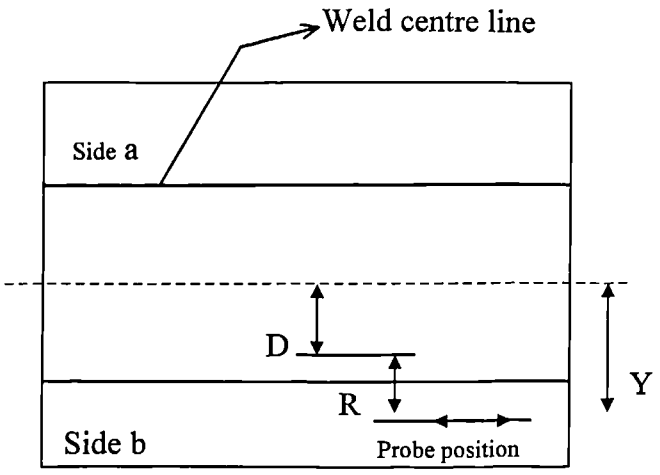


Figure 4.2 : Measurement locations relative to the weldment (not to scale) for welded specimens 4101 to 4106 in section 4.1.

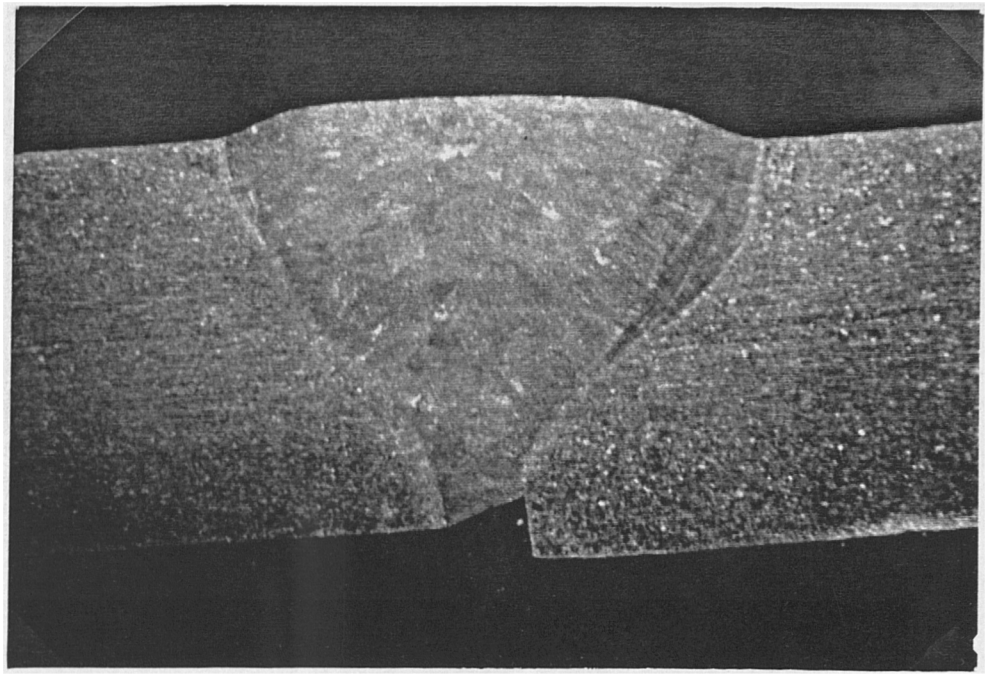

(a) |-----| 1 mm

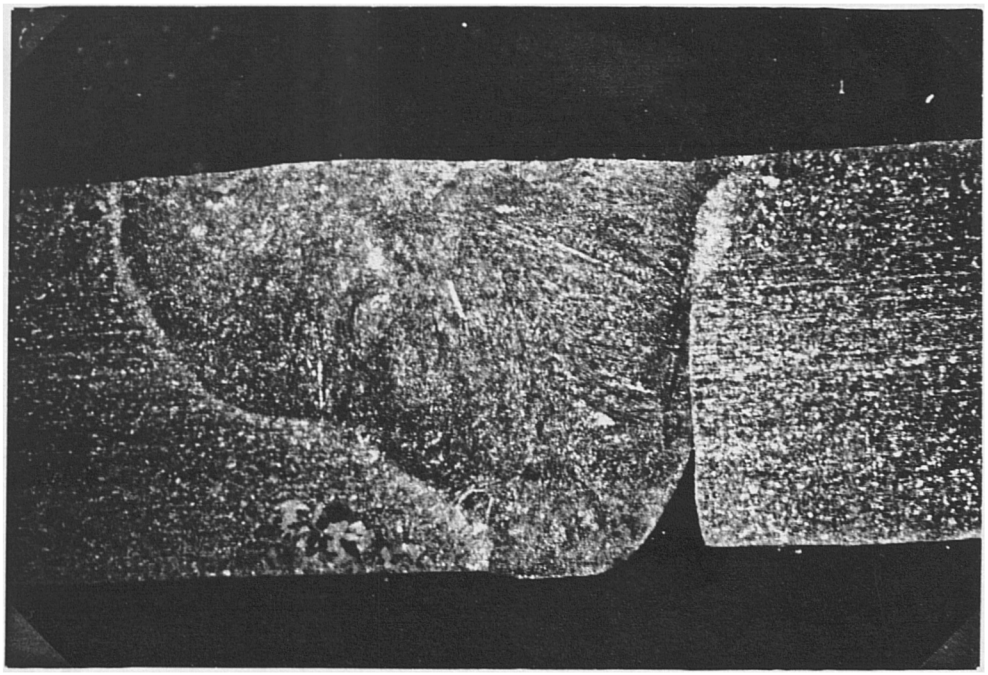

(b) |-----| 1 mm

Figure 4.3 (a,b) : Micrographs of welded specimen 4101 (a) and specimen 4102 (b)

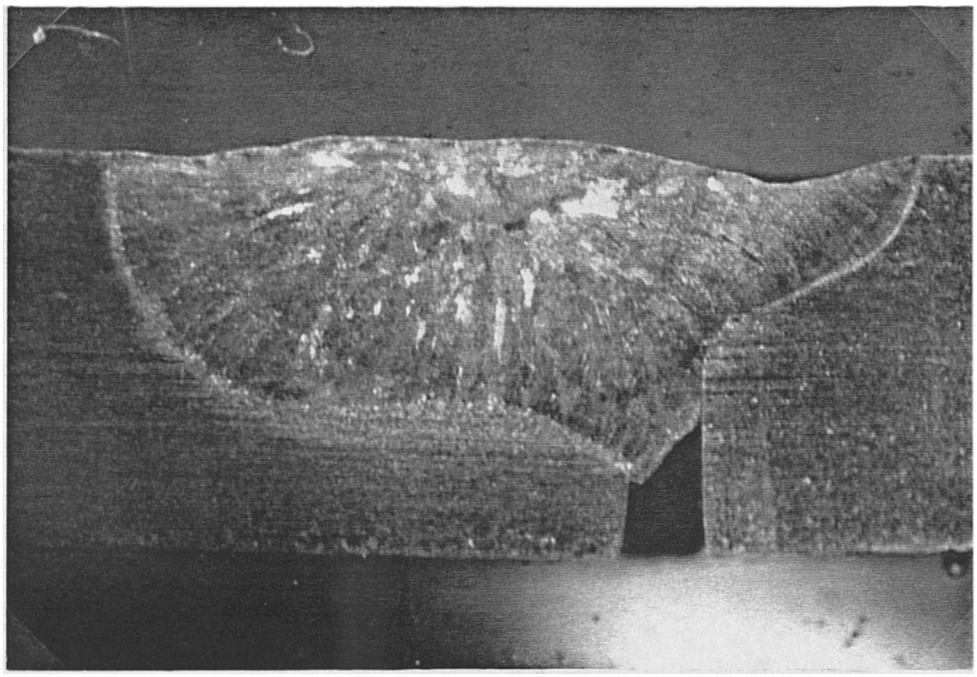

(c) |-----| 1 mm

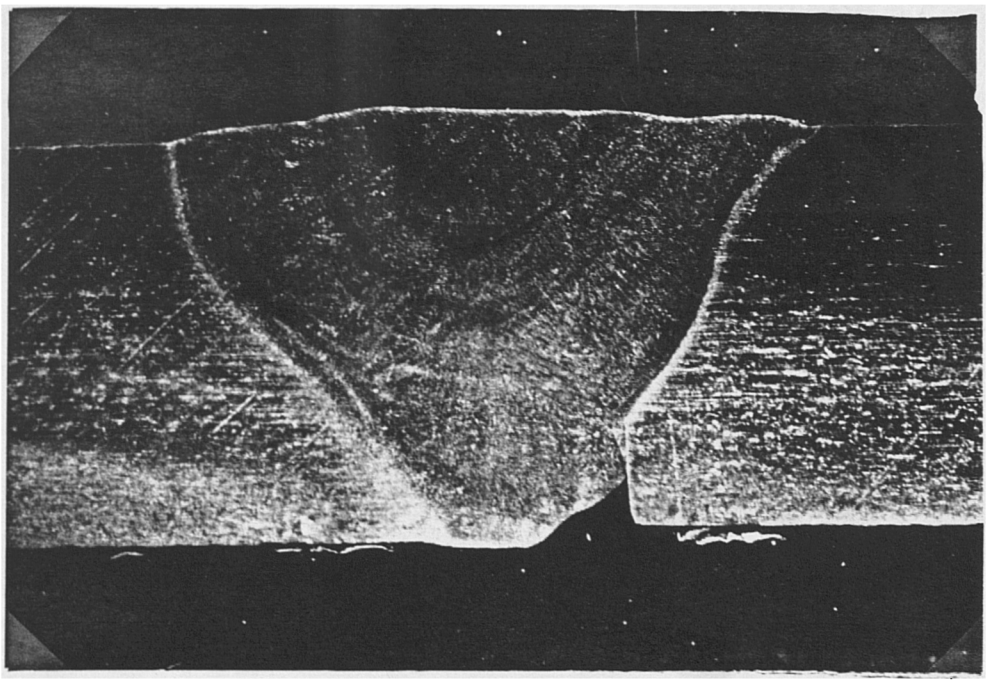

(d) |-----| 1 mm

Figure 4.3 (c,d) : Micrographs of welded specimen 4103 (c) and specimen 4104 (d)

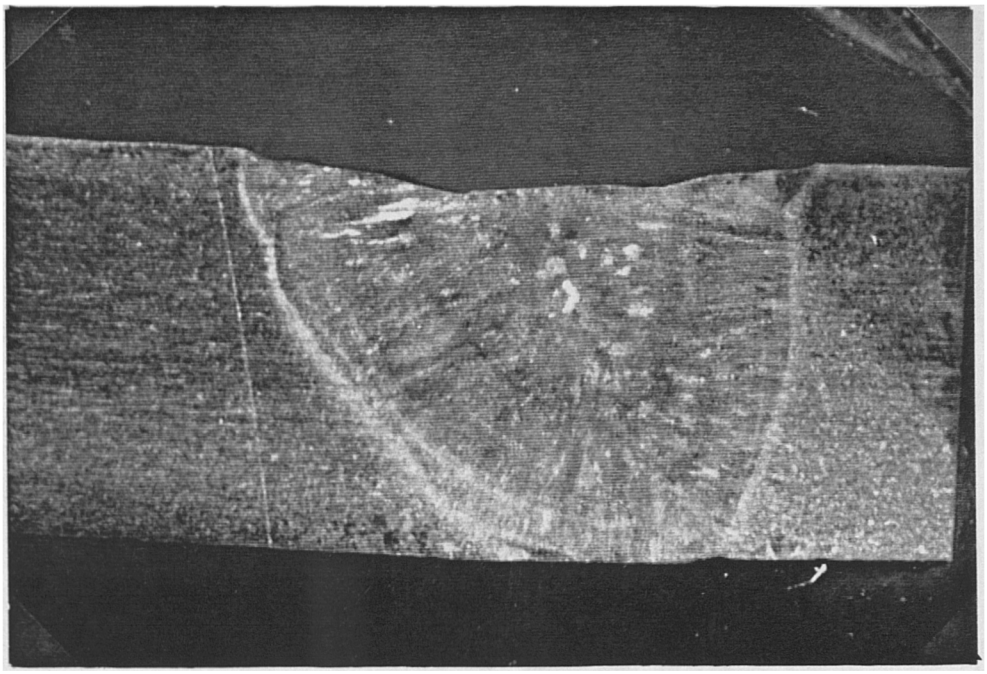

(e) |-----| 1 mm

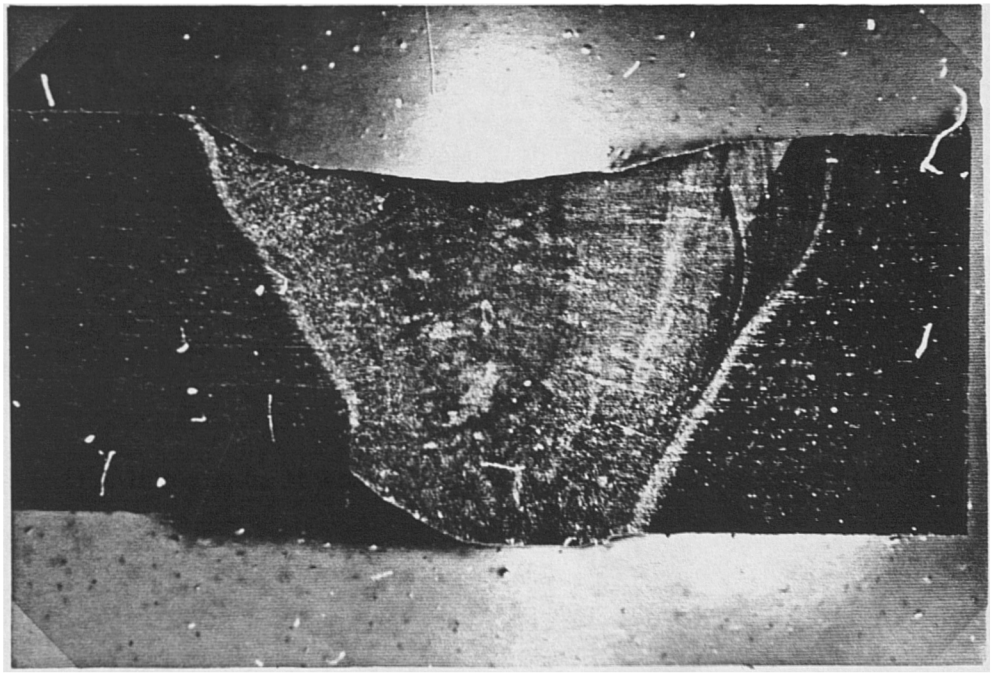

(f) |-----| 1 mm

Figure 4.3 (e,f) : Micrographs of welded specimen 4105 (e) and specimen 4106 (f)

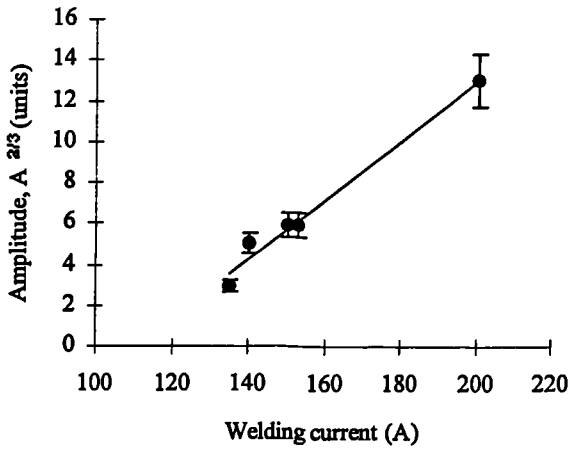


Figure 4.4 : Graph of amplitude of the ultrasonic signal versus welding current for welded specimens 4101 to 4106

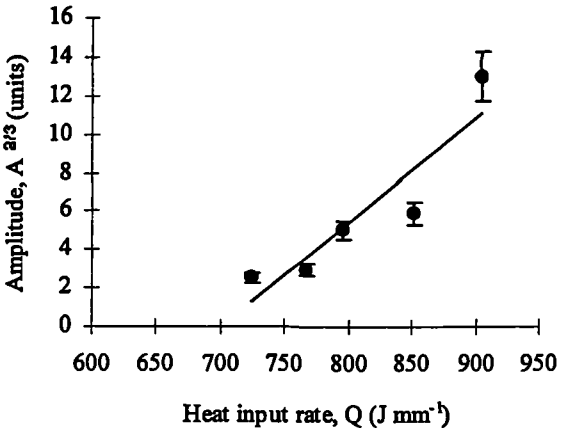


Figure 4.5 : Graph of amplitude of the ultrasonic signal versus heat input rate for welded specimens 4101 to 4106

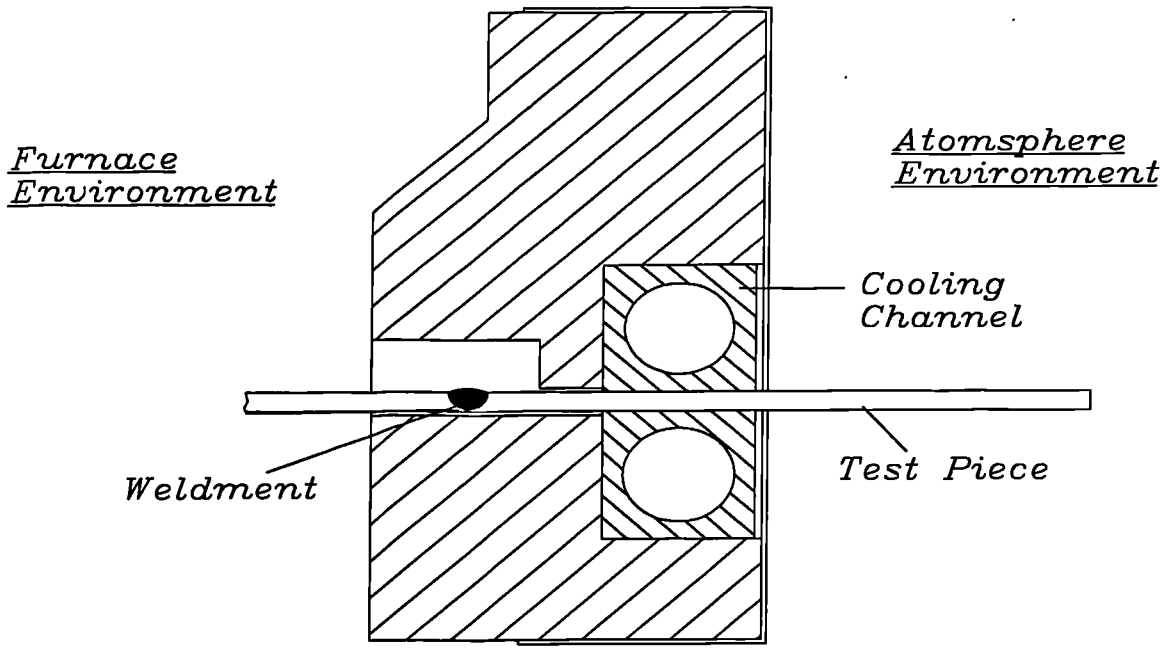


Figure 4.6 : Section view of modified furnace cover designed for the ultrasonic detection of titanium weld size at elevated temperatures

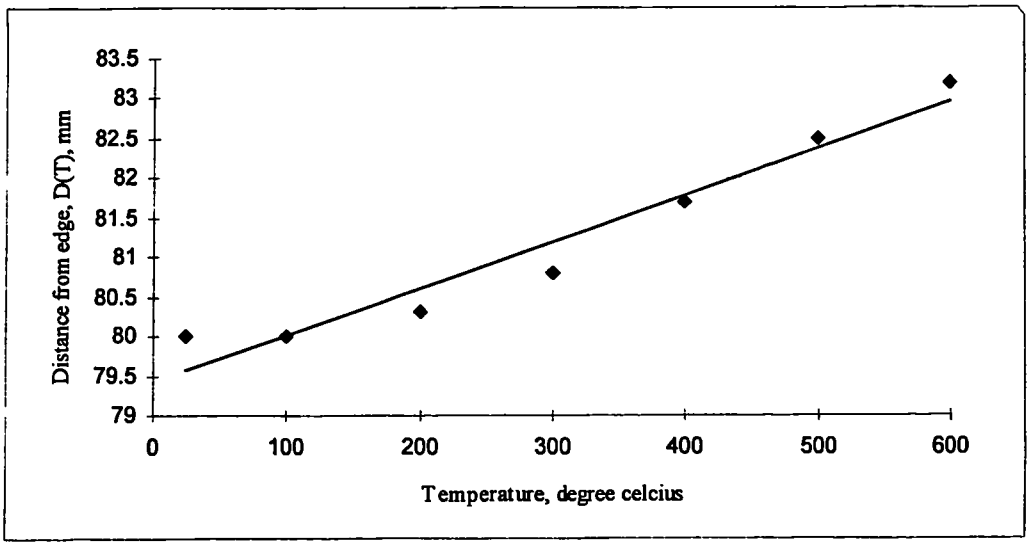


Figure 4.7 : Graph of distance from plain sheet edge, D(T) at various elevated temperatures for the ultrasonic detection of titanium weld size in section 4.2

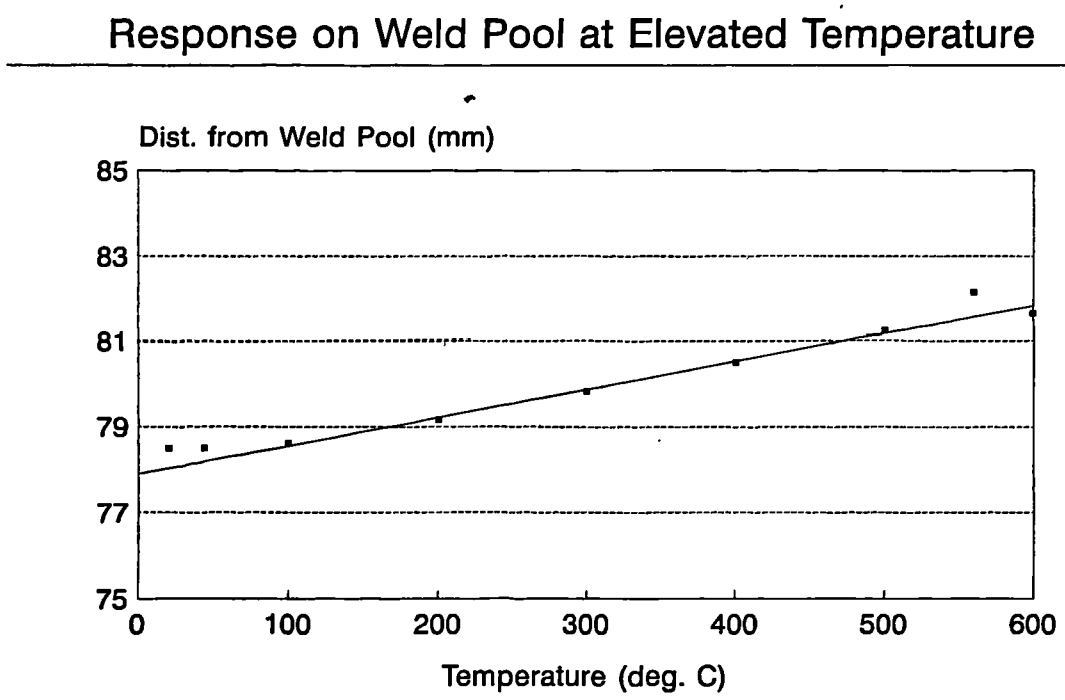


Figure 4.8 : Graph of distance from weld pool, $D_w(T)$ versus temperature for the ultrasonic detection of titanium weld size in section 4.2

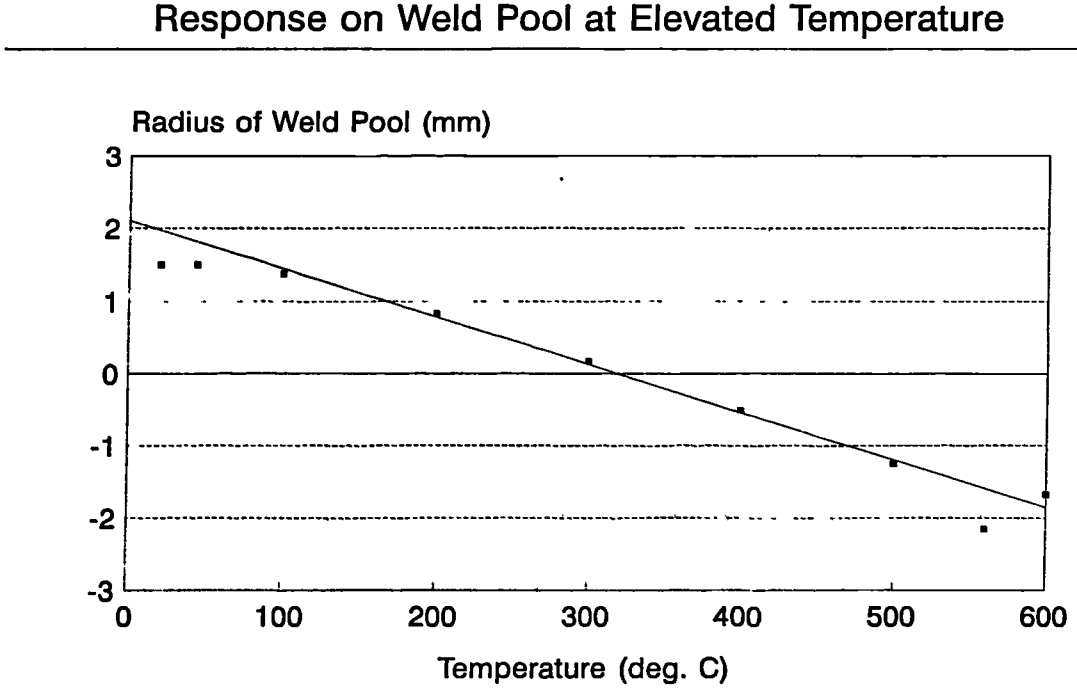


Figure 4.9: Graph of apparent radius of weld pool, $r_a$ versus temperature for the ultrasonic detection of titanium weld size in section 4.2

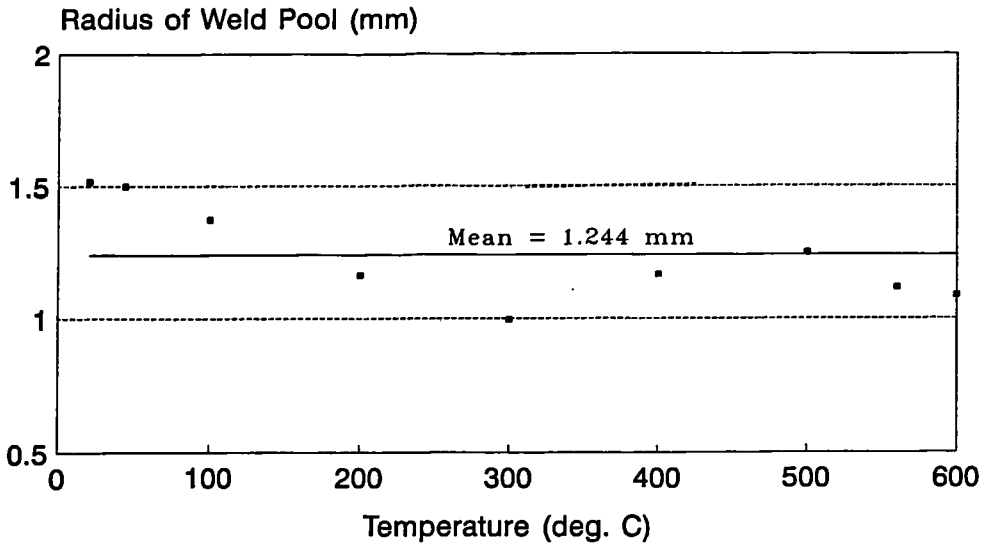


Figure 4.10 : Graph of compensated weld pool radius, r versus temperature for the ultrasonic detection of titanium weld size in section 4.2

# 5.0 QUALIFICATION OF CP GRADE TITANIUM WELDS

## 5.1 Effect of welding parameters on the geometry of the weld

### 5.1.1 Materials and experimental set-up

IMI 130 sheets (chemical composition by weight is equivalent to Grade 1 unalloyed titanium, referred to in Table 1.1) of 1.0 mm thickness were used in this section. This study was divided into two parts, group I (specimens 5101 to 5107) was made with weld beads on plate without a supply of back shielding gas, while group II (specimens 5108 to 5123) employed a back shielding gas (using the fixture described in section 3.1). Other welding conditions followed the details in section 3.5.

Regarding the welded specimens in group II, each of these was sectioned perpendicular to the weld, micro-specimens cut from each weld being for HAZ width investigation. Both HAZs adjacent to the FZ of each weld were measured from the top surface at 50X magnification, and the average HAZ width was computed.

### 5.1.2 Findings

(i) Effect of welding parameters on the depth of penetration (groups I and II)

Tables 5.1 and 5.2 show the results of the inspection of weld penetration, pool size and the degree of colouration of the welded specimens in both groups with different welding parameters.

(ii) Effect of welding parameters on the width of HAZ (group II)

Table 5.3 shows the HAZ width for group II specimens with different welding parameters.

## 5.2 Effect of welding parameters on fracture toughness (by CTOD Test)

### 5.2.1 Materials and experimental set-up

IMI 130 sheets were again used but of 2.3 mm thickness. This investigation was divided into two groups, III and IV. Group III specimens (5201 to 5211) were welded with different welding currents and at a fixed welding speed of 4.2 $mms^{-1}$. Group IV specimens (5212 to 5222) were welded with different welding speeds and at a fixed welding current of 100 A. Other welding conditions were as detailed in section 3.5.

Welded specimens were cut with an Electrical Discharge wire-cut Machine (EDM) to the dimensions shown in Figure 5.1. All the slots were made at the centreline of the weld. Fracture toughness was measured by Crack-Tip Opening Displacement Test (CTOD) with a three-point bending set-up, using a three point bending fixture which had a crosshead speed of 0.05 $mms^{-1}$.

### 5.2.2 Computations and findings

Work of fracture, $\gamma_F$, (which can be positively correlated to the fracture toughness value, $K_{1C}$) was calculated from Equation 2.16b (Tattersall & Tappin, 1966) as below :

$$\gamma_F = \frac{U}{2b(d-c)}$$

where U = the work done to completely fracture a specimen, dimensions b, c, d are shown in Figure 2.19 and,

$$U = \frac{\text{Yield load} \times \text{Yield displacement}}{2} \qquad (5.1)$$

The ratio c/d was made larger than 0.3 (refer to section 2.4.6) as suggested by Davidge and Tappin (1968). The following dimensions were measured by micrometer,

Breath, b = 60 mm
Notch depth, c = 1.0 mm
Depth, d = 2.3 mm
Length, L = 80 mm

Yield load and yield displacement were recorded and values of $\gamma_F$ were computed for different welding parameters. These are given in Tables 5.4 and 5.5 for group III and group IV specimens respectively.

Table 5.1 Results of visual inspection for group I welded specimens (1.0 mm thick IMI 130, welded *without* back shielding gas) P = pass F = fail

| Specimen No. | Welding current, A | Welding speed, $mms^{-1}$ | Heat input rate, $Jmm^{-1}$ | Degree of penetration and weld pool size (overall result) | Degree of colouration (overall result) |
|---|---|---|---|---|---|
| 5101 | 30 | 4.2 | 91 | Excessive penetration, narrow weld pool. (F) | Silver (P) |
| 5102 | 40 | 4.2 | 120 | Excessive penetration, wide weld pool.(F) | Powdery pale yellow deposit (F) |
| 5103 | 40 | 4.7 | 110 | Excessive penetration, accepted weld pool width(F) | Pale straw (P) |
| 5104 | 40 | 5.1 | 101 | Excessive penetration, accepted weld pool width(F) | Pale straw (P) |
| 5105 | 30 | 4.7 | 82 | Accepted penetration and weld pool width. (P) | Silver (P) |
| 5106 | 30 | 5.1 | 76 | Accepted penetration and weld pool width. (P) | Silver (P) |
| 5107 | 40 | 5.5 | 93 | Excessive penetration, accepted weld pool width.(F) | Silver (P) |

Table 5.2 Results of visual inspection for group II welded specimens (1.0 mm thick IMI 130, welded *with* back shielding gas) P = Pass F = Fail

| Specimen No. | Welding current, A | Welding speed, $mms^{-1}$ | Heat input rate, $Jmm^{-1}$ | Degree of penetration and weld pool size (overall result) | Degree of colouration (overall result) |
|---|---|---|---|---|---|
| 5108 | 25 | 3.8 | 84 | Lack of penetration, narrow weld bead width(F) | Dark straw (P) |
| 5109 | | 4.2 | 76 | Lack of penetration, narrow weld bead width (F) | Light blue (F) |
| 5110 | | 4.7 | 69 | Lack of penetration, narrow weld bead width(F) | Dark blue (F) |
| 5111 | | 5.1 | 63 | Lack of penetration, narrow weld bead width(F) | Dark blue (F) |
| 5112 | 30 | 3.8 | 101 | Accepted penetration and weld bead width (P) | Dark straw (P) |
| 5113 | | 4.2 | 91 | Accepted penetration and weld bead width (P) | Dark straw (P) |
| 5114 | | 4.7 | 82 | Lack of penetration, narrow weld bead width(F) | Dark straw (P) |
| 5115 | | 5.1 | 76 | Lack of penetration, narrow weld bead width (F) | Light blue (F) |
| 5116 | 35 | 3.8 | 118 | Excess penetration, wide weld bead width(F) | Silver (P) |
| 5117 | | 4.2 | 106 | Excess penetration, accepted weld bead width (F) | Dark straw (P) |
| 5118 | | 4.7 | 96 | Accepted penetration and weld bead width (P) | Dark straw (P) |
| 5119 | | 5.1 | 88 | Accepted penetration and weld bead width (P) | Dark straw (P) |
| 5120 | 40 | 3.8 | 134 | Excess penetration, wide weld bead width(F) | Dark straw (P) |
| 5121 | | 4.2 | 121 | Excess penetration, wide weld bead width(F) | Dark straw (P) |
| 5122 | | 4.7 | 110 | Excess penetration, wide weld bead width(F) | Light straw (P) |
| 5123 | | 5.1 | 101 | Accepted penetration and weld bead width (P) | Dark straw (P) |

Table 5.3 The width of HAZ for group II welded specimens (1.0 mm thick IMI 130, welded *with* shielding gas)

| Specimen no. | Welding current, A | Welding speed, $mms^{-1}$ | Heat input rate, $Jmm^{-1}$ | HAZ width, mm |
|---|---|---|---|---|
| 5108 | 25 | 3.8 | 84 | 2.3 |
| 5109 | | 4.2 | 76 | 1.9 |
| 5110 | | 4.7 | 69 | 1.9 |
| 5111 | | 5.1 | 63 | 2.0 |
| 5112 | 30 | 3.8 | 101 | 2.5 |
| 5113 | | 4.2 | 91 | 2.2 |
| 5114 | | 4.7 | 82 | 2.3 |
| 5115 | | 5.1 | 76 | 1.7 |
| 5116 | 35 | 3.8 | 118 | 3.0 |
| 5117 | | 4.2 | 106 | 2.5 |
| 5118 | | 4.7 | 96 | 2.1 |
| 5119 | | 5.1 | 88 | 1.9 |
| 5120 | 40 | 3.8 | 134 | 2.4 |
| 5121 | | 4.2 | 121 | 2.5 |
| 5122 | | 4.7 | 110 | 2.5 |
| 5123 | | 5.1 | 101 | 2.5 |

Table 5.4 The work of fracture for group III welded specimens (2.3 mm thick IMI 130 sheets, using varied welding current at a fixed welding speed of 4.2 $mms^{-1}$)

| Specimens No. | Current, A | Heat input rate, $Jmm^{-1}$ | Yield displacement, mm | Yield load, kN | Work of fracture, $\gamma_F$ $Jm^{-2}$ $x10^6$ |
|---|---|---|---|---|---|
| 5201 | 50 | 30 | 19.1 | 2.0 | 4.2 |
| 5202 | 60 | 37 | 19.4 | 1.8 | 3.8 |
| 5203 | 70 | 44 | 19.6 | 1.7 | 3.6 |
| 5204 | 80 | 51 | 19.6 | 1.7 | 3.6 |
| 5205 | 90 | 59 | 19.7 | 1.7 | 3.5 |
| 5206 | 100 | 68 | 19.7 | 1.6 | 3.5 |
| 5207 | 110 | 76 | 19.8 | 1.6 | 3.5 |
| 5208 | 120 | 85 | 19.9 | 1.6 | 3.4 |
| 5209 | 130 | 95 | 20.2 | 1.6 | 3.4 |
| 5210 | 140 | 110 | 20.2 | 1.5 | 3.3 |
| 5211 | 150 | 120 | 20.5 | 1.5 | 3.3 |

Table 5.5 The work of fracture for group IV welded specimens (2.3 mm thick IMI 130 sheets, using varied welding speed at a fixed welding current of 100 A)

| Specimen no. | Welding speed, $mms^{-1}$ | Heat input rate, $Jmm^{-1}$ | Yield displacement, mm | Yield load, kN | Work done to fracture, U, J | Work of fracture, $\gamma_F$, $Jm^{-2}$ $x10^6$ |
|---|---|---|---|---|---|---|
| 5212 | 6.8 | 42 | 18.8 | 1.7 | 16.4 | 3.6 |
| 5213 | 6.4 | 45 | 19.0 | 1.7 | 16.5 | 3.6 |
| 5214 | 5.9 | 48 | 19.1 | 1.7 | 15.9 | 3.5 |
| 5215 | 5.5 | 52 | 19.2 | 1.7 | 15.9 | 3.5 |
| 5216 | 5.1 | 56 | 19.5 | 1.6 | 15.4 | 3.4 |
| 5217 | 4.7 | 61 | 19.6 | 1.5 | 14.2 | 3.1 |
| 5218 | 4.2 | 68 | 19.6 | 1.4 | 13.8 | 3.0 |
| 5219 | 3.8 | 75 | 19.8 | 1.3 | 13.1 | 2.8 |
| 5220 | 3.4 | 85 | 19.9 | 1.2 | 12.0 | 2.6 |
| 5221 | 3.0 | 97 | 20.0 | 0.9 | 8.9 | 1.9 |
| 5222 | 2.5 | 110 | 20.2 | 0.8 | 8.0 | 1.8 |

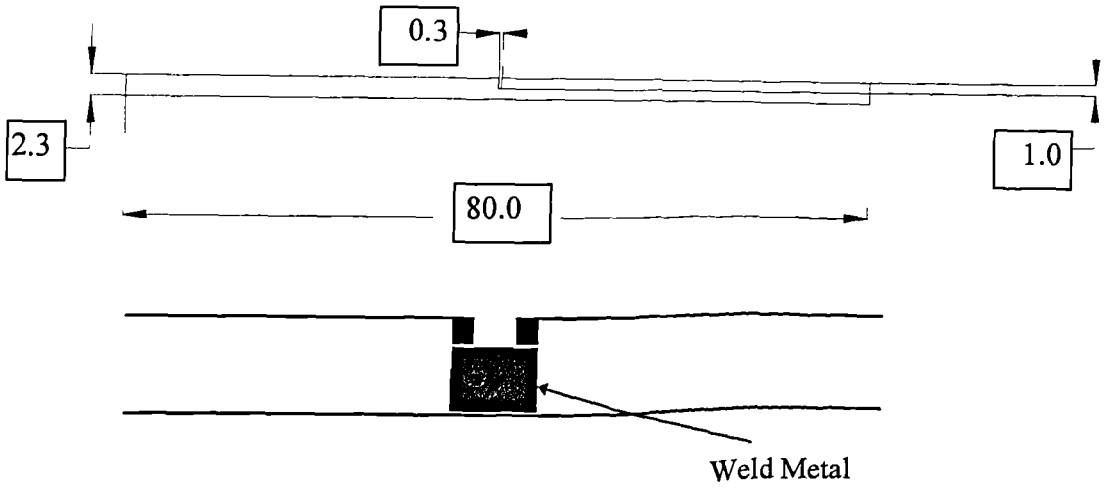


Figure 5.1 Dimensions (in mm) of welded specimens in the CTOD test.

# 6.0 QUALIFICATION OF α/β TITANIUM ALLOY- IMI 318 WELDS

## 6.1 Weld geometry and grain size of welds

### 6.1.1 Investigation of welding parameters producing acceptable welds

Materials and experimental set-up

IMI 318 sheets of 1.2 mm thickness were used in this section. Different welding currents and speeds were used to produced acceptable welds. Other welding conditions employed were those detailed in section 3.5. Micro-specimens cut from each weld were used in the investigation of HAZ width. Both HAZs adjacent to the FZ of each weld were measured from the top surface at 50X magnification, and the average HAZ width computed.

Findings

Table 6.1 shows the weld penetration (qualitatively) and the average width of HAZ of the welded specimens (6101 to 6116) with different welding parameters. HAZ widths were plotted against the heat input rates (Figure 6.1). The spectrum of welding parameters which produced welds with acceptable penetration is presented as Figure 6.2.

### 6.1.2 Effect of welding parameters on the weld penetration and weld size

Welding penetration

To study quantitatively the effect of welding current and heat input rate on weld penetration, autogenous welds (specimens 6117 to 6123) were fabricated on IMI 318 plates of 1.7 mm thickness with peak pulse welding currents between 10 A to 70 A, and a fixed welding speed of 4.2 $mms^{-1}$. Welding parameters employed and corresponding heat input rates are listed (Table 6.2). All the welded specimens were cross-sectioned to measure the penetration with the aid of a microscope, and the results are plotted against the corresponding welding currents and heat input rates in Figures 6.3 and 6.4.

Weld size

To study further the effect of the welding parameters on the weld size quantitatively, autogenous welds were again fabricated using IMI 318 plates of 1.0 mm thickness with different peak pulse welding currents (specimens 6124 to 6130) and welding speeds (specimens 6131 to 6137).

Weld specimens were again microsectioned to investigate and measure the width of the FZ and adjacent HAZs. These measured widths are given in Tables 6.3 (specimens 6124 to 6130) and 6.4 (specimens 6131 to 6137) and plotted against the corresponding heat input rates, welding currents and speeds in Figures 6.5, 6.6, 6.7 and 6.8.

### 6.1.3 Effect of welding parameters on grain size of welds

To study the effect of the welding current and welding speed on grain size, the grain size of welded specimens (Table 6.3, specimens 6124 to 6130 and Table 6.4, specimens 6131 to 6137) were measured across the weld using an image analyser. Particular attention was given to grain size distribution in the FZ, in the HAZ near to the FZ (near HAZ) and in the HAZ near to the base metal (far HAZ). Measurements were taken firstly from the FZ and then across the weld towards the base metal at 0.5 mm intervals. The grain size was determined as follows : the areas of some 100 to 150 individual grains located around the intervals were measured and averaged. In computing the areas, the diameter of each grain was measured assuming it to be circular. Results of these measurements are presented in Tables 6.5 and 6.6 in terms of mean grain areas, and are plotted against zone location at different heat input rates in Figures 6.9 and 6.10.

Further study on the grain size of welds

To further the study on grain size of welds, autogenous welds on plates were fabricated on thicker (2.7 mm) IMI 318 plates, with varying peak pulse welding currents (between 80 and 140 A, specimens 6138 to 6141) and welding speeds (between 3.4 and 5.1 $mms^{-1}$, specimens 6142 to 6146). From this work, the grain sizes in both sides of HAZ were measured and compared. Details of the welding parameters used and their corresponding heat inputs are listed in Table 6.7.

Grain sizes in the FZ and the two adjacent HAZs were re-measured using an image analyser at 1.0 mm intervals in both directions from the centre of the FZ. For ease of reference, the centre of the FZ was arbitrarily taken to be the zero point. Therefore, +3 mm and -3mm locations represented the HAZ 3mm from the right hand side and left hand side of the FZ respectively. These results are presented in Tables 6.8 and 6.9, and plotted in Figures 6.11 and 6.12, their corresponding micrographs are given as Figures 6.13 (a) to (i).

## 6.2 Hardness of IMI 318 welds

IMI 318 sheets of 3.0 mm thickness were used for this work. Different welding currents and speeds were used to fabricate autogenous welded specimens (6201 to 6210). Other welding conditions employed were as detailed in section 3.5.

The welded specimens were microsectioned and Vickers hardness testing was conducted on the microsectioned specimens. Testing was conducted at the centre of the welds using a 10 kg load.

### 6.2.1 Effect of welding parameters on the hardness of welds

Table 6.10 shows the hardness (represented by hardness number $H_v$) at the centre of the welds. Figure 6.14 presents the relationship between weld hardness found and welding current used at a fixed welding speed of 5.1 $mms^{-1}$, whilst Figure 6.15 presents the relationship between weld hardness and welding speed used at a fixed welding current of 180 A. Parent metal hardness was included for reference and comparison.

## 6.3 Factors affecting the tensile properties of welds

### 6.3.1 The effect of welding parameters on the tensile properties and fracture of welds

Materials and experimental details

To study the tensile fracture and properties of IMI 318 welds, autogenous welds were fabricated on the 2.3 mm IMI 318 plate using different welding currents (specimens 6301 to 6304) and different welding speeds (specimens 6305 to 6309). Other welding conditions and parameters were as detailed in chapter 3.5.

Transverse tensile specimens were cut to ASTM standard E8M size as shown in Figures 6.16 and 6.45. Tensile strength was tested on a laboratory tensometer, using a strain rate of 0.002 mm $mm^{-1}s^{-1}$. ASTM specified a gauge length of 25.0 mm while the original cross-sectional area of the specimens were 13.8 $mm^2$.

Reduction in area, tensile stress and strain to failure of the tensile specimens were computed and presented in Tables 6.11 (specimens 6301 to 6304) and Table 6.12 (specimens 6305 to 6308). These were then plotted against the respective heat input rates (Figures 6.17 to 6.19, 6.22 to 6.24) and welding currents (Figures 6.20 to 6.21) and welding speeds (Figures 6.25 to 6.26). Fractographs were taken (Figures 6.27 to 6.44) to reveal the fracture mode of the specimens.

### 6.3.2 Investigation of the effects of cooling rate and heat input rate on the tensile properties of welds

Materials and experimental details

It was found in previous studies (Wu, 1961; Wu, 1965) that the mechanical properties of α/β titanium alloys are cooling-rate sensitive. The study here sets out to investigate whether the same sensitivity applies to IMI 318. Once the effect of cooling rate is determined, preweld and postweld heat treatments for improving mechanical properties can be explored, if needed, in a systematic manner.

Consequently, 1.5 mm IMI 318 plate weldments were fabricated using a wide range of welding currents, speeds and current pulse-on times. Acceptable weldments were selected by visual inspection. The parameters for these welds were used again to fabricate welded specimens (6309 to 6314). Other welding conditions were as detailed in section 3.5.

To study the effect of heat input on the tensile strength of weldments in more detail, a further group of ten more (6315 to 6324) specimens were welded at lower heat inputs. Parameters used for welding both groups (specimens 6309 to 6324) are presented as Table 6.13.

Tensile tests were conducted on weldments of both groups using again the laboratory tensometer. The design of the transverse tensile specimens followed the subsize rectangular specimen in the ASTM E8M standard and is schematically presented in Figures 6.16 and 6.45. Due to the non-uniformity of the plate thickness, the thickness at gauge width and the average plate thickness of each specimen had to be measured and these measurements are presented in Table 6.14. Maximum loadings during tensile testing were recorded in Table 6.14 also.

Failure locations and the tensile strength at failure, together with the heat input used are presented in Tables 6.15 and 6.16. Cooling rates for specimens 6309 to 6314 were computed using Equation 2.4 and are presented in Table 6.15. Stress-strain curves of specimens 6309 to 6324 were recorded during the test and are presented in Figure 6.46 (a) to (q). Tensile performances were also conducted on 2 parent metal specimens (B1 and B2) for comparison purpose and their results are recorded in Tables 6.14 and 6.15. Equations 2.15a and 2.15b were used to compute weldment tensile strength at the failure location.

Table 6.1 Welding parameters used, average HAZ width and weld penetration of 1.2 mm thick IMI 318 welded specimens

| Specimen no. | Current, A | Welding speed, $mms^{-1}$ | Heat input rate, $Jmm^{-1}$ | Average HAZ width, mm | Weld penetration and weld bead width |
|---|---|---|---|---|---|
| 6101 | 30 | 3.4 | 79 | 2.2 | Accepted penetration and weld bead width (P) |
| 6102 | | 4.2 | 64 | 1.7 | Lack of penetration, narrow weld bead width (F) |
| 6103 | | 5.1 | 53 | 1.4 | Lack of penetration, narrow weld bead width(F) |
| 6104 | | 5.9 | 45 | 1.1 | Lack of penetration, narrow weld bead width(F) |
| 6105 | 40 | 3.4 | 106 | 2.4 | Excess penetration, wide weld bead width (F) |
| 6106 | | 4.2 | 85 | 2.1 | Accepted penetration and weld bead width (P) |
| 6107 | | 5.1 | 71 | 1.6 | Lack of penetration, accepted weld bead width(F) |
| 6108 | | 5.9 | 61 | 1.1 | Lack of penetration, narrow weld bead width (F) |
| 6109 | 45 | 3.4 | 119 | 2.7 | Excess penetration, wide weld bead width(F) |
| 6110 | | 4.2 | 95 | 1.9 | Excess penetration, accepted weld bead width (F) |
| 6111 | | 5.1 | 79 | 1.7 | Accepted penetration and weld bead width (P) |
| 6112 | | 5.9 | 68 | 1.4 | Lack of penetration, narrow weld bead width (F) |
| 6113 | 50 | 3.4 | 132 | 2.9 | Excess penetration, wide weld bead width(F) |
| 6114 | | 4.2 | 106 | 2.4 | Excess penetration, wide weld bead width(F) |
| 6115 | | 5.1 | 88 | 1.9 | Accepted penetration and weld bead width (P) |
| 6116 | | 5.9 | 76 | 1.7 | Lack of penetration, narrow weld bead width (F) |

Remark : P = Pass F = Failure

Table 6.2 : Welding parameters used in 1.7 mm thick IMI 318 welded specimens in section 6.1.2

| Specimen no. | Peak welding current, A | Welding speed, $mms^{-1}$ | Heat input rate, $Jmm^{-1}$ |
|---|---|---|---|
| 6117 | 10 | 4.2 | 20 |
| 6118 | 20 | 4.2 | 40 |
| 6119 | 30 | 4.2 | 60 |
| 6120 | 40 | 4.2 | 80 |
| 6121 | 50 | 4.2 | 100 |
| 6122 | 60 | 4.2 | 120 |
| 6123 | 70 | 4.2 | 140 |

Table 6.3 : The width of FZ and HAZ in 1.0 mm thick IMI 318 welded specimens with different welding currents and at a fixed welding speed of 42 $mms^{-1}$

| Specimen no. | Peak welding current, (A) | Heat input rate ($Jmm^{-1}$) | FZ, (μm), ±150μm | HAZ, (μm), ±150μm | FZ+ 2HAZ, (μm), ±150μm |
|---|---|---|---|---|---|
| 6124 | 20 | 4 | 3300 | 690 | 5300 |
| 6125 | 40 | 8 | 3900 | 1100 | 6100 |
| 6126 | 60 | 12 | 5200 | 760 | 6700 |
| 6127 | 80 | 16 | 5000 | 990 | 7000 |
| 6128 | 100 | 20 | 5100 | 1300 | 7700 |
| 6129 | 120 | 24 | 5100 | 1400 | 7900 |
| 6130 | 140 | 25 | 6200 | 940 | 8100 |

Table 6.4 : The width of FZ and HAZ in 1.0 mm thick IMI 318 welded specimens with different welding speeds and at a fixed peak welding current of 80 A

| Specimen no. | Welding speed,($mms^{-1}$) | Heat input rate ($Jmm^{-1}$) | FZ, (μm), ±150μm | HAZ, (μm), ±150μm | FZ+ 2HAZ, (μm),±150μm |
|---|---|---|---|---|---|
| 6131 | 30 | 22 | 7400 | 1400 | 10000 |
| 6132 | 34 | 20 | 6900 | 970 | 8800 |
| 6133 | 38 | 18 | 4900 | 1400 | 7800 |
| 6134 | 42 | 16 | 5000 | 990 | 7000 |
| 6135 | 47 | 14 | 4400 | 1100 | 6500 |
| 6136 | 51 | 13 | 4200 | 1100 | 6500 |
| 6137 | 55 | 12 | 2300 | 1300 | 4900 |

Table 6.5 : Grain sizes at different zone locations in 1.0 mm thick IMI 318 welded specimens with different heat input rates and at a fixed welding speed of 42 $mms^{-1}$

| Specimen no. | Heat input rate ($Jmm^{-1}$) | Grain size(mean grain area) at zone location, $\mu m^2$, $\pm 500 \mu m^2$ | | | | |
|---|---|---|---|---|---|---|
| | | 0.5mm | 1.5mm | 2.5mm | 3.5mm | 4.5mm |
| 6124 | 4 | 24000 | 24000 | 26000 | 15000 | 2400 |
| 6125 | 8 | 28000 | 23000 | 24000 | 13000 | 3800 |
| 6126 | 12 | 42000 | 25000 | 28000 | 4700 | 660 |
| 6127 | 16 | 45000 | 30000 | 32000 | 14000 | 4100 |
| 6128 | 20 | 20000 | 53000 | 46000 | 27000 | 2300 |
| 6129 | 24 | 38000 | 52000 | 56000 | 15000 | 3700 |
| 6130 | 25 | 120000 | 67000 | 35000 | 12000 | 4000 |

Table 6.6 : Grain sizes at different zone locations in 1.0 mm thick IMI 318 welded specimens with different heat input rates and at a fixed peak welding current of 80 A

| Specimen no. | Heat input rate ($Jmm^{-1}$) | Grain size(mean grain area) at zone location, $\mu m^2$, $\pm 500 \mu m^2$ | | | | |
|---|---|---|---|---|---|---|
| | | 0.5mm | 1.5mm | 2.5mm | 3.5mm | 4.5mm |
| 6131 | 22 | 68000 | 210000 | 56000 | 8500 | 3200 |
| 6132 | 20 | 73000 | 41000 | 20000 | 23000 | 4300 |
| 6133 | 18 | 40000 | 16000 | 30000 | 13000 | 3900 |
| 6134 | 16 | 28000 | 23000 | 24000 | 13000 | 3800 |
| 6135 | 14 | 22000 | 35000 | 15000 | 9500 | 1900 |
| 6136 | 13 | 27000 | 22000 | 13000 | 6500 | 4900 |
| 6137 | 12 | 3600 | 7200 | 21000 | 9700 | 2500 |

Table 6.7 : Welding parameters used in 2.7 mm thick IMI 318 welded specimens in section 6.1.3

| Parameters | Peak welding current | Welding speed | Heat input rate |
|---|---|---|---|
| Specimen No. | ( A ) | ( $mms^{-1}$ ) | ( $Jmm^{-1}$ ) |
| 6138 | 80 | 4.2 | 76 |
| 6139 | 100 | 4.2 | 95 |
| 6140 | 110 | 4.2 | 100 |
| 6141 | 140 | 4.2 | 130 |

| | | | |
|---|---|---|---|
| 6142 | 100 | 3.4 | 120 |
| 6143 | 100 | 3.8 | 110 |
| 6144 | 100 | 4.2 | 95 |
| 6145 | 100 | 4.7 | 86 |
| 6146 | 100 | 5.1 | 79 |

Table 6.8: Grain sizes at FZ and HAZ across the weld bead in 2.7 mm thick IMI 318 welded specimens with different heat input rates and at a fixed welding speed of 4.2 $mms^{-1}$

| Specimen no. | Heat input rate ( $Jmm^{-1}$ ) | Grain size (mean grain area), $\mu m^2$ | | | | | | |
|---|---|---|---|---|---|---|---|---|
| | | HAZ | N-HAZ | FZ | FZ | FZ | N-HAZ | HAZ |
| | | Zone location ( mm ) | | | | | | |
| | | -3 | -2 | -1 | 0 | 1 | 2 | 3 |
| 6138 | 76 | 22000 | 34000 | 51000 | 60000 | 46000 | 37000 | 29000 |
| 6139 | 95 | 11000 | 19000 | 59000 | 74000 | 57000 | 32000 | 11000 |
| 6140 | 100 | 9300 | 34000 | 81000 | 93000 | 65000 | 35000 | 18000 |
| 6141 | 130 | 7300 | 22000 | 58000 | 98000 | 60000 | 34000 | 9300 |

Table 6.9 : Grain sizes at FZ and HAZ across the weld bead in 2.7 mm thick IMI 318 welded specimens with different heat input rates and at a fixed welding current of 100 A

| Specimen no. | Heat input rate ( $Jmm^{-1}$ ) | Grain size (mean grain area), $\mu m^2$ | | | | | | |
|---|---|---|---|---|---|---|---|---|
| | | HAZ | N-HAZ | FZ | FZ | FZ | N-HAZ | HAZ |
| | | Zone location ( mm ) | | | | | | |
| | | -3 | -2 | -1 | 0 | 1 | 2 | 3 |
| 6142 | 120 | 21000 | 71000 | 93000 | 110000 | 93000 | 74000 | 30000 |
| 6143 | 110 | 32000 | 61000 | 90000 | 110000 | 100000 | 87000 | 35000 |
| 6144 | 95 | 7700 | 24000 | 71000 | 85000 | 61000 | 35000 | 8700 |
| 6145 | 86 | 6600 | 15000 | 38000 | 57000 | 49000 | 17000 | 5800 |
| 6146 | 79 | 8400 | 16000 | 47000 | 56000 | 55000 | 24000 | 12000 |

Table 6.10 : Hardness at centre of weld at different welding parameters for 3.0 mm thick welded specimens

| Specimen no. | Current, A | Welding speed, $mms^{-1}$ | Heat input rate, $Jmm^{-1}$ | #Hardness number, $H_v$ |
|---|---|---|---|---|
| 6201 | 195 | 5.1 | 79 | 318 |
| 6202 | 200 | 5.1 | 64 | 316 |
| 6203 | 205 | 5.1 | 53 | 313 |
| 6204 | 210 | 5.1 | 45 | 310 |
| 6205 | 215 | 5.1 | 106 | 308 |
| 6206 | 180 | 3.4 | 85 | 291 |
| 6207 | 180 | 3.8 | 71 | 300 |
| 6208 | 180 | 4.0 | 61 | 304 |
| 6209 | 180 | 4.2 | 119 | 310 |
| 6210 | 180 | 4.7 | 95 | 318 |

# These are average values out of 3 repeated measurements.

Table 6.11 : Tensile properties of 2.3 mm thick IMI 318 welded specimens with varying welding current and at a fixed welding speed of 4.2 $mms^{-1}$

| Specimen | 6301 | 6302 | 6303 | 6304 |
|---|---|---|---|---|
| Welding current /A | 80 | 100 | 110 | 140 |
| Welding voltage / V | 13.2 | 14.0 | 14.4 | 15.6 |
| Heat input rate / $Jmm^{-1}$ | 51 | 68 | 76 | 110 |
| Yield load / kN | 15.0 | 14.8 | 14.7 | 14.4 |
| Tensile strength / MPa | 1090 | 1070 | 1070 | 1040 |
| Tensile stress / MPa | 1190 | 1160 | 1150 | 1120 |
| Area of reduction / % | 8.5 | 7.9 | 7.3 | 6.4 |
| Strain to failure / % | 10.2 | 8.5 | 7.8 | 7.0 |

Table 6.12 : Tensile properties of 2.3 mm thick IMI 318 welded specimens with varying welding speed and at a fixed welding current of 100 A

| Specimen | 6305 | 6306 | **6302** | 6307 | 6308 |
|---|---|---|---|---|---|
| Speed / $mms^{-1}$ | 5.1 | 4.7 | 4.2 | 3.8 | 3.4 |
| Heat input rate / $Jmm^{-1}$ | 56 | 61 | 68 | 75 | 85 |
| Yield load / kN | 14.9 | 14.8 | 14.7 | 14.5 | 14.3 |
| Tensile strength / MPa | 1080 | 1070 | 1070 | 1050 | 1040 |
| Tensile stress / MPa | 1180 | 1170 | 1160 | 1140 | 1060 |
| Area of reduction / % | 8.8 | 8.2 | 7.9 | 7.5 | 1.7 |
| Strain to failure / % | 9.8 | 9.2 | 8.5 | 7.9 | 4.9 |

Table 6.13 : Welding parameters used in 1.5 mm thick IMI 318 welded specimens in section 6.3.2

| Specimen | Specimen no. | Welding current, A | Welding speed, $mms^{-1}$ | Pulse-on time, s |
|---|---|---|---|---|
| IMI 318 | 6309 | 110 | 1.3 | 0.5 |
| | 6310 | 130 | 0.38 | 0.4 |
| | 6311 | 180 | 0.76 | 0.4 |
| | 6312 | 210 | 0.97 | 0.4 |
| | 6313 | 210 | 0.61 | 0.3 |
| | 6314 | 235 | 0.87 | 0.3 |
| IMI 318 | 6315 | 60 | 1.2 | 0.3 |
| | 6316 | 60 | 1.3 | 0.3 |
| | 6317 | 60 | 1.5 | 0.3 |
| | 6318 | 60 | 1.6 | 0.3 |
| | 6319 | 60 | 1.8 | 0.3 |
| | 6320 | 75 | 1.4 | 0.3 |
| | 6321 | 70 | 1.4 | 0.3 |
| | 6322 | 65 | 1.4 | 0.3 |
| | 6323 | 60 | 1.4 | 0.3 |
| | 6324 | 55 | 1.4 | 0.3 |

Table 6.14 : Maximum loading, gauge width and gauge thickness in 1.5 mm thick IMI 318 tensile test specimens

| Specimen no. | Gauge width, W, mm | Thickness at gauge width, $T_G$ , mm | Average plate thickness, $T_b$ , mm | Maximum Loading, kN |
|---|---|---|---|---|
| B1 | 6.03 | 1.50 | 1.50 | 9.8 |
| B2 | 6.03 | 1.51 | 1.51 | 9.9 |
| 6309 | 5.95 | 1.59 | 1.53 | 9.8 |
| 6310 | 5.96 | 1.53 | 1.49 | 9.6 |
| 6311 | 5.96 | 1.55 | 1.50 | 9.7 |
| 6312 | 5.95 | 1.56 | 1.50 | 9.7 |
| 6313 | 5.97 | 1.61 | 1.52 | 9.8 |
| 6314 | 5.97 | 1.60 | 1.52 | 9.7 |
| | | | | |
| 6315 | 6.02 | 1.50 | 1.50 * | 9.4 |
| 6316 | 6.02 | 1.56 | 1.50 | 9.8 |
| 6317 | 6.02 | 1.57 | 1.50 | 9.8 |
| 6318 | 6.02 | 1.56 | 1.50 | 9.8 |
| 6319 | 6.02 | 1.47 | 1.50 | 9.2 |
| 6320 | 6.02 | 1.61 | 1.50 | 10.1 |
| 6321 | 6.01 | 1.59 | 1.50 | 10.0 |
| 6322 | 6.02 | 1.58 | 1.50 | 9.8 |
| 6323 | 6.02 | 1.48 | 1.50 | 9.3 |
| 6324 | 6.02 | 1.50 | 1.50 | 9.5 |

* $T_b$ of specimens 6315 to 6324 were not measured, however, it was estimated to be 1.5 mm (± 2 %), the original plate thickness.

Table 6.15 : Tensile strength of weldments and their failure location in 1.5 mm thick IMI 318 welded specimens with higher heat input rates (specimens 6309 to 6314)

| Specimen no. | Failure location | Tensile strength, MPa, at failure location, ( ) shows the strain to failure in % | Heat input rate, $Jmm^{-1}$ | Cooling rate, R, $Ks^{-1}$ |
|---|---|---|---|---|
| B1 | parent metal | 1080 | | |
| B2 | parent metal | 1080 | | |
| | | | | |
| 6309 | FZ | 1040 (4.1) | 350 | 950 |
| 6310 | FZ | 1050 (2.1) | 1100 | 580 |
| 6311 | BM | 1080 | 760 | 1050 |
| 6312 | FZ | 1040 (4.0) | 690 | 830 |
| 6313 | FZ | 1020 (1.6) | 830 | 380 |
| 6314 | FZ | 1020 (3.1) | 650 | 680 |

Table 6.16 Tensile strength of weldments and their failure location in 1.5 mm thick IMI 318 welded specimens with lower heat input rates (specimens 6315 to 6324)

| Specimen no. | Failure location | Tensile strength (MPa) at failure location | Heat input rate, $Jmm^{-1}$ |
|---|---|---|---|
| 6315 | BM | 1040 | 220 |
| 6316 | BM | 1090 | 200 |
| 6317 | BM | 1090 | 180 |
| 6318 | BM | 1090 | 160 |
| 6319 | BM | 1020 | 140 |
| 6320 | BM | 1120 | 230 |
| 6321 | BM | 1110 | 220 |
| 6322 | BM | 1090 | 200 |
| 6323 | BM | 1030 | 190 |
| 6324 | BM | 1050 | 180 |

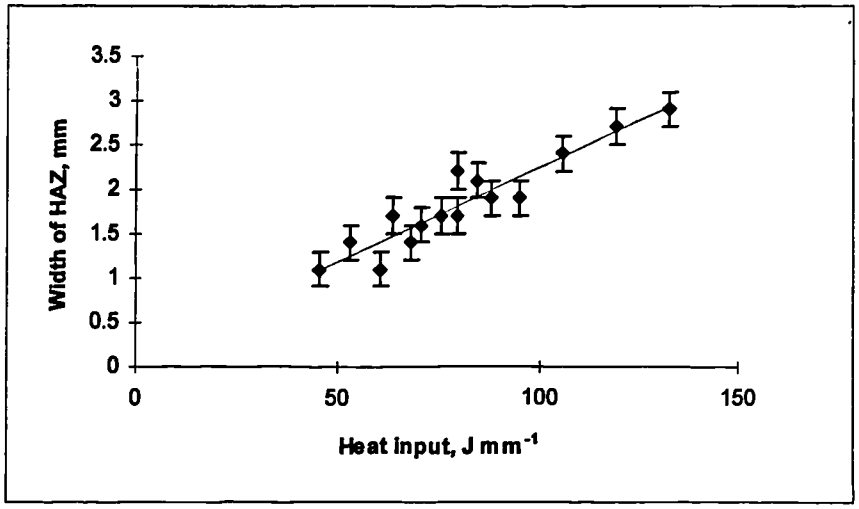


Figure 6.1 : Width of HAZ versus welding heat input rate (1.2 mm thick IMI 318 welded specimens 6101 to 6116))

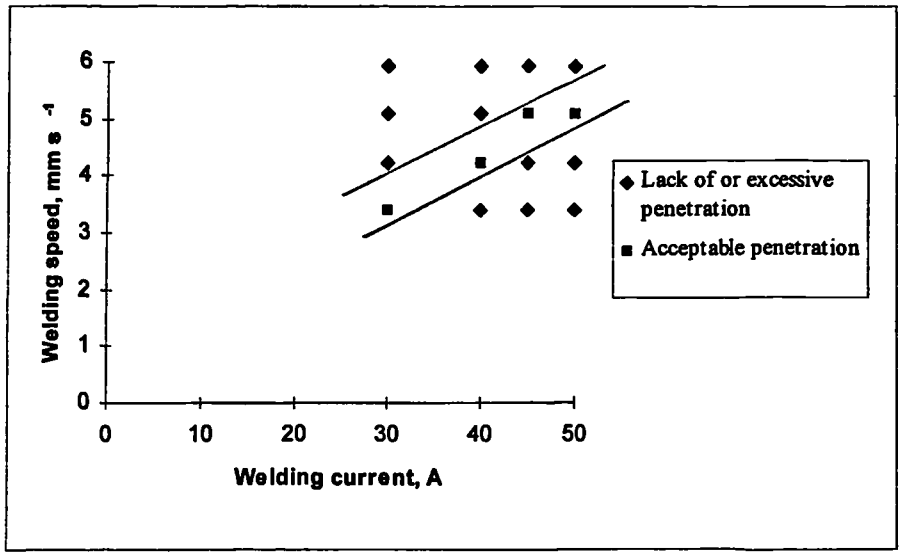


Figure 6.2 : Welding spectrum which produced welds with acceptable penetration (1.2 mm thick IMI 318 welded specimens 6101 to 6116)

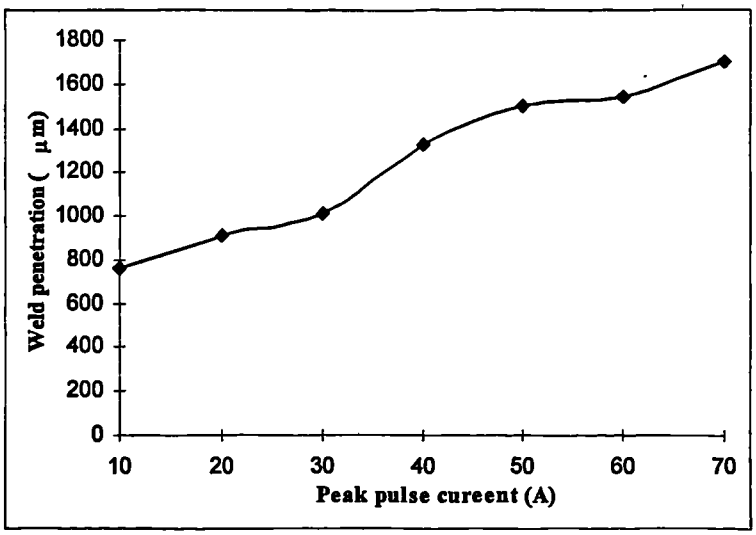


Figure 6.3 : Weld penetration versus peak pulse current for 1.7 mm thick IMI 318 welded specimens at a fixed welding speed of 4.2 $mms^{-1}$ *(specimens 6117 to 6123)*

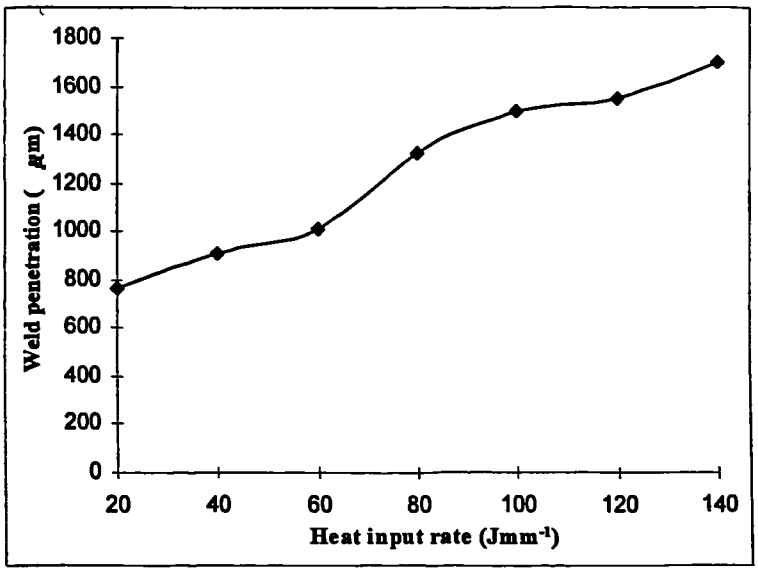


Figure 6.4 : Weld penetration versus heat input rate for 1.7 mm thick IMI 318 welded specimens at a fixed welding speed of 4.2 $mms^{-1}$ (specimens 6117 to 6123)

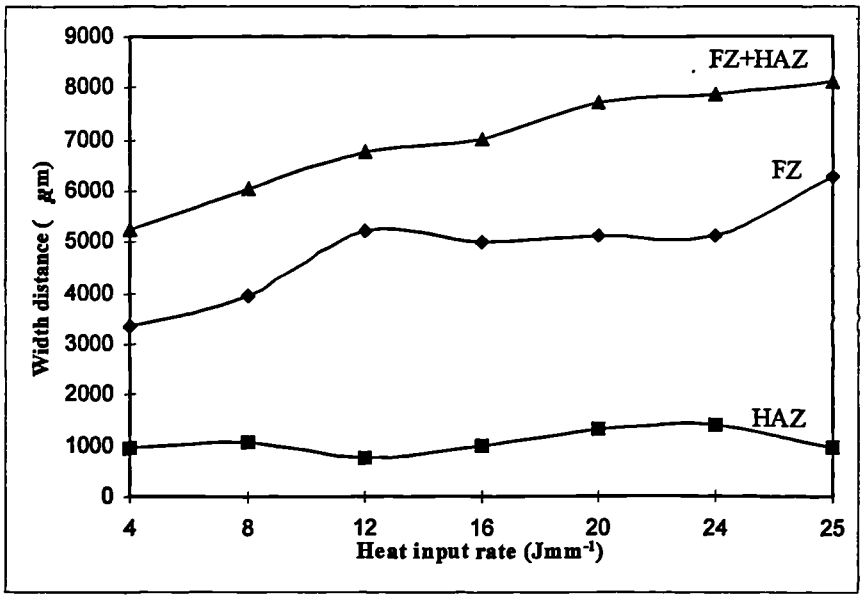


Figure 6.5 : Widths of FZ & HAZ versus heat input rate for 1.0 mm thick IMI 318 specimens at a fixed welding speed of 42 $mms^{-1}$ (specimens 6124 to 6130)

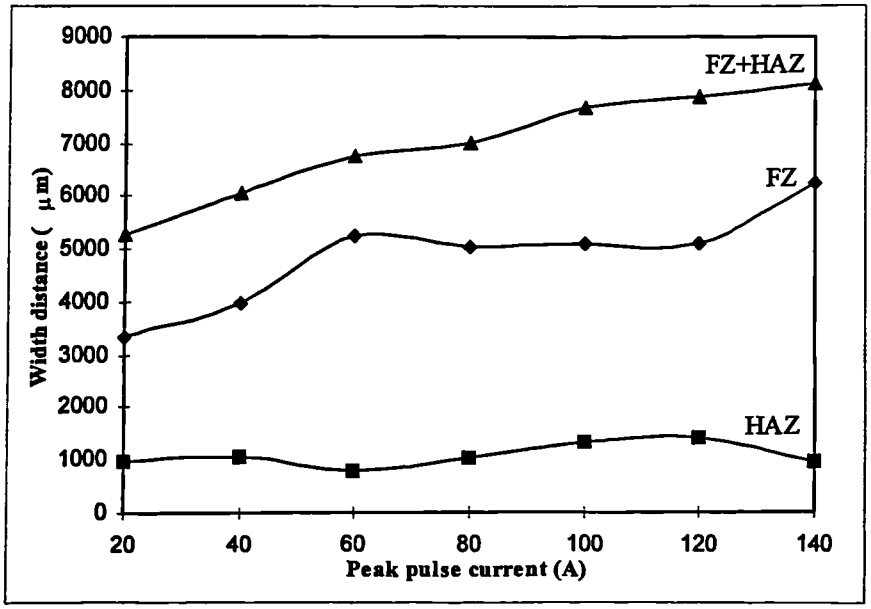


Figure 6.6 : Widths of FZ & HAZ versus welding current for 1.0 mm thick IMI 318 specimens at a fixed welding speed of 42 $mms^{-1}$ (specimens 6124 to 6130)

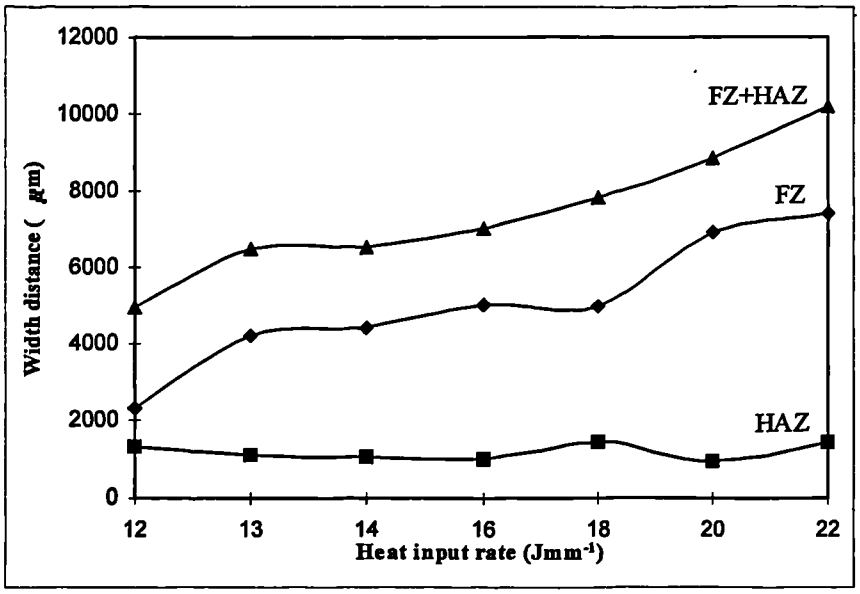


Figure 6.7 : Widths of FZ & HAZ versus heat input rate for 1.0 mm thick IMI 318 welded specimens at a fixed welding current of 80 A (specimens 6131 to 6137)

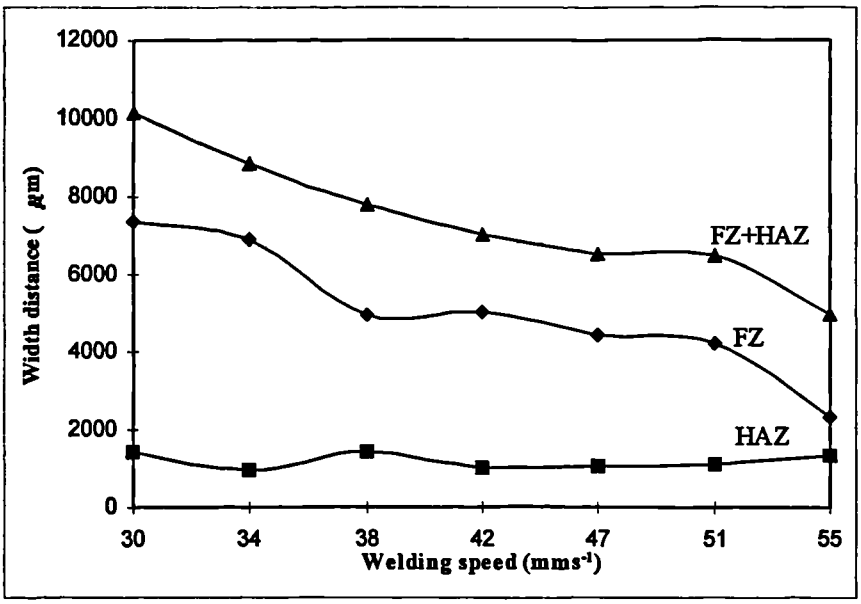


Figure 6.8 : Widths of FZ & HAZ versus welding speed for 1.0 mm thick IMI 318 welded specimens at a fixed welding current of 80 A (specimens 6131 to 6137)

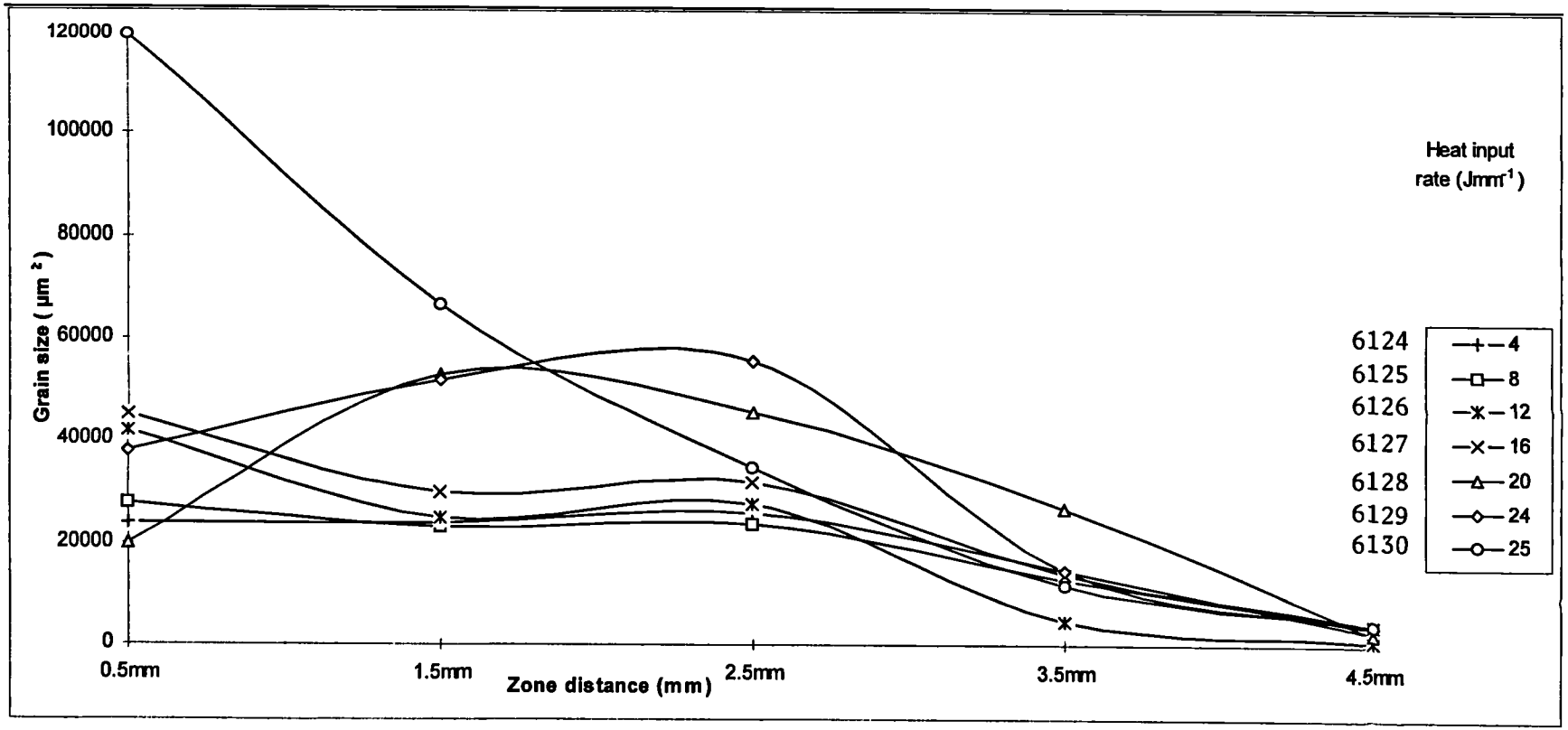


Figure 6.9 : Grain sizes at different zone locations for 1.0 mm thick IMI 318 welded specimens with varying welding current and heat input rate and at a fixed welding speed of 42 $mms^{-1}$ (specimens 6124 to 6130)

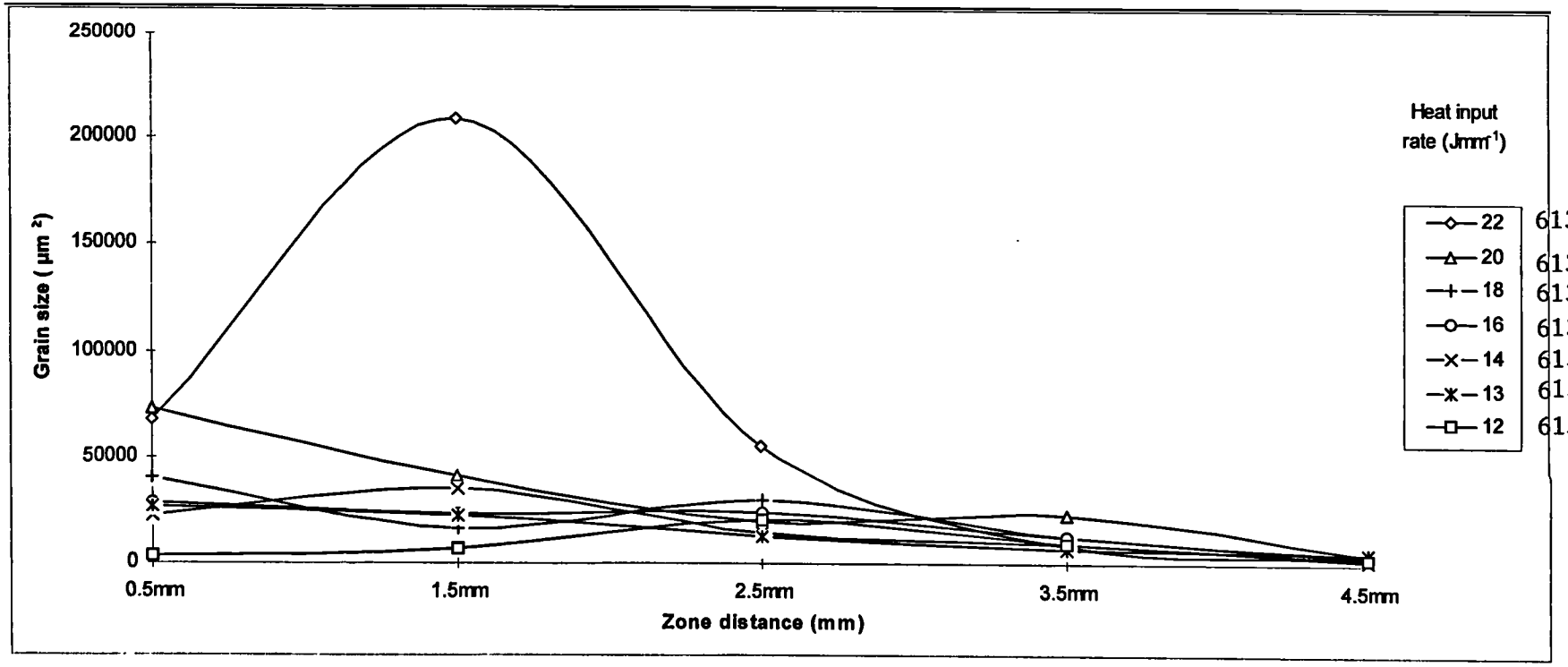


Figure 6.10 : Grain sizes at different zone locations for 1.0 mm thick IMI 318 welded specimens with varying welding speed and heat input rate and at a fixed welding current of 80 A (specimens 6131 to 6137)

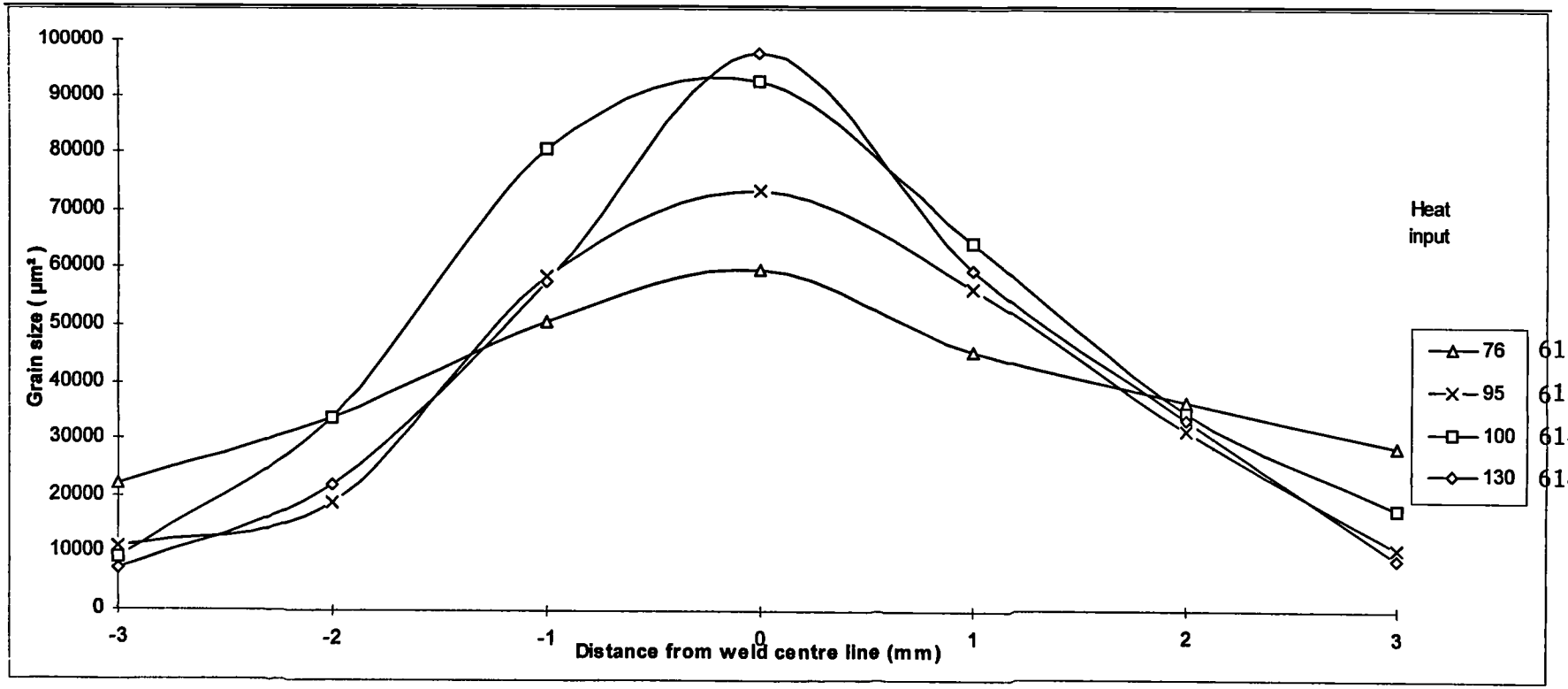


Figure 6.11 : Grain size distribution at FZ and HAZ across the weld bead for 2.7 mm thick IMI 318 welded specimens with varying heat input rate and welding current and at a fixed welding speed of 4.2 $mms^{-1}$ (specimens 6138 to 6141)

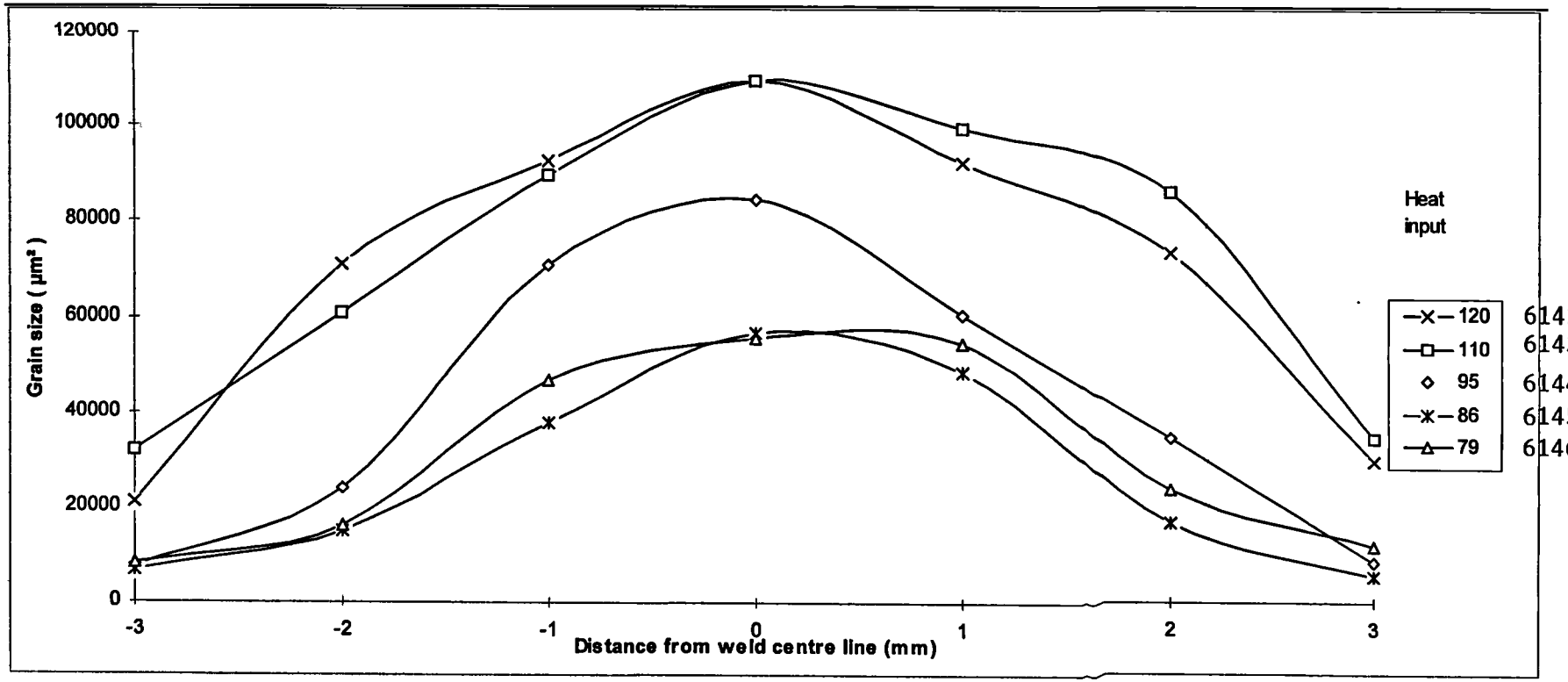


Figure 6.12 : Grain size distribution at FZ and HAZ across the weld bead for 2.7 mm thick IMI 318 welded specimens with varying heat input rate and welding speed and at a fixed welding current of 100 A (specimens 6142 to 6146)

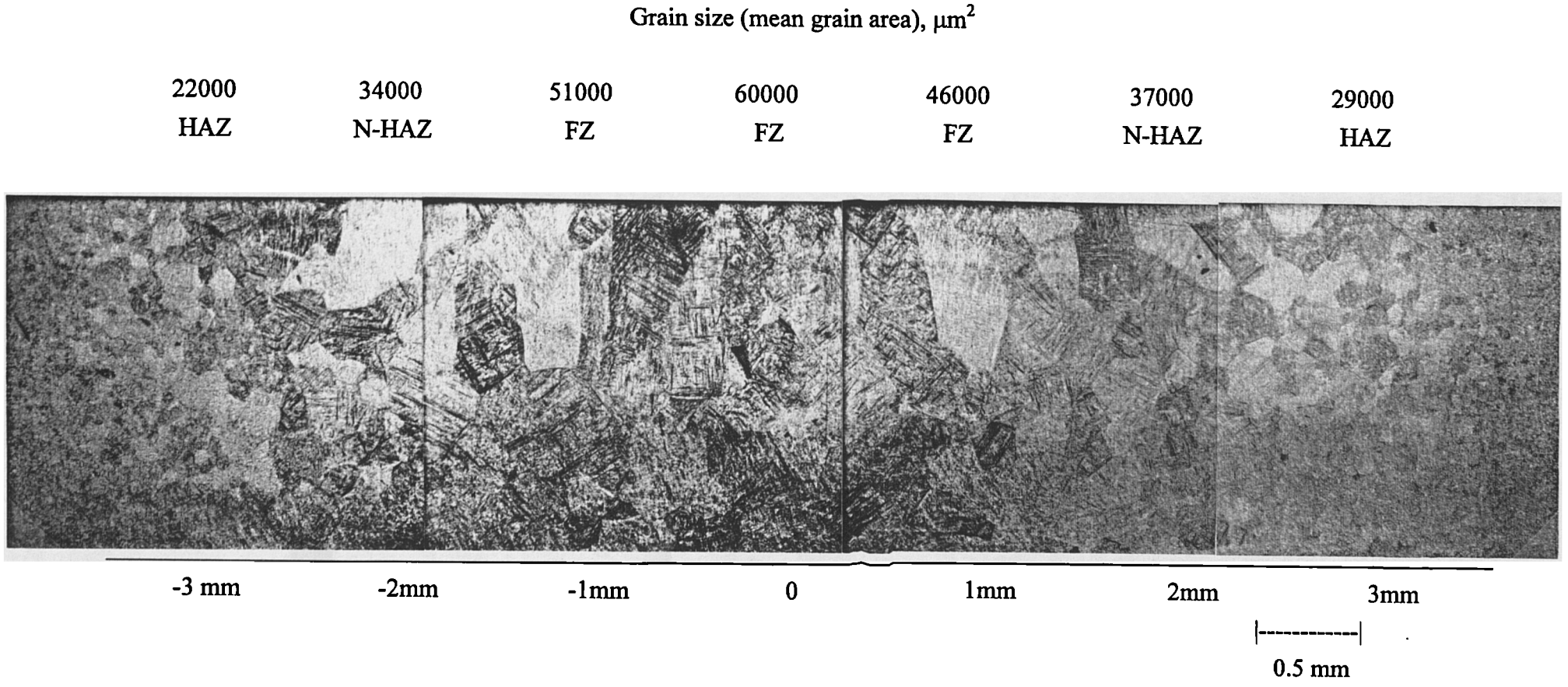


Figure 6.13 (a) : Micrographs of **specimen 6138** taken at and around fusion zone of 2.7 mm IMI 318 weld (Table 6.8)

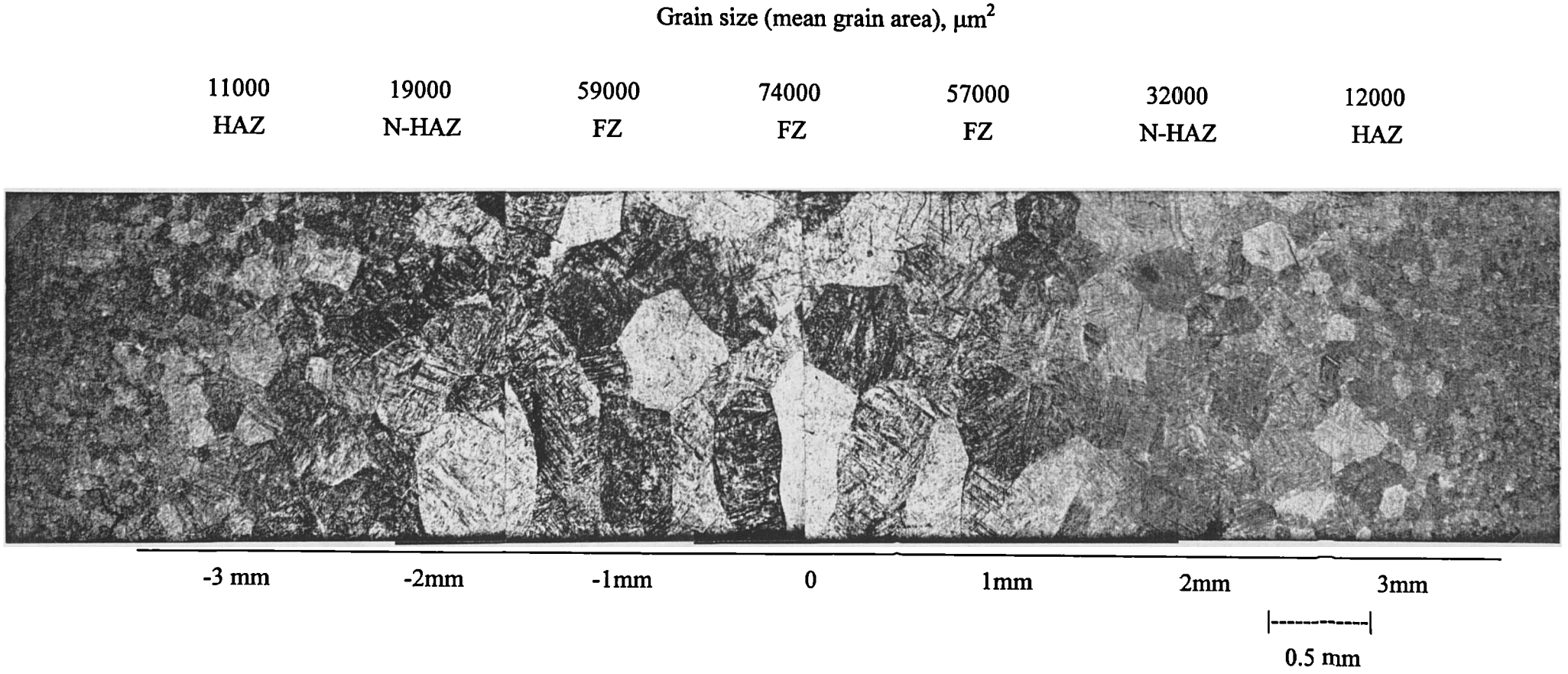


Figure 6.13 (b) : Micrographs of **specimen 6139** taken at and around fusion zone of 2.7 mm IMI 318 weld (Table 6.8)

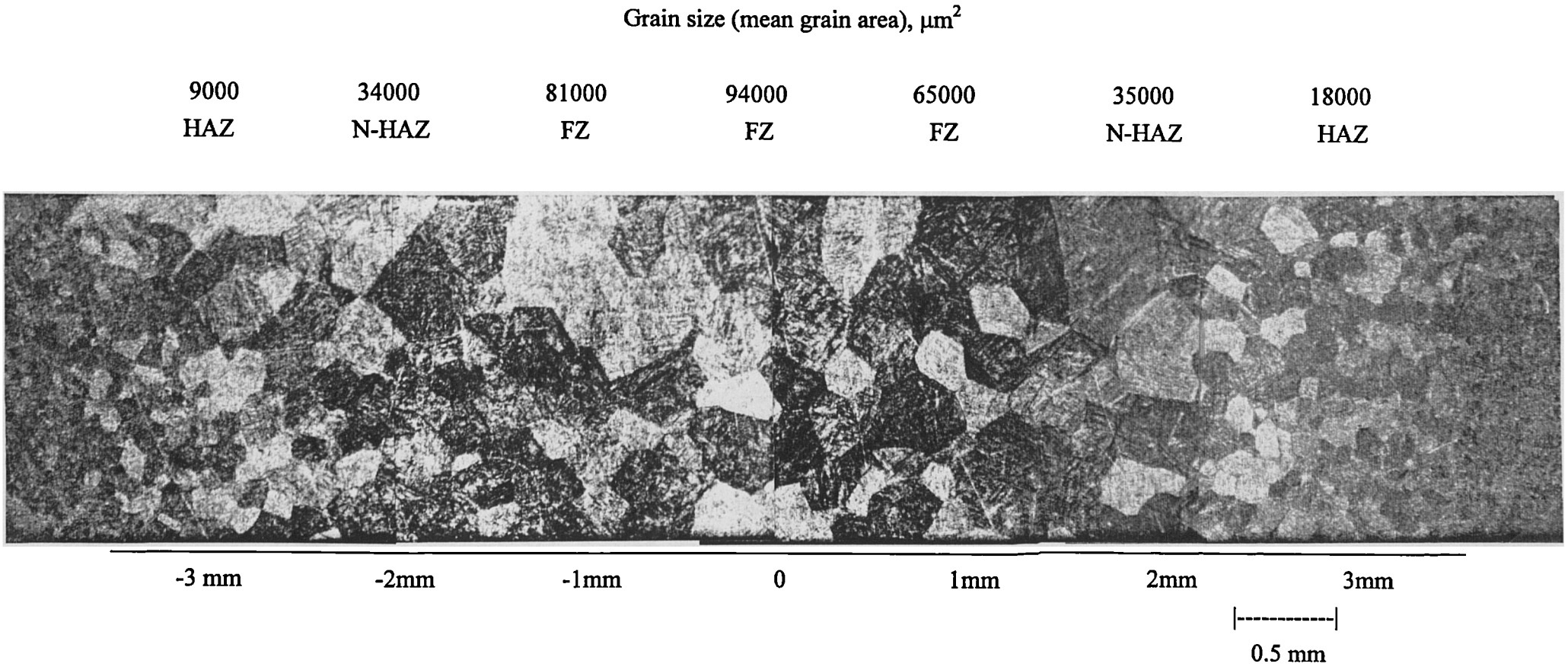


Figure 6.13 (c) : Micrographs of **specimen 6140** taken at and around fusion zone of 2.7 mm IMI 318 weld (Table 6.8)

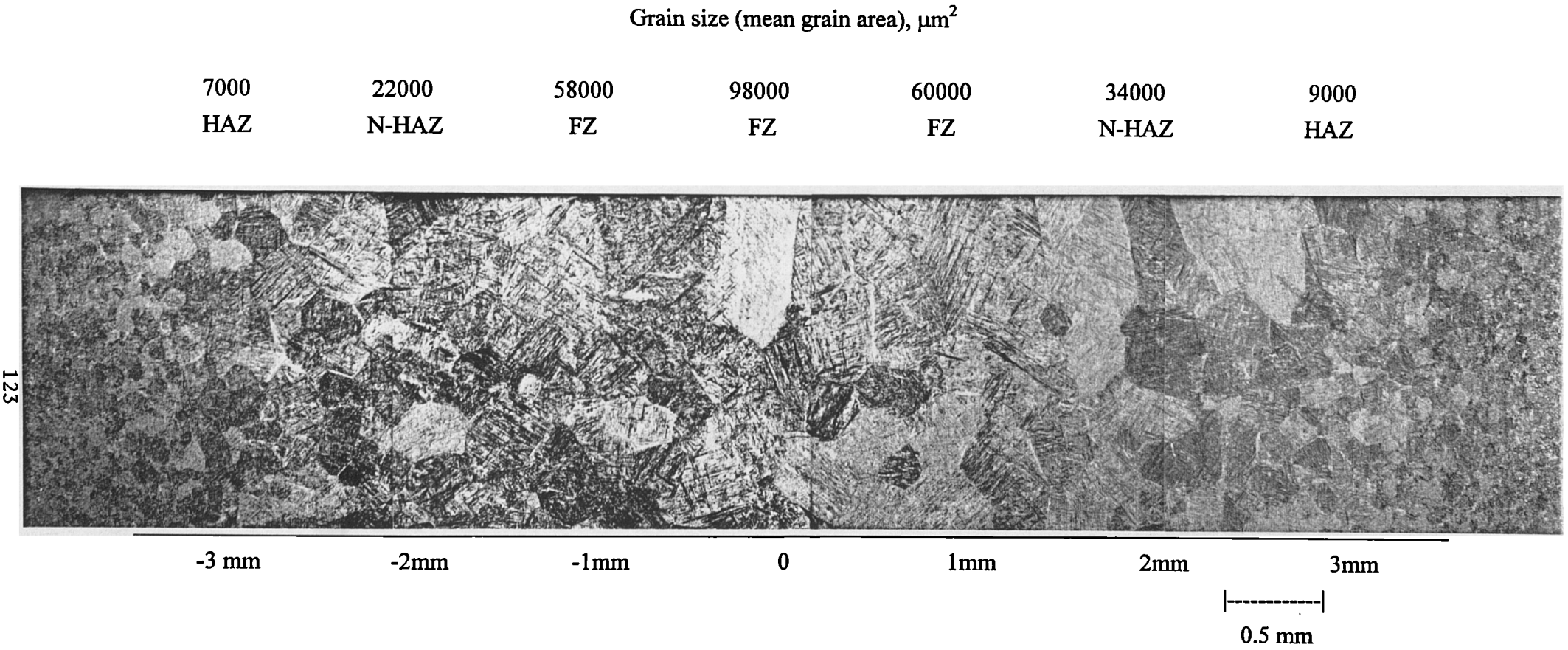


Figure 6.13 (d) : Micrographs of **specimen 6141** taken at and around fusion zone of 2.7 mm IMI 318 weld (Table 6.8)

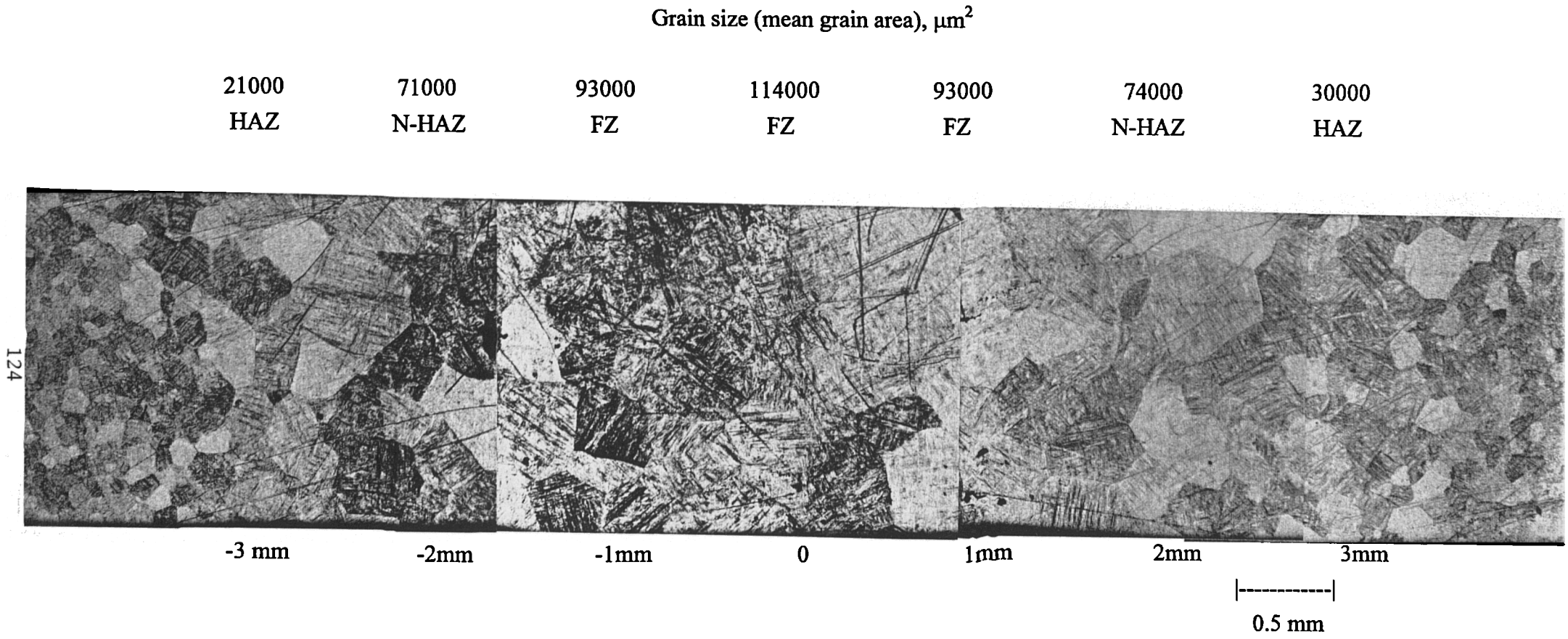


Figure 6.13 (e) : Micrographs of **specimen 6142** taken at and around fusion zone of 2.7 mm IMI 318 weld (Table 6.9)

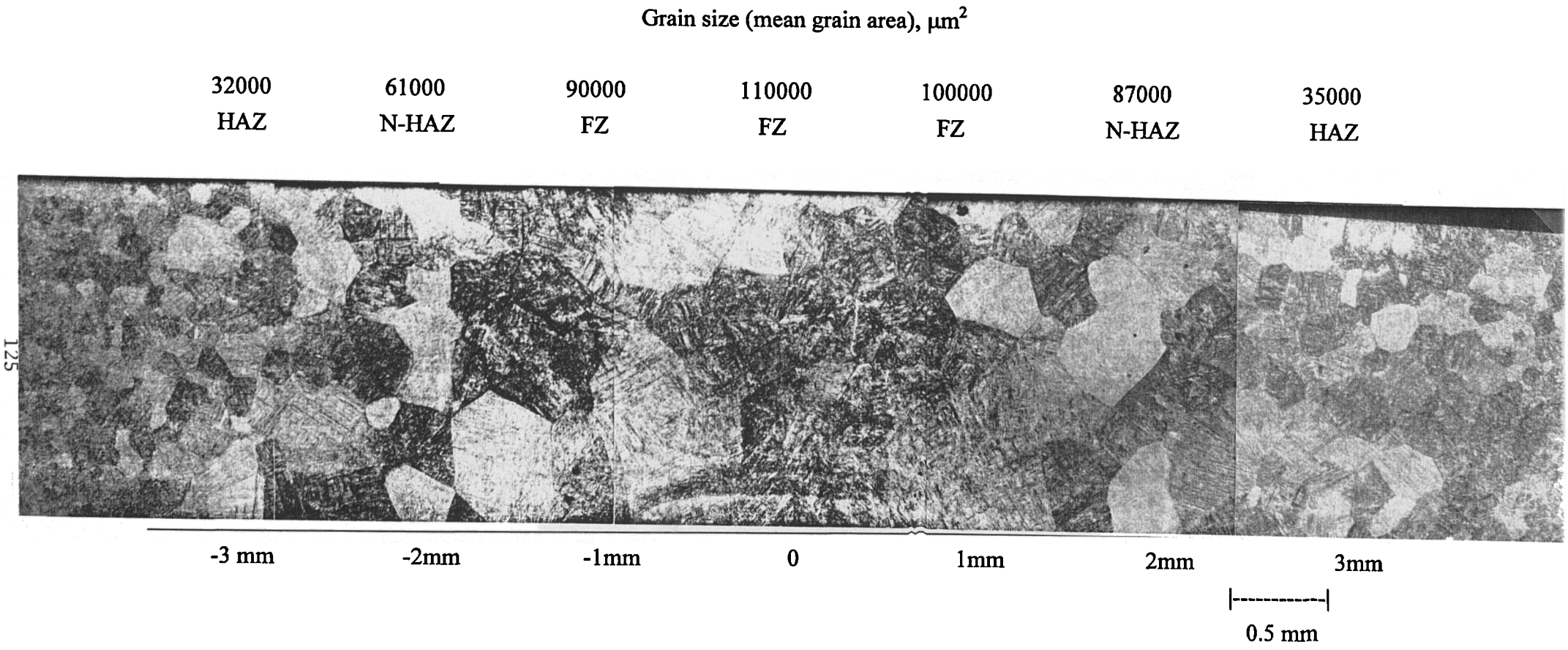


Figure 6.13 (f) : Micrographs of **specimen 6143** taken at and around fusion zone of 2.7 mm IMI 318 weld (Table 6.9)

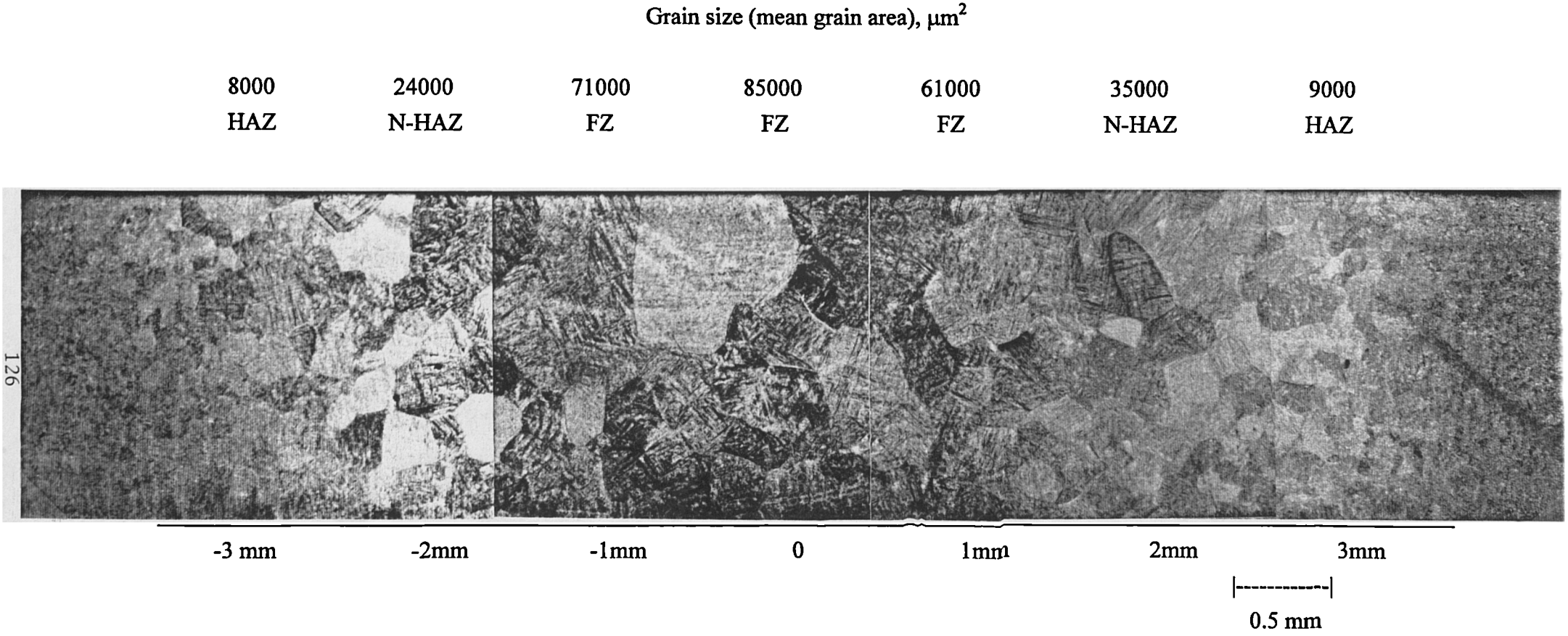


Figure 6.13 (g) : Micrographs of **specimen 6144** taken at and around fusion zone of 2.7 mm IMI 318 weld (Table 6.9)

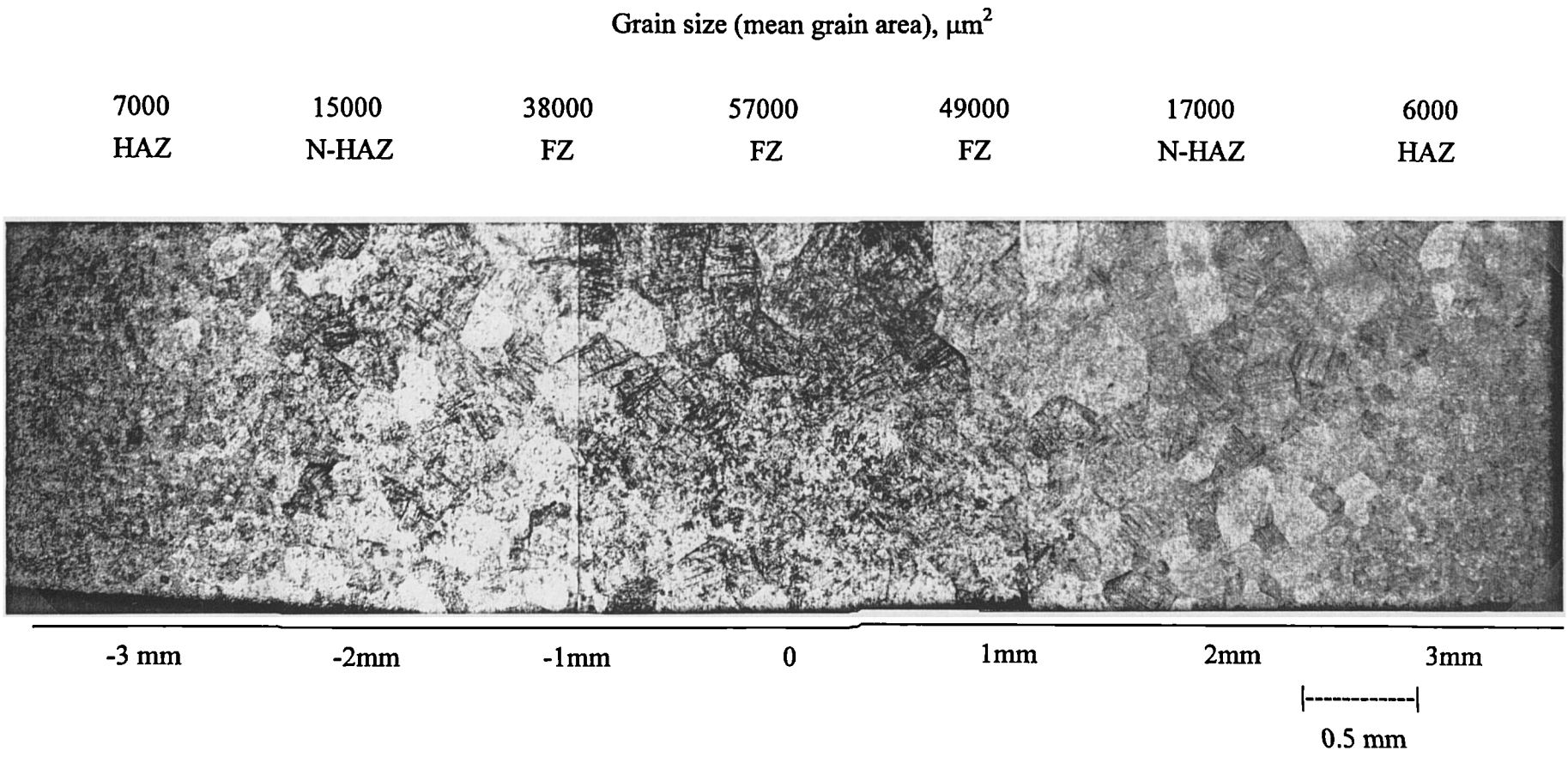


Figure 6.13 (h) : Micrographs of **specimen 6145** taken at and around fusion zone of 2.7 mm IMI 318 weld (Table 6.9)

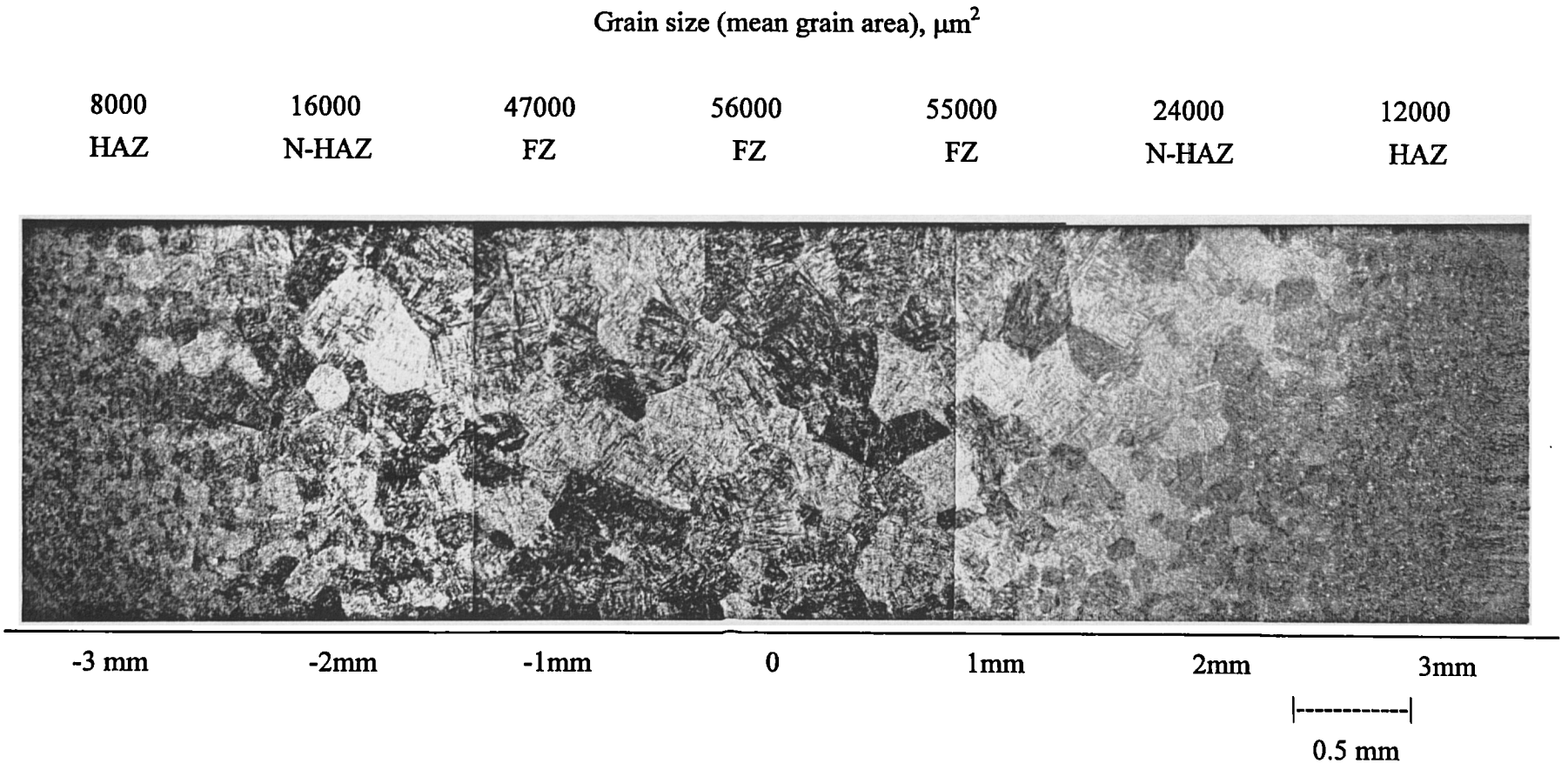


Figure 6.13 (i) : Micrographs of **specimen 6146** taken at and around fusion zone of 2.7 mm IMI 318 weld (Table 6.9)

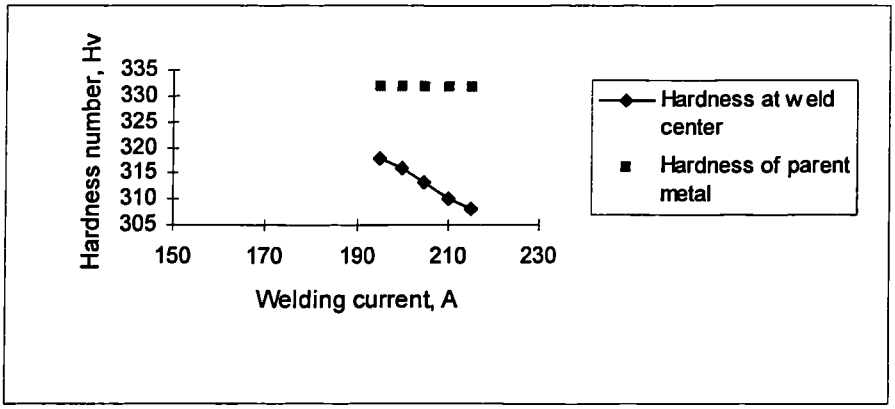


Figure 6.14 : Hardness versus welding current for 3.0 mm IMI 318 welds at a fixed welding speed of 5.1 $mms^{-1}$

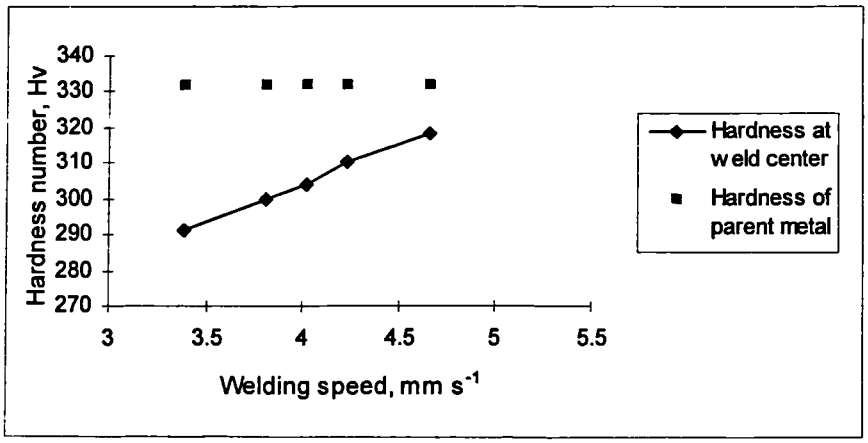


Figure 6.15 : Hardness versus welding speed for 3.0 mm IMI 318 welds at a fixed welding current of 180 A

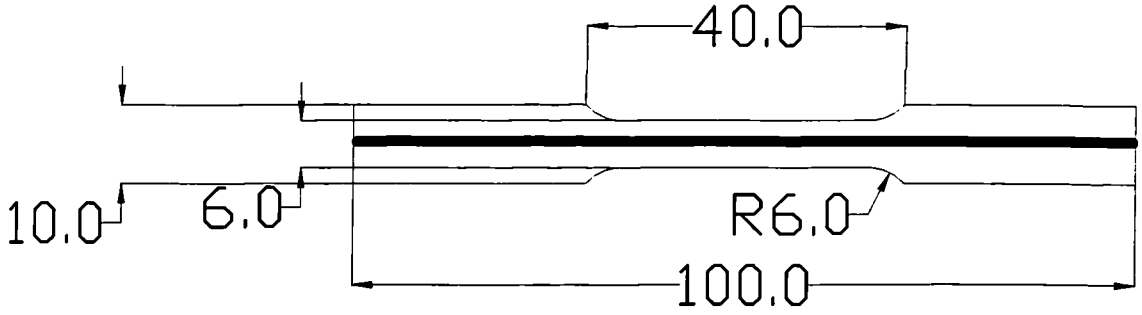


Figure 6.16 : Schematic drawing and dimensions (in mm) of tensile specimens in IMI 318 weldments (specimens 6301 to 6324) (not to scale)

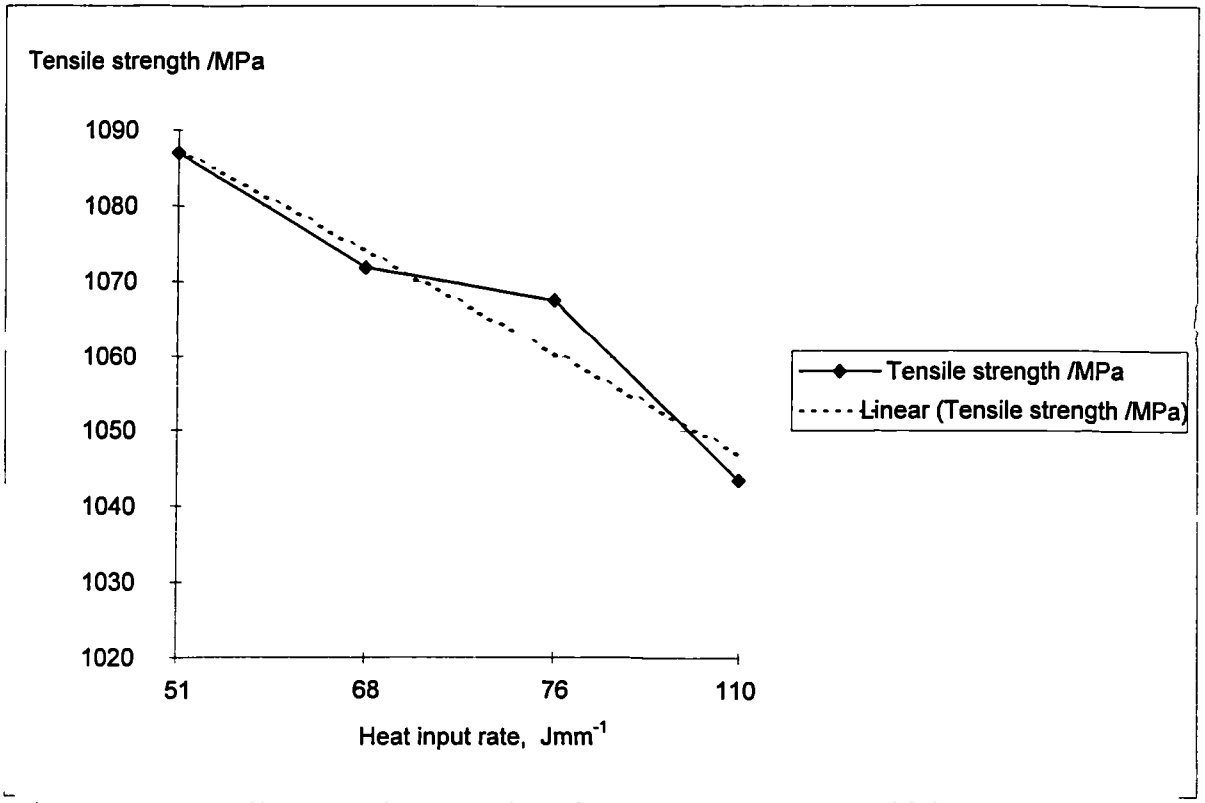


Figure 6.17. Tensile strength versus heat input rate for 2.3 mm thick IMI 318 welded specimens at a fixed welding speed of 4.2 $mms^{-1}$ (specimens 6301 to 6304).

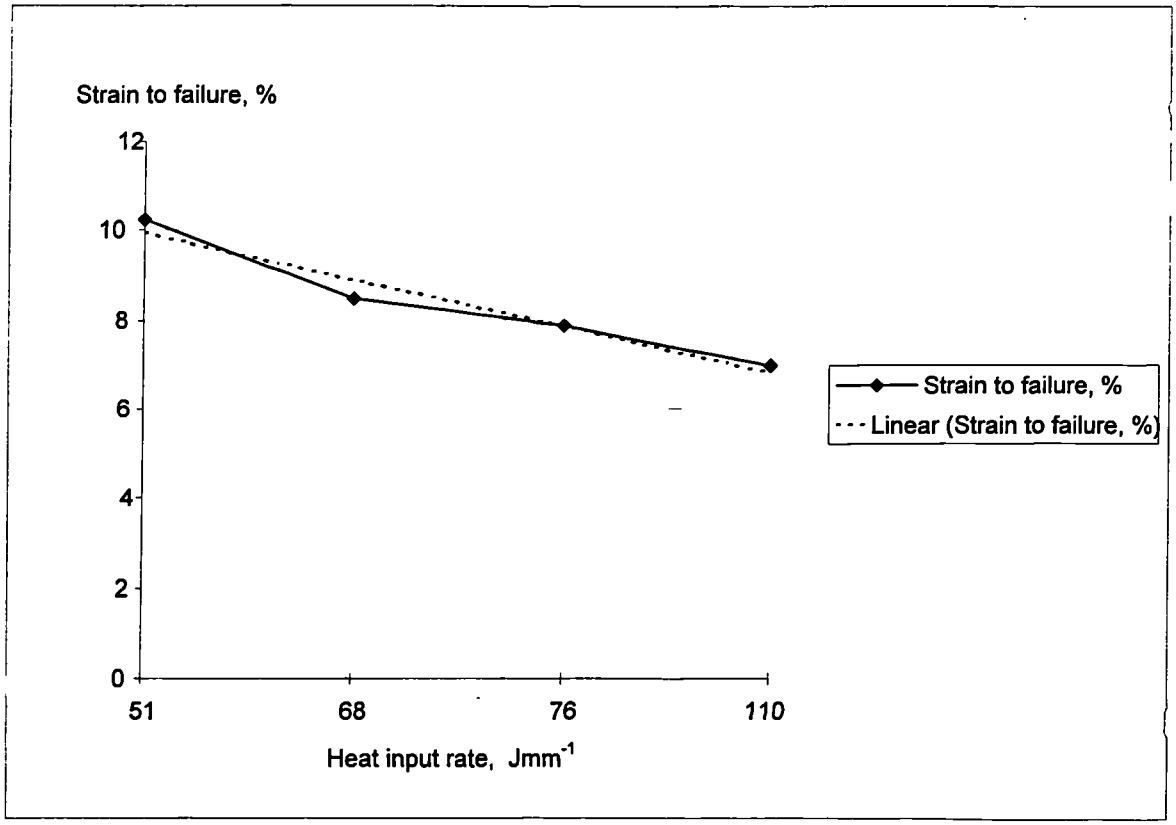


Figure 6.18. Strain to failure versus heat input rate for 2.3 mm thick IMI 318 welded specimens at a fixed welding speed of 4.2 $mms^{-1}$ (specimens 6301 to 6304).

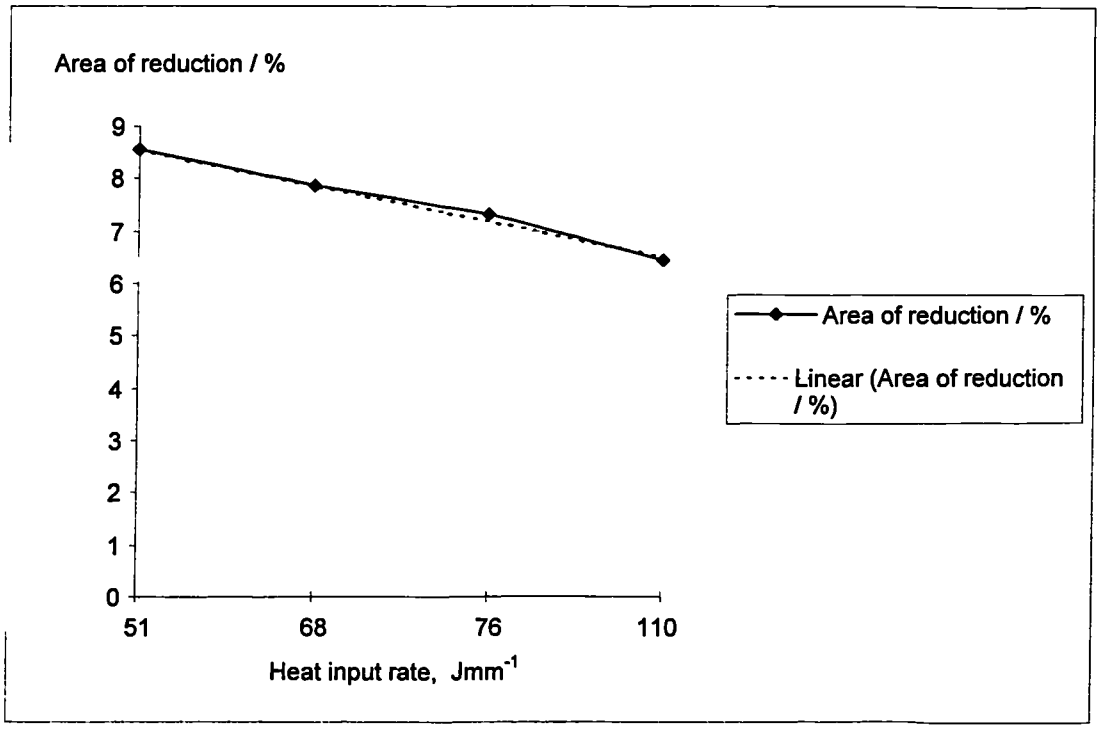


Figure 6.19. Area of reduction versus heat input rate for 2.3 mm thick IMI 318 welded specimens at a fixed welding speed of 4.2 $mms^{-1}$ (specimens 6301 to 6304).

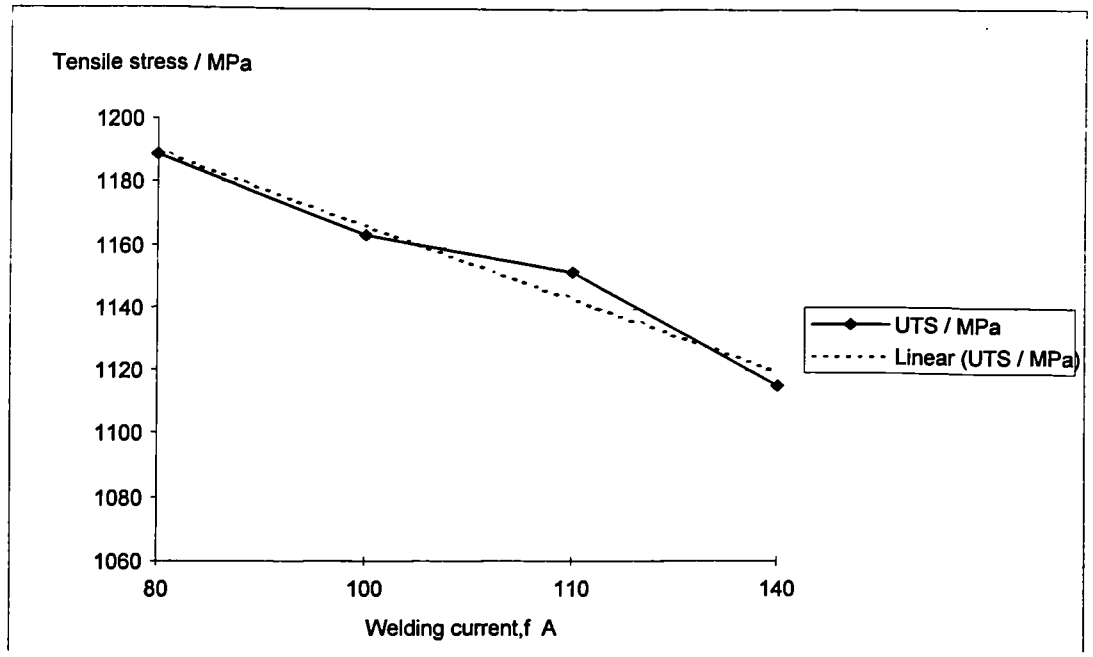


Figure 6.20. Tensile stress versus welding current for 2.3 mm thick IMI 318 welded specimens at a fixed welding speed of 4.2 $mms^{-1}$ (specimens 6301 to 6304).

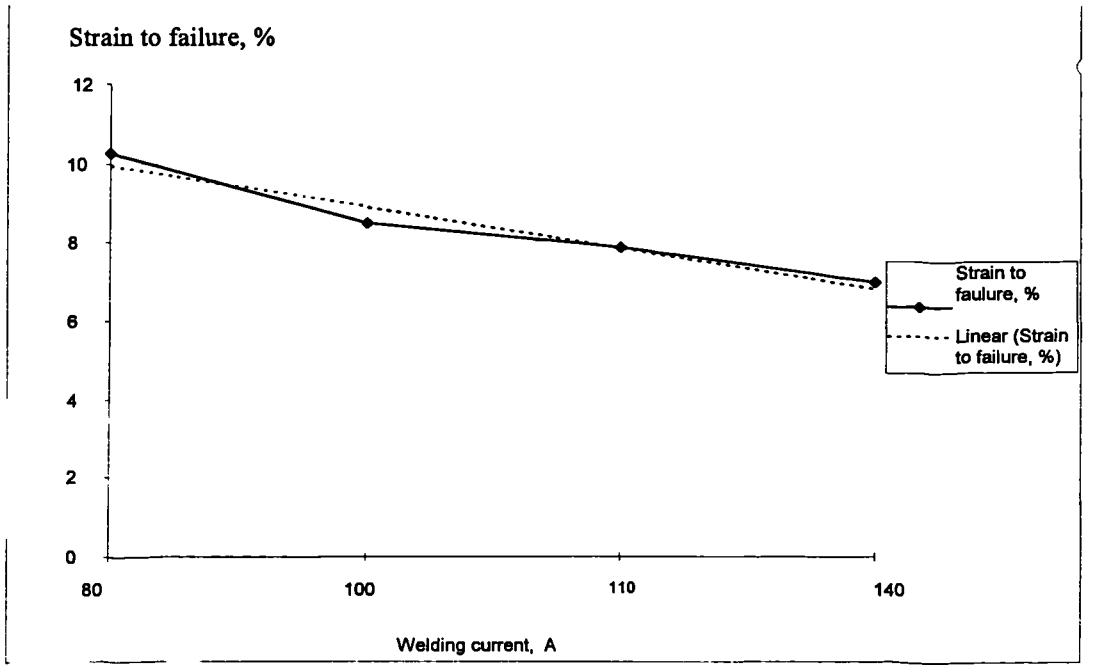


Figure 6.21. Strain to failure versus welding current for 2.3 mm thick IMI 318 welded specimens at a fixed welding speed of 4.2 $mms^{-1}$ (specimens 6301 to 6304).

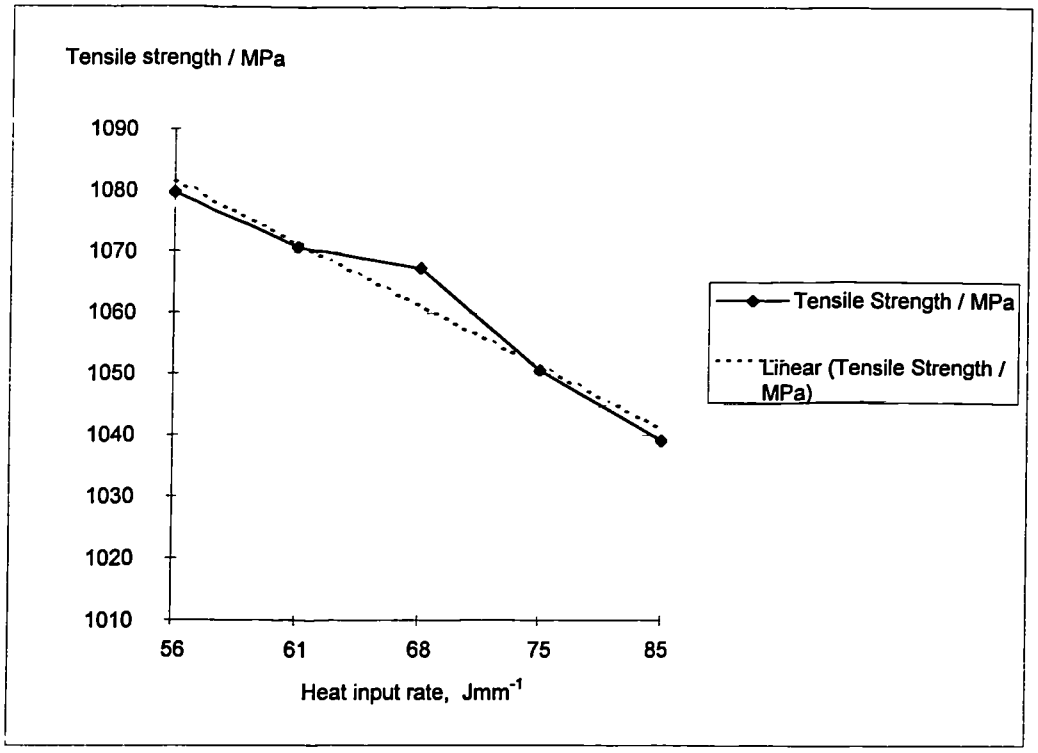


Figure 6.22. Tensile strength versus heat input rate for 2.3 mm thick IMI 318 welded specimens at a fixed welding current of 100 A (specimens 6305 to 6309)

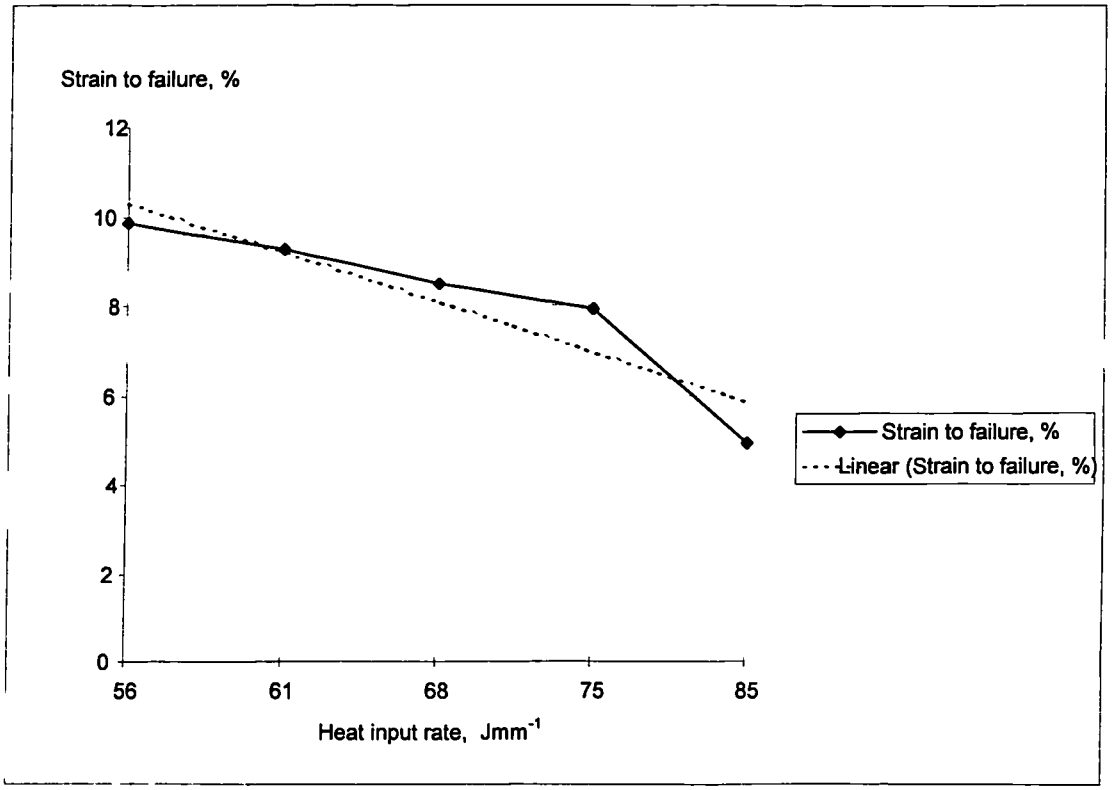


Figure 6.23. Strain to failure versus heat input rate for 2.3 mm thick IMI 318 welded specimens at a fixed welding current of 100 A (specimens 6305 to 6309)

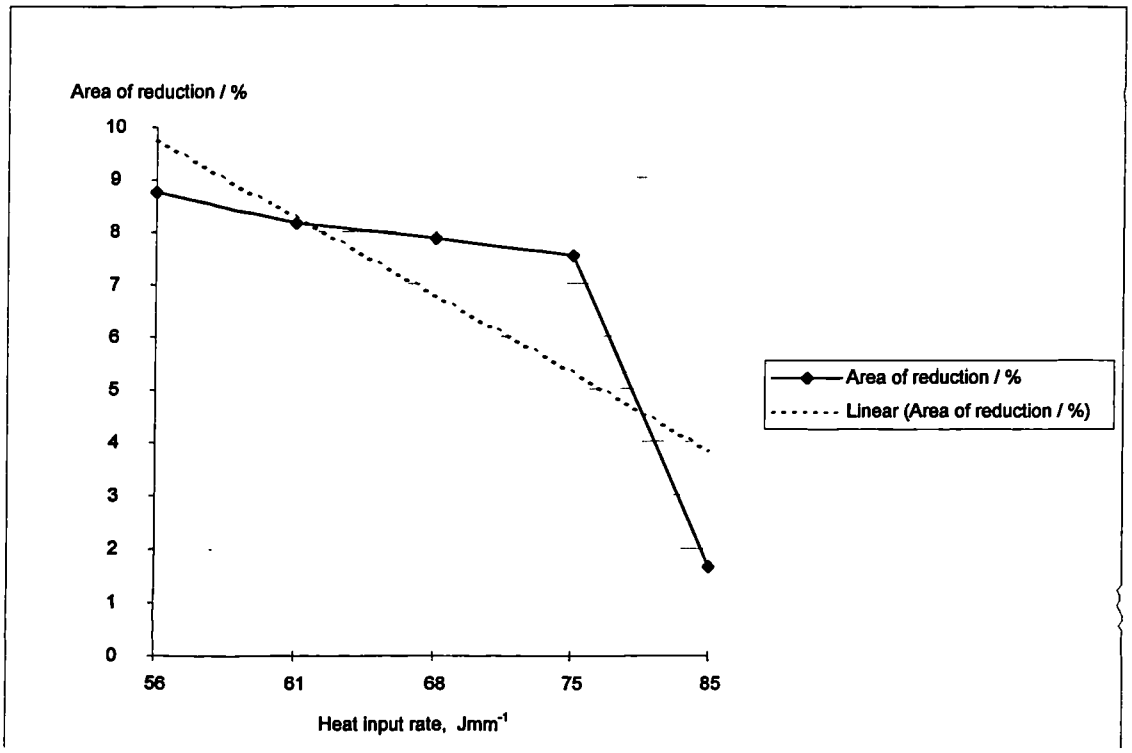


Figure 6.24. Area of reduction versus heat input rate for 2.3 mm thick IMI 318 welded specimens at a fixed welding current of 100 A (specimens 6305 to 6309)

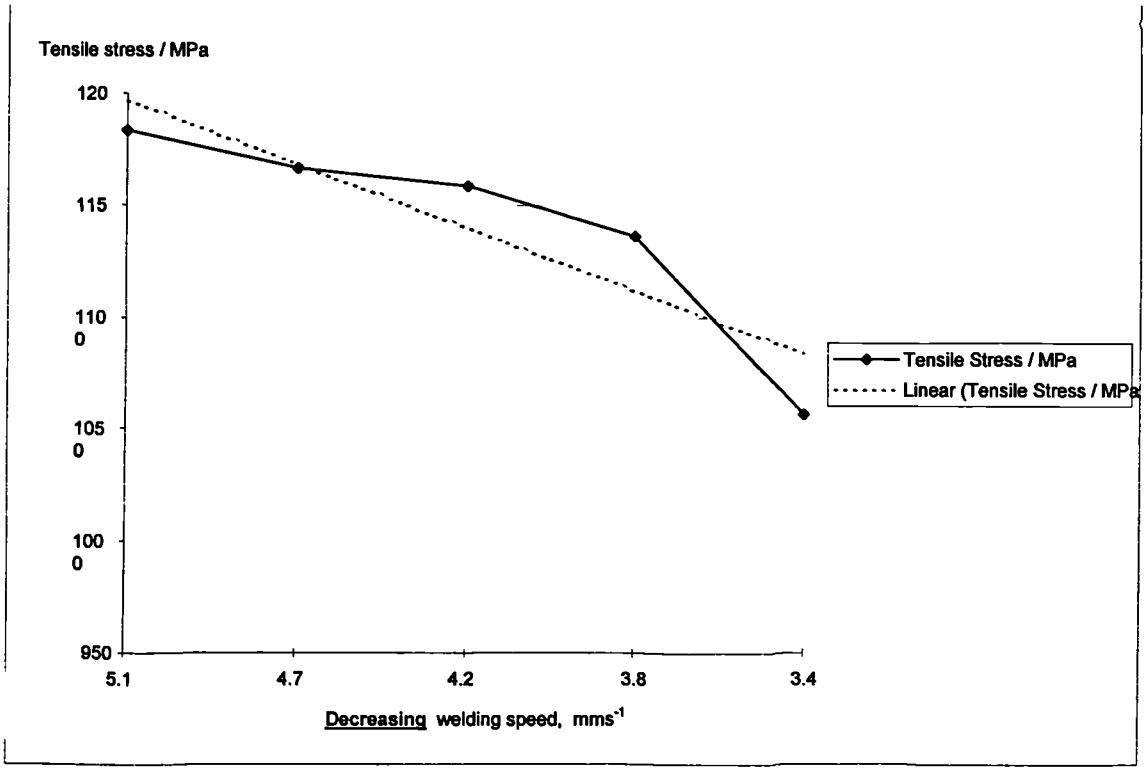


Figure 6.25. Tensile stress versus welding speed for 2.3 mm thick IMI 318 welded specimens at a fixed welding current of 100 A (specimens 6305 to 6309)

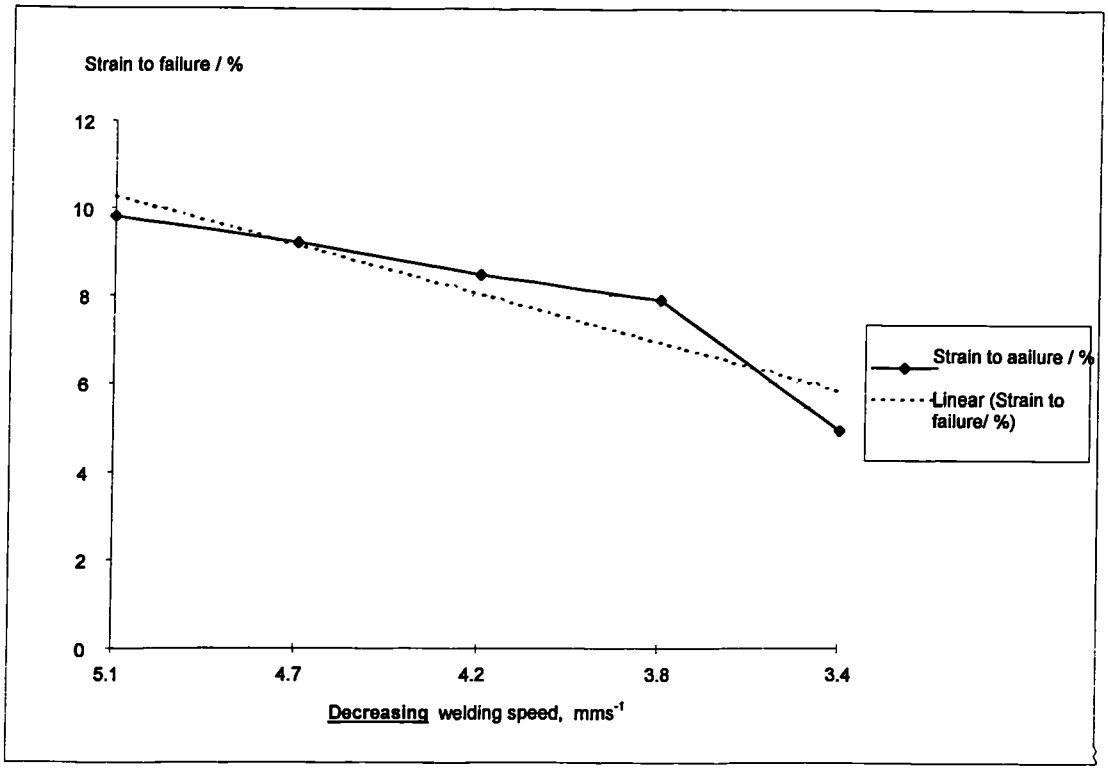


Figure 6.26. Strain to failure versus welding speed for 2.3 mm thick IMI 318 welded specimens at a fixed welding current of 100 A (specimens 6305 to 6309)

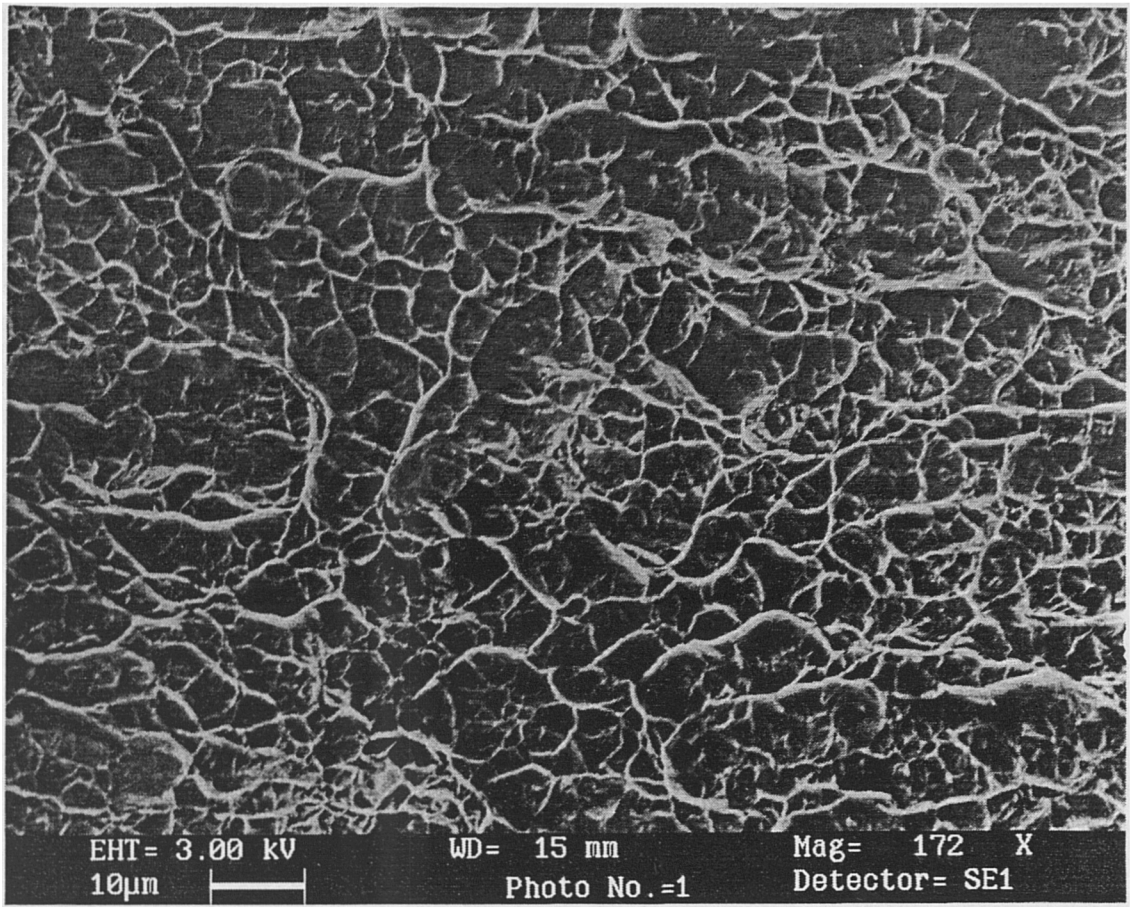


Figure 6.27 : Specimen 6301 (current 80 A, speed 4.2 $mms^{-1}$) Dimple rupture was observed in terms of the cuplike depressions.

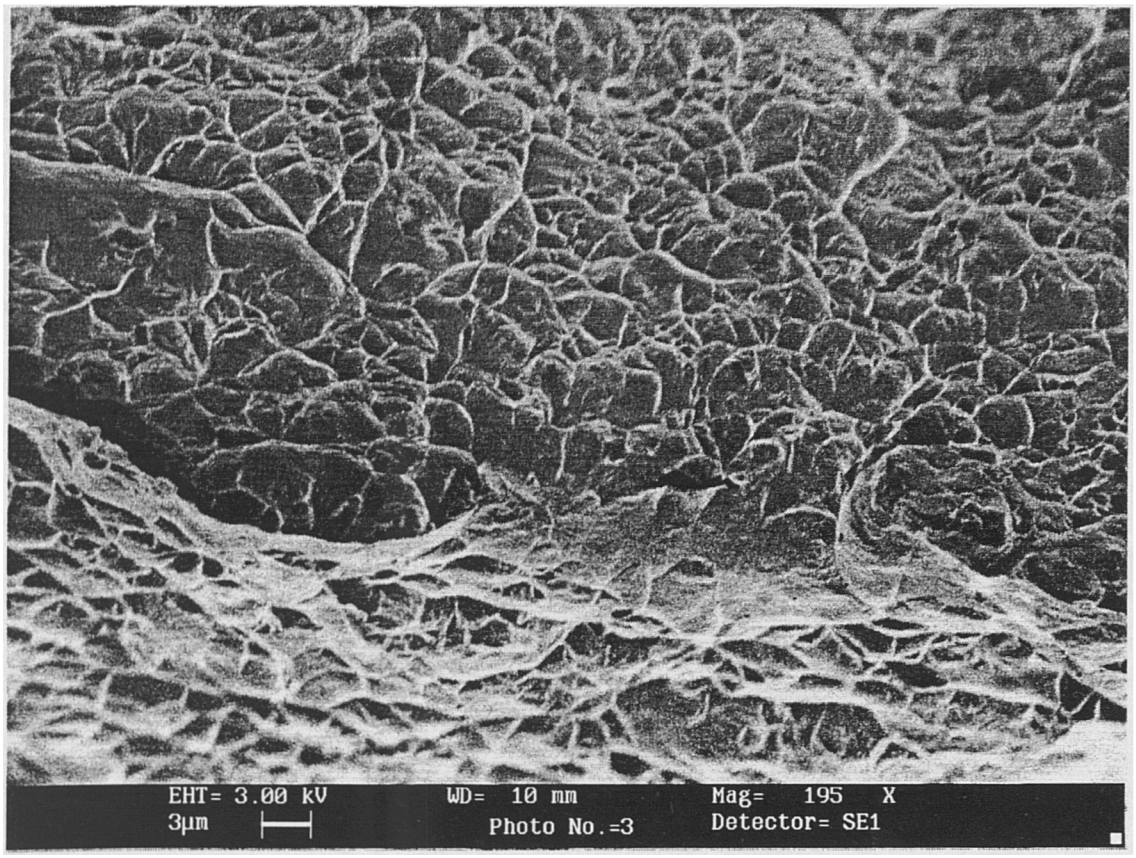


Figure 6.28 : A close-up view of the surface of Figure 6.27. The fracture surface showed very clear cuplike depressions. No porosity or cracks were observed in the surface.

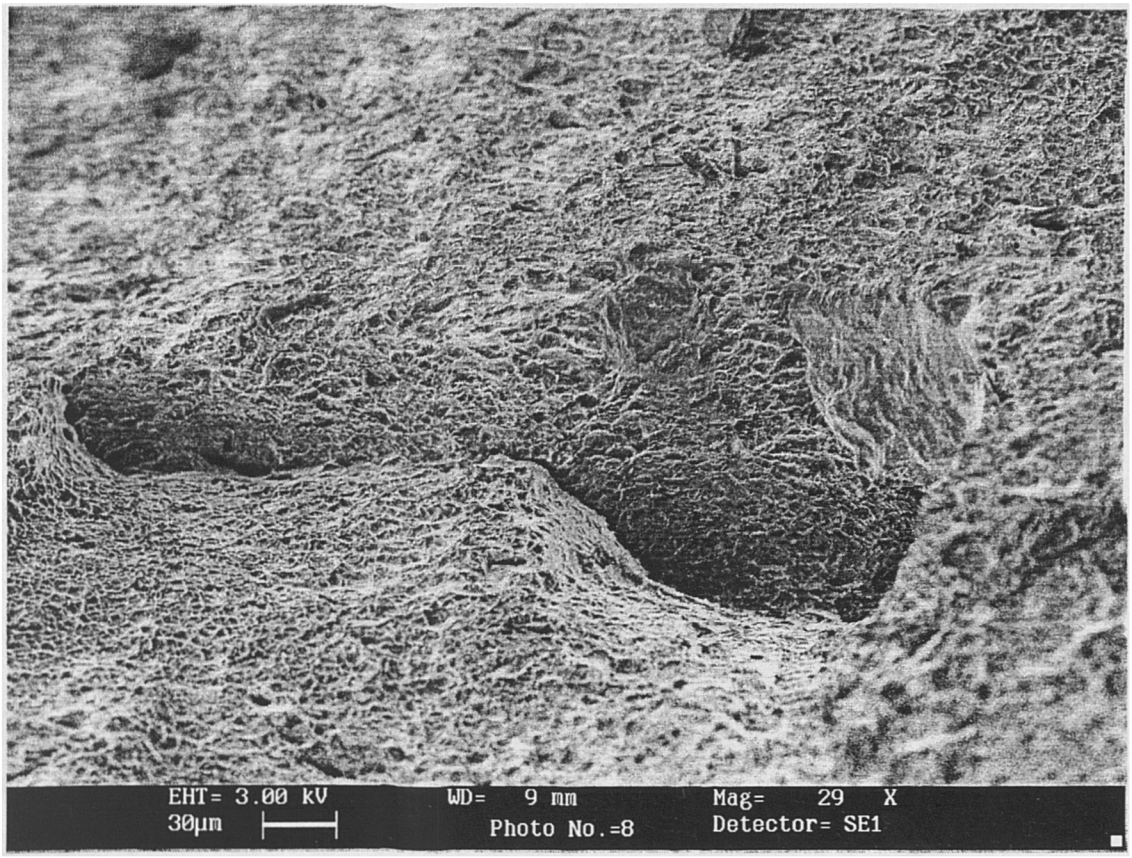


Figure 6.29 :(Specimen 6302, current 100 A, speed 4.2 $mms^{-1}$) A low magnification view of the fracture surface of the specimen. Cuplike depressions were observed due to dimple rupture.

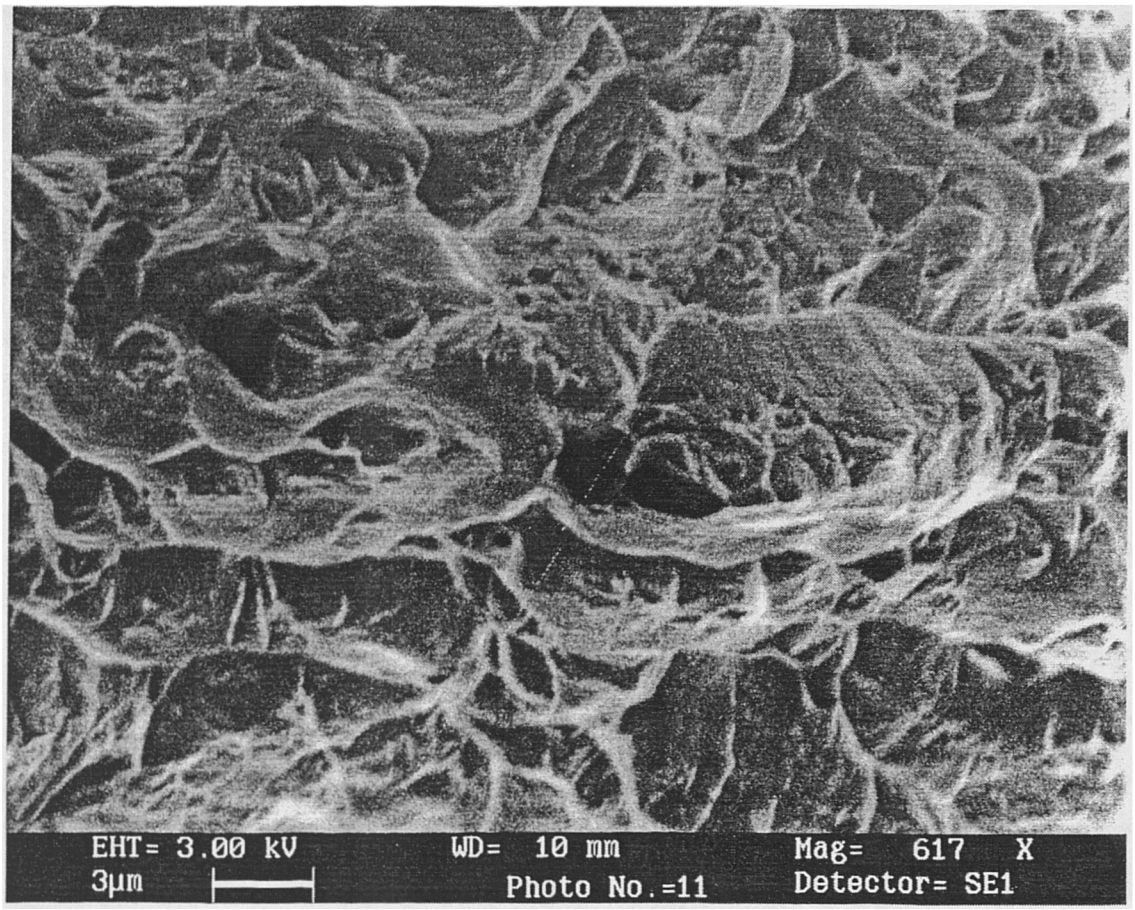


Figure 6.30 : Close-up view of Figure 6.29.
Cuplike depressions were observed more clearly and this type of pattern arises from dimple rupture. The dimple size was larger than that of specimens 6301 (Figure 6.28). A small amount of pores were observed.

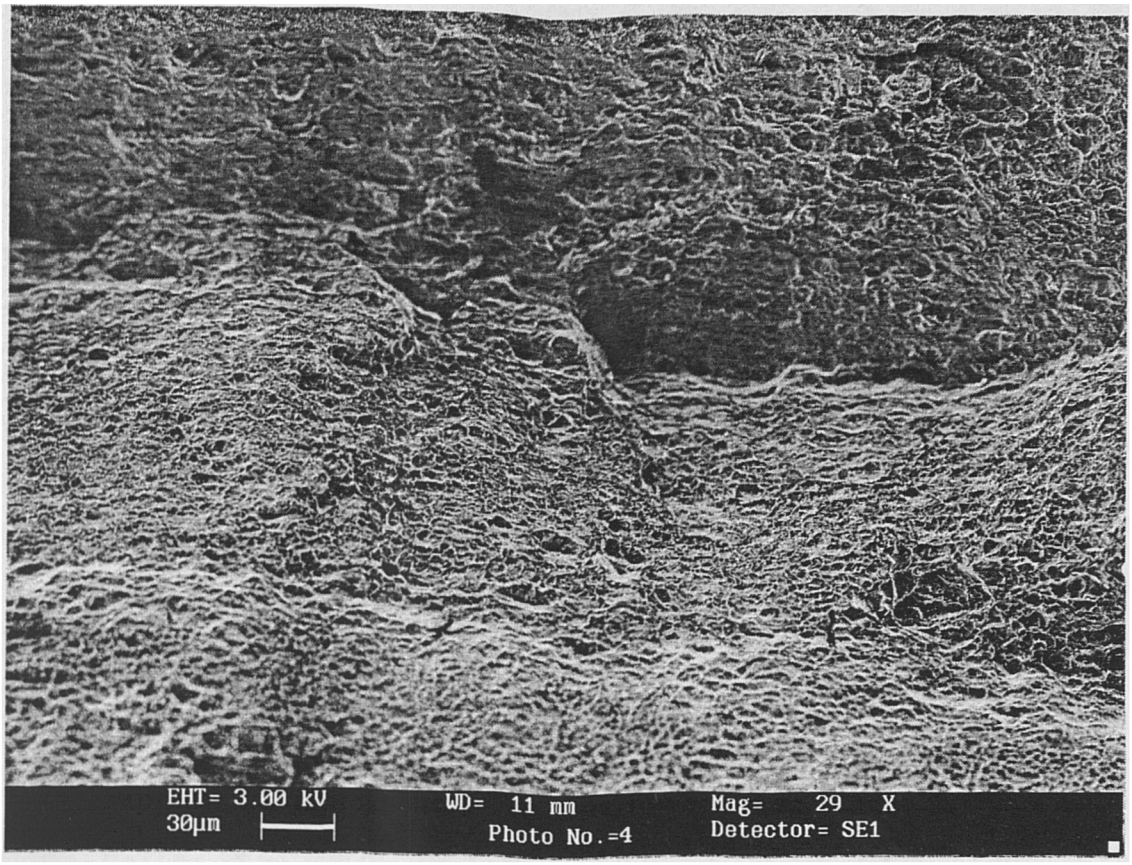


Figure 6.31 : (Specimen 6303, current 110 A, speed 4.2 $mms^{-1}$). The surface shows typical patterns of dimple rupture. Dimples here is shallower than that in specimen 6302. Porosity is observed in the specimen and was more extensive than in specimens 6302 (Figures 6.29 & 6.30).

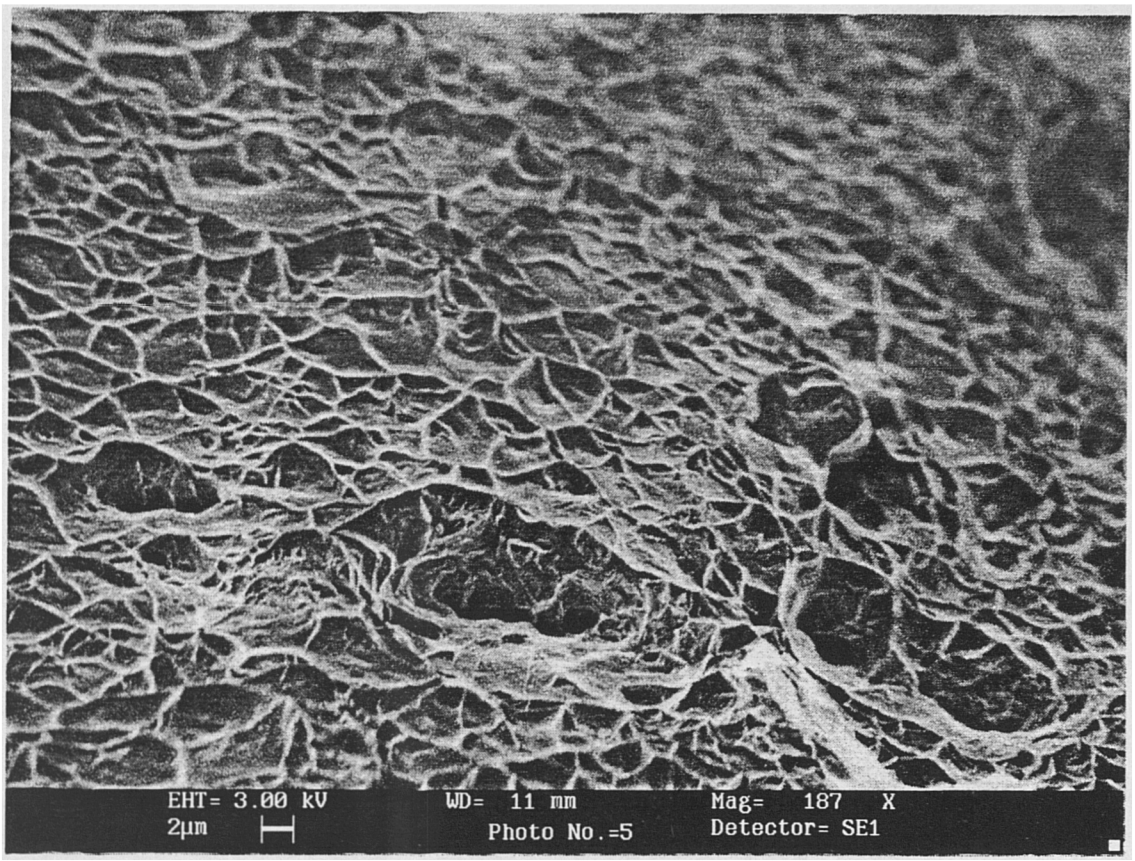


Figure 6.32 :Close-up view of Figure 6.31.
The surface shows cuplike depressions and it is the fracture surface of a dimple rupture. However, the dimples are more shallow than those of specimen 6301 (Figure 6.28).

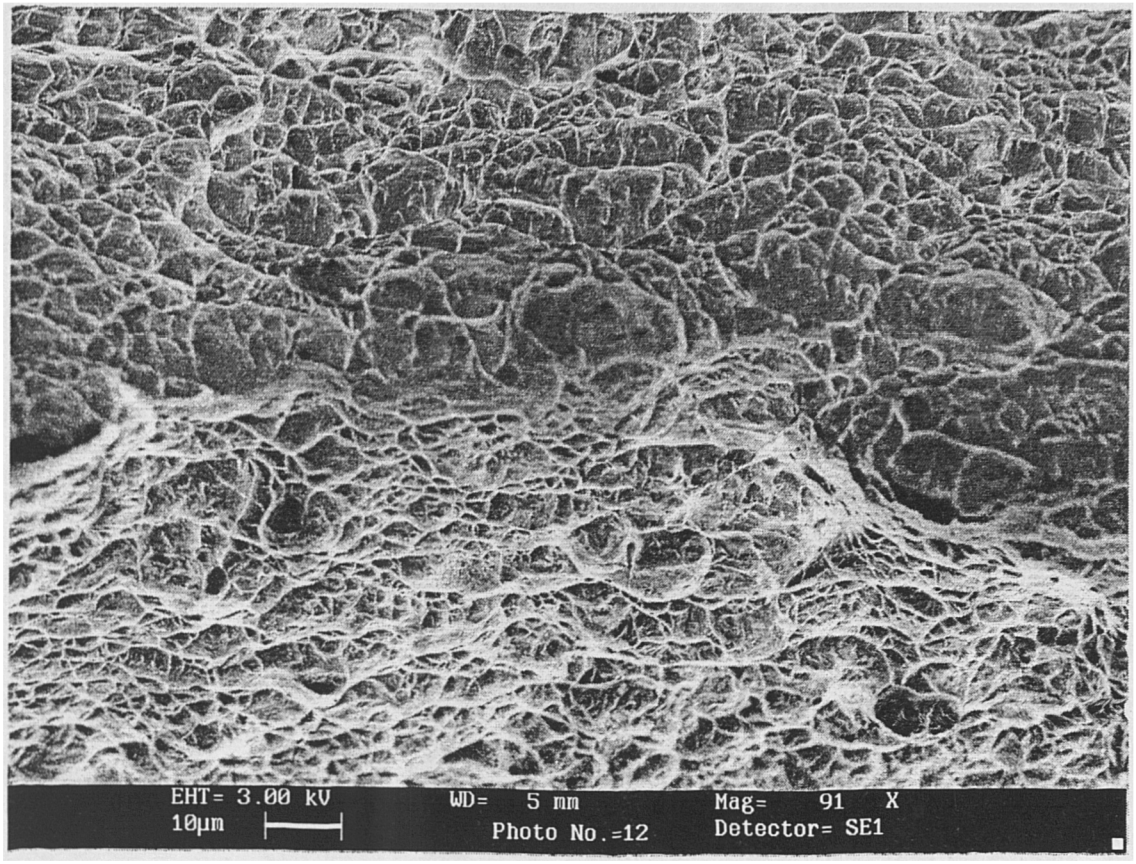


Figure 6.33 : Specimen 6304 (current 140A, speed 4.2 $mms^{-1}$).The fracture surface showed cuplike depressions and showed the characteristics of dimple rupture. The amount of porosity observed was more than that of specimens 6302 and 6303 (Figures 6.29 to 6.32).

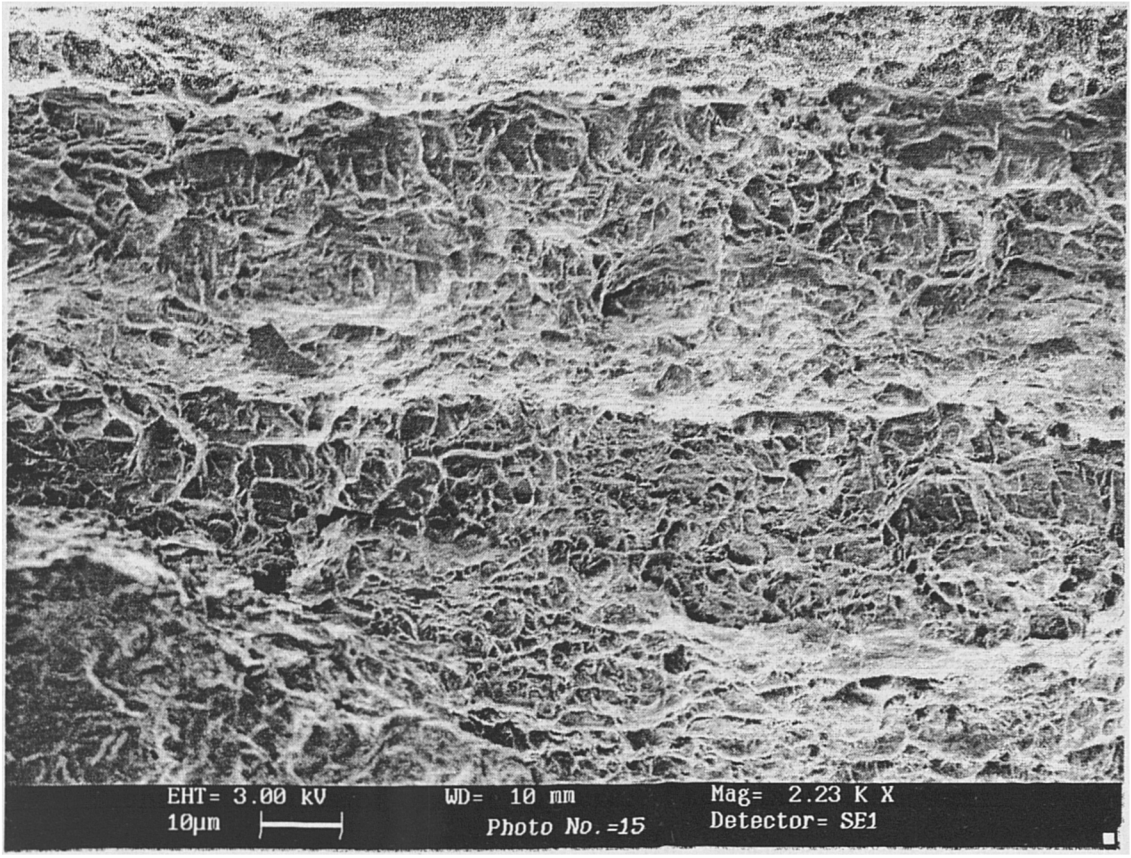


Figure 6.34 : Close-up view of Figure 6.33.
Cuplike depressions were observed and showed the characteristics of dimple rupture. The dimple size was larger but more shallow than the dimple sizes of specimens 6301 to 6303 (Figures 6.27 to 6.32).

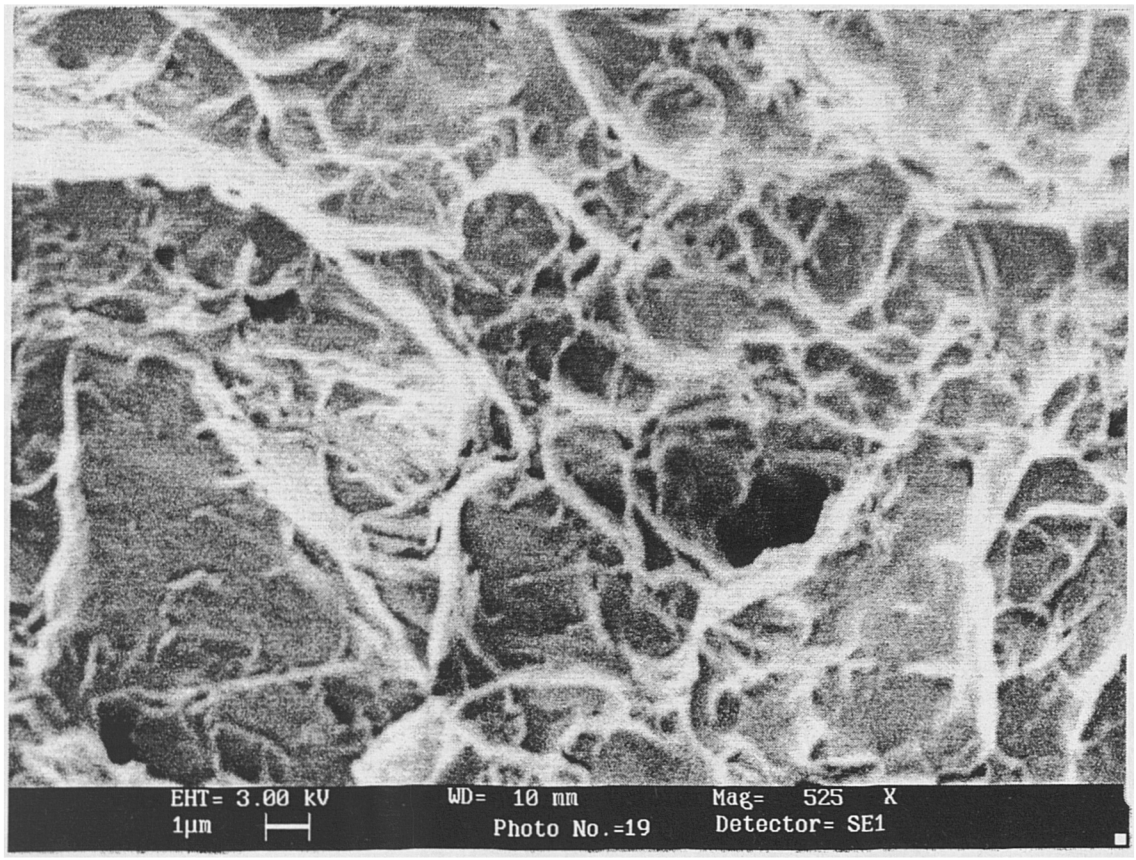


Figure 6.35: Specimen 6305 (current 100 A, speed 5.1 $mms^{-1}$). Close-up view of specimen 6305. A 3µm pore was observed. The surrounded fracture surface shows cuplike depressions and was formed by dimple rupture.

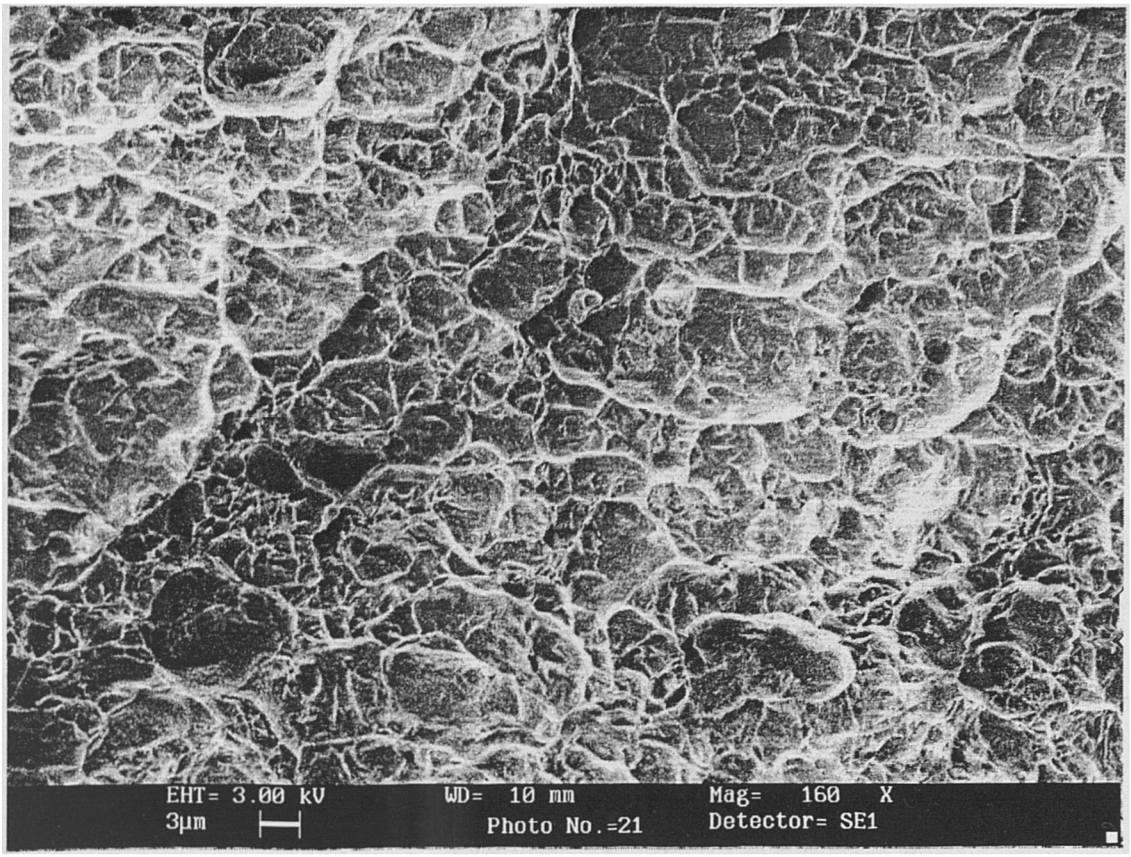


Figure 6.36. A view at lower magnification than Figure 6.35 of specimen 6305. The view shows cuplike depressions of dimple rupture. Large amounts of porosity were observed.

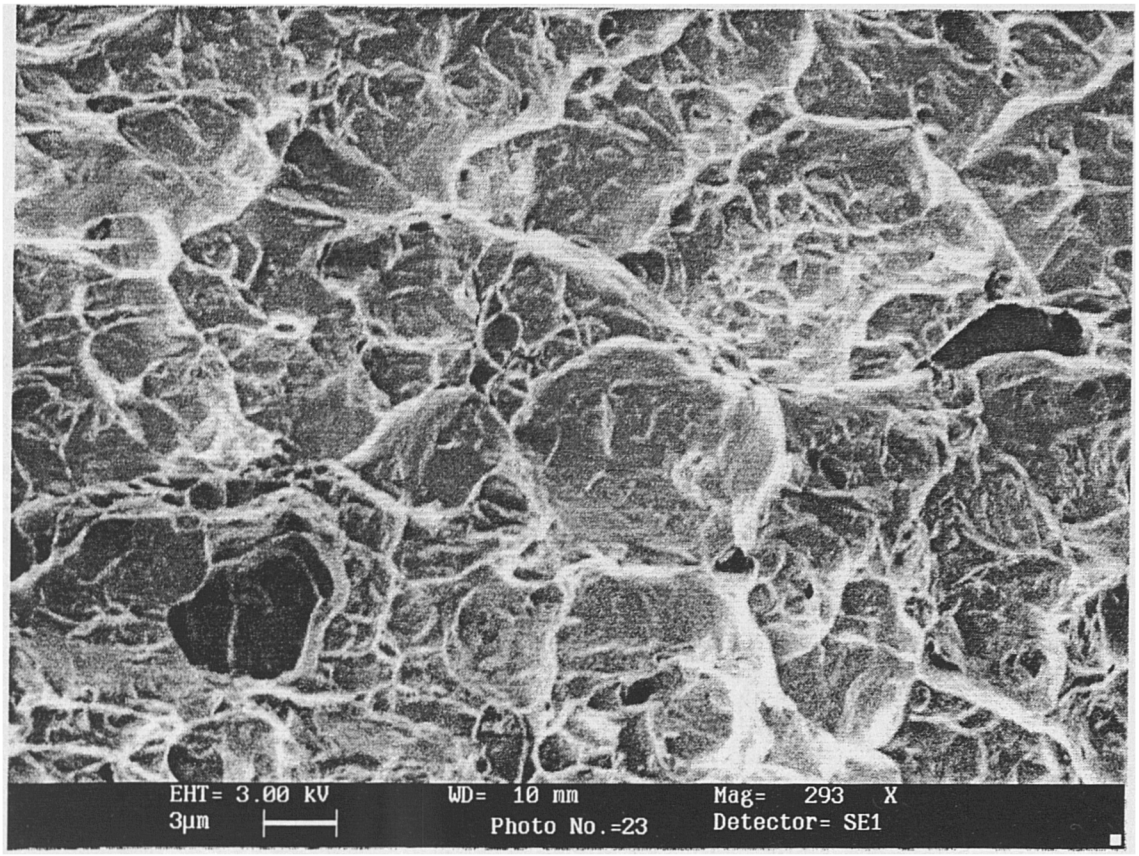


Figure 6.37 : A close-up view of Figure 6.36 shows the diameter of pores is around 6 µm. A large quantity of pores was observed.

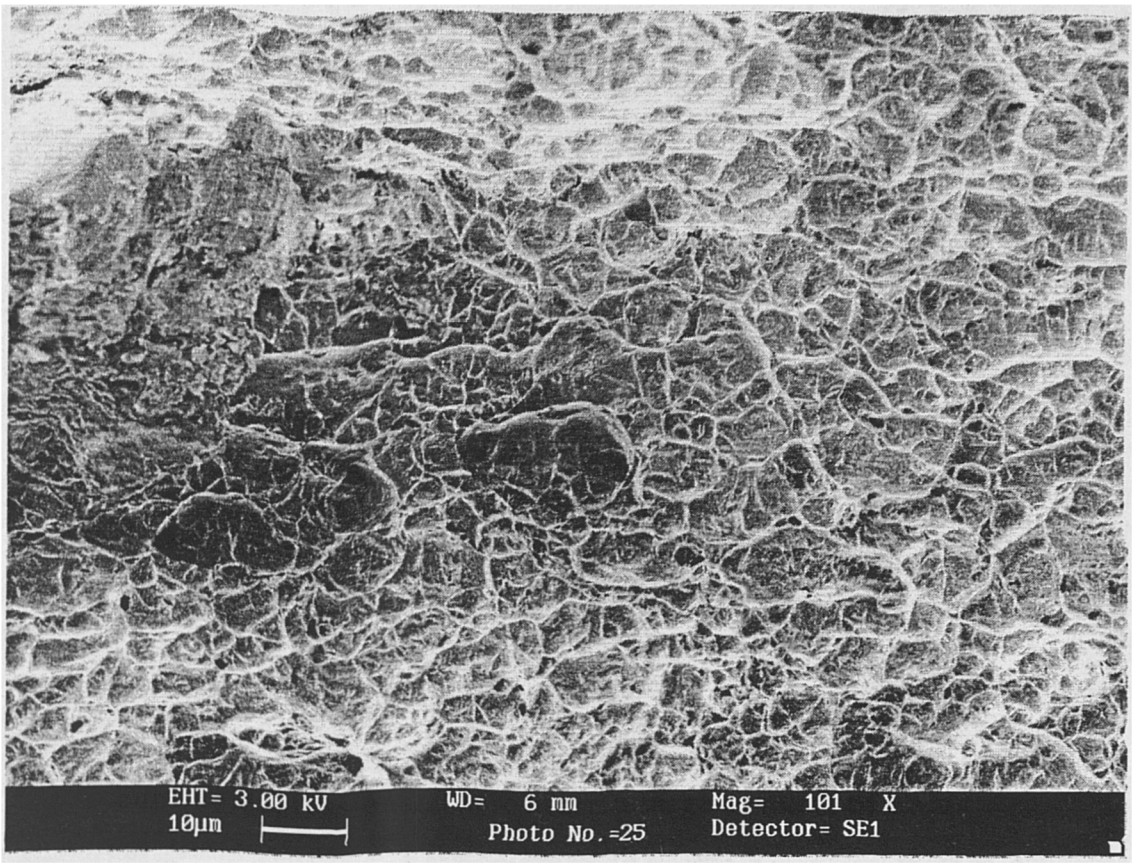


Figure 6.38: Specimen 6306 (current 100 A, speed 4.7 $mms^{-1}$). Dimple rupture was observed due to the cuplike depressions. There were a large amount of pores on the surface. Visually, the dimple sizes were larger but more shallow than the dimple sizes of specimen 6305 (Figures 6.35 to 6.37).

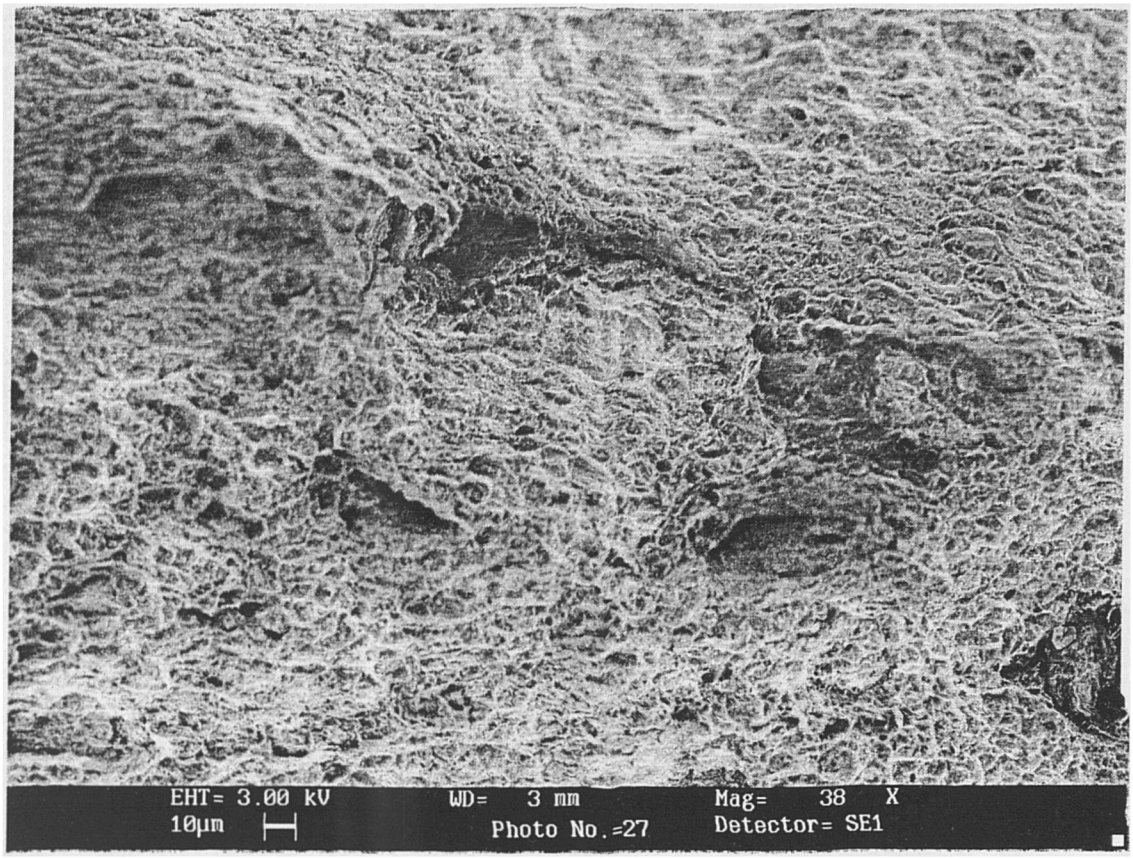


Figure 6.39 : Specimen 6307 (current 100 A, speed 3.8 $mms^{-1}$). Cuplike depressions were observed in the fracture surface which is characteristic of dimple rupture. Large amount of pores existed. The dimple size was similar to specimen 6306 (Figure 6.38) but more shallow than specimen 6305 (Figure 6.36).

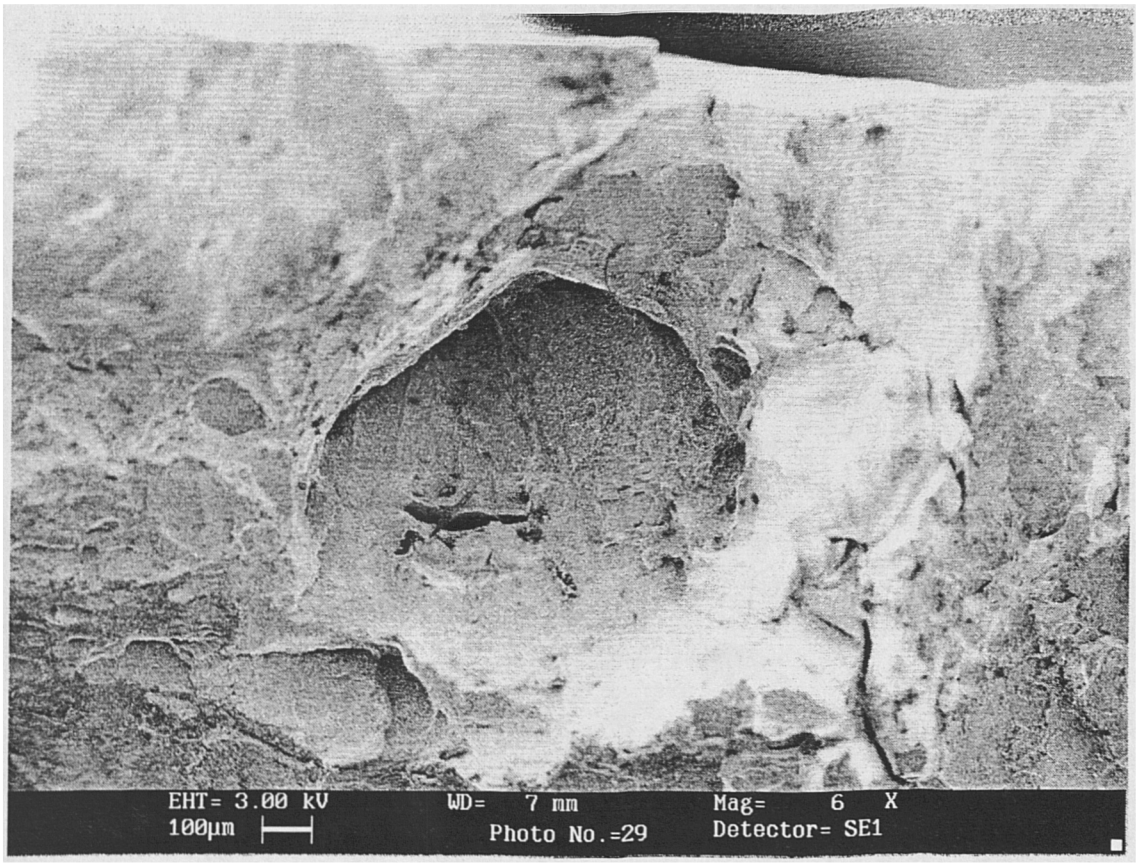


Figure 6.40: Specimen 6308 (current 100 A, speed 3.4 $mms^{-1}$). A low magnification view of specimen 6308. Cracks were observed. There were two main cracks : The one in the centre one and the other in the lower right corner.


Figure 6.41: Close-up view of the crack in the centre of Figure 6.40. Notice that the crack has dimensions about 260µm × 40 µm. The surroundings of the crack show dimple rupture.

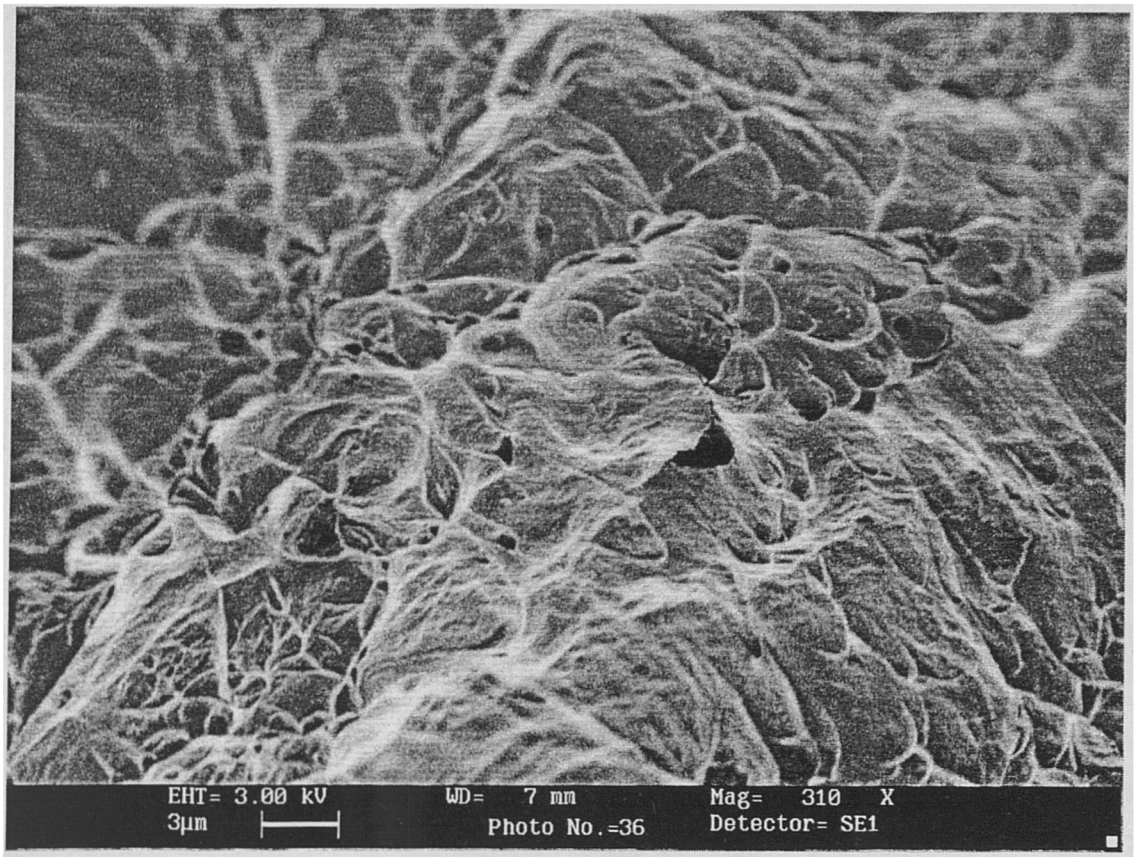


Figure 6.42 : Close-up view of the surroundings of the crack in Figure 6.41. Cuplike depressions were observed. Notice that the surface contained a small amount of pores .

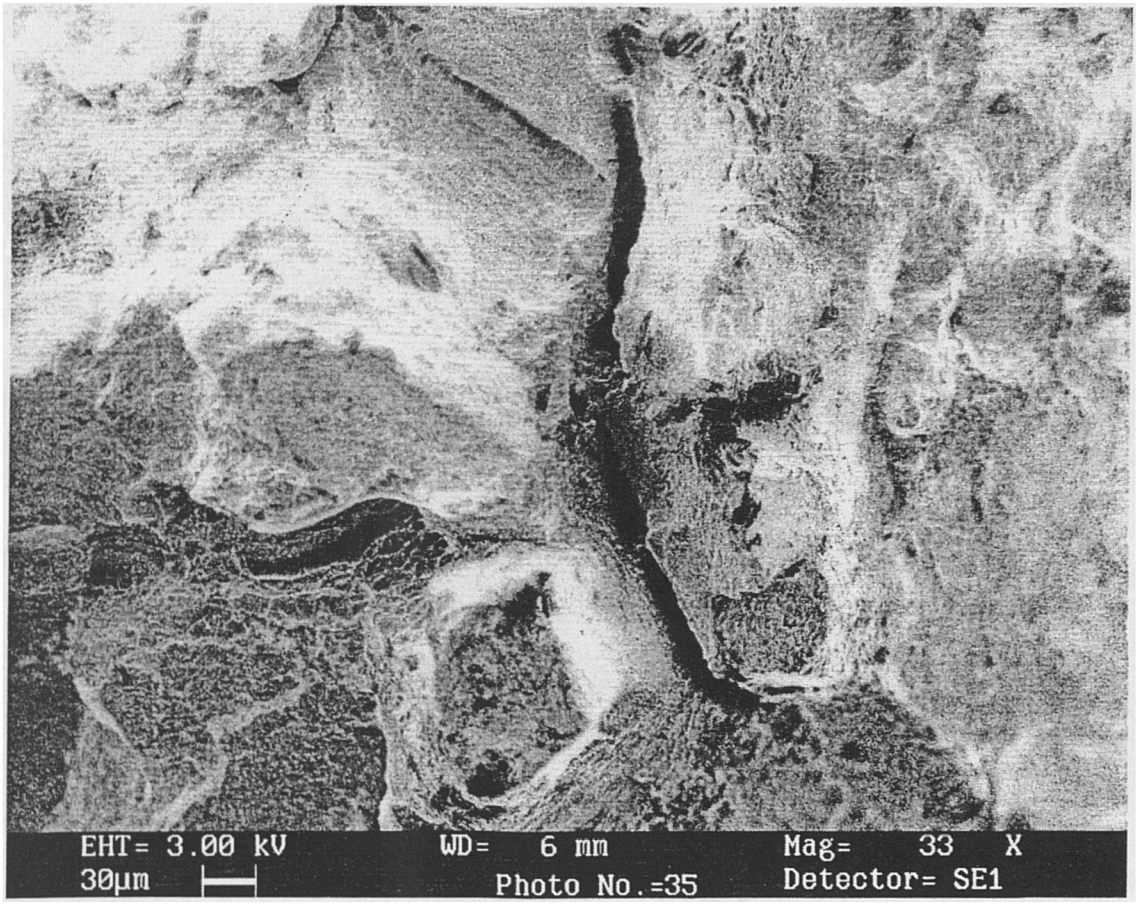


Figure 6.43 : A close-up view of the crack in the lower right corner of Figure 6.40. A river pattern of crack was observed.

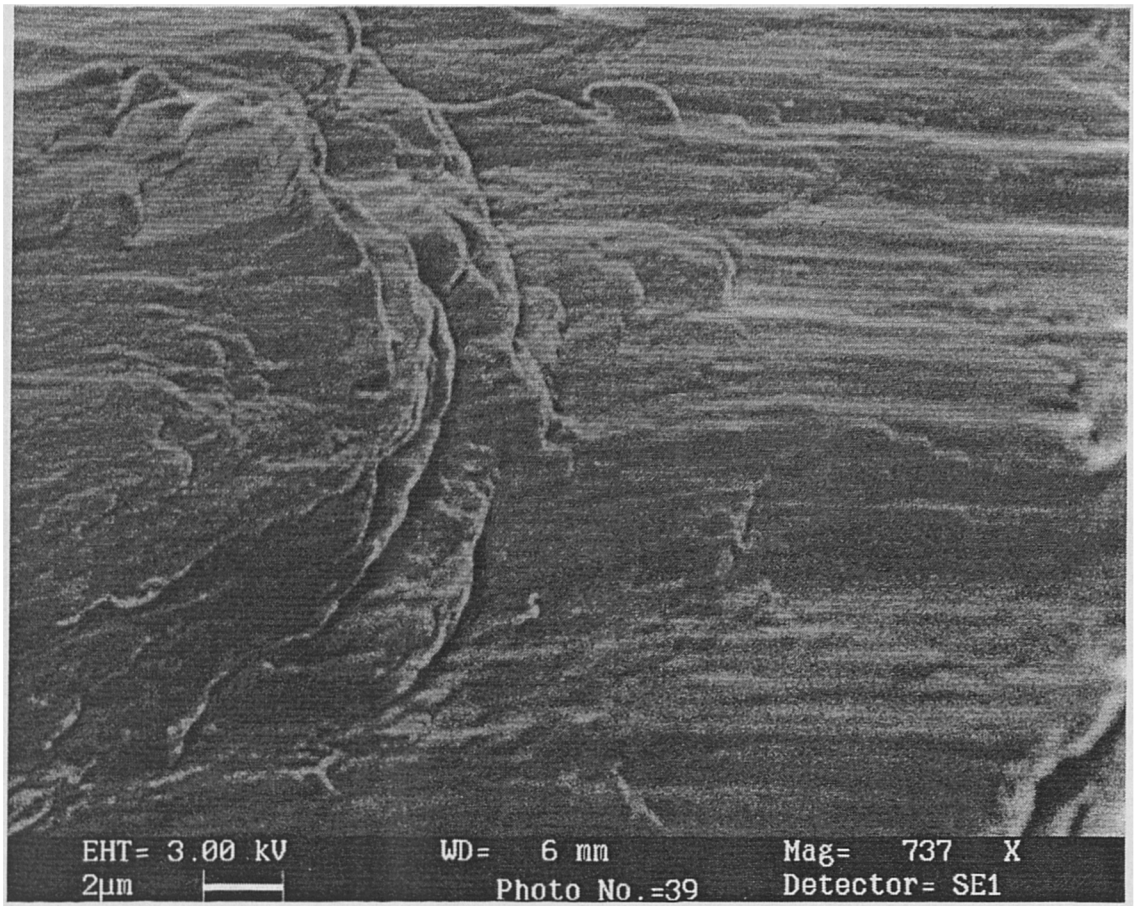


Figure 6.44 : Close-up view of the surroundings of the crack in Figure 6.43. Cleavage rupture was observed around the crack. As this specimen shows both dimple rupture and cleavage rupture, the fracture mode was quasi-cleavage rupture.

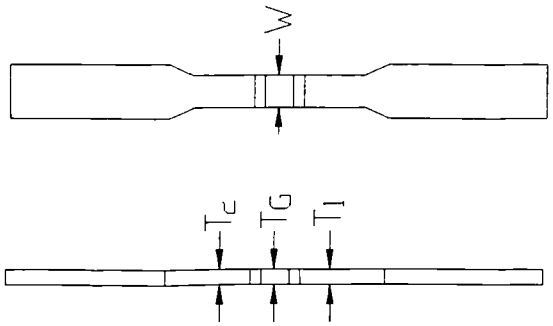


Figure 6.45 : Schematic drawing of the tensile specimens in IMI 318 welds, specimens 6301 to 6324 (average of $T_1$ & $T_2$ equals the average plate thickness $T_b$)

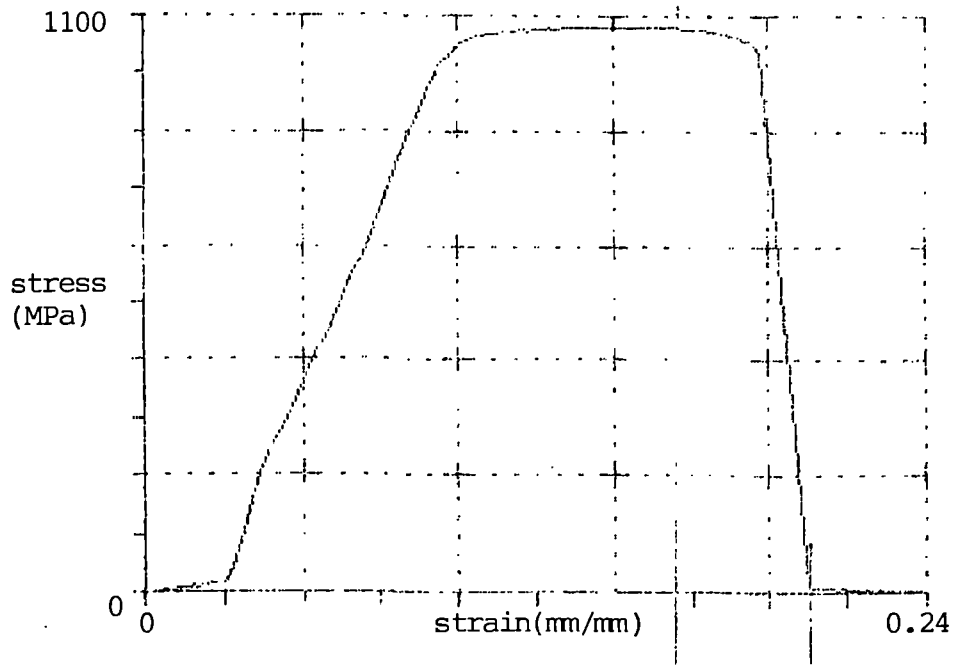


Figure 6.46(a): Stress-strain curve of specimen 6309 of 1.5mm IMI 318 weldment

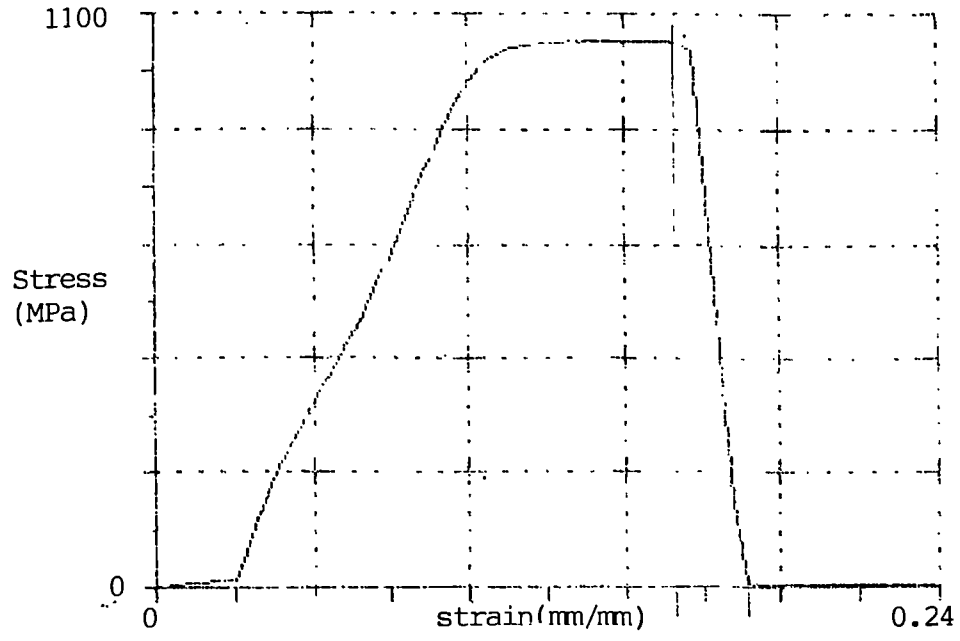


Figure 6.46(b): Stress-strain curve of specimen 6310 of 1.5mm IMI 318 weldment

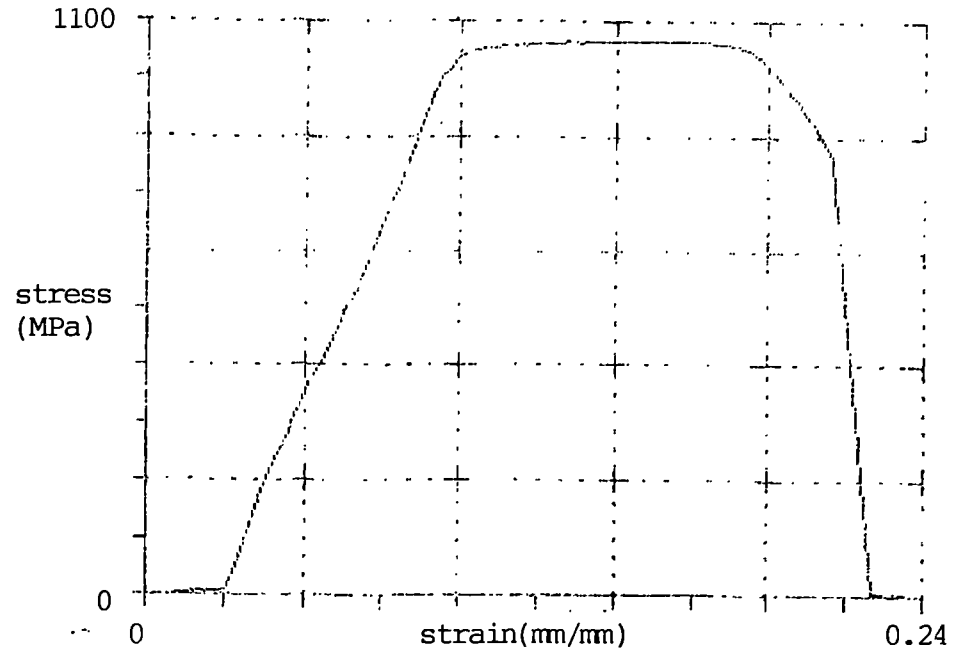


Figure 6.46(c): Stress-strain curve of specimen 6311 of 1.5mm IMI 318 weldment

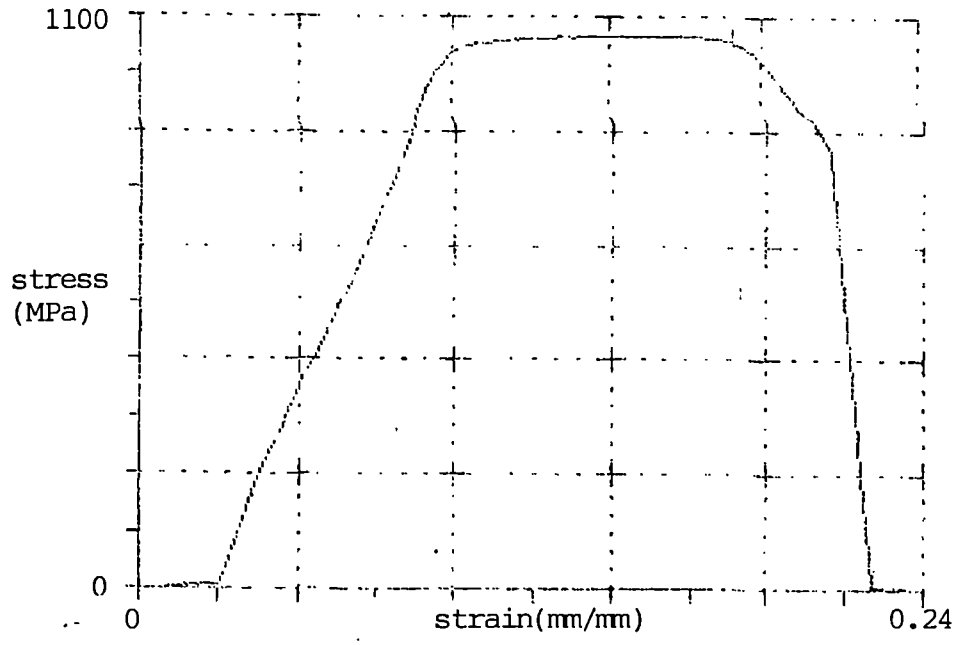


Figure 6.46(d): Stress-strain curve of specimen 6312 of 1.5mm IMI 318 weldment

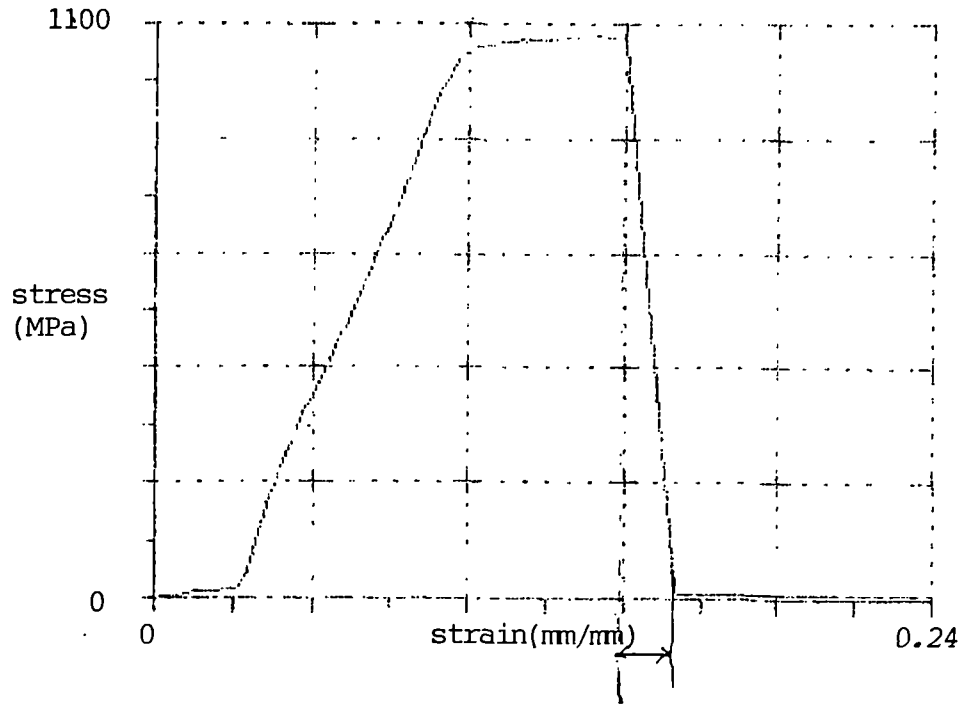


Figure 6.46(e): Stress-strain curve of specimen 6313 of 1.5mm IMI 318 weldment

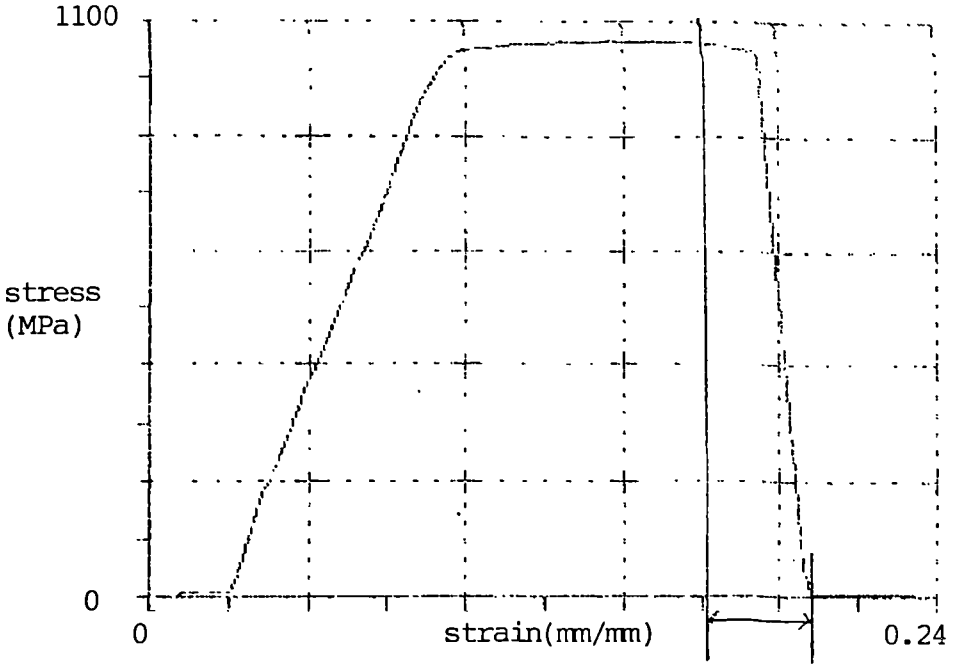


Figure 6.46(f): Stress-strain curve of specimen 6314 of 1.5mm IMI 318 weldment

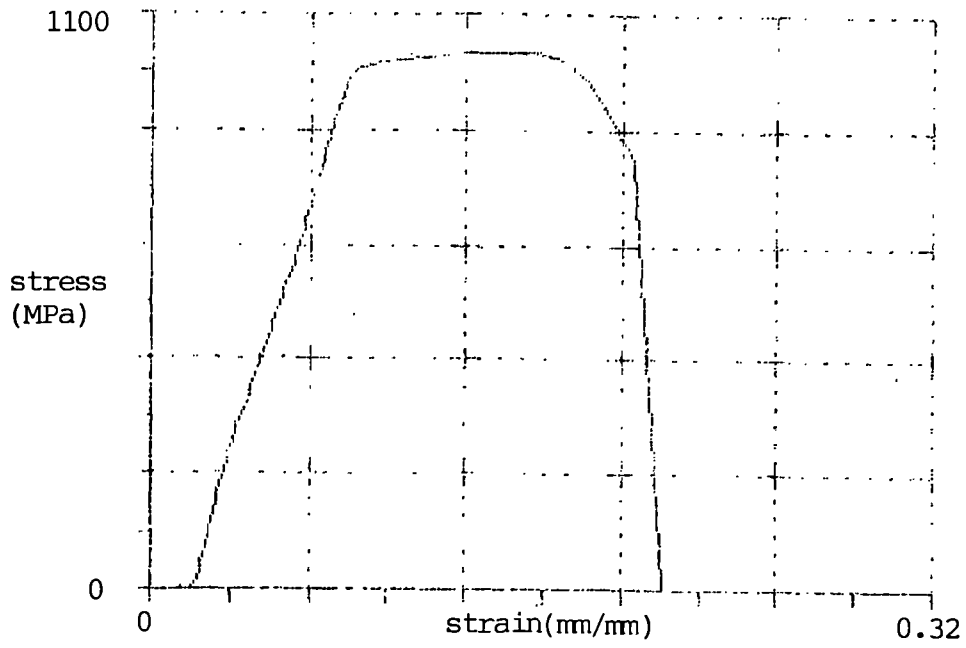


Figure 6.46(g): Stress-strain curve of specimen 6315 of 1.5mm IMI 318 weldment

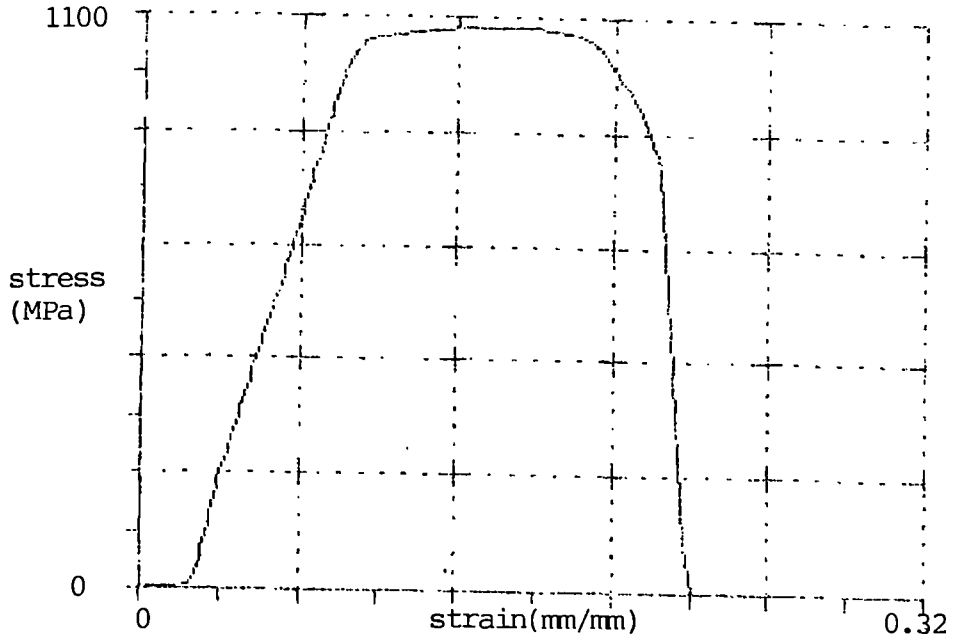


Figure 6.46(h): Stress-strain curve of specimen 6316 of 1.5mm IMI 318 weldment

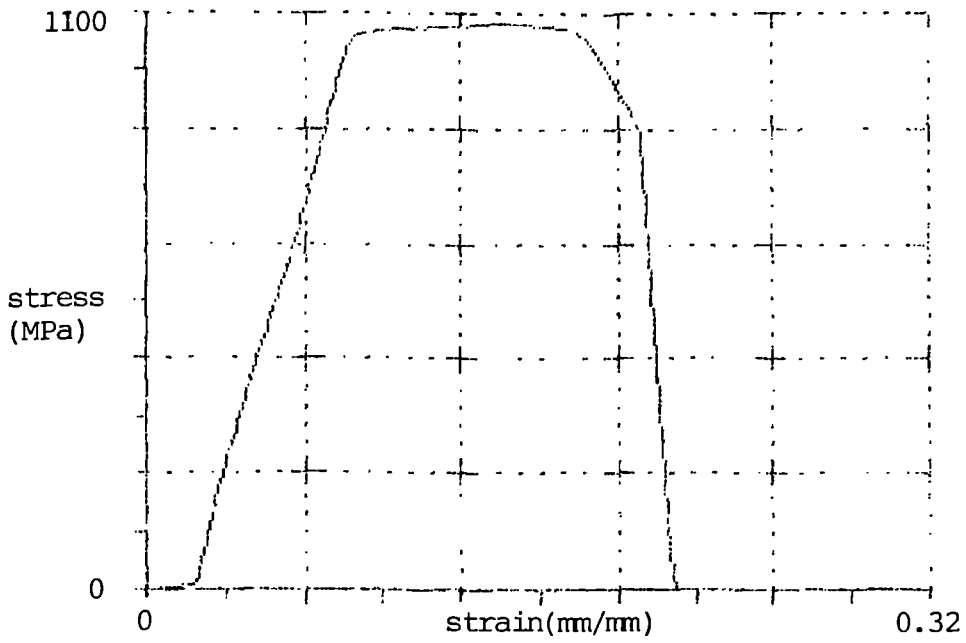


Figure 6.46(i): Stress-strain curve of specimen 6317 of 1.5mm IMI 318 weldment

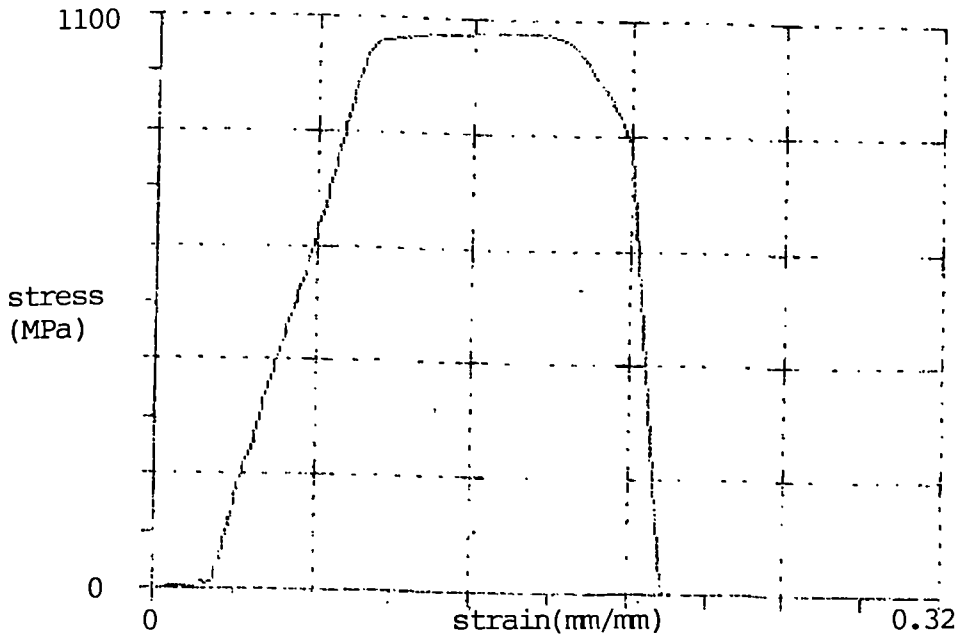


Figure 6.46(j): Stress-strain curve of specimen 6318 of 1.5mm IMI 318 weldment

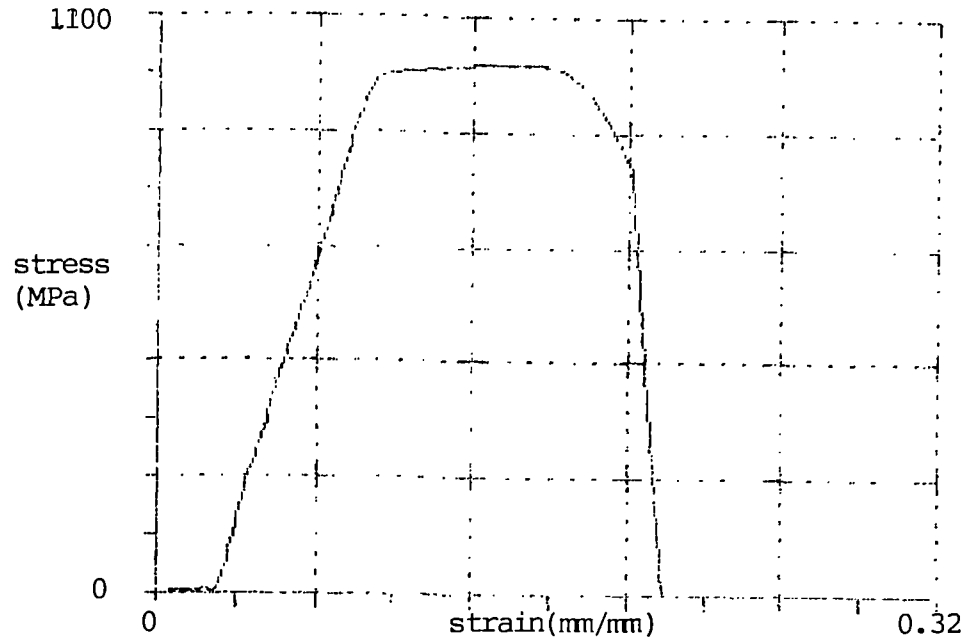


Figure 6.46(k): Stress-strain curve of specimen 6319 of 1.5mm IMI 318 weldment

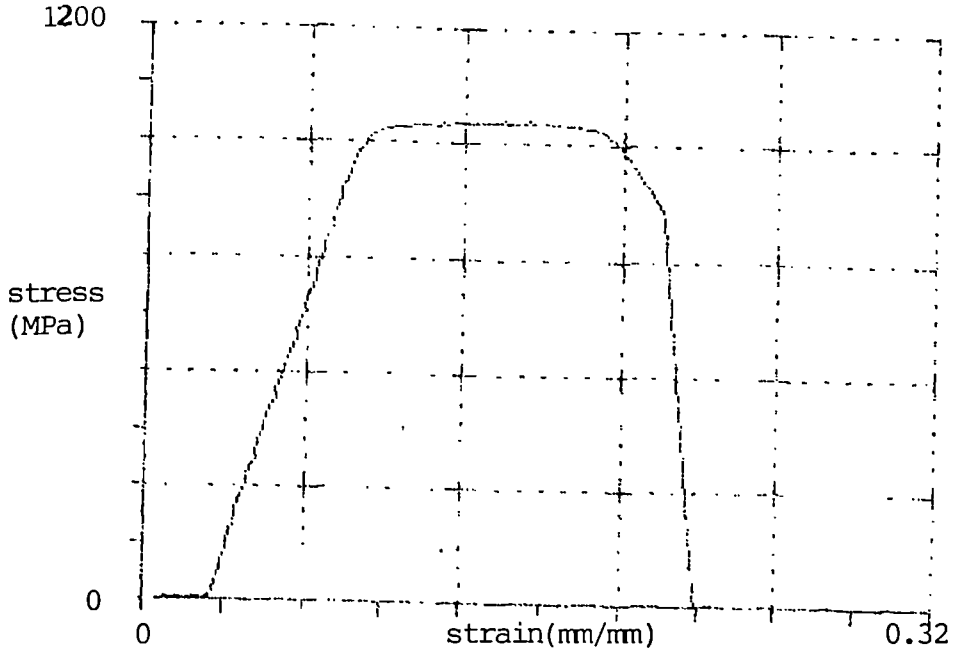


Figure 6.46(l): Stress-strain curve of specimen 6320 of 1.5mm IMI 318 weldment

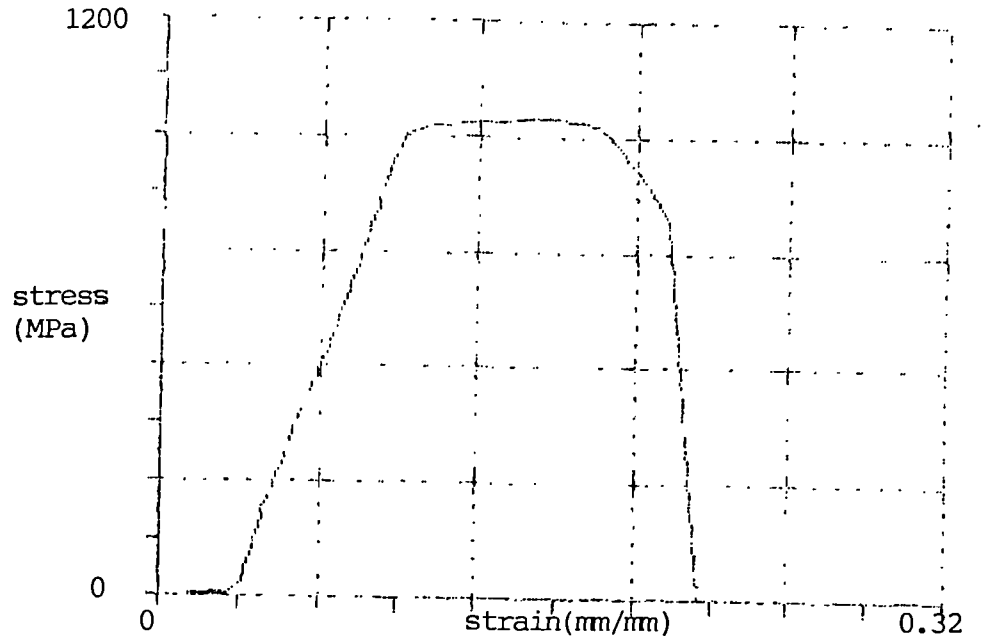


Figure 6.46(m): Stress-strain curve of specimen 6321 of 1.5mm IMI 318 weldment

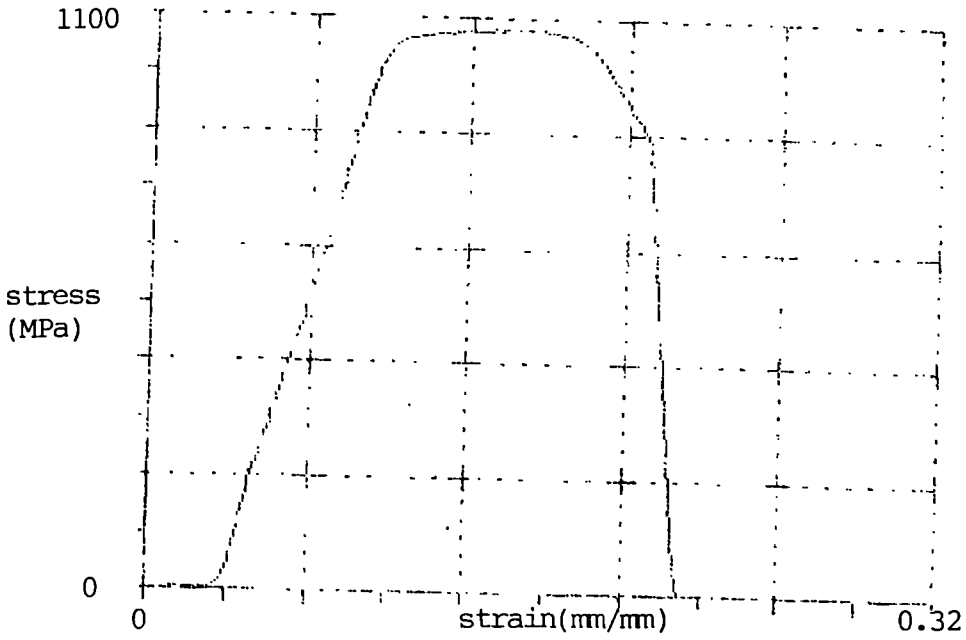


Figure 6.46(n): Stress-strain curve of specimen 6322 of 1.5mm IMI 318 weldment

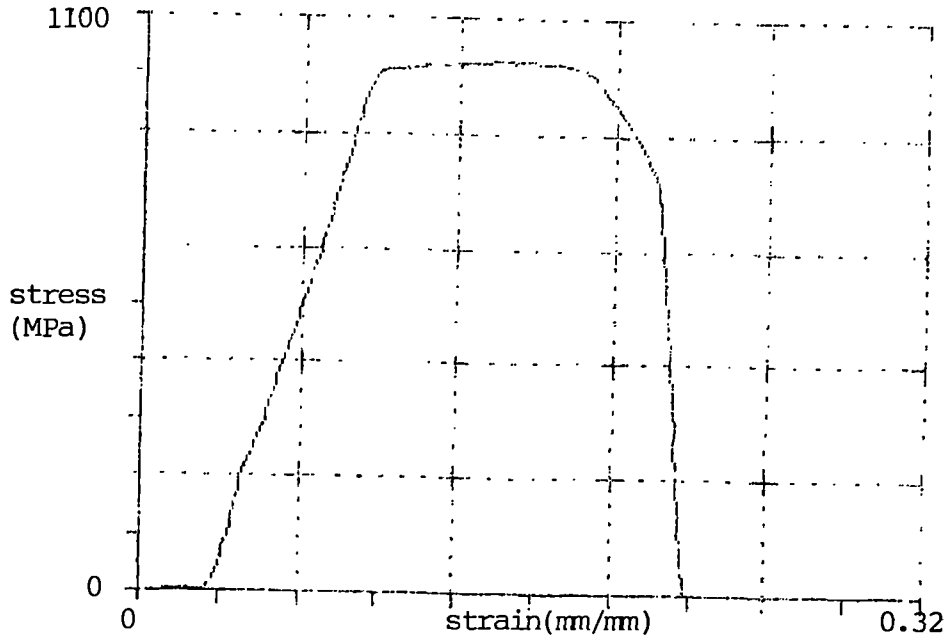


Figure 6.46(o): Stress-strain curve of specimen 6323 of 1.5mm IMI 318 weldment

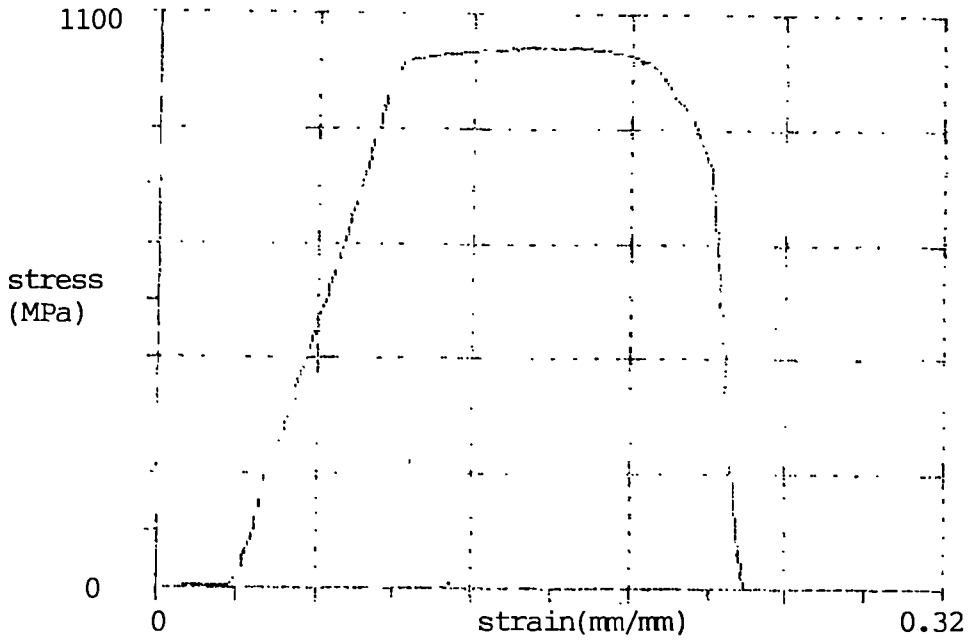


Figure 6.46(p): Stress-strain curve of specimen 6324 of 1.5mm IMI 318 weldment

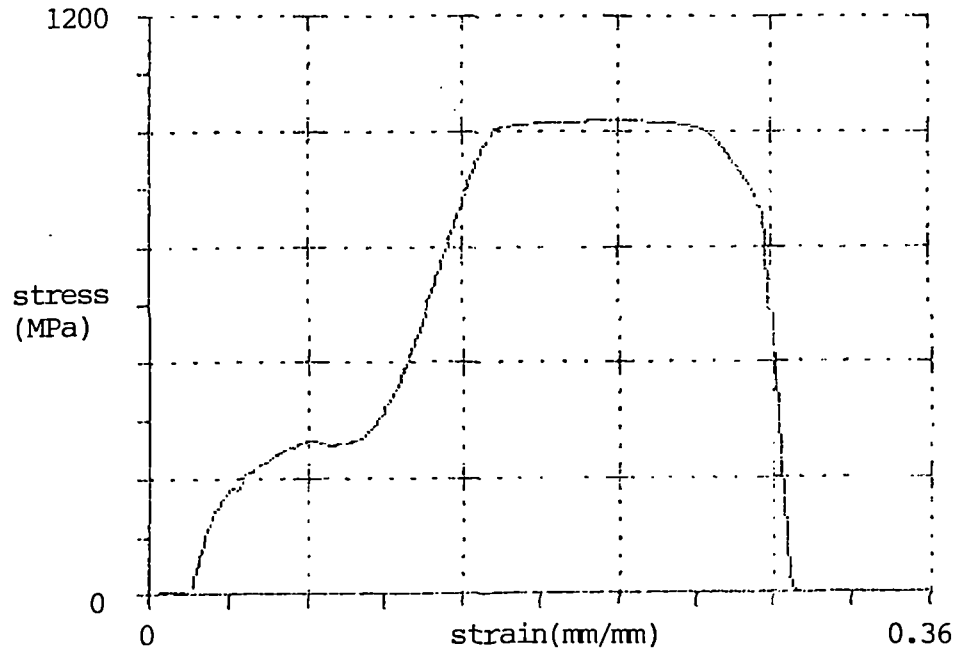


Figure 6.46(q): Stress-strain curve of control specimen (parent metal) of 1.5mm IMI 318

# 7.0 DISCUSSION

## 7.1 Control of weld penetration depth by hardware and software

Modern automatic arc welding equipment is very sophisticated, controlling the major machine functions such as welding current, arc voltage, welding speed and mechanical motions of the torch, etc. Some machines are microprocessor controlled. However, with few exceptions, information about the physical state (location and geometry) of the weld is not used in real-time process control. Exceptions to this are systems which use optical or infra-red sensors to measure the size of the fusion zone surface on the opposite side from the torch of thin materials being welded (Vilkas, 1966).

In almost all cases, the human operator "closes the loop", adjusting the welding parameters during the process based on his observations. Thus weld quality is still strongly dependent on operator skill and experience for many automated arc welding applications.

Weld bead penetration is often critical, in many cases, the operator rarely is able to determine visually the extent of penetration. A sensing technique which can directly measure the extent of weld bead penetration (preferably from the same side as the welding torch) and provide real-time information for closed-loop control of the machine parameters is a real need.

In section 2.5 of the literature survey, ultrasonic detection techniques were shown to be able to sense the location and the geometry of a weld in arc welding processes for close-loop process control. In addition to the sensing technology, the implementation of such a system would require :

I. Microprocessor controlled welding power supply;

II. A model of relationship between process parameters and weld bead geometry (Smartt and Key, 1981), i.e., how must the welding parameters be changed to achieve a desired change in weld bead geometry;

III. A process sensing algorithm, i.e., what must be done with the sensor signal to extract the desired penetration information;

IV. A control system which takes the signals from the sensors and converts them into a form which can be used for feedback control of the welding machine;

V. A process control data base, i.e., the selection of the optimum parameters taking into account the process model, sensing and welding hardware.

Amongst the above requirements, item I is readily available and item II was investigated (sections 5.1 and 6.1) and is presented in sections 7.4.1, 7.4.2 and 7.5.1. An attempt to write the algorithm of item III was presented to relate the sensor signal to the desired penetration information (section 3.4). This involved the use of an algorithm to calculate the actual penetration depth after sampling, transmitting and converting the signal from the ultrasonoscope. The resulting signal was used for finding the average penetration depth values between the ultrasonic signal and the penetration depth.

The control system (item IV) was made possible by using this derived algorithm and the design and construction of the hardware to control the welding speed which was previously presented (section 3.2). The algorithm in item III was achieved by comparing the detected and computed average value of the penetration in real-time with the required depth of penetration. The resulting difference was used in the algorithm to calculate the required change in the welding parameters. Any one of the following relationships could be assumed, according to the algorithm :

- Depth = k v
- Depth = k $v^n$
- Depth = k ($e^{mv}$ -1)

where v is welding voltage and k, m are real constants.

The following examples illustrate application of the above 3 relationships and the algorithm. Letters or numbers in boldface represent what the users key in. The number underscored at the end is the corrected value of the required welding parameter.

Example 1

The required depth of weld in millimetres is : **10.0**
The acceptable fraction of penetration depth (input must be ≤ 1.0) : **1.0**
Type in the welding parameter to be corrected (v for voltage and i for current) : **v**

The voltage shown on the welding set-up is : **2.0 V**
Choose one of the following relations between depth of weld and voltage :
1) Depth = k v
2) Depth = k $v^n$
3) Depth = k ($e^{mv}$ -1)
If no relationship is exact, choose the one that would best approximate the relationship.
Choose relationship (1, 2 or 3) : **1**

Please input the number of signal samples (the required number of samples >=3) : **5**

Depth of weld corresponding to the received ultrasonic signal for each sample :-
Sample depth 1 : 1.729492 mm
Sample depth 2 : 1.729980 mm
Sample depth 3 : 1.729492 mm
Sample depth 4 : 1.733398 mm
Sample depth 5 : 1.727539 mm

The maximum sample depth is (round down to 3 significant figures) : 1.733 mm
The minimum sample depth is (round down to 3 significant figures) : 1.728 mm
The average actual depth is (round down to 3 significant figures) : 1.730 mm

The acceptable depth of weld is 10.0 mm.

The welding voltage should be adjusted to 3.6 V and the new depth of weld will be 10.0 mm.

Example 2

The required depth of weld in millimetres is : **54.0**
The acceptable fraction of penetration depth (input must be ≤ 1.0) : **1.0**
Type in the welding parameter to be corrected (v for voltage and i for current) : **v**
The voltage shown on the welding set-up is : **3.0 V**
Choose one of the following relations between depth of weld and voltage :
1) Depth = k v
2) Depth = k $v^n$
3) Depth = k ($e^{mv}$ -1)

If no relationship is exact, choose the one that would best approximate the relationship.
Choose relationship (1, 2 or 3) : **2**
The voltage is estimated to the power of **: 3**

Please input the number of signal samples (the required number of samples >=3) : **8**

Depth of weld corresponding to the received ultrasonic signal for each sample :-
Sample depth 1 : 2.689875 mm
Sample depth 2 : 2.689941 mm
Sample depth 3 : 2.996094 mm
Sample depth 4 : 2.922852 mm
Sample depth 5 : 3.122559 mm
Sample depth 6 : 3.125000 mm
Sample depth 7 : 3.216797 mm
Sample depth 8 : 3.187500 mm

The maximum sample depth is (round down to 3 significant figures) : 3.253 mm
The minimum sample depth is (round down to 3 significant figures) : 2.690 mm
The average actual depth is (round down to 3 significant figures) : 3.064 mm

The acceptable depth of weld is 54.0 mm.

The welding voltage should be adjusted to 4.8 V and the new depth of weld will be 54.0 mm.

Example 3

The required depth of weld in millimetres is : **2.9**
The acceptable fraction of penetration depth (input must be ≤ 1.0) : **1.0**
Type in the welding parameter to be corrected (v for voltage and i for current) : **v**
The voltage shown on the welding set-up is : **5.0 V**
Choose one of the following relations between depth of weld and voltage :
1) Depth = k v
2) Depth = k $v^{n}$
3) Depth = k ($e^{mv}$ -1)

If no relationship is exact, choose the one that would best approximate the relationship.
Choose relationship (1, 2 or 3) : **3**
The value of m is **: 3**

Please input the number of signal samples (the required number of samples >=3) : **6**

Depth of weld corresponding to the received ultrasonic signal for each sample :-
Sample depth 1 : 3.129883 mm
Sample depth 2 : 3.130859 mm
Sample depth 3 : 3.128906 mm
Sample depth 4 : 3.128418 mm
Sample depth 5 : 3.129883 mm
Sample depth 6 : 3.133301 mm

The maximum sample depth is (round down to 3 significant figures) : 3.133 mm
The minimum sample *depth is (round down to 3 significant figures) : 3.128 mm*
The average actual depth is (round down to 3 significant figures) : 3.130 mm

The acceptable depth of weld is 2.9 mm.

The welding voltage should be adjusted to 4.9 V and the new depth of weld will be 2.9 mm.

Although the algorithm assumes only three relationships, any other relationships, if proved to be more appropriate, could be employed and used within the algorithm. The flexibility of this approach enables the algorithm to be extended to other welding processes which have explicit relationships between penetration depth and the controlling parameters of the welding processes.

A custom written C-program performed these calculations in addition to the approximations involved and the program then produced an optimised signal for welding current or speed correction. This signal was converted back from a digital-to-analogue signal by the AD/DA converter. Finally, the signal passed to the welding machine and fixture and adjusted the required welding current and speed.

This methodology was also applied to the pulse frequency of the pulsed TIG process. As these welding parameters directly affect weld penetration, the program continuously controlled the penetration until the depth obtained reached the predetermined level. In this form, the system became an adaptive closed-loop control system for automatic welding process.

Control and adjustment of welding speed (amongst other controllable welding parameters) was presented in detail in section 3.2. This adjustment was required because the grain size and some major mechanical properties of $\alpha/\beta$ titanium welds are dependent on the cooling rate of welds (Johnson *et al.*, 1986). This proved to be the case with IMI 318 plate of various thicknesses (as will be shown in sections 7.5.2, 7.5.3 and 7.5.4). Cooling rates are dependent on welding parameters, especially speed, and speed was therefore chosen for control (as described in section 3.2). These control and adjustment procedures provided adaptive control via speed feedback and employed an automatic speed controller.

The process control data base (in item V) was built up by the software and knowledge-based system for acceptable welding parameters, by using the Computer Data Book (CDB as presented in section 3.3). These welding parameters fabricated welds with desirable weld geometry, grain size and mechanical properties in the as-welded condition and were stored and retrieved using a Windows operating system. This information was included in the data base as input information for titanium of different thicknesses. The initial data on the process were the input information and information from the ultrasonic sensor. The output signals controlled the welding conditions : current, welding speed, pulsing frequency etc. Though some work on developing knowledge-based systems has been reported (Costa and Norrish, 1991; Shankar *et al.*, 1991), the purpose there was to assist detection of cracking or other defects on the basis of weld history and data from ultrasonic testing. Little work has been published to relate welding penetration to welding parameters, grain size and mechanical properties of welds, which was attempted in the present study.

As shown in section 3.2, some hardware was designed and constructed in the control unit to overcome the problems caused by the high frequency (HF) arc starting in a TIG process. When the system was initially tested under HF starting, the penetration control unit broke down. The problem was overcome by using a "modified" commercial electronic mains filter. An advantageous feature of this control unit compared to other

microcomputer-based systems, was undoubtedly the automatic HF arc initiation. In the microcomputer-based system, HF arc initiation could not be employed without the software program becoming corrupted (Ahmed and Lucas, 1990). Even the hardware control system could not be switched on simultaneously with the HF unit, because line-transmitted or airborne HF caused breakdown of the electronic components (refer to section 3.2), This problem was satisfactorily resolved in the overall control sequence, where the penetration control unit and stepping motor remained switched off while the HF unit was switched on at the same time as the welding power source. As soon as the arc was established, the HF unit was switched off and both the control unit and stepping motor were switched on automatically and exercised control of penetration. This sequence provided reliable arc ignition and initiation of the welding operations and was fast enough to prevent any delay in the control of weld pool penetration.

Finally, the work in section 3.1 was no less significant for the process control of welding the titanium plates. This work provided an inert gas back-shielding which was demonstrated (in section 5.1) to be determinative in producing good quality welds. It also helped to minimise distortion of the welds which could have affected the uniformity of arc length and heat input on a single specimen.

Though much work has been done in weld monitoring using ultrasonics, the emphasis has been on collection, conditioning and analysis of ultrasonic data using very sophisticated electronic instruments (Stares *et al.*, 1989; Stares *et al.* 1990; Bull *et al.* 1993). Very little work has been published on the approach and methodology of setting up a feedback control system. The present study here was able to utilise ultrasonic data and their relationships with welding parameters to set-up a feedback control system for TIG arc welding. Not only was the methodology detailed in this thesis, but also examples given. Though the present study was on a small-scale laboratory-base, work on the same methodology and approach could also be applied on a larger scale.

Various indirect measurement techniques on penetration have been investigated recently, however, many of them exhibit drawbacks one way or the other; for example in the electro-optical technique, the optical systems are intolerant of smoke or aerosol generation at the weld site and also of liquid metal spatter (Johnson *et al.*, 1986). Furthermore, in penetration control using weld pool oscillations, its excitation and the associated physics of its detection are quite complex and not yet well understood (Richardson and Ludewig, 1989); and in using binary vision systems and near-infrared

light emissions, controlling penetration from the rear side of the weld is not possible (Stone *et al.*, 1990; Bentley and Marburger, 1992). In the study here, the ultrasonic sensing technique was proved as a direct measurement tool for weld penetration.

## 7.2 Detection of geometry and grain size in weld by ultrasonic shear waves -- A feasibility study on stainless steel (Yung *et al.*, 1997b)

### 7.2.1 Relationship between the ultrasonic signal and the weld geometry

Table 4.2 shows that the mean value of D (centre distance) which is the distance between the weld boundary (the reflector of the ultrasonic shear waves) and the nominal centre line of the weld, is smaller than half of the measured weld pool width. Since the ultrasound reflector is the fusion boundary, it is obvious that the reflector distance from the centre, D, can not be larger than half the weld pool width.

Some measurements are found to give a negative distance from the centre line (e.g. in specimens 4102 and 4105). This is possible when the reflector is located on the far side of the weld (as shown in Figure 7.1(a)). From the signal obtained in this situation, 'grass' along with the peak, was seen, which implies that coarser grain structures exist in the HAZ and the FZ. Hence, there is evidence that the reflector is on the far side of the weld, this being substantiated by the micrographs (Figures 4.3b and 4.3e) taken, which show that the weld root did not coincide with the weld centre line.

Further interesting information is observed. In some specimens (e.g. specimen 4103), the value of D for side a is 6.5 mm but 1.5 mm for side b. This suggests misalignment of the fusion zone, as shown in Figure 7.1(b). On the other hand, other specimens (e.g. specimens 4101 and 4104) show a symmetrical alignment, since the values of D from both sides are approximately the same, once more this is substantiated by micrographs (see for example Figures 4.3a and 4.3d). Thus FZ alignment with respect to the nominal weld centre line, could be determined from the D values measured on both sides of the weld.

### 7.2.2 Relationship between the welding parameters and the grain size

For most samples, noticeable signals were received and displayed on the ultrasonoscope when the gain level was 110 dB. Therefore, all amplitudes were recalculated to the gain level of 110 dB to allow accurate comparison. The amplitude of these received signals and the welding parameters of the corresponding weldments are shown in Table 4.3.

Depending upon the structural and positional make-up of a single grain, ultrasound will be scattered by grain boundaries with a change in ultrasound velocity. Attenuation resulted from scattering due to the inhomogeneities at the interface boundaries. It was reported that the attenuation was observed to increase with increasing grain size (Firestone, 1948; Roth, 1948). If d was the grain size, $\lambda$ was the wave length of the ultrasound and A the reflected signal amplitude, neglecting diffraction losses and multiple-scattering, in the Rayleigh range which was characterised by :

$$0.02 \leq d/\lambda \leq 0.2 \tag{7.1}$$

then :

$$d = K_d A^{2/3} \tag{7.2}$$

where $K_d$ is a constant depending on the experimental set-up.

It was later shown that $A^{2/3}$ changes positively with d (Hecht *et al.*, 1981). Using this as background, graphs of amplitude were plotted against welding current (I) and heat input (Q) (from Table 4.3) and presented in Figures 4.4 and 4.5. It can be seen that both the welding current and the heat input rate change positively with amplitude (A) similar to Equation (7.2) viz. :

$$A^{2/3} = K_i I, \quad (K_i \text{ is a constant}) \tag{7.3}$$

and heat input rate :

$$A^{2/3} = K_q Q, \quad (K_q \text{ is a constant}) \tag{7.4}$$

Combining Equation (7.2) with Equations (7.3) and (7.4) gives :

$$I = K_1 d, \quad (K_1 \text{ is a constant}) \tag{7.5}$$

$$Q = K_2 d, \quad (K_2 \text{ is a constant}) \tag{7.6}$$

The above can be explained in terms of the final grain size around the FZ boundary increasing with elevated peak temperature and enhanced residence time (time of heating

and cooling). Maximum peak temperature is related to heat input (Adams, 1958) and therefore welding current (section 2.2.3), Equation 7.5 can be justified. Typical residence time for two-dimensional heat flow may be estimated from charts previously published (Christensen *et al.*, 1965). These charts show typically that residence time was roughly proportional to Q (the heat input). Thus heat input directly affected the grain size, which further justifies Equation (7.6) above. An attempt was made to employ conventional shear waves to investigate the quality of welds in thin plates and obtain information related to the grain size around the weld's FZ boundary and the geometry of the weld bead. Although a post-weld study, some good understanding of the weld was provided. By calculating the ultrasonic time-of-flight a quantitative measure of the weld pool width is suggested, as was the alignment and symmetry of the pool about the weld line. This provided a means to obtain information related to the weld quality without microsectioning the weld. It was also found that the relative grain sizes around the weld's FZ, (resulting from different welding parameters and heat inputs), can be indicated by their corresponding ultrasonic attenuation. Mathematical relationships between ultrasonic attenuation (received signal amplitude) and welding current and heat input rate were established.

As welding current and heat input rate affect phase transformations, a dependence of ultrasonic attenuation on phase transformations is expected. This is in contrast to previous work (Stares *et al.*, 1990) which suggested that phase transformations in stainless and ferritic steels did not seem significantly to degrade the attenuation of the transmitted ultrasonic signals. There may be a reason for this; compression waves were used in the said study while shear waves were used in the present study. It was found that for compression waves, the amplitude reflection coefficient was approximately 0.1 in steel (Parker, 1982), whereas shear waves cannot propagate through liquids and therefore would be expected to undergo 100% reflection at the solid/liquid interface. Therefore with more reflected wave energy, the degree of attenuation of shear wave with different microstructural phases will be more apparent. In fact, other previous studies on austenitic and galvanised steels, nickel, zinc and aluminium have demonstrated that there is a strong change in ultrasonic attenuation corresponding to transformation (Papadakis *et al.*, 1972; Rokhlin *et al.*, 1989) and that ultrasonic attenuation measurements serve as a very sensitive indicator of microstructures and microstructural alterations in metallic materials (Green, 1981). Notwithstanding this, the degree of sensitivity was found to vary with the type of ultrasonic waves and materials used. For example, in an experimental study of longitudinal ultrasonic wave attenuation versus grain size measurements for carbon-

manganese ferrite-pearlite steel, the dependence of attenuation on grain size was of third-order (Klinman and Stephenson, 1980); whereas in the present study on stainless steel using shear waves, the dependence was of order 2/3. It is therefore believed that the attenuation sensitivity on grain size for titanium alloy will be of a different magnitude.

For the on-line use of the technique presented here, it is essential that the information on reflected ultrasonic signals can be efficiently analysed, accurately and automatically. This enables changes in welding parameters to be made quickly. During welding, the microstructure around the weld bead is changing continuously, there is a need to use a fast data acquisition system to control the system via the ultrasonic signals. These data are fed back to a control unit which controls and/or varies the welding parameters, thus providing closed-loop, real-time monitoring and control of the weld process, weld bead geometry and grain size. Related work was also undertaken on the adaptive control of weld depth and is presented in section 3.4 and discussed in section 7.1.

## 7.3 Ultrasonic detection of size of titanium weld at elevated temperatures (Yung *et al.*, 1996)

### 7.3.1 Mathematical relationship between ultrasonic velocity and weld bead size at different temperatures

The actual measured quantity is the travelling time t(T) of the ultrasonic signal in titanium at temperature T and $V_r$, V(T) are the ultrasound velocities at room temperature (RT) and temperature T respectively. D(T) denotes the apparent distance travelled by the ultrasound for the plain sheet sample, $D_w(T)$ denotes that for the bead on plate sample. $D_c$ is constant which is 80 mm. Using these notations :

$$D(T) = V_r\, t(T) \tag{7.7}$$

$$D(T) = mT + k \quad \text{from Figure 4.7, m is slope of graph and k is constant} \tag{7.8}$$

$$\therefore \quad t(T) = (mT + k) / V_r = m'T + k' \tag{7.9}$$

Since the actual distance travelled *does not change as the temperature increases*, all changes noted were due to the variations in velocity and time. If the temperature dependence of D(T) and $D_w(T)$ come solely from the temperature dependence of the ultrasound velocity, then

$$D_c = V(T)\, t(T) \tag{7.10}$$

$$\therefore \text{ from (7.9)}, \quad V(T) = D_c / t(T) = D_c / (m'T + k') \tag{7.11}$$

$$(7.10)\ \&\ (7.7) \Rightarrow \quad D(T) = D_c\, (V_r / V(T)) \tag{7.12}$$

$$\text{Similarly,} \quad D_w(T) = (D_c - r)\, (V_r / V(T)) \tag{7.13}$$

where r is the true weld pool radius

### 7.3.2 Plain sheet : ultrasonic response at edge at elevated temperatures

From Figure 4.7, it can be seen that the echo's position relative to the sheet edge changed approximately linearly with temperature. The slope of this line was determined as 0.0059 $mmK^{-1}$, a very small value. This slope implied that when the temperature increased by 100 °C, the apparent distance travelled by the ultrasonic wave increased by 0.59 mm. Since the apparent increase in distance actually corresponds to the time of ultrasound wave travel, then the travel time changed approximately linearly with temperature.

From Equation 7.11, it could be expected that the ultrasound velocity would decrease as temperature increases. Furthermore, by differentiating V(T) of Equation 7.11 with respect to temperature T, then it may be shown that :

$$dV(T)/dT = -(D_c * m') / (m'T + k')^2 \qquad (7.14)$$

Thus, it appears that the square of temperature affects the linear rate of change of ultrasound velocity. The findings in the present study are similar to those from previous work on aluminium, steel and brass (Papadakis *et al.*, 1972; Salama, 1985; Mark and Gauthier, 1993) where it was found that the shear velocity of all three metals decreased linearly with increased temperature. It may therefore be believed that shear wave velocity will decrease linearly with increased temperature for both IMI 318 and CP titanium. The findings in this study substantiated this belief.

### 7.3.3 Bead on plate welds : ultrasonic response at weld pool at elevated temperatures

The measured distance ($D_w(T)$), apparently travelled from the probe to the weld pool boundary is shown in Figure 4.8. This apparent increase in distance was due to the velocity reduction of ultrasonic waves at elevated temperatures. As shown previously, this increase in apparent distance changed approximately linearly with temperature at an increasing rate of 0.0066 $mmK^{-1}$. Since the apparent radius (uncompensated) of the weld pool $r_a$ together with $D_w(T)$, equal the distance between the ultrasonic probe to the weld pool centre line (experimentally fixed at 80 mm); increases in $D_w(T)$ causes $r_a$ to decrease (as shown in Figure 4.9) with a slope -0.0066 $mmK^{-1}$, crossing the Y axis at 2.1 mm.

The data and graph in Figure 4.7, (which show the additional distance travelled by the ultrasound due to the temperature effect), were then used to calculate the weld pool radius. For instance at 500°C, the additional distance travelled (from Figure 4.7) was 2.5 mm, then from the data in Figure 4.8, the apparent distance travelled, $D_w(T)$ was 81.3 mm. Hence, the actual distance travelled was 78.8 (81.3 mm minus 2.5 mm). As $D_w(T)$ and the weld pool radius add up to 80.0 mm (experimentally fixed), therefore, the weld pool radius after compensation at a nominal 500 °C may be shown to be (80.0-78.8) mm = 1.2 mm. Table 4.4 gives the apparent weld pool radius after compensation at various temperatures.

Compared to the actual radius (diameter) of the weld pool previously measured which was 2.5 mm (5.0 mm), all the compensated radii in Table 4.4 were calculated to be smaller. One of the major reasons for this error was due to the presence of the HAZ during welding. This change in the HAZ microstructure increased grain sizes resulting in attenuation of the ultrasonic waves. The attenuation was seen in terms of the extended travel time of the ultrasound. There exists a compensation factor (C) for computing the actual weld pool radius to compensate for HAZ microstructural effects. However, this factor may also be dependent on many other parameters and would probably be more useful if a large data base were developed. Nevertheless, if a real-time weld pool radius computations were needed during welding, the methodology used for computing C could still be employed. However, since the HAZ microstructure changes continuously, there exists a need to use a sufficiently fast data acquisition system simultaneously to compute the pool radius. Such data could then be fed back to a control unit, which in turn controlled and/or varied the welding parameters. This would provide a closed-loop and real-time monitoring system for welding. Once more, the work given in section 3.4 could be the starting point for this purpose.

After investigating the ultrasonic response at different temperatures, it was found that the data obtained are not best approximated by a straight line. A better fit to the data shown in Figure 4.7 requires interpolation. A Lagrange interpolation method was employed for these data. From this work, the polynomial P(T) obtained is :

$$P(T) = -1.2 \times 10^{-8} T^3 + 1.9 \times 10^{-5} T^2 - 1.7 \times 10^{-3} T + 80 \qquad (7.15)$$

Using this polynomial, a differing radius for each temperature was computed. However, this represented only a 6% deviation from the original result. It was demonstrated, thus, that nonlinearity could be tolerated.

If the effect of temperature variation of the ultrasound velocity were to be eliminated, Equations (7.12) and (7.13) could be re-arranged and, as the factor of V(T) appears both in D(T) and $D_w(T)$, then,

$$D_w(T) / D(T) = (D_c - r) / D_c = 1 - r / D_c \quad (7.16)$$

$$\Rightarrow \quad r = D_c \{ 1 - D_w(T) / D(T) \} \quad (7.17)$$

From this equation (7.17), the weld pool radius can be computed for a range of temperatures (as presented in Table 7.1). It was found that the weld pool radii ranged from 1.0 mm to 1.4 mm (with an average of 1.2 mm). This relationship between the weld pool radius r and temperature, if any, can be seen from Table 7.1, if data at temperatures above 600 °C are available.

Within the range of temperatures used in the experiment, the maximum location error of weld pool radius was ± 0.2 mm which was 17% of the average weld pool radius (1.2 mm). This was larger than a previous study on weld pool radius assessment taking into account the variation of ultrasonic velocity in austenitic steel with temperature, which found a location error of 14% (Ogilvy and Temple, 1990). This was because this previous study used a theoretical model which assumed a perfect solid-liquid interface or simple geometry. However, such an assumption cannot be realised in practice. Thus the small variation in location error of the weld pool suggested that the solid-liquid interface is not a perfect one or the weld was not of a simple geometry.

From this work, it was clearly shown that for titanium, the ultrasonic travel time of shear waves changed linearly with temperature and that the ultrasound velocity changed inversely with temperature. This was in line with the findings of a previous work on steel which when measuring the velocities at elevated temperatures, found that the ultrasound velocity changed almost inversely with temperature (Fenn and Wooton, 1986). The findings in the present study validated the same relationship between ultrasound velocity and temperature in titanium thin-plate.

Furthermore, it was demonstrated that the rate of ultrasound velocity change correlates to the square of the temperature. The relationships derived in section 7.3.1 were used to determine the weld pool radii, these radii appeared to be smaller than the measured radius due to the thermal effects on ultrasound velocity and the presence of a changed microstructure within the HAZ. Decreases in the indicated weld pool diameter can be compensated by a notional factor. However, this factor apparently depends on many other parameters and is probably only useful where a large data base has been developed. If the temperature effects of the ultrasound velocity to determine the weld pool radius could be eliminated, then the ratio $D_w(T)$ / $D(T)$ could give a better indication of the relationship between the weld pool radius and the temperature if enough data above 600 °C were available. However, though temperature transducers with high-temperature delay lines that can withstand tip temperatures in excess of 1000 °C are commercially available, the coupling medium will become less viscous and does not even support shear wave transmission at high temperatures (Mark and Gauthier, 1993). To enable the use of ultrasound as a contact-type sensor for on-line feedback control, it will be helpful if a commercial coupling medium is available for shear wave transmission at elevated temperatures beyond 600 °C. Alternatively, a non-contact or momentary contact method of sound inducement and detection has to be used. One method that has recently been investigated is laser-induced sound in the weld pool coupled with a contact transducer for sound detection (Fenn, 1989). Another means found reliable is ultrasonic coupling using a pseudo-immersion technique in which the ultrasonic transducer was coupled to the workpiece via a gel-filled tube (Siores, *et al.*, 1988)

## 7.4 Qualification of CP grade titanium welds

### 7.4.1 Effect of welding parameters on the depth of weld penetration

The results in Tables 5.1 and 5.2 show that the heat input greatly affects the depth of weld penetration. For constant welding speed, the welding current affected the heat input per unit length to the weld and hence the weld penetration. Insufficient weld pool heating was caused by too low a welding current which resulted in lack of penetration. On the other hand, too high a welding current caused defects like undercut and even caused burn-through of the metal. At a constant welding current, varying welding speeds resulted in differing heat inputs and hence the amount of molten metal produced per unit time varied. This would affect the degree of penetration. Visual inspection revealed the approximate range of heat input required to produce welds with good penetration. Assuming an arc efficiency of 0.6, these heat input ranges were between 45 - 50 $Jmm^{-1}$ (welding without back shielding gas, group I specimens 5101 to 5107) and between 53 - 60 $Jmm^{-1}$ (welding with back shielding gas, group II specimens 5108 to 5123).

Comparing the welding parameters used in group I and group II, it was found that, for the same material, the optimum range of heat input was higher with back shielding gas than without. This was because some heat was removed by the shielding gas, therefore the arc efficiency was lower. More energy would then be required to melt sufficient metal to achieve complete penetration. Moreover, the range was larger in the case with back shielding gas, which proved that a wider spectrum of welding parameters could be used with back shielding gas.

Based on the results in Table 5.2, Figure 7.2 shows the relationship of welding parameters to weld penetration with back shielding gas (group II specimens 5108 to 5123). From this graph, it may be seen that sound welds could be produced using a definite range of welding speed and current. At a low current of 25 A, lack of penetration welds resulted regardless of the speed used. On the other hand, at a high current of 40 A, excessive penetration welds resulted, also regardless of welding speed. Thus, it can be seen that welding current plays an important role in controlling weld penetration depth. This agrees with a previous study (Thomas *et al.*, 1992) which found that welding current has a more significant effect on increase of penetration depth, whereas welding speed has a relatively smaller effect.

Between the two limiting currents of 25A and 40A, the welding speed could be adjusted to obtain acceptable penetration. In this study, a welding speed of 3.8 to 5.1 $mms^{-1}$ was found to produce a satisfactory weld for a given current of 32 A. In summary, to produce acceptable welds on CP grade titanium of 1.0 mm thickness, welding parameters around or near the line of acceptance A in Figure 7.2 should be used.

### 7.4.2 Effect of welding parameters on the width of HAZ

One of the uses of the peak temperature equation (Equation 2.3) could be the calculation of the width of the weld HAZ. However, to calculate this width accurately, the outer HAZ extremity needs be clearly identified with a specific peak temperature, which in turn is associated with some characteristic change in the structure or properties of the weld. In the case of the CP titanium used, the peak temperature at the outer extremity of the HAZ was the $\alpha/\beta$ transformation temperature.

The necessary data for CP titanium to allow calculation of the HAZ width, derived from previous work (*Duncan and Hanson, 1980; Polmear, 1995*), are shown below :

| | | | |
|---|---|---|---|
| Peak temperature ($T_p$) $\equiv$ $\alpha/\beta$ transformation temperature = | 882 $^oC$ | = | 1155 K |
| Melting point ($T_m$) of the CP titanium = | 1670 $^oC$ | = | 1943 K |
| Room temperature ($T_o$) = | 20$^oC$ | = | 293 K |
| Density ($\rho$) of the CP titanium = | 4.51 $kgmm^{-3}$ | | |
| Specific heat of solid metal (C) of the CP titanium = | 528 $Jkg^{-1}K^{-1}$ | | |
| Thickness of sheet (t) = | 1.0 mm | | |

Substituting the above data into Equation 2.3 gives

$H_{net} = 20\ Y$ for CP titanium

or $Y = 0.05\ H_{net}$,

where $H_{net}$ = net energy input rate, $Jmm^{-1}$

$Y$ = width of HAZ, mm

The width of HAZ and corresponding heat input rate of all group II specimens (5108 to 5123) are plotted in Figure 7.3. This suggests a positive relationship between the heat input rate and the width of the HAZ. This positive relationship is valid regardless of whether the penetration of the welds is sufficient or not. Also, if only specimens with

acceptable penetration in group II (specimens 5108 to 5123) are included, the experimental results presented in Figure 7.4 become closer to a linear relationship.

The positive relationship between heat input rate and weld pool width found here agrees with the findings of Hinata and co-workers (1993). The relationship can be explained by weld pool morphology which indicates that the anode area formed on the weld pool surface just below the electrode tends to spread more in the circumferential direction of the weld pool when heat input is increased. This increases the width of the weld pool.

### 7.4.3 Effect of welding parameters on the fracture toughness

As the work of Ahmady (1987) and Kaufman (1967) have shown there is an approximately positive correlation between work of fracture and $K_{IC}$ data, the following discussion on the work of fracture also applies to the fracture toughness of IMI 130.

It can be seen from Table 5.4, that the yield load of group III specimens (5201 to 5211) show a negative relationship with the welding current, the yield load decreasing with increases in the welding current. As a result, the work of fracture $\gamma_F$ and therefore the fracture toughness decreases when the welding current increased (as shown in Figure 7.5). Table 5.5 shows that the relationship between yield load of group IV specimens (5212 to 5222) and welding speed is a positive one. Yield load decreased when the welding speed decreased, yield displacement increased when welding speed was decreased. As a result, the work of fracture $\gamma_F$ and therefore the fracture toughness decreased when the welding speed was decreased, as shown in Figure 7.6.

However when comparing Figures 7.5 and 7.6, it is obvious that the effect of welding speed is more than that of welding current on the work of fracture, and therefore on the fracture toughness of IMI 130.

(i) Heat input rate

It could be seen with specimens of both groups, III and IV (specimens 5201 to 5222), that the value of $\gamma_F$ decreased with increased heat input (Figures 7.7 and 7.8). This was because when the heat input increased, the peak temperature generally increased, and thus

the grain size of the weld metal also increased. As a result, the higher the heat input, the coarser the grain structure, leading to decreased fracture toughness of the specimens. As discussed in the literature review (section 2.2.5), when the heat input was increased, the temperature gradient decreased and thus $G/S_R$ ratio (where G is the temperature gradient in the direction of solidification and $S_R$ is the rate of advance of the solidification front) was reduced. The lower the $G/S_R$ ratio, the coarser the subgrain structure of the weldment. It was also expected that both the weld metal and the HAZ would show similar microstructures of coarse saw-tooth-like $\alpha$ or needle-like $\alpha$ for IMI 130. This saw-tooth like $\alpha$ structure coarsened when the heat input was increased, therefore, the value of $\gamma_F$ decreased as the grain size coarsened, and the ductility was reduced.

(ii) Cooling rate

It is shown in Figure 7.6 that fracture toughness decreased when the welding speed decreased. As a lower welding speed induces a lower cooling rate, the dependence of fracture toughness on cooling rate is obvious : fracture toughness decreased at a lower cooling rate. This agrees with the previous work by Lukens and Morris (1982). It was found that rapidly cooled CP titanium has better tensile strength and fracture toughness but possesses lower ductility than it does after slow cooling. Furthermore, as lower cooling rate favours grain growth, this means that fracture toughness decreases when the grain size increases. This substantiates the validity of Equation 2.17 in the literature review which predicts a negative relationship between fracture toughness and grain size.

However, it is well established that for CP titanium, upon quenching (high cooling rate) from above the $\beta$ transus, results in a fully martensitic phase, whereas a Widmanstatten microstructure is formed with a low cooling rate, for example in an air-cooling situation (Donachie, 1988). The slower progress of cracks through the Widmanstatten microstructure should result in a notable higher fracture toughness. These trends have already been noted when considering CP titanium and appear to apply generally in $\alpha/\beta$ alloys. In other words, a lower cooling rate should result in a higher fracture toughness in the weld metal. This is apparently in contrast to the finding in this section. However, it is reported that mechanical properties including fracture toughness of CP titanium are comparatively insensitive to microstructures (Polmear, 1995), and in the absence of a quantified cooling rate for comparison, it is believed that the grain size effect is dominant and even swamps that of the Widmanstatten microstructure at lower cooling rate.

## 7.5 Qualification of α/β titanium alloy - IMI 318 welds

### 7.5.1 Effect of welding parameters on the weld penetration and weld size

(i) Weld penetration

As seen in Figure 6.2, a range of welding parameters was used to produce 1.2 mm IMI 318 welds with acceptable penetration. Similar to the findings of 1.0 mm CP titanium in section 7.4, a welding speed of 3.4 to 5.1 $mms^{-1}$ was found to produce a satisfactory weld for a given current of 30 to 50 A. However, unlike the 1.0 mm CP titanium, it was found that the maximum used welding speed of 5.9 $mms^{-1}$ did not give satisfactory welds regardless of current used. Since higher welding speeds result in lower heat inputs, it is substantiated that there exists a minimum heat input and therefore a maximum welding speed, to produce welds with acceptable penetration.

For 1.7 mm thick IMI 318 welds, Figures 6.3 and 6.4 reveal that penetration varies positively (almost linearly) with the welding current as did the heat input rates at fixed welding speed. This is in line with a previous finding that weld penetration varies linearly with welding current (Wealleans and Allen, 1969). However, in the study of penetration using a stationary TIG arc (Hinata *et al.*, 1993), it was found that the weld penetration changed positively with the welding current, however there exists a critical and specific current value beyond which the penetration decreases when the welding current is increased. This critical current value was also found to be dependent on the type of material to be welded. Also, the critical value identified by Hinata and co-workers (1993) was found before full penetration took place. In the findings here, such a critical current was not evident within the range of welding currents being used, up to full weld penetration.

This finding may be explained in terms of the material being used. In the experiments of Hinata and co-workers (1993), steel was used. It is reported in a number of papers (Lancaster, 1990; Mukai *et al.*, 1990) that weld penetration in steel is strongly affected by trace elements such as sulphur and phosphorous. The critical current value depends on the concentration of these elements. However, such trace elements were not evident in the IMI 318 material. Other impurities in the alloy, if any, did not result in such a critical welding current either.

(ii) The width of weld

For 1.2 mm IMI 318 welds, as revealed in Figure 6.1, there is an apparent linear increase of HAZ width with heat input. However, if only specimens with acceptable weld penetration were selected, the variation of HAZ width was only between 1.7 to 2.1 mm at heat input rates between 79 to 88 $Jmm^{-1}$. Therefore the HAZ was virtually unaffected by heat input rate. This was the same finding as in 1.0 mm thick IMI 318 detailed as follows, except that the HAZ width was higher due to a higher range of heat inputs used.

For 1.0 mm thick IMI 318, as seen from Figures 6.5 to 6.8, the total width of the weld (comprising the FZ and two adjacent HAZs) was found to enlarge with the increase of heat input rate and the increase of welding current (at fixed welding speed) and the decrease of welding speed (at a fixed welding current). These relationships were also seen in a previous study (Wealleans and Allen, 1969). By contrast, little change was found in the HAZ width, regardless of any change in the welding current and speed. Thus, the HAZ width was virtually unaffected by both these welding parameters, thus the increase of weld size must be due solely to the increase of FZ width. Notwithstanding this, there was a small plateau seen in the FZ width relative to current in Figure 6.6 (specimens 6124 to 6130), when the FZ width was around 5 mm. This occurred at peak pulse currents between 60 A and 120 A and the corresponding heat input rates (Figure 6.5) between 12 to 24 $Jmm^{-1}$. Figure 6.7 (specimens 6131 to 6137) did not reveal the same phenomenon with the same changes of heat input rate (due only to changes of welding speed); this plateau mainly resulting from changes in welding current.

The increase of the width of the FZ can be understood in the light of welding physics. During the TIG welding, the intense plasma stream results in an arc force which is basically a shear force. This shearing force orients the flow of weld metal in the circumferential direction. Furthermore, the arc force was found to be a function of the welding current (Hinata *et al.*, 1993), with large arc forces at larger welding currents. Therefore, when larger welding currents are used, the width of the FZ and the weld size increase which is the result obtained here.

On the other hand, it was reported (Hinata *et al.*, 1993) that when the TIG arc was used at a current higher than a specific value, a more pronounced increase of arc force and therefore width of the weld was seen. This happened when a higher arc time was used. However, the findings here did not reveal such a pronounced effect in any current value

within the experimental settings. This may be because the arc time used in the study was not as high. Higher arc time results in a larger amount of fusion of the base metal which enhances the arc force to push the weld front in the circumferential direction.

### 7.5.2 Effect of welding parameters on grain size of welds (Yung *et al.*, 1997c)

(A) 1.0 mm thick IMI 318 (specimens 6124 to 6137)

(i) *Grain size distribution and welding parameters*

In Table 6.5 and Figure 6.9 (specimens 6124 to 6130), in the HAZ (between 2.5 mm and 4.5 mm from the weld centre line), there was a general decrease in grain size when moving towards the parent metal. In the far HAZ (between 3.5 to 4.5 mm from weld centre line), the grain size was found to be virtually the same, regardless of changes in welding current and heat input. However, in the near HAZ region (2.5 mm from weld centre line), the average grain sizes were larger for higher welding currents and larger heat inputs.

In the FZ between 0.5 and 2.5 mm from the weld centre line, it was found that the first two specimens 6124 and 6125, with the lowest welding currents and heat inputs, did not demonstrate much change in grain size. In specimens 6126 and 6127, a small variation in grain size could be seen whereas for specimens 6128 to 6130, a much larger variation was observed. It is worth noting that specimen 6130, with the highest welding current and heat input, had a grain area of 120000 $\mu m^2$ at 0.5 mm from the weld centre line, which was the largest grain size observed amongst the specimens in the group and also had the largest variation in FZ grain size.

In Table 6.6 and Figure 6.10 (specimens 6131 to 6137), in the HAZ, most specimens showed the expected decrease of grain size when moving towards the base metal. Across the whole spectrum of the HAZ between 2.5 mm and 4.5 mm from the weld centre line, all specimens had virtually the same grain size regardless of welding speed and corresponding heat input rate used. This was more obvious than in specimens 6124 to

6130, thus it may be said that, changes in welding speed and corresponding heat input rate did not result in a significant change in HAZ grain size.

This is in contrast to the findings of Watanabe and co-workers (1995) where it was found that the lower the heat input rate, the smaller the grain size at the HAZ region. This difference in findings may be attributed to the difference in the range of welding parameters being used. In their case, lower welding speeds and currents were used (material thickness is the same as in this section).

In the FZ between 0.5 and 2.5 mm from the weld centre line, it was found that the first two specimens 6131 and 6132 with the lowest welding speed but the highest heat input had the greatest grain size variation, with the largest grain size located in the FZ. By contrast, other specimens made with higher welding speeds did not exhibit much change in grain size across the FZ.

Considering both Figures 6.9 and 6.10, it was found that the specimens with the highest welding current and lowest welding speed, (both with the highest heat input), had the largest grain size, these exhibited the greatest grain size variation across the FZ in their own specimen groups. This is in agreement with the findings in most titanium welding applications (Hallum & Baeslack, 1990). It was reported that grain sizes in the FZ are primarily determined by weld energy input and cooling rate which are changed through modification of welding current and speed respectively. Higher energy input (i.e. higher welding current) and lower cooling rate (i.e. lower welding speed) result in coarser grain size. Obviously, the findings here further support this phenomenon.

(ii) *Largest grain size and welding parameters*

For ease of comparison and reference, the location of the largest grain size across the weld bead of specimens in Figures 6.9 and 6.10 are marked with "•" which are then re-drawn in Figure 7.9. The largest grain size in the measurement (all of them were located within the FZ) is then plotted against the heat input rate for the two specimen groups (6124 to 6137) and this data is presented in Figure 7.9. It is obvious that for both specimen groups the maximum grain size was affected by, and varied positively with, the heat input rate.

Using individual welding parameters, the maximum grain size changed positively with increase of welding current in specimens 6124 to 6130, and with decrease of welding speed in specimens 6131 to 6137. However, when taking the results of both groups together and looking at the range of heat input between 20 to 25 $Jmm^{-1}$, (which are the higher ends of heat input in both groups), it was found that the effect of the change in welding speed (specimens 6131 to 6137) on the maximum grain size was much more than that of the change in welding current (specimens 6124 to 6130).

In a study by Becker and Adams (1979) on the weldment of the α/β alloy Ti-6Al-6V-2Sn of 1.6 mm thickness, it was reported that as the pulse time at peak welding current is reduced, the grain size at the FZ decreases. Since the origin of the coarse grain comes from cooling and solidification taking place during the high-current portion of the pulse cycle, a reduction in pulse time at peak welding current merely reduces the time for this cooling and solidification to occur. The findings here agree with those of Becker and Adams (1979) in that the change in grain size is dominated by the change in welding speed and change in cooling rate. It is therefore believed that cooling and solidification mechanism are still prime factors in the determination of grain size.

(B) 2.7 mm thick IMI 318 (specimens 6138 to 6146)

(i) *Grain size distribution and welding parameters*

As can be seen from Figures 6.11 and 6.12, grain size distribution was symmetrical around the centre of the FZ. Grain size also exhibited a decreasing trend with distance away from the FZ centre, in other words, the grain size was largest at the centre of the FZ. This was in contrast to the findings obtained in the previous section on thinner (1.0 mm) plates. This may be due to the fact that for very thin plates (at or below 1.0 mm thick), there exists a displacement in the finite heat source (Shah *et al.*, 1995) which complicate the heat flow equations originated by Rosenthal (1946) and those later modified by others (refer to section 2.2.3). Furthermore, for plate of 1.0 mm thickness, the mechanical effect of the heat source on the liquid metal pool may contribute to the complication of the welding metallurgy and grain growth mechanisms (Frolov *et al.*, 1994).

In Figure 6.11, the largest grain size was found in specimen 6141 which received the highest heat input (130 $Jmm^{-1}$) and the highest welding current (140 A). From Figure

6.12, the largest grain size was found in specimen 6142 which received the highest heat input (120 $Jmm^{-1}$) but the lowest welding speed (3.4 $mms^{-1}$).

These findings not only are the same as for the 1.0 mm thick weldments in the previous section but also substantiate the claim in previous research on grain growth (Shah *et al.*, 1995) that the cooling time (may be controlled by welding speed) and the peak temperature ($T_p$) during weld thermal cycle (may be controlled by welding current) affect the grain size most significantly.

To study the effect of individual welding parameters on the grain size, the area of largest grain size across the weld (usually at the centre of the FZ) was plotted against heat input (Figures 7.10 and 7.11), and against the welding current and welding speed (Figures 7.12 and 7.13 respectively). To study the effect of the same parameters on HAZ grain size, the grain size at 3 mm locations from the FZ on both sides of the weld were plotted (Figures 7.14 and 7.15).

As revealed in Figure 7.12. the grain size in FZ varied positively with the welding current. With other parameters unchanged, increasing the welding current in general results in an increase of peak temperature encountered in the FZ. Supported by the findings of Shah and co-workers (1995), the final grain size increases with increasing peak temperature, and therefore with increasing welding current.

Furthermore, as can be seen from Figures 7.10 to 7.11, the largest grain size varied positively with heat input rate. Apart from peak temperature in the FZ, the final grain size in the grain-growth region for any given alloy also depends on the solidification time which is proportional to the heat input rate. As mentioned in the literature review (section 2.2.4), the dendrite spacing is proportional to the square root of the solidification time (Nippes, 1983), and it is not surprising to see the heat input rate has a profound effect on the grain size.

On the other hand, the solidification time can be reduced by using a heat source operating at high welding speed. Thus, increasing the welding speed will lower the solidification time and therefore the dendrite spacing and will result in a smaller grain size. This is the trend demonstrated in Figure 7.13. This also agrees with the findings in the work of Watanabe and co-workers (1995).

In the HAZ of specimens in both groups, as revealed in Figures 7.14 and 7.15, the effect of welding current and speed on the grain size is minimal. The observed small variations in grain size are believed to be due to an inherent error arising from the limited number of grains in the field of view and from changing directionality characteristics.

(ii) *Grain size and cooling rate*

To relate the effect of welding cooling rate on grain size, the cooling rate on specimens 6138 to 6141 at different temperatures were computed using Equation 2.4. A similar procedure was adopted for specimens 6142 to 6246. Transformation of the crystal structure took effect at the β transus temperature 1156 K, the cooling rate in the specimens was computed at this temperature and was plotted against the largest FZ grain size in Figures 7.16 and 7.17. The consolidated result from both Figures 7.16 and 7.17 is that the higher the cooling rate the smaller the grain size.

As mentioned in the literature survey (section 2.2.5), the increase of cooling rate in TIG welding will result in a decrease of grain size due to finer cell spacing (Kou, 1987). In fact, a later study by Mohandas and co-workers (1996) investigated the effect of welding parameters on the microstructures of IMI 318 weldments of 3 mm thickness. It is found that the grains are finer at higher pulsing frequency. The higher pulsing frequency is equivalent to a more rapid heating and cooling cycle which reduces the cooling time during the pulsed TIG welding. A higher cooling rate has essentially the same effect in minimizing the grain growth, thus resulting in a smaller grain size. Another study by Shah and co-workers (1995), proved that at a lower cooling rate (and longer cooling time), the size of transformed β grain increases. This effect is particularly prominent in the case of higher peak temperature ($T_p$).

Thus, based on the findings in 1.0 mm and 2.7 mm thick IMI 318 welded specimens in this section, it is evident that both the peak temperature experienced in the weld (primarily controlled by welding current), the solidification time (proportional to heat input rate) and the cooling rate (determined by welding speed) play an direct and important role in controlling the final grain size of the welds.

### 7.5.3 Effect of welding parameters on hardness of the IMI 318 welds

Figure 6.14 shows that the hardness was almost inversely proportional to the welding current. The lowest hardness was 308, a lower value by 24 than that of the base metal. Furthermore, the welding current that would produce a weld with the same hardness value as the parent metal (Vickers hardness number of 332) would be approximately 180 A (as can be seen by extrapolation of the plots).

Figure 6.15 shows the hardness of the specimens welded at different speeds. This figure shows that the hardness was almost directly proportional to the welding speed. The lowest hardness was 291, a lower value by 41 than that of base metal. Again, if the two plots in the figure were extrapolated, the welding speed that would produce a weld with the same hardness as the parent metal would be about 5.1 $mms^{-1}$.

This relationship between the hardness of the weld and the welding parameters could be explained by their cooling rate. The cooling rate itself was proportional to the welding speed and inversely proportional to the heat input rate. Thus, a lower welding speed induced a lower cooling rate which resulted in a lower hardness of the welds.

In previous studies by Wu (1961, 1965), it has been claimed that the mechanical properties of $\alpha/\beta$ titanium alloys including hardness are cooling-rate sensitive. Lower cooling rates promote the formation of alpha plates and alpha colonies. A greater ease of slip and smaller resistance to plastic deformation is encountered within the alpha plates and across alpha colonies as compared to that in the fine martensitic product (Mahajan and Baeslack, 1979). This results in a lower hardness value of the welds.

In fact, it was reported that IMI 318 weld metal, when subjected to a very high cooling rate (for example in the case of laser welding), exhibited a Vicker hardness value 100 higher than that of the base metal. The increase of hardness was found to be closely related to an increased amount of hard martensite resulting from the high cooling rate below $\beta$-transus (Ogawa *et al.*, 1987). It was also found that the decrease of grain size at a high cooling rate during solidification also contributed to an increase of hardness of weld.

For example, at 100 $Ks^{-1}$, a prior-β grain size was found up to 1 mm, and that corresponding to 1000 $Ks^{-1}$ had decreased to about 300 μm.

Furthermore, the results in this section agree with the findings of Baeslack and Mullins (1984) in their investigation of cooling rate effects in thin-plate welds of Ti-6Al-2Sn-4Zr-2Mo. Different cooling rates from 500 $Ks^{-1}$ (representative of water quenching) down to 7 $Ks^{-1}$ (representative of air cooling) were used. It was found that lower cooling rates promote an increase in the quantity and coarseness of the alpha plate colonies which result in a decrease in the hardness of the welds.

### 7.5.4 Factors affecting tensile properties of the IMI 318 welds (Yung *et al.*, 1997a)

(A) Fractographic and tensile studies on 2.3 mm thick welded specimens (specimens 6301 to 6308)

*(i) Fracture modes*

As observed in the fractographs (Figures 6.27 to 6.44), most of the specimens showed a dominant presence of dimples which were indicative of ductile failures by a microvoid coalescence mechanism; microviods being nucleated at the regions of localised strain discontinuity. As the strain in the material increased, these pores grew, coalesced, and eventually formed a continuous fracture surface. This fracture mode exhibited numerous cup-like depressions in the specimens (referred to as dimples), and the fracture mode was a dimple or ductile rupture under monotonic loading conditions. The same fracture mode is commonly observed in other α/β titanium alloys. However, a quasi-cleavage fracture mode was observed in specimen 6308. It was a localised and isolated feature on a fracture surface, and exhibited characteristics of both cleavage and plastic (or ductile) deformation. A quasi-cleavage fracture was initiated at the central cleavage facets. As this crack radiated, the cleavage facets blended into areas of dimple ruptures, the cleavage steps becoming tear ridges (Figures 6.43 & 6.44).

Cracks in specimen 6308 were believed to be reheat cracks caused by the current pulses during the welding cycle. As the welding speed decreased, the material at a point say (x,y,z) was reheated more by the current pulses.

There was no general relationship observed between the welding parameters and the fracture mode. Within the set of welding parameters used, all specimens exhibited dimple fractures, except specimen 6308 which was welded at the lowest speed.

*(ii) Dimples*

For specimen group 6301 to 6304 and specimen group 6305 to 6308, the dimple size was larger when the welding current increased (Figures 6.27 to 6.34) and welding speed decreased (Figures 6.35 to 6.44), the dimple size being governed by the number and distribution of any microvoids nucleated. Small dimples were formed when numerous nucleating sites were activated and adjacent microvoids coalesced before they had an opportunity to grow to larger sizes. On the other hand, when the nucleation sites were few and widely spaced, the microvoids grew to a large size before coalescing and the result was a fracture surface that contained larger dimples.

It was evident in specimen group 6301 to 6304 that increasing welding current decreased the number of nucleation sites and increased the size of microvoids. This resulted in the fracture surface of this specimen group containing larger dimples. As the number of nucleation sites decreased, the grain size increased (and vice versa). In the same manner in specimen group 6305 to 6308, a decrease of welding speed caused a decrease in cooling rate. More time was available for the nucleation sites and voids to grow larger in size. This resulted in a larger dimple size on specimens with lower welding speeds.

*(iii) Effect of welding current on tensile properties of 2.3 mm thick welded specimens (specimens 6301 to 6304)*

Specimen group 6301 to 6304 showed that tensile strength slightly decreased (maximum 5 % in this study, from 1090 MPa to 1040 MPa) with an increase of the heat input rate (Figure 6.17). It was also observed that the tensile strength slightly decreased (maximum 6 % in this study) with increases of the welding current (Figure 6.20). Moreover, in Figures 6.18, 6.19 and 6.21, the area of reduction and strain to failure were found to decrease (maximum 35 % and 31 % respectively) as welding current and heat input rate increased. This was further substantiated by the relative shallow dimples in the fractograph of higher current (110 A) specimen 6303 (Figure 6.32) as compared to that of lower current (80 A) specimen 6301 (Figure 6.28). The effect of the peak thermal cycle temperature (due to changes in welding current) on tensile ductility is found to be greater than that on the tensile strength of the weld. This is commonly seen in most metals (Lancaster, 1993) and is now found to be equally applicable in IMI 318 welds.

Thus, increasing the welding current reduces the tensile properties (strength and ductility) of the IMI 318. This implies that tensile properties (strength and ductility) decrease with an increase of the thermal cycle peak temperature, which matches previous findings (Lewis and Wu, 1963). This is because when the welding current increased, peak temperature also increased, which resulted in a decrease of the thermal gradient (G). This induces a lower $G/S_R$ ratio (the solidification parameter, referred to in section 2.2.5) since the rate of advance ($S_R$) of the solidification front is the same (when the welding speed is fixed). With a lower $G/S_R$ ratio, the weld subgrain structure changes from cellular to dendritic (Kou, 1987).

Furthermore, the dendritic spacing increases as the solidification time is lengthened by the increase in welding current and heat input rate (refer to Equation 2.13, section 2.2.4). It is believed that this increase in dendritic spacing is responsible for the reduction of the tensile properties in the weld metal of the alloy.

It is worth noting that the as-welded ductility corresponding to the lowest heat input in this study, was 10.2 %. This is comparable to that of the base metal (typical 10% and 14% in $\beta$ annealed and $\alpha+\beta$ annealed conditions respectively; Donachie, 1985; Polmear, 1995). This is in contrast to the poor as-welded ductility reported in a previous study on laser and TIG weldment of IMI 318 (Baeslack and Banas, 1981). It was suggested there

that the poor as-welded ductility is generally attributed to a large prior beta grain size and an acicular martensitic microstructure. Also, it was claimed that the situation cannot be improved by controlling weld heat input alone; since a lower energy input reduces the beta grain size, but also increases the cooling rate and promotes a more needle-like martensitic structure; and that it is necessary to resort to a post-weld heat treatment to impart sufficient ductility to the FZ. Such a claim is obviously not substantiated here.

IMI 318 welds contain a brittle martensitic phase after high cooling rates, though this is not discussed in any detail in the literature. It was reported that the critical cooling rate, below which no martensite is formed, is around 9 $Ks^{-1}$ (Weigand, 1963); this is well below the cooling rate of welds made on thin metal. In other words, martensitic microstructures cannot be avoided in thin plate welds. While it is generally agreed that lower energy input will increase the cooling rate and promote the hard martensitic structure which worsens the ductility, the relative contribution of grain size and martensite towards ductility was not quantified as yet. Furthermore, laser weldment in the above study of Baeslack and Banas (1981) was made with a very low heat input and therefore a very high cooling rate, resulting in a large amount of hard and brittle martensite, which was an extreme case. In the study here, it is believed that there exists a range of low energy inputs, where the weldment is not largely martensitic in microstructure; that lower energy input reduces beta grain size (as reported in section 7.5.2) and this swamps the effect of brittle martensite and thus results in an as-welded ductility comparable to the base metal. In fact, it was found that electron beam welds have a fine grain size and are more ductile which suggests that some gains in ductility might be possible by the use of grain refinement techniques (Borggreen and Wilson, 1980). Also, an earlier work observed that no reduction in ductility was found when the weld structure was acicular (Ogden *et al.*, 1956). It may be that the effect is small until the grain size becomes large compared with the sheet thickness.

In another study of electron beam and TIG welding of 2.6 mm thick IMI 318, it was reported that the TIG as-welded ductility was only 4% as against the 14% of base metal, and it was suggested that the low ductility should be attributed to the presence of large quantities of serrated alpha in the microstructures which resulted from the relatively high heat input of 78 $Jmm^{-1}$ (Thomas and Vahudevan, 1991). In the study here, a low ductility of 4.9% was also found in specimen 6308 where a relatively high heat input 85 $Jmm^{-1}$ was used. However, at a low heat input of 51 $Jmm^{-1}$ (in specimen 6301), a ductility of 10.2% which is comparable to the base metal was identified. The heat input of 51 $Jmm^{-1}$

is considerably lower than 78 $Jmm^{-1}$ used in the study of Thomas and Vahudevan (1991), and it is believed that the more ductile acicular α instead of serrated α was the resulting microstructure.

*(iv) Effect of welding speed on tensile properties of 2.3 mm thick welded specimens (specimens 6305 to 6308)*

In contrast to the previous group 6301 to 6304, the specimen group 6305 to 6308 had tensile strengths which slightly decreased (maximum 4 % in this study) with an increase of the heat input rate (Figure 6.22), by reducing the welding speed. It was also observed that the tensile stress also slightly decreased (maximum 3 % in this study) with a decrease of the welding speed (Figure 6.25). These observations match previous findings (Lewis and Wu, 1963; Watanabe *et al.*, 1995). Cooling rate increased with increases in welding speed under the same heat input, therefore, it would appear that the prior β grain size became finer as the welding speed increased since the higher the cooling rate the finer the cell spacing. Again, from the Hall-Petch relationship, the tensile strength increased by decreasing the grain size, thus, the tensile strength increased with an increase of the welding speed.

Moreover, in Figure 6.26, the ductility in terms of strain to failure was found to decrease (maximum 20 % in this study, specimen 6308 was not included in the computation) when the welding speed decreased. This was further supported by the more shallow dimples in the fractograph of specimen 6306 (Figure 6.38) at a lower welding speed of 4.7 $mms^{-1}$ than that of specimen 6305 (Figure 6.36) at a higher welding speed of 5.1 $mms^{-1}$. The ductility even dropped to a minimum (4.9 % strain to failure) in specimen 6308 at the lowest welding speed, which exhibited quasi-cleavage fracture.

It is expected that the lower the welding speed, the coarser the cell structure will be, and, the higher the tendency for segregation and the higher the risk of cracking. Moreover, as the welding speed decreases, more material will be reheated by the next current pulse, the top bead also may cause re-heating of the underlying bead, this will increase the risk of reheat cracking. In fact, specimen 6308 showed brittle but hardened behaviour during the tensile test, since the ductility was very small. This may have resulted from the hardening effect of air contaminants, such as nitride or oxide.

It is well known that oxygen and nitrogen have high solubilities in titanium. This is particularly severe when a high heat input (as in the case of low welding speed) is used. Severe absorption of these interstitials causes embrittlement. It was observed in a previous study (Barrett and Lane, 1954), that the nitrogen and oxygen content of titanium weld increased with the amount of nitrogen and oxygen in the welding atmosphere. The bend ductility was very sensitive to these interstitials; as little as 0.25% oxygen caused some loss in ductility. The effect became more pronounced as the oxygen content of the atmosphere was raised. A nitrogen content of between 0.10 and 0.20% in the weld caused sufficient embrittlement to lower ductility in the bend test. The result here also agrees with other work which found that arc welds in titanium sheet containing 0.13% nitrogen had very low bend ductility (Martin, 1953). An improper value of inert gas flow or impurity in the shielding inert gas may well be the reason for this contamination by interstitials.

(B) The effects of cooling rate and heat input rate on tensile properties of welds in thinner (1.5 mm thick) welded specimens (specimens 6309 to 6324)

*(i) Range of welding parameters producing welds with acceptable quality in specimens 6309 to 6314*

As seen from Table 6.13, welds with acceptable visual quality were formed with welding currents between 110 to 235 A, and welding speeds between 0.38 to 1.3 $mms^{-1}$, with pulse times between 0.3 to 0.5 s. Within this welding parameter envelope (Table 6.15), the as-welded alloy had at least a UTS of 1020 MPa (which was only a 6 % reduction as compared to that of the parent metal (1080 MPa)). The strongest weld (specimen 6310) had a strength of 1050 MPa which is only 3 % lower than that of the parent metal. This agreed with the findings of Thomas and co-workers (1993) for the electron-beam welding of IMI 318 which exhibited a reduction of 4 % in tensile strength. All the IMI 318 weld specimens (except specimen 6311) fractured in the FZ.

*(ii) Effect of cooling rate on the tensile strength of weldment (specimens 6309 to 6314)*

To study the effect of cooling rate on the strength of weldment quantitatively, Equation 2.4 was used to compute the cooling rate for the specimens. Equation 2.12 was not used

in this case as it only serves as a means of comparing the heat flow conditions of welds and depicting a general relationship between cooling rate and heat input rate. In addition, since different pulse-on times were used in specimens 6309 to 6314, the pulsing variables affected the welding metallurgy and grain morphology of titanium welds, as found in a study by Mohandas and Reddy (1996). Thus, it is preferable to use the conventional approach (and therefore Equation 2.4) to compute the cooling rate in this section.

It is worth noting that specimen 6311, which was the only one which fractured in the base metal, had the highest cooling rate (1050 $Ks^{-1}$ at the alloy's melting temperature 1595 °C) amongst the six (6) welds prepared in this group. The relatively higher strength made specimen 6311 break in the base metal region. This agrees with the results of Wu's study (1981) on another $\alpha/\beta$ alloy where it is suggested that the martensite ($\alpha'$) and fine $\alpha$ platelets produced at higher cooling rates strengthen the FZ.

A previous study showed that the cooling rate appears to be especially critical in relation to the tensile properties for Ti/6Al/2Sn/4Zr/6Mo (Greenfield & Duvall, 1975). The same finding is observed in this study. In fact, the work of Wu (1961, 1965) suggests that the mechanical properties of some $\alpha/\beta$ titanium alloys are cooling-rate sensitive. The same sensitivity is found in the present study of IMI 318.

Figure 7.18 shows a trend of increasing tensile strength with increasing cooling rate. This indicates that within a particular range of cooling rate, there is a positive relationship between the cooling rate and the weldment strength. This positive relationship is also seen in the works of Baeslack and Mullins (1984) and Mohandas and Reddy (1996). The lower strengths at lower cooling rates can be attributed to a greater ease of slip within the alpha plates and across alpha colonies resulting from lower cooling rates as compared to that within the fine martensitic product resulting from higher cooling rates.

The positive relationship can also be explained in terms of the morphology and transformation of the microstructures. Both the amount of $\alpha'$ and the $\alpha$-platelet size are uniquely related to cooling rate. On cooling, the $\beta$ phase becomes unstable at the $\alpha/\beta$ transformation temperature, and $\alpha$ phase precipitates by rejecting $\beta$ stabilisers.

At low cooling rate, the time for nucleation and growth of $\alpha$ phase is longer and the size of $\alpha$-platelets is larger. Furthermore, $\beta$ stabilisers diffuse from the growing of phases into

the surrounding β phases. This enrichment of β stabilisers increases the amount of stable β phase. Therefore, less unstable β phase is available to transform into α'.

It is expected that the nucleation and growth process will be suppressed by increasing the cooling rate. When the cooling rate is high, there is less time for nucleation and growth of α phases, and the size of α platelets is small. Since less α phase transforms from β, the β phase is more diluted in β stabilisers. Thus, more α' is transformed below the martensite temperature ($M_s$).

It was found (Becker *et al.*, 1992) that the α' begins to age immediately after it is formed during cooling and when it is aged, the fine α that precipitated from it increases the strength of the weld. It is therefore believed that the combined effects of increasing α' and decreasing α-platelet size are responsible for the increasing strength at higher cooling rate in this study.

The above phase transformations can be verified by x-ray diffraction measurements. However at the time of this experimental work, such equipment was not available to the author. It is recommended to employ the diffraction technique for further study in the future.

*(iii) Effect of cooling rate on tensile ductility (specimens 6309 to 6314)*

The fracture surfaces of the parent metal (as shown in control specimens B1 and B2) of the plate material were dull and porous, having a cup-and-cone microscopic appearance with clear macroscopic necking. These features indicated that a ductile fracture had occurred during tensile testing. On the other hand, specimens which fractured in their FZs had a faceted and shiny surface without any necked regions. These features showed that the fracture of the weld metal was brittle-like, implying that the ductility of the alloy had deteriorated in the FZ upon welding due possibly to oxygen and nitrogen contamination.

With reference to Table 6.15, the weldments exhibited strains between 1.6 % and 4.1 %. This reveals a substantial loss of ductility as compared to the 16 % strain of the parent metal (Thomas *et al.*, 1993). The significant reduction in ductility or embrittlement is commonly seen in most α/β titanium alloys (Lampman, 1990; Baeslack *et al.*, 1993).

The reduction of ductility was further substantiated by comparing the stress-strain curves of the welded specimens with that of the control specimens (Figure 6.46). Welded specimens gave strains to failure of only 1/3 to 1/2 of that of the control specimens. A previous work was able to elucidate this drop in ductility resulting from welding by studying the effect of cooling time on grain size (Kivineva *et al.*, 1995). It was observed that the reduction of ductility was due to the combined effect of the low ductility of martensite and larger grain sizes.

The possible oxide contaminant in the welding atmosphere may also enhance this reduction of ductility. It was found in a study that ductility was lowered as oxygen content increased in titanium and that there was a general increase of the grain size with increasing oxygen content (Simbi and Scully, 1996). Doubtlessly, the grain coarsening effect further adversely affects the ductility of the weld.

The effect of cooling rate on the ductility of IMI 318 welds could be seen by comparing the strain to failure of specimens 6309 to 6314 with different cooling rates in Table 6.15. Figure 7.19 shows the relationship between the strain to failure and the cooling rate. The relationship is predominantly a positive one. In other words, the strain to failure was related positively to the cooling rate. It is found that the higher the cooling rate, the higher the strain to failure and hence the higher the ductility of the welds. This agrees with the work of Wu (1981) on an $\alpha/\beta$ alloy (Ti-6Al-6V-2Sn) where the ductility (in terms of elongation) improves when cooling rate (represented by different welding processes) increases.

*(iv) Effect of heat input rate on tensile strength of weldment (specimens 6315 to 6324)*

Specimens prepared in this specimen group (6315 to 6324) had lower heat inputs than the previous specimen group (6309 to 6314). As discussed in section 2.2.4 and seen from Equation 2.12, the cooling rate is in general inversely proportional to the heat input rate. This relationship was also claimed in a previous work (Murthy and Sundaresan, 1995). It was therefore expected that the cooling rates of specimens 6315 to 6324 would be higher than those of specimens 6309 to 6314. Thus specimens 6315 to 6324 as a whole should have higher strengths than that of specimens 6309 to 6314. This result was observed here.

The comparatively higher cooling rate of specimens 6315 to 6324 caused all of them to fracture in the base metal, which implied that the weldments had higher strengths than the base metal. Thus, again cooling rate was found to have the determining effect on weldment strength. It is suggested that finer $\alpha$ platelets were produced at higher cooling rates and this strengthened the FZ of the welds.

Moreover as found in an earlier x-ray diffraction study (Wu, 1981) on an $\alpha/\beta$ titanium alloy, higher cooling rate results in a larger proportion of martensite ($\alpha'$) in FZ. The $\alpha'$ help to lock any slip and inhibit any deformation (Young *et al.*, 1974). This also improves the strength of the weld metal.

Thus, it is believed that the combined effect of finer $\alpha$ platelets and a larger proportion of $\alpha'$ contribute to the higher strength of the weld metal at lower heat input rates (or higher cooling rates).

Table 7.1 : Computed weld pool radius r at different temperatures (with the effect of temperature variation on the ultrasound velocity eliminated) in the ultrasonic detection of titanium weld size

| Temperature (°C) | $D_w(T)$, mm | D(T), mm | r, mm |
|---|---|---|---|
| 100 | 78.6 | 80.0 | 1.4 |
| 200 | 79.2 | 80.3 | 1.2 |
| 300 | 79.8 | 80.8 | 1.0 |
| 400 | 80.5 | 81.7 | 1.1 |
| 500 | 81.3 | 82.5 | 1.2 |
| 600 | 81.7 | 83.2 | 1.4 |

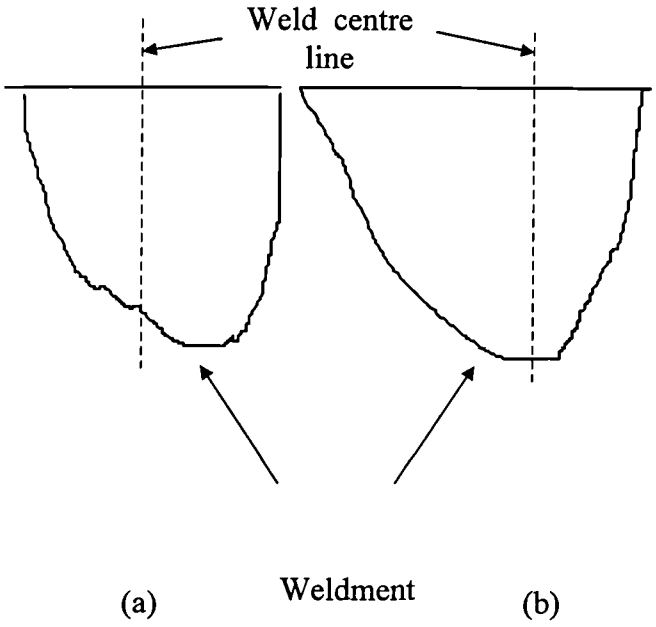


Figure 7.1(a,b) : Sketch of alignment of weld bead relative to the weld centre line

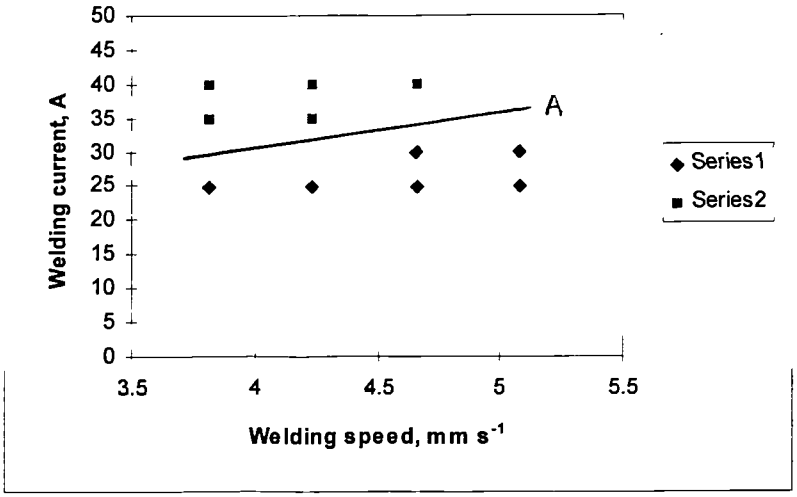


Figure 7.2 Effect of welding parameters on quality of welds for 1.0 mm thick IMI 130 (group II specimens, 5108 to 5123)
(series 1, lack of penetration; series 2, excessive penetration)

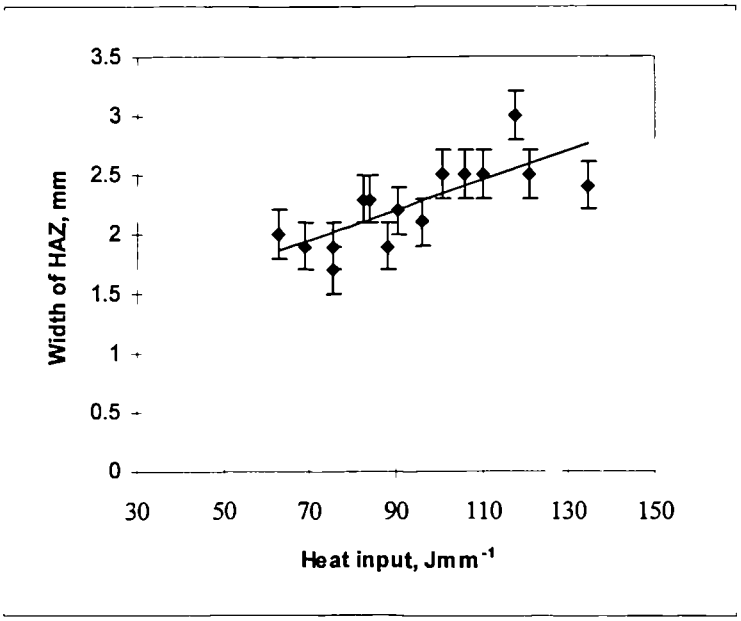


Figure 7.3 Width of HAZ versus heat input rate for 1.0 mm thick IMI 130 welded specimens (**all** specimens in group II, 5108 to 5123)

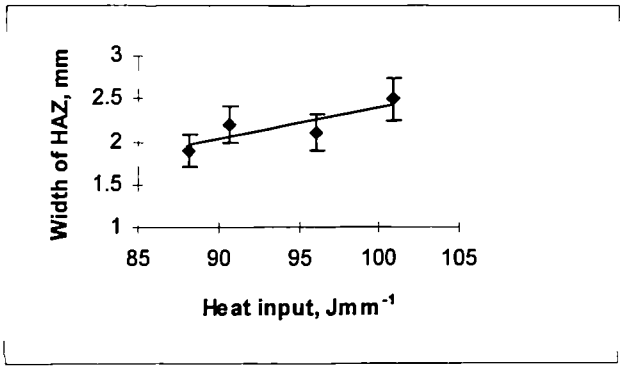


Figure 7.4 Width of HAZ versus heat input rate for 1.0 mm thick IMI 130 welded specimens (**only specimens with acceptable penetration** in group II, 5108 to 5123)

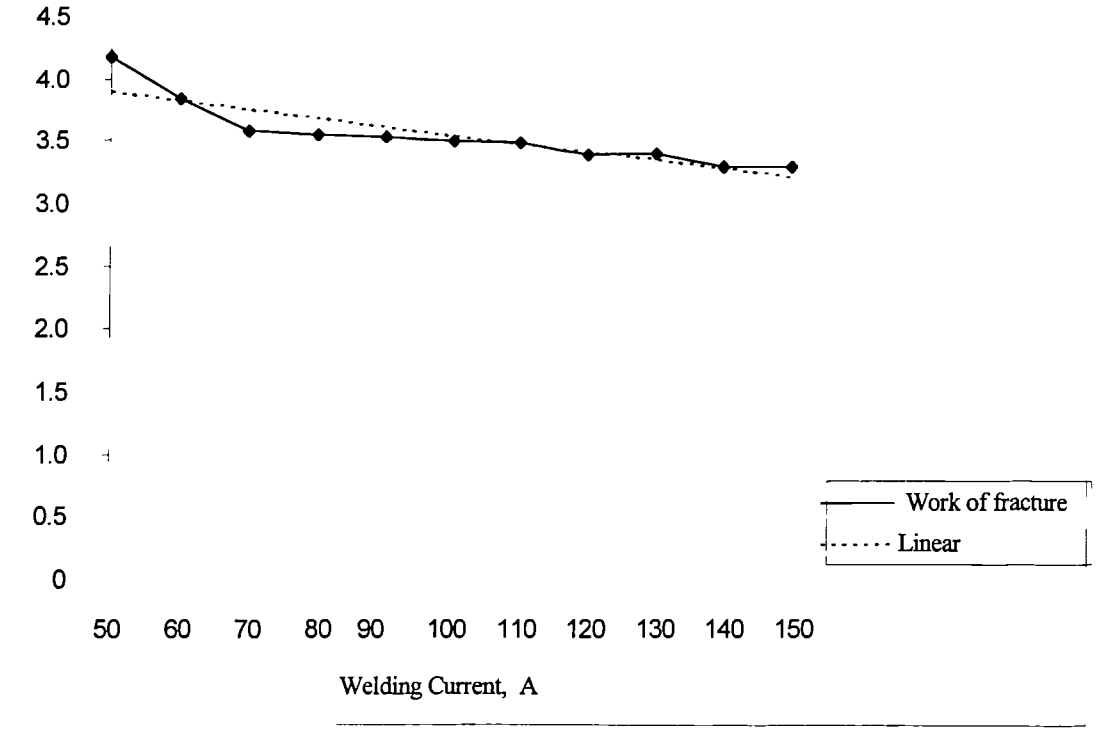


Figure 7.5 Work of fracture versus welding current for 2.3 mm thick IMI 130 welded specimens (group III specimens 5201 to 5211)

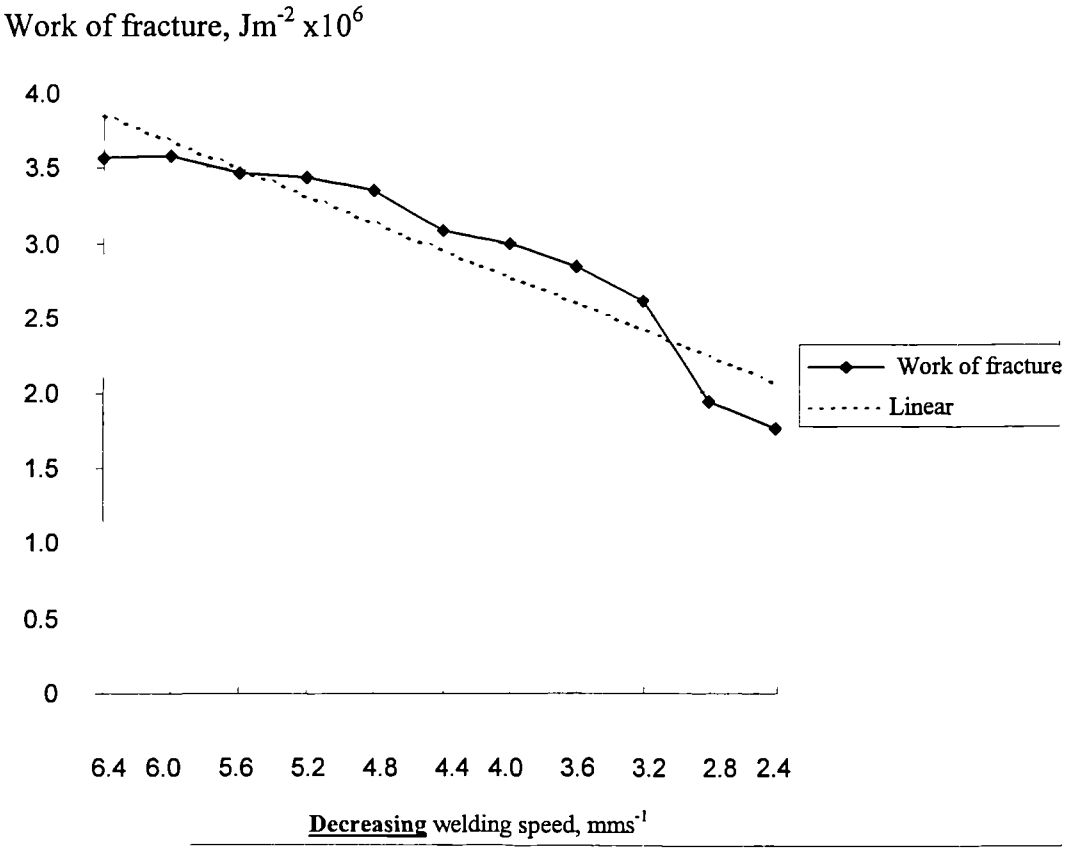


Figure 7.6 Work of fracture versus welding speed for 2.3 mm thick IMI 130 welded specimens (group IV specimens 5212 to 5222)

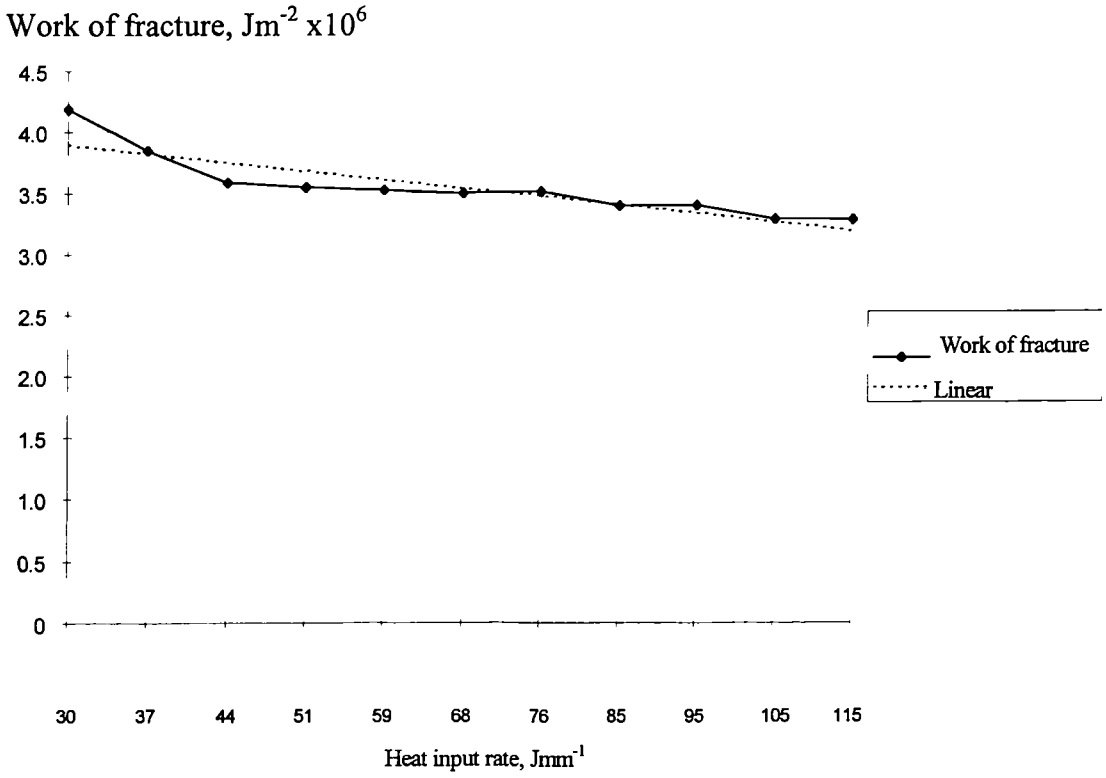


Figure 7.7 Work of fracture versus heat input rate for 2.3 mm thick IMI 130 welded specimens (group III specimens 5201 to 5211)

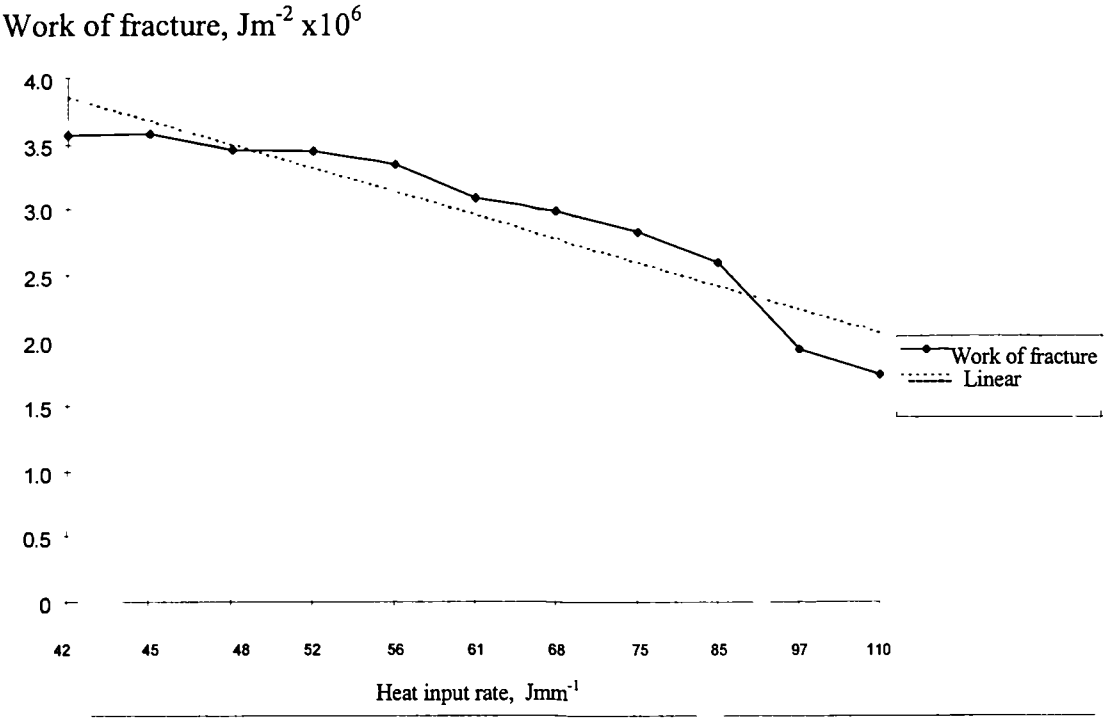


Figure 7.8. Work of fracture versus heat input rate for 2.3 mm thick IMI 130 welded specimens (group IV specimens 5212 to 5222)

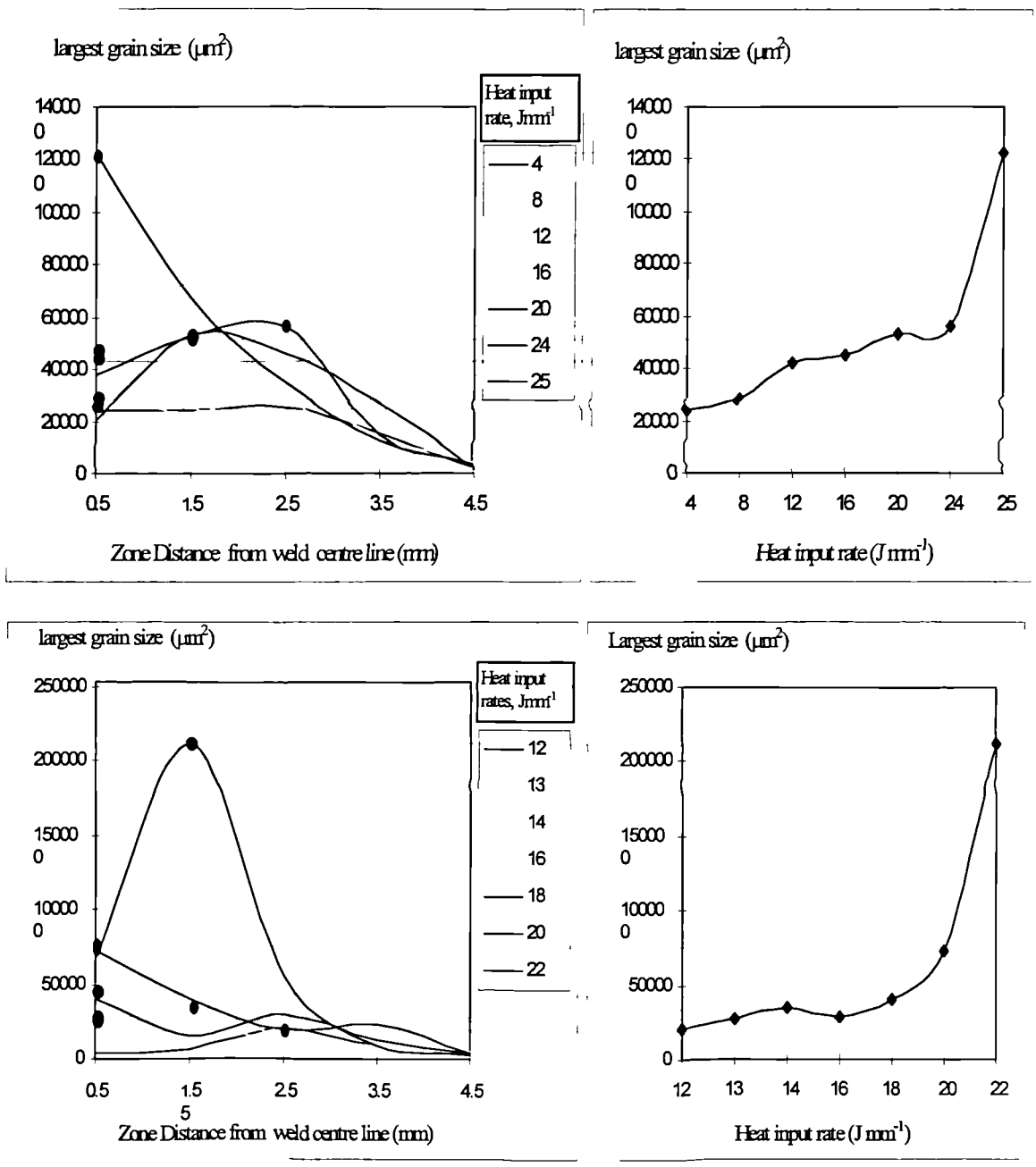


Figure 7.9 : Largest grain size versus heat input rate for 1.0 mm thick IMI 318 welded specimens (upper graphs : specimens 6124 to 6130 at a fixed welding speed of 42 $mms^{-1}$; lower graphs : specimens 6131 to 6137 at a fixed welding current of 80 A)

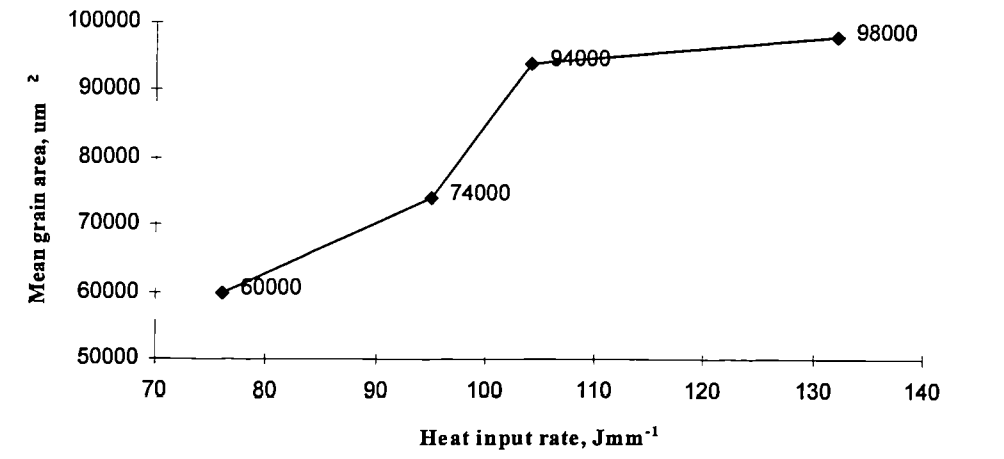


Figure 7.10 : Largest mean grain area versus heat input rate for 2.7 mm thick IMI 318 welded specimens with varying welding current and at a fixed *welding speed of 4.2 mms$^{-1}$ (specimens 6138 to 6141)*

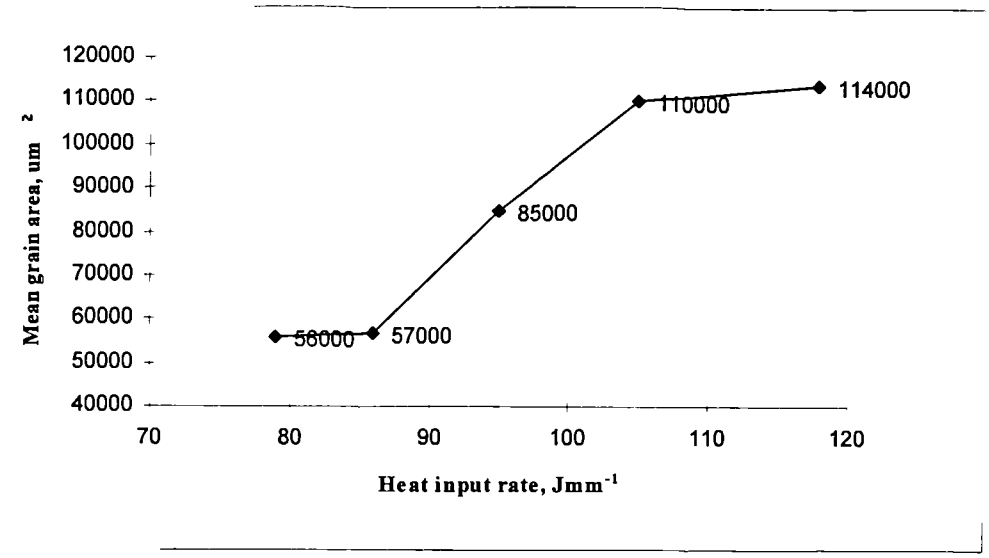


Figure 7.11 : Largest mean grain area versus heat input rate for 2.7 mm thick IMI 318 welded specimens with varying welding speed and at a fixed welding current of 100 A (specimens 6142 to 6146)

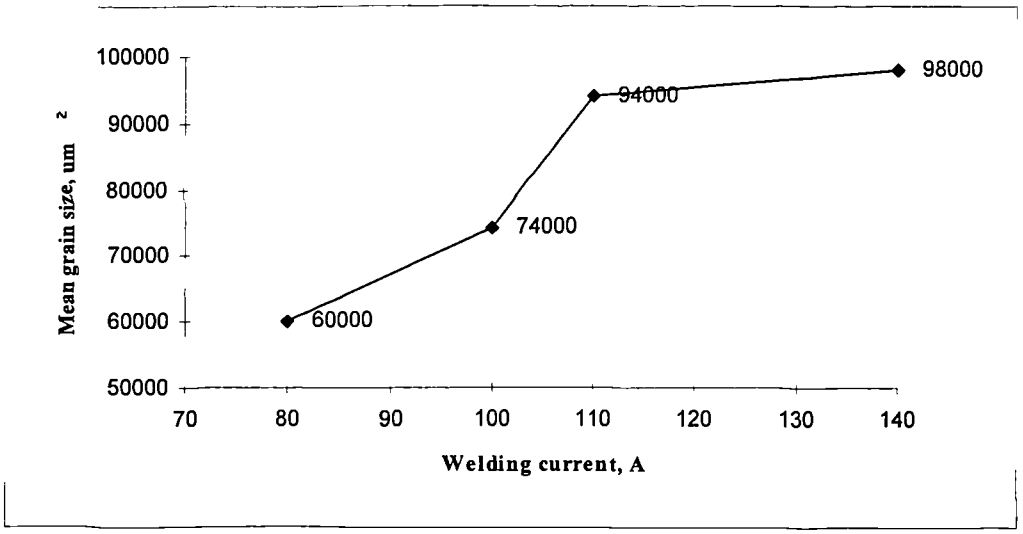


Figure 7.12 : Largest mean grain area versus welding current for 2.7 mm thick IMI 318 welded specimens at a fixed welding speed of 4.2 $mms^{-1}$ (specimens 6138 *to* 6141)

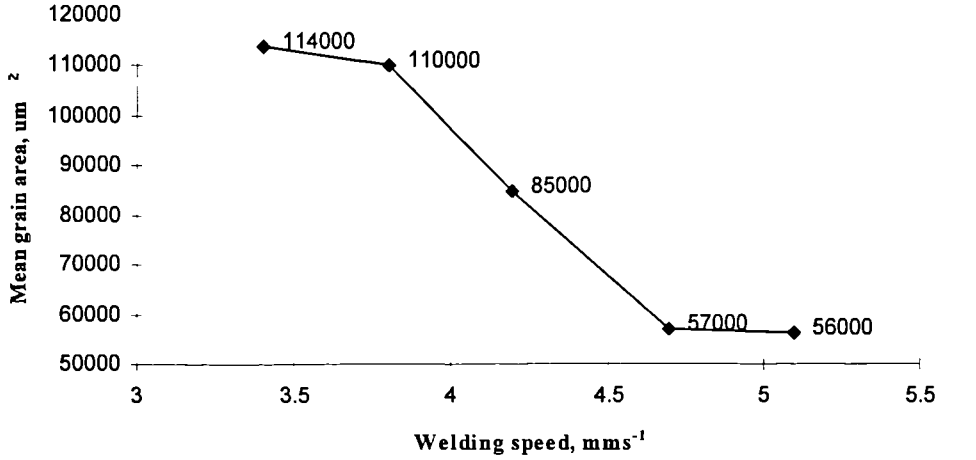


Figure 7.13 : Largest mean grain area versus welding speed for 2.7 mm thick IMI 318 welded specimens at a fixed welding current of 100 A (specimens 6142 to 6146)

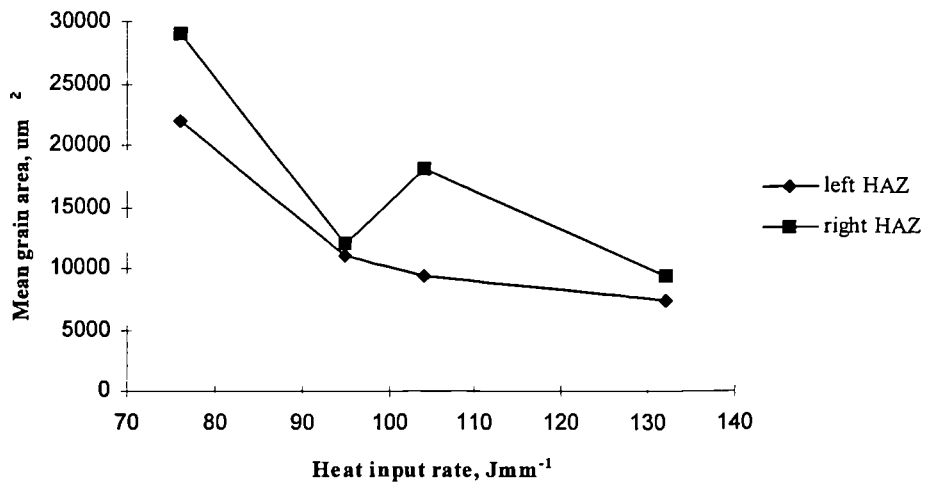


Figure 7.14 : Mean grain area in HAZ (at 3 mm on both sides of FZ) versus heat input rate for 2.7 mm thick IMI 318 welded specimens with varying welding current and at a fixed welding speed of 4.2 $mms^{-1}$ (specimens 6138 to 6141)

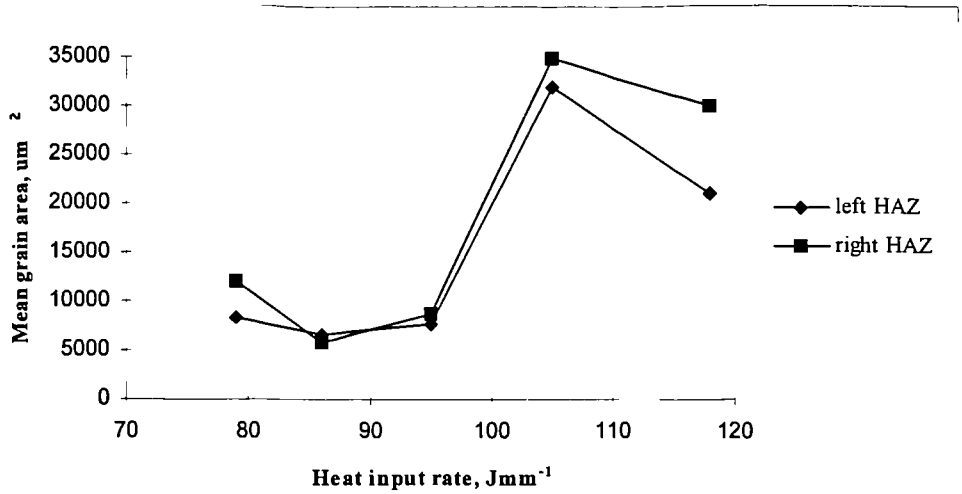


Figure 7.15 : Mean grain area in HAZ (at 3 mm on both sides of FZ) versus heat input rate for 2.7 mm thick IMI 318 welded specimens with varying welding speed and at a welding current of 100 A (specimens 6142 to 6146)

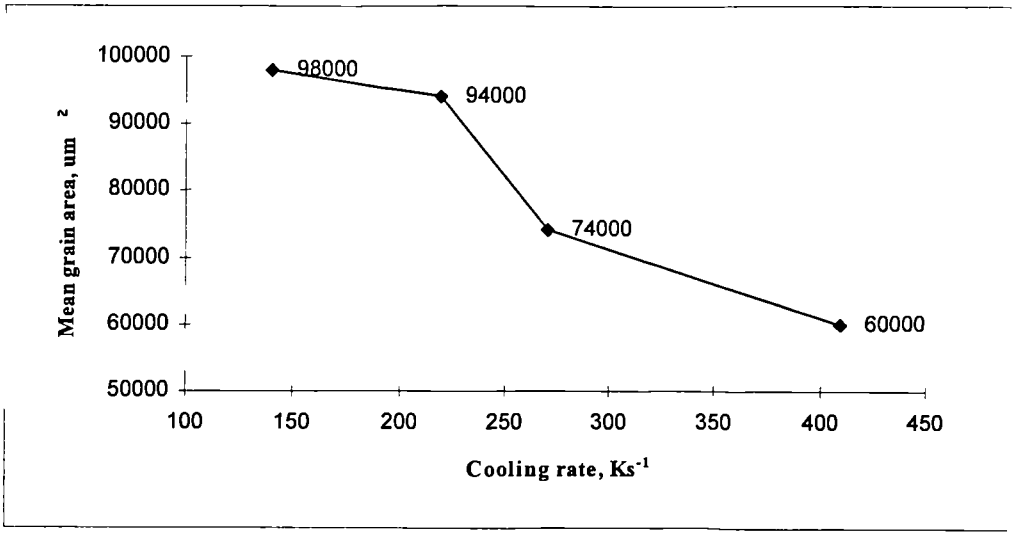


Figure 7.16 : Largest mean grain area versus cooling rate for 2.7 mm thick IMI 318 welded specimens with varying welding current and at a fixed welding speed of 4.2 $mms^{-1}$ (specimens 6138 to 6141)

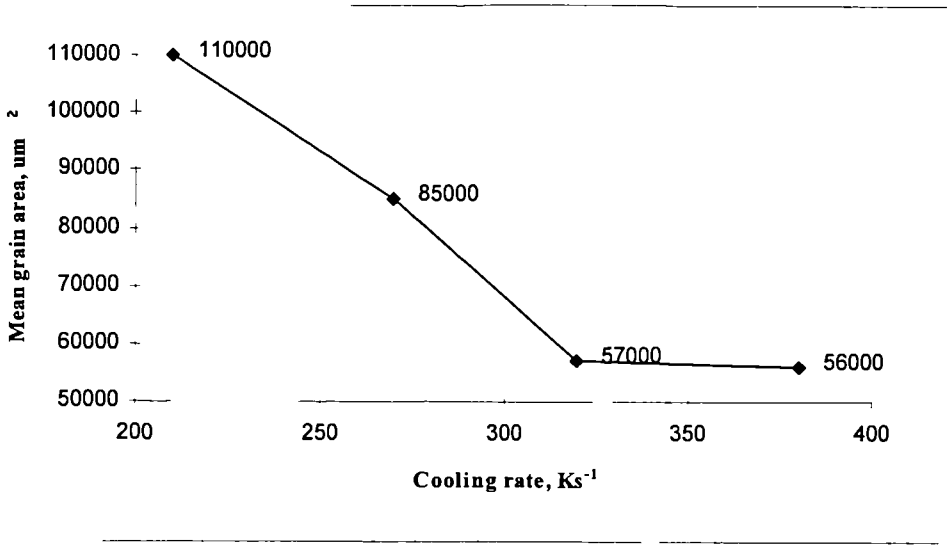


Figure 7.17 : Largest mean grain area versus cooling rate for 2.7 mm thick IMI 318 welded specimens with varying welding speed and at a welding current of 100 A (specimens 6142 to 6146)

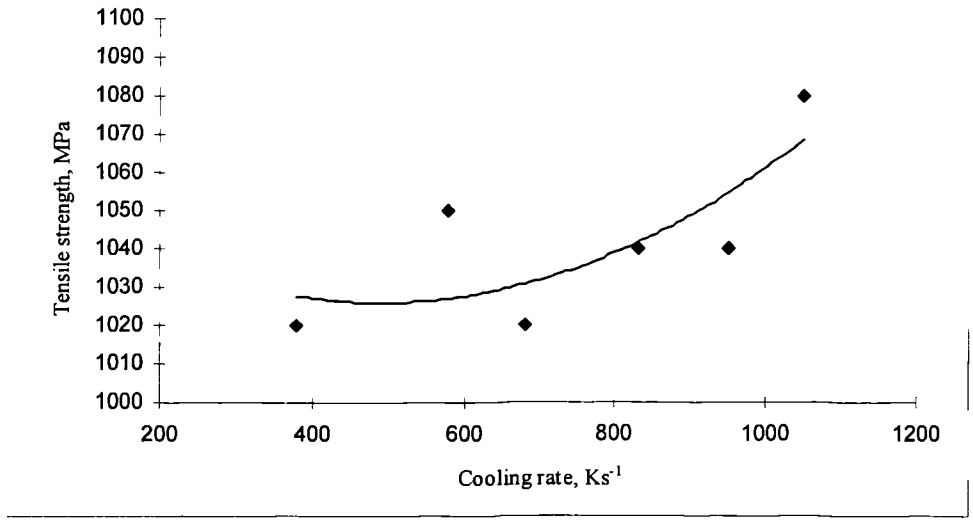


Figure 7.18 : Tensile strength versus cooling rate (at 1595 °C, the β transus) for 1.5 mm thick IMI 318 welded specimens (specimens 6309 to 6314)

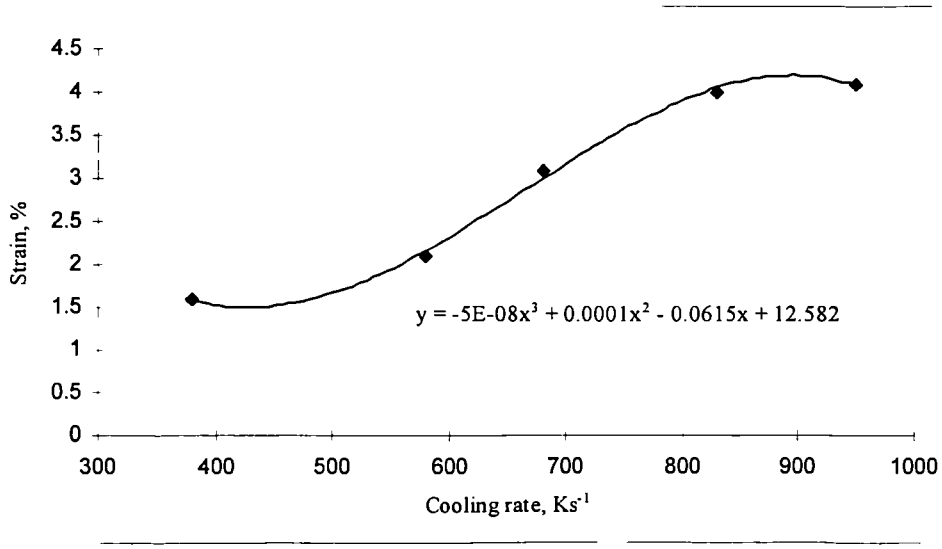


Figure 7.19 : Strain to failure versus cooling rate (at 1595 °C, the β transus) for 1.5 mm thick IMI 318 welded specimens (specimens 6309 to 6314)

## 8.0 CONCLUSIONS

In the present study, some of the important controlling factors and parameters in welding CP grade titanium and IMI 318 thin-plate were investigated. This not only provided a better understanding on the qualification of titanium welds, but also provided a useful database for the control of the TIG welding process in real time so as to produce welds with both desirable weld geometry, grain size and mechanical properties. This was achieved by the development of a closed-loop adaptive control system which employed hardware, software and a knowledge-based algorithm. The adaptive control was made in real time after the ultrasonic response of titanium at elevated temperatures was studied.

The result of the current work also gave confidence in improving the mechanical properties of welds in IMI 318 by controlling the heat input per unit length and cooling rate in the as-welded condition, without resorting to more complicated post-weld heat treatments. The following conclusions have been made on the basis of the work presented in this thesis, and these are :

8.1 (a) A closed-loop adaptive control system was developed which took the signals from the ultrasonic sensors and converted them into a form which was used for feedback control of the welding machine. An algorithm was written to relate the ultrasonic signal to the penetration depth of the weld. The difference between the "detected" penetration depth was compared with the required depth to give a regulating signal to the welding machine. The calculations and the approximations were carried out by a program written in C language.

(b) The control and adjustment of the welding parameters, e.g. welding speed, were enabled by building a hardware control circuit which took in the aforesaid regulating signal and converted it to a driving signal to change the speed of the welding torch. On the other hand, a process control data base was built up using software and a knowledge-based system for acceptable welding parameters which were determined by acceptable penetration depth, grain size and mechanical properties. The relationships between these three factors and welding parameters were determined in the experiments. A schematic diagram showing the flow of the closed-loop adaptive control system is presented in Figure 8.1

8.2(a) It was found that by using conventional shear waves, information related to the grain size around the weld's FZ boundary and the geometry of the weld bead could be made known. In particular, the alignment as well as the symmetry of the pool about the weld line was indicated.

(b) Also, it was found that the relative grain sizes around the weld's FZ, resulting from different welding parameters and heat input rates, could be indicated by their corresponding ultrasonic attenuation (A). The relationships indicated that both the welding current and heat input rate changed positively with $A^{2/3}$.

8.3(a) The travelling time of ultrasonic shear waves was found to change linearly with the temperature and the ultrasound velocity changed inversely with the temperature. Also, the *square of temperature affected the rate of change of* ultrasound velocity.

(b) The weld pool radii determined by ultrasonic means appeared to be smaller than the actual measured radius due to the temperature effect on the ultrasound velocity and the presence of the altered microstructure within the HAZ. A compensation factor was introduced which would be useful when a large data base has been developed.

8.4(a) In the TIG welding of CP grade titanium, it was found that for the same material, the optimum range of heat input was higher in the case with back shielding gas than that without the gas. Moreover, in the case with back shielding gas, a wider spectrum of welding parameters could be used to produce welds with good penetration. This proved that welding with back shielding gas was more controllable.

(b) There exists a positive relationship between the heat input rate and the width of the HAZ on CP grade titanium welds. This relationship was valid regardless of whether the penetration of the welds was sufficient. Also, if only specimens with acceptable penetration were included, a clear linear relationship was evident.

(c) Considering the fracture toughness of CP grade titanium weld, it was found that the fracture toughness of the weld decreased with higher heat input rate. This was ascribed to the grain growth which was affected by the temperature gradient. When the heat input rate was increased, the temperature gradient (G) was decreased and thus $G/S_R$ (where $S_R$ is the rate of advance of the solidification front) ratio was reduced. The lower the $G/S_R$ ratio, the coarser the subgrain structure of the weldment.

8.5(a) On the TIG welding of IMI 318, not much change was found in the size of the HAZ regardless of changes in the welding current and speed. The increase of weld size was solely due to the increase of FZ width. The weld penetration varied positively (almost linearly) with the welding current as well as the heat input rate.

(b) In the study of the relationship between grain size and welding parameters, in the HAZ, the average grain size was found to be larger for larger welding currents and heat input rates. On the other hand, a change in welding speed did not result in a significant change in grain size in the whole HAZ zone. In the FZ, the maximum grain size was affected by and varied positively with the heat input rate. The highest heat input rate (induced by either the highest welding current or the lowest welding speed) resulted in the largest grain size and exhibited the most variation across the FZ. However, the effect of change in the welding speed on the FZ grain size was much more than that obtained by changes in the welding current. This proved that the cooling rate (determined by the welding speed) and solidification mechanism are determining factors on grain size. In fact, it was found that the lower the cooling rate the larger the grain size appeared.

(c) The hardness of IMI 318 welds was found to be almost inversely proportional to the welding current and directly proportional to welding speed. For IMI 318 plates of 3.0 mm thickness, using a welding current of 180 A and welding speed of 5.1 $mms^{-1}$, welds with hardness comparable to the parent metal could be produced.

(d) The tensile strength decreased with the increase of current and heat input rate. This was explained in the light of the Hall-Petch relationship. The yield strength decreased with an increase of grain size due to the fact that the prior β grains and the needle-like α phase precipitates both became coarser during cooling. By contrast, the tensile strength decreased with the decrease of the welding speed. As the welding speed decreased, the ductility (in terms of the strain to failure and reduction in area) decreased with increase in martensite content since slip occurred less easily in the very fine martensite phase than in the α phase. It was also found that the lower the welding speed the coarser the cell structure would be and, the higher the risk of cracking by segregation and re-heating.

(e) For 1.5 mm thick IMI 318, welds with strengths comparable to the parent metal (only 3 to 6 % lower) were produced using a welding spectrum with welding currents between 110 and 235 A, welding speeds between 0.38 and 1.3 $mms^{-1}$, and pulse-on times between 0.3 and 0.5 s. A trend of increasing tensile strength of the weld with increase of cooling rate was observed. Also, it was found that the greater the cooling rate, the greater was the strain to failure and therefore the ductility. In fact, their relationship is predominantly a positive one. Some factors were identified or expected to be responsible for affecting the strength of the IMI 318 welds. Amongst these, the combined effect of finer α platelets and larger proportion of α' contribute to the higher strength of the weld metal at lower heat input rates (or higher cooling rates).

# 9.0 SUGGESTIONS FOR FURTHER WORK

(I) Ultrasonic data on IMI 318 up to melting point

As mentioned in section 2.5.4, to allow real-time control and monitoring of the weld quality, the correction to the beam path length (or time-of-flight) due to changes in velocity needs to be found at various temperatures. Therefore, there is a need to investigate the change of ultrasonic velocity with temperature up to the melting point of titanium alloys. However, due to the limitation of the present equipment and set-up, the carbolite furnace can only go up to a temperature of 600 °C, beyond which the increase of temperature becomes uncontrollable. Therefore, one suggestion is to acquire a controlled heating medium with a temperature range up to 2000 °C to continue to produce the necessary data for the titanium alloy IMI 318.

(II) Effect of other parameters on the ultrasonic detection of the weld pool diameter

In section 7.3, it was found that the weld pool diameter, detected by ultrasonic means, could be compensated for by a factor. However, this factor might also depend on other parameters which were outside the scope of the work in this thesis. Examples of these parameters are the frequency of the ultrasonic probe used, the insulation between the hot and cold zones around the furnace, the cooling channel (refer to Figure 4.6) and its associated cooling rate etc. It is suggested that these parameters should be studied independently to reveal any effect on the ultrasound velocity in IMI 318.

(III) Signal processing technique for small ultrasonic signals

As discussed in section 7.2, for most of the specimens, it was necessary to set the gain level at 110 dB to boost the ultrasonic signals received with noticeable amplitude and enable them to be displayed on the ultrasonicscope. If the ultrasonic signals reflected from liquid/solid interfaces of the molten weld pool are particularly small, it is suggested that there is a need to use a much more sophisticated signal processing technique for the detection and analysis of the data. The development of such techniques remains to be done.

(IV) Fast-response system in the case of lower cooling rate

If the investigations of the present study are to be extended to a much higher cooling rate (by altering the welding parameters), the response time of the hardware and software (including the algorithm and the knowledge-based system) in chapter 3 may not be fast enough to process the data and signals since the weld pool freezes more quickly. This would require increased response of various components within the system. It would need a welding power source with a faster response and redesigned computer interfacing.

(V) The feasibility of controlling weld bead cooling rate in real time

As cooling rate was proven in sections 7.4 and 7.5 to be one of the determining factors for weld penetration, grain size and mechanical properties, alternative methods to measure the cooling rate in real time may be useful. One suggestion is to employ an infra-red camera in a manner similar to that described by Lukens and Morris (1982), and a direct close-loop control of the cooling rate with the error in cooling rate being used to signify the required change in weld bead heat input. This then needs to be incorporated into the present control system.

(VI) Complex weld geometries

For welding geometries more complex than the autogenous weld bead on stationary flat thin-plate considered in this thesis, a more detailed knowledge of the effects of temperature gradients on wave propagation will be necessary.

(VII) Study of fracture toughness on IMI 318

Metallurgical and materials engineers are often called on to design titanium alloys having high strengths yet with some ductility. Therefore, a significant amount of work in this thesis was devoted to the understanding and control of the strength and the tensile properties of IMI 318. However, fracture toughness is another property that determines the usefulness of the alloy in industry. In fact, aerospace requirements call for increased tensile strength above that of IMI 318 while still maintaining good fracture toughness. Although investigations of fracture toughness were conducted on CP grade titanium in section 7.4, it is suggested extending the same study on thin-plate IMI 318, particularly on the relationship between the $K_{IC}$ value and the welding parameters in the as-welded condition.

(VIII) Other techniques to improve mechanical properties in the as-weld condition

As one of the objectives in this study is the qualification of IMI 318 TIG welds in the as-welded condition, one suggestion is to look into other techniques which may result in the improvement of mechanical properties in the as-welded condition. One potential area of study is to employ the bead-over-bead (B-o-B) technique in single-pass TIG welding of thin plates. In fact, Radhakrishna and co-workers (1996) have reported the successful application of a bead-over-bead technique on electron-beam welded IMI 318 plates of 5 mm thickness to improve the toughness of the welds. It will be sensible to investigate the application of this technique to TIG welded IMI 318 thin plate.

**References**


Adams, C. M. Jr., "Cooling rate and peak temperatures in fusion welding", *Welding Journal*, Vol. 37, (5), 1958, pp. 210s-215s.

Ahmady, S.M.H., "Solidification, structure and mechanical properties of A357 aluminum alloy", *Ph.D Thesis* (D82530), Southampton University, 1987.

Ahmed, N. and Lucas, W., "Penetration control in TIG welding - development of a hard-wired control unit", *Research report 411*, The Welding Institute, UK. 1990.

Alleyne, D.N. and Cawley, P., "Optimization of Lamb Wave Inspection Techniques", *Non-Destructive Testing & Evaluation International.*, 25, (1), 1992, pp. 11-22.

Baeslack, W.A.III, "Grain-Boundary Deformation Behaviour in a Metastable Beta-Titanium Alloy", *Metallography*, (13), 1982, pp. 277-281.

Baeslack, W.A.III and Banas, C.M., "A Comparative Evaluation of Laser and Gas Tungsten Arc Weldments in High-Temperature Titanium Alloys", *Welding Journal*, 60 (7), 1981, 121s-130s.

Baeslack, W.A.III, Davis, J.R. and Cross, C.E., "Selection and weldability of conventional titanium alloys", *ASM handbook, Vol. 6*, Welding, Brazing and Soldering, ASM International, USA, 1993, pp. 507-523.

Baeslack, W.A.III and Mullins, F. D., "Cooling rate effects in Ti-6Al-2Sn-4Zr-2Mo weldments", *Metallurgical Transaction A*, Vol. 15A, 1984, pp. 1948-1952.

Banas, C.M., "Electron Beam, Laser Beam and Plasma Arc Welding Studies", *NASA Report CR-132386*, NASA Langley Research Center, March 1974.

Barrett, J.C., "Effect of atmospheric contaminants on arc welds in titanium", *Welding Journal*, 33 (3), 1954, pp. 121s-128s.

Barrett, J.C. and Lane, I.R., "Effect of atmospheric contaminants on arc welds in titanium", *Welding Research Supplement*, March 1954, pp. 121s-129s.

Beachem, C.D., *Hydrogen damage*, ASM, Metals Park, OH, USA, 1977.

Becker, D.W. and Adams, C.M. Jr., "The role of pulsed GTA welding variables in solidification and grain refinement", *Welding Journal*, 58 (5), 1979, pp. 143s-152s.

Becker, D.W., Messler, R.W. and Baeslack, W.A., "Titanium welding - a critical review", *Titanium Welding*, USA, 1992, pp. 255-275.

Beevers, C.J., Warren, M.R. and Edmonds, D.V., *Journal of Less-common Metals*, 14, 1968, pp. 387-396.

Belov, A.F. and Polkin, I.S., *German metallurgical society workshop*, University of Nuremberg, Erlangen, July 12, 1982.

Bentley, A.E. and Marburger, S.J., "Arc welding penetration control using quantitative feedback theory", *Welding Journal*, 71 (11), Nov 1992, pp. 397s-405s.

Berry, J.P., *Journal of Mechanics, Physics and Solids*, (8), 1960, pp. 194-207.

Borggreen, K. and Wilson, I., "Use of postweld heat treatment to improve ductility in thin sheets of Ti-6Al-4V", *Welding Journal*, 59 (1), 1980, pp. 1s-9s.

Broderick, T.F., Jackson, A.J., Jones, H. and Froes, F.H., "The effect of cooling conditions on the microstructure of rapidly solidified Ti-6Al-4V", *Metallurgical Transactions A*, v16A, (11), 1985, p1951-1958.

Bromage, K., "Arc efficiency and heat flow in inert-gas welds", *British Welding Journal*, 15 (9), 1968, pp. 493-500.

Brooks, C.R., *Heat Treatment, Structure and properties of nonferrous alloys*, ASM International, USA, 1982.

Bull, C.E., Stacey, K.A. and Calcraft, R., "On-line weld monitoring using ultrasonics", *British Journal of NDT*, 35 (2), 1993, pp. 57-64.

Charlotte W., *Welding Handbook, 7th edition, Volume 1*, American Welding Society, USA, 1981.

Chen, S.J. and Devletian, J.H., "Microstructure and mechanical properties of electroslag welds in Ti-6Al-4V alloy", *Welding Journal*, v69, (9), 1990, p319s-324s.

Chesnutt, J.C., Rhodes, C.G. and Williams, J.C., "Relationship between mechanical properties, microstructures, and fracture topography in alpha + beta titanium alloys", *Fractograph-Microscopic Cracking Processes, ASTM STP 600*, 1976, p. 99-138.

Christensen, N., Davies, V.L. and Gjermundsen, K., "Distribution of Temperatures in Arc Welding", *British Welding Journal.*, 12, 1965, pp. 54-74.

Clarke, C.F., Hardie, D. and Ikdea, B.M., "The effect of hydrogen content on the failure of pre-cracked titanium specimens", *Corrosion Science*, 36, (3), 1994, p487-509.

Cole, P.T., "The generation and reception of ultrasonic surface waves in mild steel at high temperatures", *Ultrasonics*, 16, July 1978, pp. 151-155.

Conrad, H., *Acta Metallurgica et Materialia,* 14, 1966, pp. 1631-1632.

Conrad, H., Keshavan, M.K. and Sargent, G.A., *Proceedings of Second International Conference on Mechanical behavior of materials*, ASM, OH, USA, 1978, pp. 538-568.

Cook, E.G. and Valkenburg, H.E., "Surface Waves at Ultrasonic Frequencies", *American Society for Testing of Materials Bulletin.*, (198), 1954, pp. 81-84.

Cornu, J., *TIG and Related Processes : Advance Welding Systems*, *Volume 3*, IFS publication, 1988.

Costa, S.C. and Norrish, J., "Computer prediction of welding defects at the procedure stage", *Welding and Metal Fabrication*, 59 (5), May 1991, pp. 186-190.

Covington, L.C., *Corrosion*, 35, 1979, pp. 378-382.

Davidge, R.W. and Tappin, G., "The effective surface energy of brittle materials", *Journal of Materials Science*, (3), 1968, pp. 165-173.

Davidson, D.L. and Campbell, J.B., "Fatigue Crack Growth through the Lamellar Microstructure of an Alloy Based on TiAl at 25 °C and 800 °C ", *Metallurgical Transaction A*, (24), 1993, pp. 1555-1574.

Donachie, M.J., *Metals Handbook* (Desk Edition), Chapter 9 on titanium, American Society for Metals, 1985.

Donachie, M.J., *Titanium : A technical guide*, Metals Park, OH, USA, American Society for Metals, 1988.

Duffill, C., Haywood, G., Scruby, B. and Stares, J., "On-line assessment of weld quality using ultrasonics", *Harwell Report AERE 13401*, USA, 1989.

Duncan, R.M., and Hanson, B.H., *The selection and use of titanium,* Oxford University Press, 1980.

Easterling, K.E. *Introduction to the Physical Metallurgy of Welding, 2nd edition.* Oxford, U.K. : Butterworth Heinemann Ltd., 1992.

Enjo, T., Kuroda, T. and Nishizawa, M., "Microstructure and mechanical properties in weld heat-affected zone of titanium alloy", *Transaction of JWRI* , 17 (2), 1988, p.113-118.

Erokhin, A.A. and Oboturov, V.I., "Role of surface contaminants on formation of pores during welding of titanium", Svar Proizv, 1971 (8), p. 57-59.

Fan, Z. and Miodownik, A.P., "On the fracture toughness of Alpha-Beta titanium", *Journal of Material Science Letters*, 12 (21), 1993, pp. 1665-1668.

Fenn, R., "Monitoring and controlling welding by ultrasonic means", *British Journal of Non-Destructive Testing*, 31 (2), 1989, pp. 82-86.

Fenn, R. and Stroud, R.R., "The Measurement and Control of Penetration during Submerged-Arc Welding", Paper 5, *International Conference on Offshore Structures, The Welding Institute, London*, 1982 pp. 5-1 to 5-5.

Fenn, R. and Stroud, R.R., "Microcomputer control of weld penetration", *Proceedings of Conference of Computers in Welding Research*, Australian Welding Society, Paper #3, Sydney, 1983, pp. 10-14.

Fenn, R. and Wooton, J.J., "Longitudinal ultrasonic wave velocity and attenuation dependence on temperature between 20 to 1374 degree C.", *Nondestructive Testing Communications*, Vol. 2, 1986, pp. 115-126.

Firestone, F.A., "Tricks with supersonic reflectoscope", *Non-Destructive Testing*, 7, 1948, pp. 5-19.

Frolov, V.A., Mamaev, V.S., Bronin, N.S. and Volkov, P.G., "Light beam welding thin sheets of titanium alloys", *Welding International*, 8 (1), 1994, pp. 41-42.

Fromm, E., *Physical Chemistry*, NF, 147, 1986, pp. 611-75.

Fuerschbach, P.W. and Knorovsky, G.A., "A study of melting efficiency in plasma arc and gas tungsten arc welding", *Welding Journal*, 70 (11), 1991, pp. 287s-297s.

George, E., *Welding Metallurgy - Carbon and alloy steels, Vol. 1*, 3rd Edition, 1965, p. 180.

Giedt, W.H., Tallerico, L.N. and Fuerschiback, "GTA welding efficiency, calorimetric and temperature field measurements", *Welding Journal*, 68 (1), 1989, pp. 28s-32s.

Gittos, M.F. and Scott, M.H., "Effect of contamination by air on the TIG welding of commercially pure titanium sheet", *Titanium '92 Science and Technology*, TMS publication, 1993, (1), pp. 601.

Goldak, J., Bibby, M., Moore, J., House, R. and Patel, B., "Computer Modeling of Heat Flow in Welds". *Metals Transactions B*, 17B (3), 1986, pp. 587-600.

Green, R.E., "Effect of metallic microstructure on ultrasonic attenuation", *Nondestructive Evaluation*, 1981, pp. 115-132.

Greenfield, M.A. and Duvall, D.S., "Welding of an advanced high strength titanium alloy", *Welding Journal*, v54, (3), 1975, pp. 73s-80s.

Greenfield, M.A. and Pierce, C.M., "Postweld Aging of a Metastable Beta Titanium Alloy", *Welding Journal*, 52(11), Nov.1973, Research Supplement, pp. 524s- 527s.

Greenfield, M.A., Pierce, C.M. and Hall, J.A., "The effect of microstructure on the control of mechanical properties in alpha-beta titanium alloys", *Titanium Science and Technology*, vol. 3, 1972, p.1731-1743.

Grist, F.J., "Improved, lower cost aluminum welding with solid state power source", *Welding Journal*, 54 (5), 1975, pp. 348-357.

Gurevich, S.M., Zamkov, V.N. and Prilutsky, V.P., "The formation of weld porosity when fusion welding titanium", *Svar Priozv*, 1968 (12), pp. 19-22.

Hallum, D.L. and Baeslack, W.A.III, "Nature of grain refinement in titanium alloy welds by micro-cooler inoculation", *Welding Journal*, 69 (9), 1990, pp. 326s-336s.

Hatch, W., "Development of welding practices for titanium alloy 8Mo-8V-2Fe-3Al", *Technical report to army materials and mechanics research agency*, Watertown, Ma., AMMRC PTR-73-4, March 1973.

Hecht, A., Thiel, R., Neumann and Mundry, E., "Nondestructive Determination of Grain Size in Austenitic Sheet by Ultrasonic Backscattering", *Material Evaluation*, 39, (1981) pp. 934-938.

Heiple, C.R. and Roper, J.R., " Mechanism for minor element effect on GTA fusion zone geometry", *Welding Journal*, 61 (4), 1982, pp. 97s-102s.

Hess, W.F., Merrill, L.L. Nippes, E.F. and Bunk, A.P., "The Measurement of Cooling Rates Associated with Arc Welding and their Application to the Selection of Optimum Welding Conditions". *Welding Journal*, 22 (9), 1943, pp. 377s-422s.

Hinata, T., Yasuda, K., Kasuga, K. and Onzawa, T., "Study of penetration using a stationary TIG arc : Low-speed DC-TIG welding", *Welding International*, 7 (3), 1993, pp. 189-194.

Inoue, H. and Ogawa, T., "Effect of Weld Cooling Rate on the Microstructure and Properties of Ti-6Al-4V Weldment", *Nippon Steel Corporation*, Sagamihara, Japan, 1989.

Jaffee, R.I. and Campbell, I.E., *Transaction of AIME*, 185, 1949, pp. 646-654.

James, A.W. and Bowen, P., "Elevated temperature crack growth resistance of TiAl under monotonic and cyclic loading", *Material Science Engineering A*, (153), 1992, pp. 486-492.

James, A.W., Chave, R.A., Hippsley, C.A. and Bowen, P., *Journal of Physics*, (3), 1993, pp. 411-421.

Jhaveri, P., Moffatt, W.G. and Adams C.M., Jr., "The Effect of Plate Thickness and Radiation on Heat Flow in Welding and Cutting". *Welding Journal*, 41 (1), 1962, pp. 12s-16s.

Johnson, J.A., Carlson, N.M., Bolstad, J.O., Smartt, H.B., Ward, M.B., Allemeier, R.T., Lott, L.A. and Kunerth, D.C., "Automated Welding Process Sensing and Control", *Proceedings of Second International Symposium on the Nondestructive Characterisation of Materials*, 1986, pp. 409-417.

Kaufman, J.G., *Journal of Material Letters*, (8), 1967, p. 889.

Kessler, H.D., Sherman, R.G. and Sullivan, J.f., *Journal of Metals*, 7, 1955, pp. 242-246.

Kivineva, E., Hannerz, N. and Sjoberg, R., "Microstructure of Ti-6Al-4V weld metal and simulated HAZ", *Proceedings of the International Conference on Off shore Mechanics and Arctic Engineering*, Vol. 3, ASME, NY, 1995, pp. 401-407.

Klinman, R. and Stephenson, E.T., "Relation between mechanical properties, grain size, and ultrasonic attenuation in plain carbon steel", *Metallurgical Transactions*, 11, 1980.

Kotfila, R.J. and Burte, H.M., "Hydrogen contamination in titanium and titanium alloys", *WADC Technical Report 54-616*, Wright-Patterson Air Force Base, OH, USA, 1955.

Kou, S., "Simulation of Heat Flow During the Welding of Thin Plates". *Metals Transactions A*, 12 (12), 1981, pp. 2025-2030.

Kou, S., *Welding Metallurgy*, Wiley, USA, 1987.

Kubiak, E.J. and Rowand, R.R., "Lamb Wave Inspection System for Thin-Sheet Metals", *6th International Conference on Non-Destructive Testing*, Report No. K5, 1970, pp. 47-57.

Kumpfert, J., Kim, Y.W. and Dimiduk, D.M., "Effect of microstructure on fatigue and tensile properties of the gamma TiAl alloy Ti-46.5Al-3.0Nb-2.1Cr-0.2W", *Material Science and Engineering A*, 192/193 (2), 1995, pp. 465-473.

Lampman, S., "Wrought Titanium and Titanium Alloys", *ASM Handbook, Vol. 2*, Ed. 10, Properties and Selection: Non-Ferrous alloys and special-purpose materials, ASM International, USA, 1990, 592-633.

Lancaster, J.F., "Welding arc physics", *Technical report of Welding Arc Research Committee*, Japan Welding Society, 1990, p. 311.

Lancaster, J.F., *Metallurgy of Welding*, 5th Edition, Chapman and Hall, U.K., 1993.

Lenning, G.A., Craighead, C.M. and Jaffee, R.I., *Transactions of AIME*, 200, 1954, pp. 367-376.

Levy, V. and Wickham, R., "Fusion welding unalloyed titanium sheet without filler rod.", *Welding Journal,* 34 (5), 1955, p413-419.

Lewis, R.E. and Wu, K.C., "A study of weld heat-affected zones in the titanium 6Al-6V-2Sn alloy", *Welding Journal*, 42 (6), 1963, 241s-249s.

Lewis, R.E., Caplan, I.L., and Coons, W.C., "the Elevated Temperature Ductility Dip Phenomenon in Alpha, Near-Alpha and Alpha-Beta Titanium Alloys," *Titanium Science and Technology : Proceedings of the Fifth International Conference on Titanium*, 1985, pp. 895.

Lin, F.S., Starke, E.A. Jr., Chakrabortty, S.B. and Gysler, A., "The effect of microstructure on the deformation modes and mechanical properties of Ti-6211 : part 1, Widmanstatten structures", *Metallurgy Transaction A*, (15), 1984, p.1229-1246.

Lott, L.A., "Ultrasonic detection of molten/solid interfaces of weld pools", *Material Evaluation*, (42), 1984, pp. 337-341.

Lott, L.A., Johnson, J.A., and Smartt, H.B., "Real-Time Ultrasonic Sensing of Arc Welding Processes", *Proceedings of Symposium on Nondestructive Evaluation Applications and Material Processing,* American Society for Metals, 1983, pp. 13-22.

Lott, L.A., Johnson, J.A. and Smartt, H.B., "Real-time ultrasonic sensing of arc welding processes", *Idaho Report EGG-M-05283*, USA, December 1984.

Lukens, W.E. and Morris, R.A., "Infrared Temperature Sensing of Cooling Rates for Arc Welding Control", *Welding Journal*, 61(1), Jan. 1982, pp. 27-33.

Mahajan, Y. and Baeslack, W.A.III, *Scripta Metallurgica et Materialia*, (13), 1979, pp. 1125-1129.

Mark, D.K. and Gauthier J., "Ultrasonic measurement of longitudinal and shear velocities of materials at elevated temperatures", *Ultrasonics*, 31 (4), 1993, pp. 245-249.

Martin, D. C., "Effects of carbon, oxygen and nitrogen on welds in titanium", *Welding Journal*, 32 (3), 1953, 139s-154s.

McCue, D and Irving, B., "Gas Tungsten Arc Welding : It's built to handle titanium", *Welding Journal*, Nov., 1991, pp. 31-36.

Metcalfe, J.C. and Quigley, M.B.C., "Arc and pool stability in GTA welding", *Welding Journal*, 56 (5), 1977, pp. 133s-139s.

Meyn, D.A., *Metallugical Transaction*, 5, 1974, pp. 2405-2414.

Mills, K., *Metals Handbook* (9th Edition), Volume 9 : Metallography and Microstructures, American Society for Metals, USA, 1985.

Misra, M.S., Olson, D.L. and Edwards, G.R., "The Influence of Process Parameters and Specific Additions on Epiaxial Growth in Multiple Pass Ti-6Al-4V Welds", *Grain Refinement in Castings and Welds*, TMS/AIME, Warrendale, PA, 1982.

Mitchell, D.R., "Porosity in titanium welds", *Welding Journal*, 44 (4), 1965, pp. 157s-167s.

Mitchell, D.R. and Feige, N.G., "Welding of Alpha-Beta Titanium Alloys in One Inch Plate", *Welding Journal*, 46 (5), 1967, pp. 193s - 202s.

Mitchell, D.R. and Tucker, T.J., "The properties and Transformation Characteristics of Welds in Ti-6Al-2Sn-4Zr-2Mo Titanium Alloys", *Welding Journal*, 48 (1), 1969, pp. 23s-33s.

Mohandas, T., Banerjee, D. and Mahajan, Y.R., "Studies on fusion zone fracture behaviour of electron beam welds of an $\alpha+\beta$ titanium alloy", *Journal of Materials Science*, 31, 1996, pp. 3769-3775.

Mohandas, T. and Reddy, G.M., "Effect of frequency of pulsing in gas tungsten arc welding on the microstructure and mechanical properties of titanium alloy welds : A technical note", *Journal of Materials Science Letters*, 15, 1996, pp. 626-628.

Morton, P.H., "The Contribution of Physical Metallurgy to Engineering Practice", *Rosenhain Centenary Conference*, The Royal Society, 1976.

Mukai, Kato, Nishio, Yoshida, Anzai and Yamada, "Effects of S and Al on penetration form in TIG welding", *Proceedings of 47th National Conference of Japan Welding Society*, 1990, p. 105.

Muncaster, P.W., *Practical TIG welding - A survey of the process and equipment*, Abington Publishing, Cambridge, UK, 1991.

Murthy, K.K. and Sundaresan, S., "Microstructure and tensile properties of the fusion zone in Ti-6Aal-4V weldments", *International Journal for the Joining of Materials*, 7 (4), 1995, pp. 129-135.

Nakayama, J., *Journal of American Ceramic Society*, (48), 1965, pp. 583.

Nippes, E.F., *Metal Handbook* (9th Edition) : Welding, Brazing and Soldering, American Society for Metals, USA, 1983.

Nippes, E.F., Merrill, L.L. and Savage, W.F., "Cooling rates in arc welds in 1/2 in. plate", *Welding Journal*, 28 (11), 1949, pp. 556s-564s.

Obata, Y., Morl, Y. and Aoki, K., *Proceedings of the 5th International Conference on Titanium*, Vol. 2, 1984, pp. 807.

Ogawa, T., Nagatani, T. and Inoue, H., "Effect of cooling rate on microstructure in weld metal of Ti-6Al-4V", *Transaction of the Iron and Steel institute*, 27, 1987, p. 66.

Ogden, H.R., Holden, F.C. and Jaffe, R.I., "Mechanical properties of Ti-Cr-Mo alloys as affected by grain size and grain shape", *Transactions of ASM*, 48, 1956, p. 627.

Ogilvy, J.A. and Temple, J.A.G., "Theoretical assessment of the errors involved in ultrasonic location and sizing of molten weld pools", *Ultrasonics*, 28 (11), 1990, pp. 375-381.

Okada, A., "Applications of melting efficiency and its problems", *Journal of the Japan Welding Society*, 46 (2), 1977, pp. 53-61.

Okazaki, K. and Conrad, H., *Transactions of Japan Institution of Metals*, 14, 1973, pp. 364-367.

Papadakis, E.P., Lynnworth, L.C., Fowler, K.A. and Carnevale, E.H., "Ultrasonic attenuation and velocity in hot specimens by the momentary contact method with pressure coupling, and some results on steel to 1200 °C", *Journal of the Acoustical Society of America*, 52 (3), Part II, 1972, pp. 850-857.

Parker, R.L., "Ultrasonic measurement of solid/liquid interface during solidification and melting of metals", *Proceedings of Physics in the Steel Industry Conference*, No. 84, 1982, pp. 254-271.

Parker, R.L., Manning, J.R. and Peterson, N.C., "Application of pulse-echo ultrasonic to locate the solid/liquid interface", *Journal of Applied Physics*, 58 (11), 1985, pp. 4150-4164.

Peters, M. and Williams, J.C., "Microstructure and mechanical properties of a welded (alpha + beta) Ti alloy", *Metallurgy Transaction A*, (15), 1984, pp. 1589-1596.

Pollard, B., "The effects of minor elements on the welding characteristics of stainless steel", *Welding Journal*, 67 (9), 1988, pp. 202s 213s.

Polmear, I.J., *Light Alloys-Metallurgy of the Light Metals*, Edward Arnold, London, 1995.

Prokhorov, N.N., *Welding Physics*, 1986 (9), pp. 30-32.

Pu, Z.J., Wu, K.H., Shi, J and Zou, D., "Effect of notches and microstructure on the fracture toughness of TiAl-based alloys", *Material Science and Engineering A*, A192/193 (2), 1995, pp. 347-355.

Radhakrishna, C., Reddy, J.R. and Rao, K.P., "Bead-Over-Bead Technique in Electron Beam Welding of Ti6Al4V", *Prakt. Metallogr.* 33 (12), 1996, pp. 618-628.

Redmond, J.D., *Metals Handbook* (Desk Edition), American Society for Metals, 1985, p. 15-2.

Richardson, R.W. and Ludewig, H.K., "The effect of weld parameter variations on pool oscillations in full-penetration welds", *Research report MR 8901*, Edison Welding Institute, USA, January 1989.

Rokhlin, S.I., Meng, S. and Adler, L., "In-process ultrasonic evaluation of spot welds", *Materials Evaluation*, 47, August 1989, pp. 935-943.

Rosenthal, D., "Mathematical Theory of Heat Distribution during Welding and Cutting" *Welding Journal*, 20 (5), 1941, pp. 220s-234s.

Rosenthal, D., "The Theory of Moving Source of Heat and its Application to Metal Treatments", *Transactions ASME*, (68), 1946, pp. 849-866.

Roth, W., "Scattering of ultrasonic radiation in polycrystalline metals", *Journal of Applied Physics*, 19, 1948, pp. 901-910.

Salama, K., "Relationship between temperate dependence of ultrasonic velocity and stress", *Review of Progress in Quantitative Nondestructive Evaluation*, 4B, 1985, pp. 1109-1119.

Sargent, G.A., Keshavan, M.K. and Conrad, H., *Titanium and titanium alloys*, Vol. 1, NY, Plenum Press, 1976, pp. 679-689.

Schwenk, W., Kaehler, W.A. and Kennedy, J.R., "Weldability of titanium alloy sheets 6Al-6V2Sn and 8Al-1Mo-1V", *Welding Journal*, 46 (2), 1967, pp. 54s-73s.

Sewell, R.A., "Gas purging for pipe welding", *Welding and Metal Fabrication*, 57 (1), 1989, pp. 20-22.

Shah, A.K., Kulkarni, S.D., Gopinathan, V. and Krishnan, R., "Weld heat-affected zone in Ti-6Al-4V alloy, Part I--computer simulation of the effect of weld variables on the thermal cycles in the HAZ", *Welding Journal*, 74 (9), 1995, pp. 297s-304s.

Shah, A.K., Kulkarni, S.D., Gopinathan, V. and Krishnan, R., "Weld heat-affected zone in Ti-6Al-4V alloy, Part II--modeling and experimental simulation of growth and phase transformations", *Welding Journal*, 74 (10), 1995, pp. 325s-338s.

Shankar, R., Williams, R. and Avioli, M.J., "Knowledge-based ultrasonic examination assistant", *Materials Evaluation*, October 1991, pp. 1316-1321.

Shih, D.S., Robertson, I.M. and Birnbaum, H.K., *Acta Metallurgica et Materialia,* 36, 1988, pp. 111-124.

Simbi, D.J. and Scully, J.C., "The effect of residual interstitial elements and iron on mechanical properties of commercially pure titanium", *Materials Letters*, 26, 1996, pp. 35-39.

Simpson, R.P. and Wu, K.C., "Microstructure-property control with postweld heat treatment in Ti-6Al-6V-2Sn", *Welding Journal* , 53 (1), 1974, pp. 13s-18s.

Simpson, W.A. and McClung, R.W., "Quantitative attenuation technique for materials characterization", *Materials Evaluation*, November 1991, pp. 1409-1413.

Siores, E., Egharevba, F. and Fenn, R., "Adaptive control in arc welding utilizing ultrasonic sensors", *Developments in Automated and Robotic Welding*, Waller, D.N., ed., The Welding Institute, UK, 1988, pp. 115-124.

Smartt, H.B and Key, J.F., "An investigation of factors controlling GTA weld bead geometry", *Proceedings of ASM Conference on Trends in Welding Research in the United States*, LA, USA, Nov. 1981.

Smith, D.E., "Mechanical testing of welds", *Welding Journal*, 60 (1), 1981, pp. 33-37.

Smith, W.F., *Structure and properties of engineering alloys*, second edition, McGraw Hill, 1993.

Soboyejo, W.O., Deffeyes, J.E. and Aswath, P.B., "Investigation of room and elevated temperature fatigue crack growth in Ti-48Al", *Material Science Engineering A*, (138), 1991, pp. 95-101.

Soboyejo, W.O. and Mercer, C., "On the implications of deformation-induced crack-tip deformation in a gamma-based titanium aluminide intermetallic", *Scripta Metallurgica et Materialia*, (30), 1994, pp. 1515-1520.

Stares, I.J., Duffil, C., Ogilvy, J.A. and Scruby, C.B., "On-line weld pool monitoring and defect detection using ultrasonics", *NDT International*, 23 (4), 1990, pp. 195-200.

Stares, I.J., Haywood, B.C. and Scruby, C.B., "On-line assessment of weld quality using ultrasonics", *Harwell Laboratory report*, AERE-R13410, USA, 1989.

Stark, L.E., Bartlo, L.J. and Porter, H.G., *Welding Journal*, 41, 1962, pp. 805.

Stone, D., Smith, J.S. and Lucas, J., "Sensor for automated weld bead penetration control", *Measurement Science Technology*, 1, 1990, pp. 1143-1148.

Stroud, R., *PhD Thesis*, Department of Metallurgy, Brunel University, 1983.

Stroud R., "Problems and Observations whilst Dynamically Monitoring Molten Weld Pools using Ultrasound", *British Journal of Non-Destructive Testing*, (31), 1989, pp. 29-32.

Swifthook, D.T. and Gick, A.E.F., "Penetration Welding with Lasers". *Welding Journal*, 52 (11), 1973, pp. 492s-499s.

Tattersall, H.G. and Tappin, G., "The work of fracture and its measurement in metals, ceramics and other materials", *Journal of Material Science*, (1), 1966, pp. 296-301.

Thomas, G., Ramachandra, R., Ganeshan, R. and Vahudevan, R., "The effect of pre- and post-weld heat treatments on the mechanical properties of electron beam welded Ti-6Al-4V alloy", *Journal of Material Science*, Vol. 28, 1993, pp. 4892-4899.

Thomas, G., Ramachandra, R., Nair, M.J., Nagarajan, K.V. and Vahudevan, R., "Effect of Preweld and Postweld Heat Treatment on the properties of GTA Welds in Ti-6Al-4V sheet", *Welding Journal*, Jan 1992, pp. 15s-20s.

Thomas, G. and Vahudevan, R., "Metallographic investigation of Ti-6Al-4V welds", *Practical Metallurgy*, 28, 1991, pp.171-178.

Uwer, D. and Degenkolbe, J., "Characterization of the Influence of Welding Temperature Cycles on the Mechanical Properties of Welded Joints". *Stahl und Eisen*, 97 (24), 1977, pp. 1201-1207.

Vilkas, E.P., *Welding Journal*, Vol. 45, 1966, pp. 410-416.

Vishnu, P.R., Li, W.B. and Easterling, K.E., "Heat flow model for pulsed welding", *Material Science and Technology*, 7 (7), 1991, pp. 649-659.

Voldrich, C.B., "On the welding of titanium alloys", *Welding Journal*, v32, (6), 1953, p497-515.

Wareing, A.J., "Control of TIG welding in practice", *Welding and Metal Fabrication*, 56 (8), 1988, pp. 375-380.

Wasz, M.L., Brotzen, F.R. and Mclellan, R.B., *Scripta Metallurgica et Materialia*, 28, 1993, pp. 483-487.

Wasz, M.L., Ko, C.C., Brotzen, F.R. and Mclellan, R.B., *Scripta Metallurgica et Materialia*, 23, 1989, pp. 2039-2042.

Wasz, M.L., Ko, C.C., Brotzen, F.R. and Mclellan, R.B., *Scripta Metallurgica et Materialia*, 24, 1990, pp. 2043-2046.

Watanabe, T., Shibata, S. and Goto, H. "Grain-Boundary Behaviour in the Heat Affected Zone of an Austenitic Stainless Steel and its Relations to Weld Metal Grain Growth". *Quarterly Journal of the Japan Welding Society*, 13 (2), 1995, pp. 262-269.

Wealleans, J.W. and Allen, B., "Effect of process variables in TIG welding", *Welding and Metal Fabrication*, 37 (5), May 1969.

Weigand, H.H., "Zur Umwandlurgivon $\alpha+\beta$ Titanlegierungen mit Aluminum", *Z. Metallkde*, 54, 1963, p. 43.

Wells, A.A., "Heat flow in welding", *Welding Journal*, 31 (5), 1952, pp. 263s-267s.

Williams, D.N. and Jaffee, R.I., *Journal of Less-common Metals*, 2, 1960, pp. 42-48.

Williams, D.N., Koehl, B.G. and Bartlett, E.S., *Journal of Less-common Metals*, 19, 1969, pp. 385-398.

Woolcock, A. and Ruck, R.J., "Argon shielding techniques for TIG welding titanium", *Metal Construction*, 12 (5), 1980, pp. 219-224.

Woolcock, A., "The effect of welding speed and edge preparation on the incidence of porosity in TIG welded titanium", *Titanium and titanium alloys, scientific and technological aspects*, Vol. 2, Plenum Press, New York, 1982, pp. 1189-1196.

Wu K.C., "Qualitative evaluation of the heat-affected zone in the tungsten inert gas welding of titanium alloys", *Water Arsenal memorandum report*, 19 May, 1961.

Wu, K.C., "Weldability study of titanium 8Al-1Mo-1V", *Northrop report NOR 65-250*, October 1965.

Wu, K.C., "Correlation of properties and microstructure in welded Ti-6Al-6V-2Sn", *Welding Journal*, v60, (11), 1981, pp. 219s-226s.

Yonesawa, K., "Welding of titanium and titanium alloys", *Welding International*, 1 (12), 1987, pp. 1131-1142.

Young, M., Levine, E. and Margolin, H., "Deformation behavior of alpha, beta and martensite in Ti-6246 alloy", *Proceedings of ASME Material Science Symposium*, Detroit, USA, 1974.

Yue, T.M., Ha, H.U.and Musson, N.J., "Grain size effects on the mechanical properties of some squeeze cast light alloys", *Journal of Material Science*, (30), 1995, pp. 2277-2283.

Yung, K.C., Fenn, R. and Ralph, B., "A temperature model for ultrasonic measurement of titanium welds". *Transaction of The Hong Kong Institution of Engineers*, Vol. 2, Number 3, March 1996, pp. 33-37.

Yung, K.C., Ralph, B., Fenn, R. and Lee, W.B., "Investigation on welding parameters affecting the tensile properties of titanium welds". *Journal of Materials Processing Technology*, Vol. 63, No.1-3, Jan. 1997, pp.759-764.

Yung, K.C., Ralph, B., Fenn, R. and Lee, W.B, "The control of thin-plate weld geometry and microstructure". *Journal of Materials Processing Technology*, Vol. 63, No. 1-3, Jan. 1997, pp. 802-805.

Yung, K.C., Ralph, B. and Fenn, R., "A study on the effect of welding parameters and heat input rates on titanium weld's grain size". *Technical papers of North American Manufacturing Research Institute of SME*, MS97-192, May 1997, pp. 149-154.

Zhang, J., "Tensile deformation and fracture in high purity titanium: In situ observation by scanning electron microscopy", *Materials Science and Engineering A*, A114, (2), 1989, pp. 89-96.

# Appendix A

## The set-up and the use of calibration blocks for ultrasonic testing

## Appendix A : The set-up and the use of calibration blocks for ultrasonic testing

In order to ensure the accuracy and reliability of the ultrasonic inspection instrumentation, a certain number of calibrations should be made. These calibrations consist of three major elements, which are : checking the characteristic of the angle-beam probe, checking the performance of the ultrasonic inspection unit, as well as calibration of the angle-beam search units. Different international standards are available for these purposes. These are listed in the following :

a) BS 2704 (1978) Calibration blocks for use in ultrasonic flaw detection

b) ASTM E 164 Instructions for use of the international institute of welding (IIW) test block and other calibration blocks for ultrasonic testing.

c) ASTM E 428-91 Standard practice for fabrication and control of steel reference blocks used in ultrasonic inspection

d) ASTM E 1158-90 Standard guide for material selection and fabrication of reference blocks for the pulsed longitudinal wave ultrasonic examination of metal

Reference block is required in all calibrations. There are five types of reference block available for different purposes. Figure A1 shows the dimensions of the IIW test block while Figure A2 shows the dimensions of the miniature angle-beam test block.

In checking different characteristics of a test probe, different set-up are required. For example, Figure A3 shows the various set-up of the angle-beam pulse echo probe with an IIW test block to determine the index point, the beam angle and the straight-beam resolution, as well as to calibrate the instrument time-base.

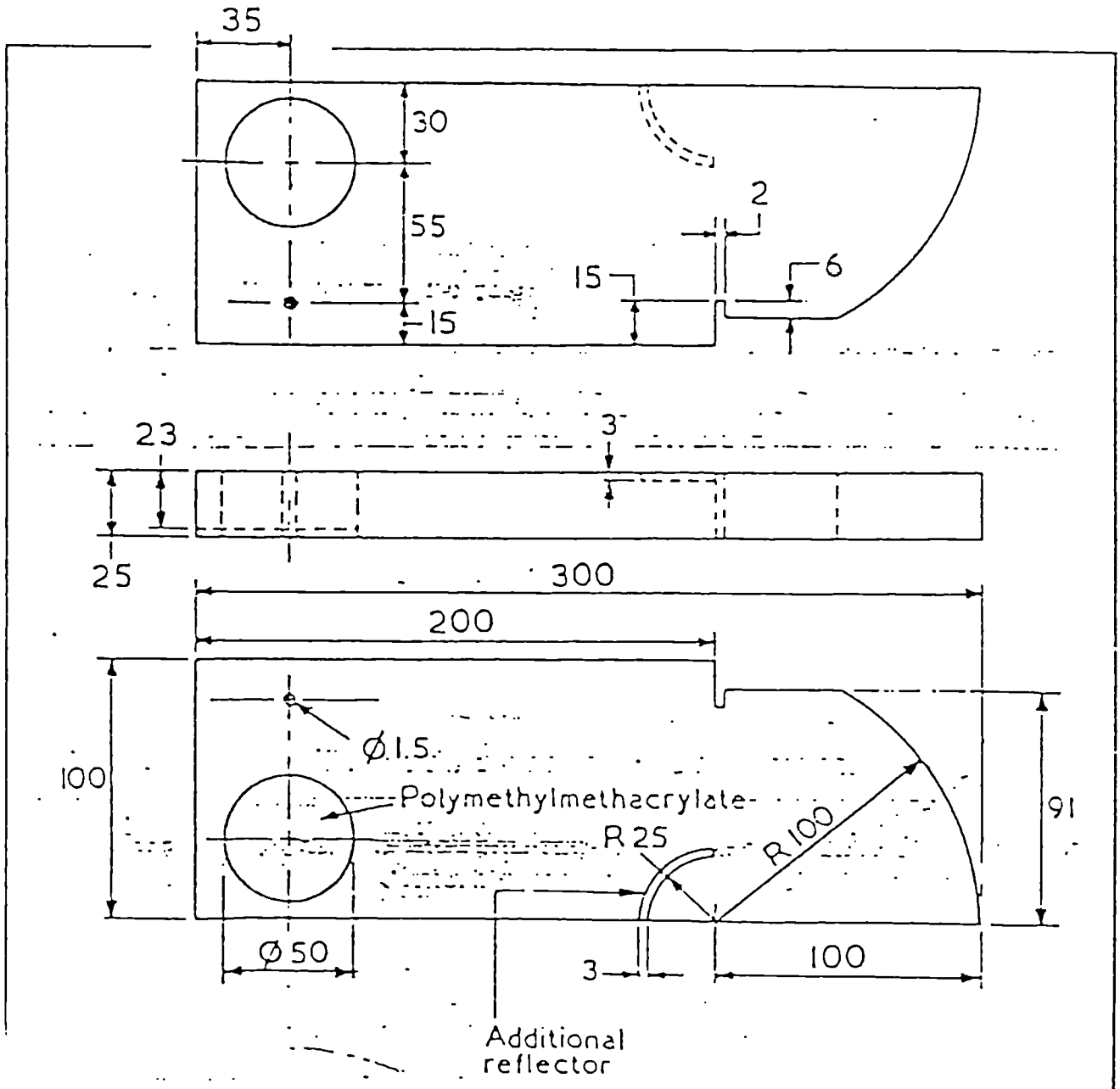


NOTE. All dimensions in millimetres. Figure A1 : Dimensions of the IIW block

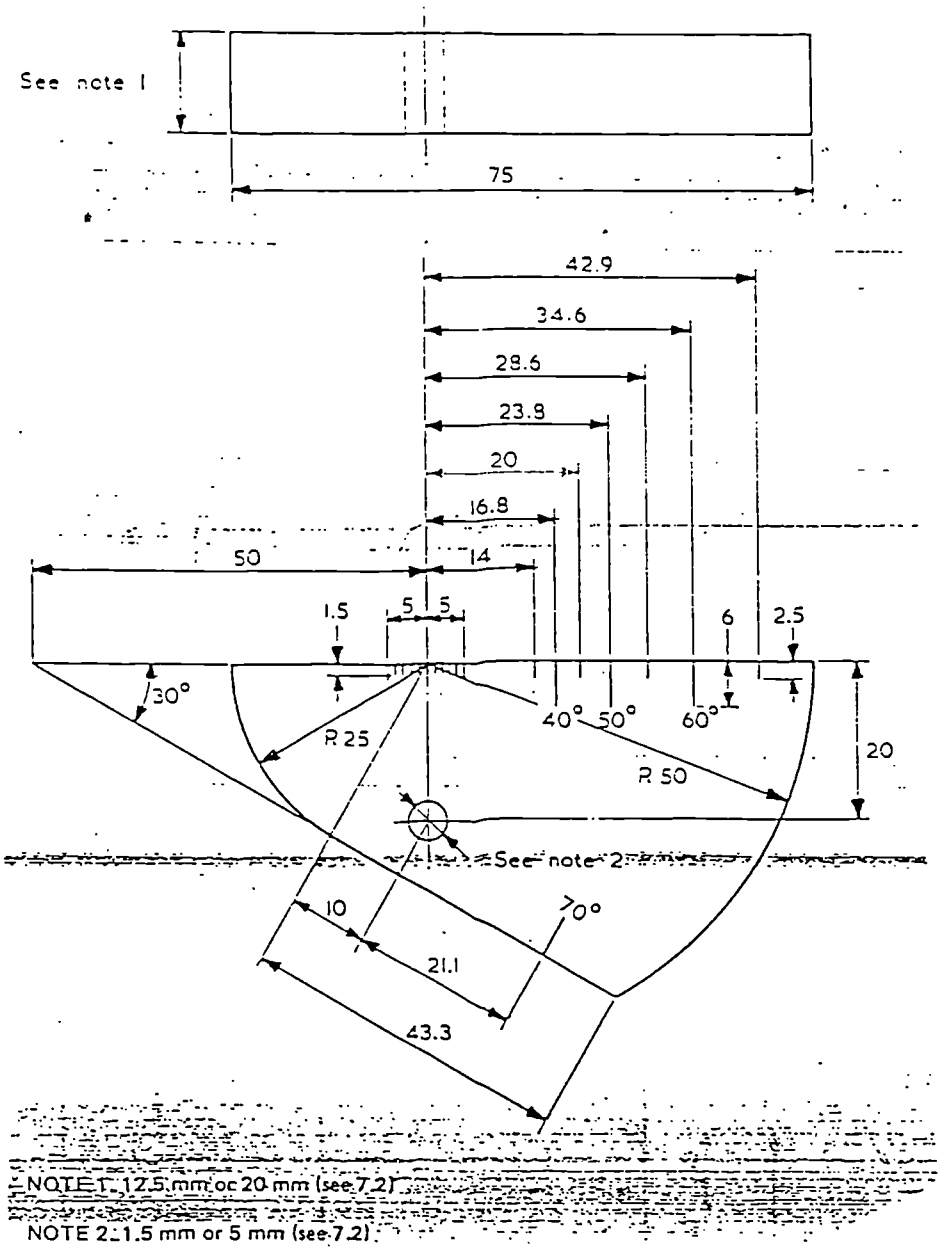


Figure A2 : Miniature angle-beam block (Block 4). Dimensions.

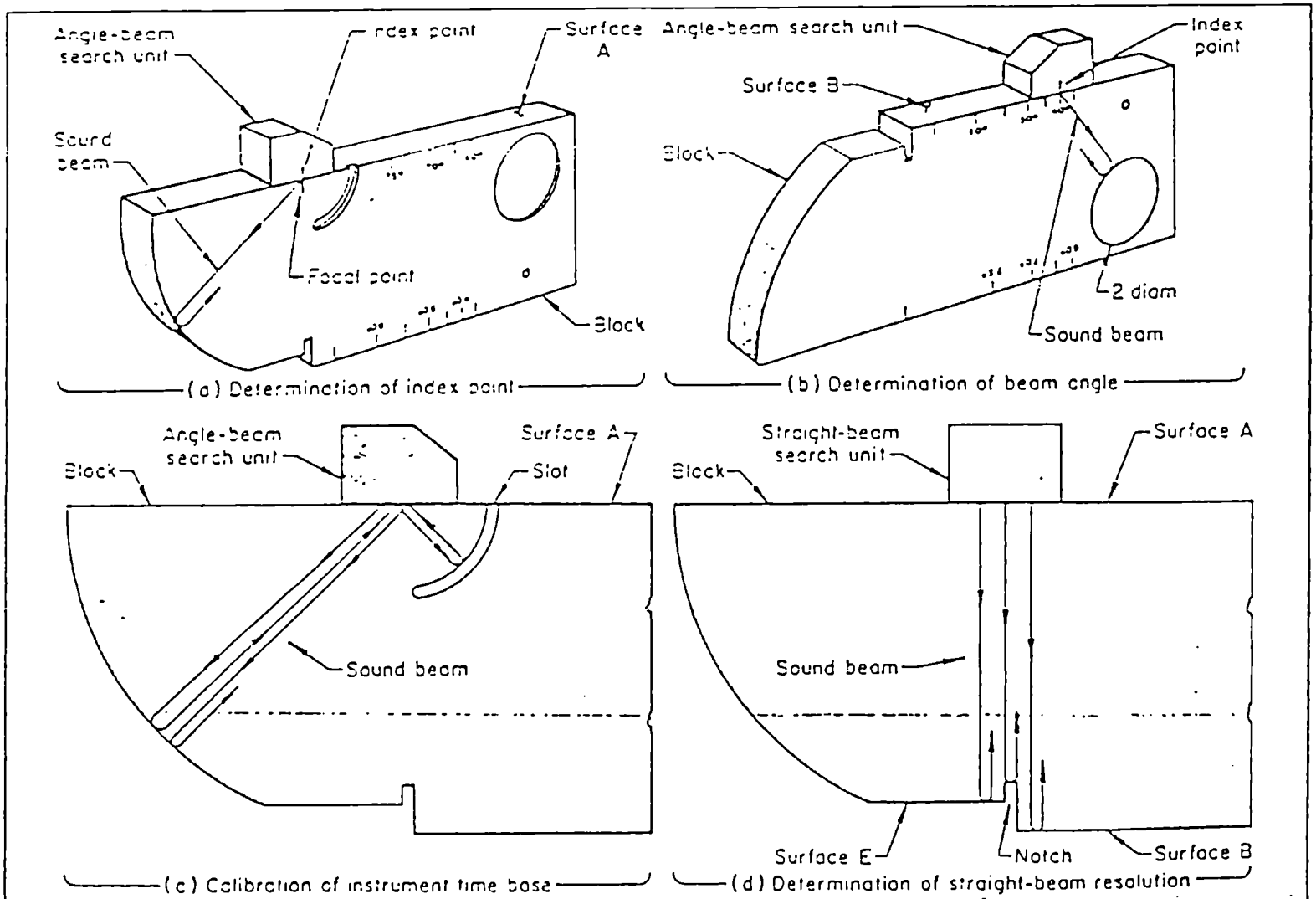


Figure A3 : Positioning of angle-beam and straight-beam search units for calibration using the International Institute of Welding (IIW) type of standard reference block

# Appendix B

## Detail part drawings

## of the welding and clamping fixture

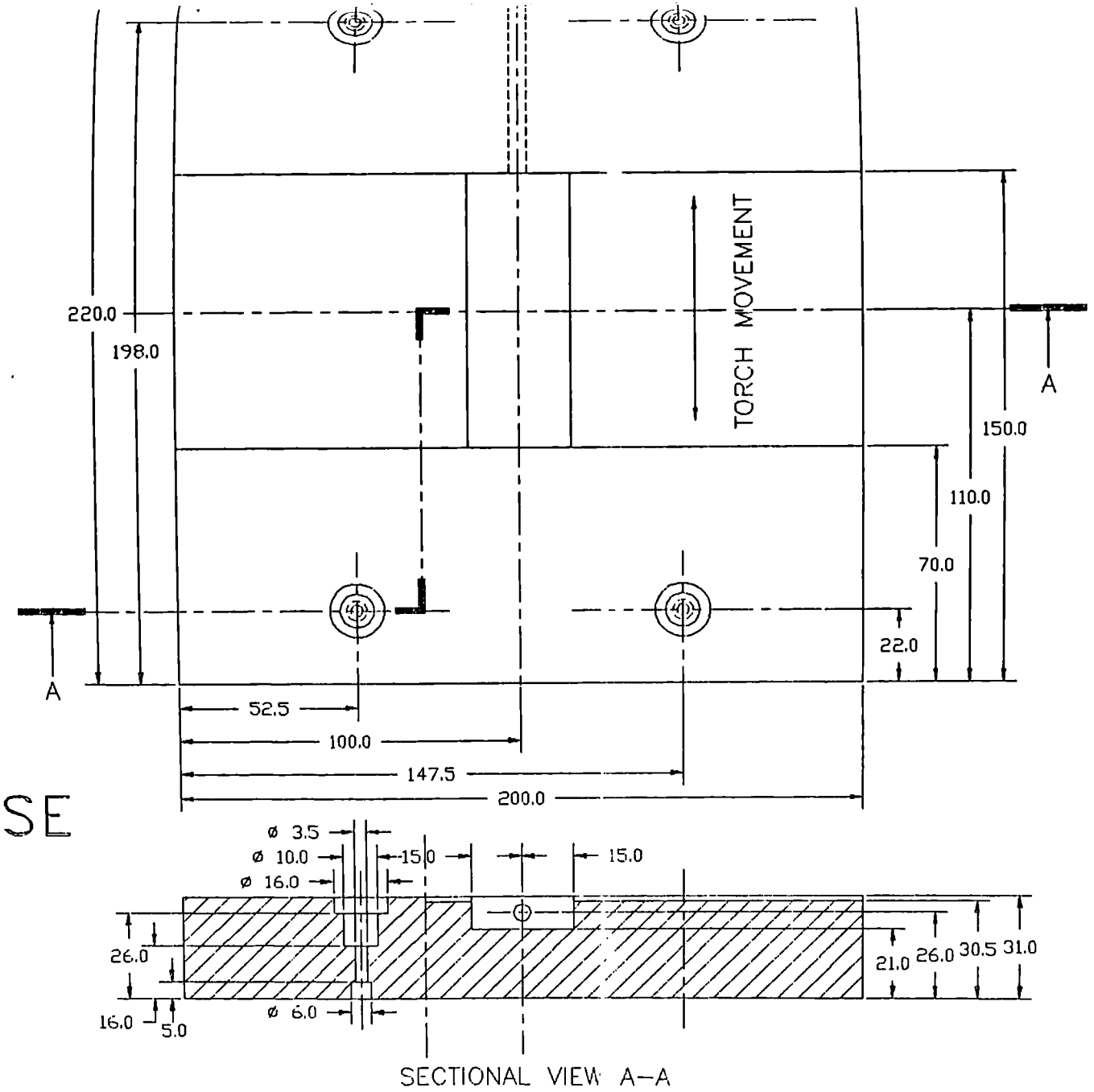


Figure B1 : Part drawing of the base in welding fixture

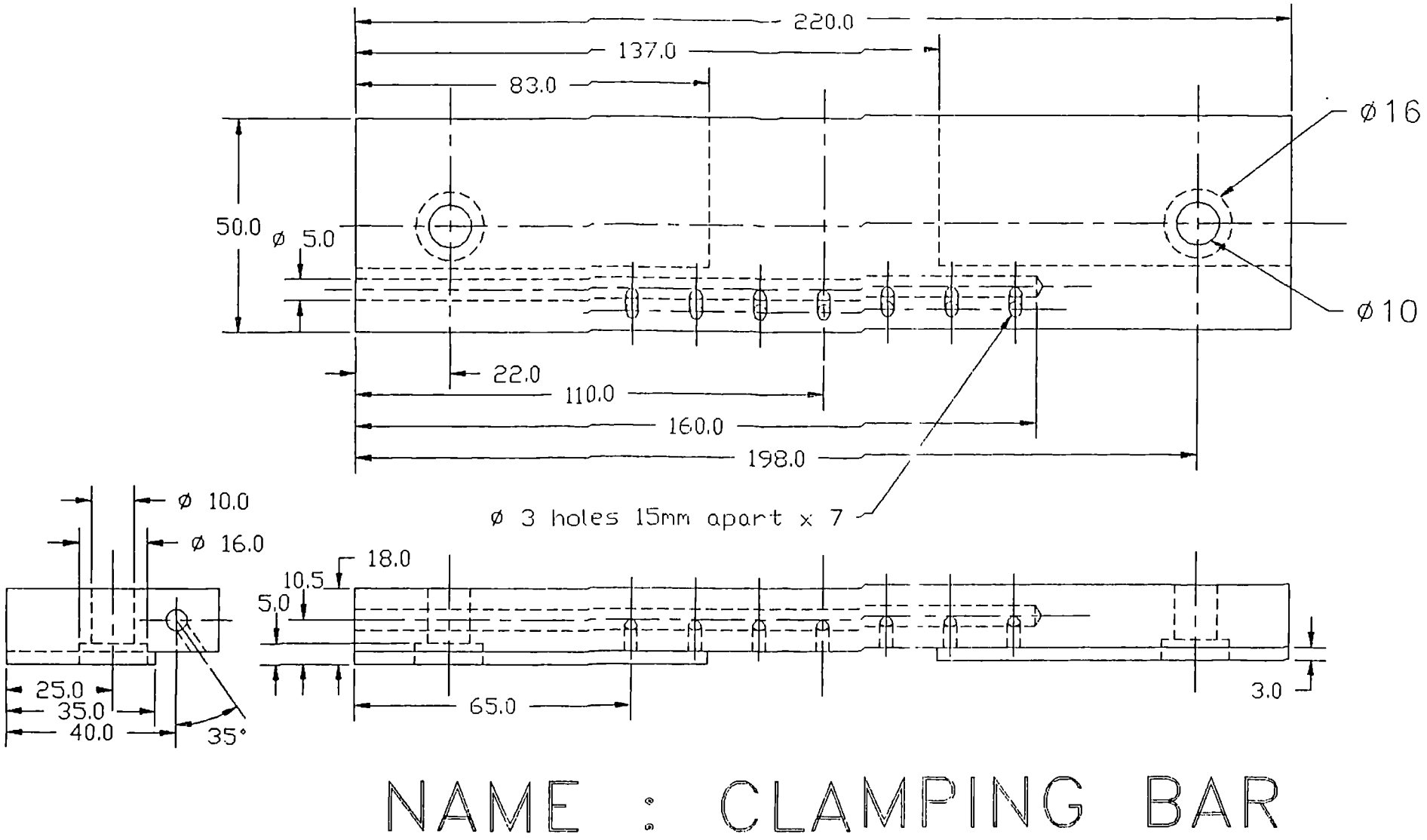


Figure B2 : Part drawings of the clamping bar in clamping fixture

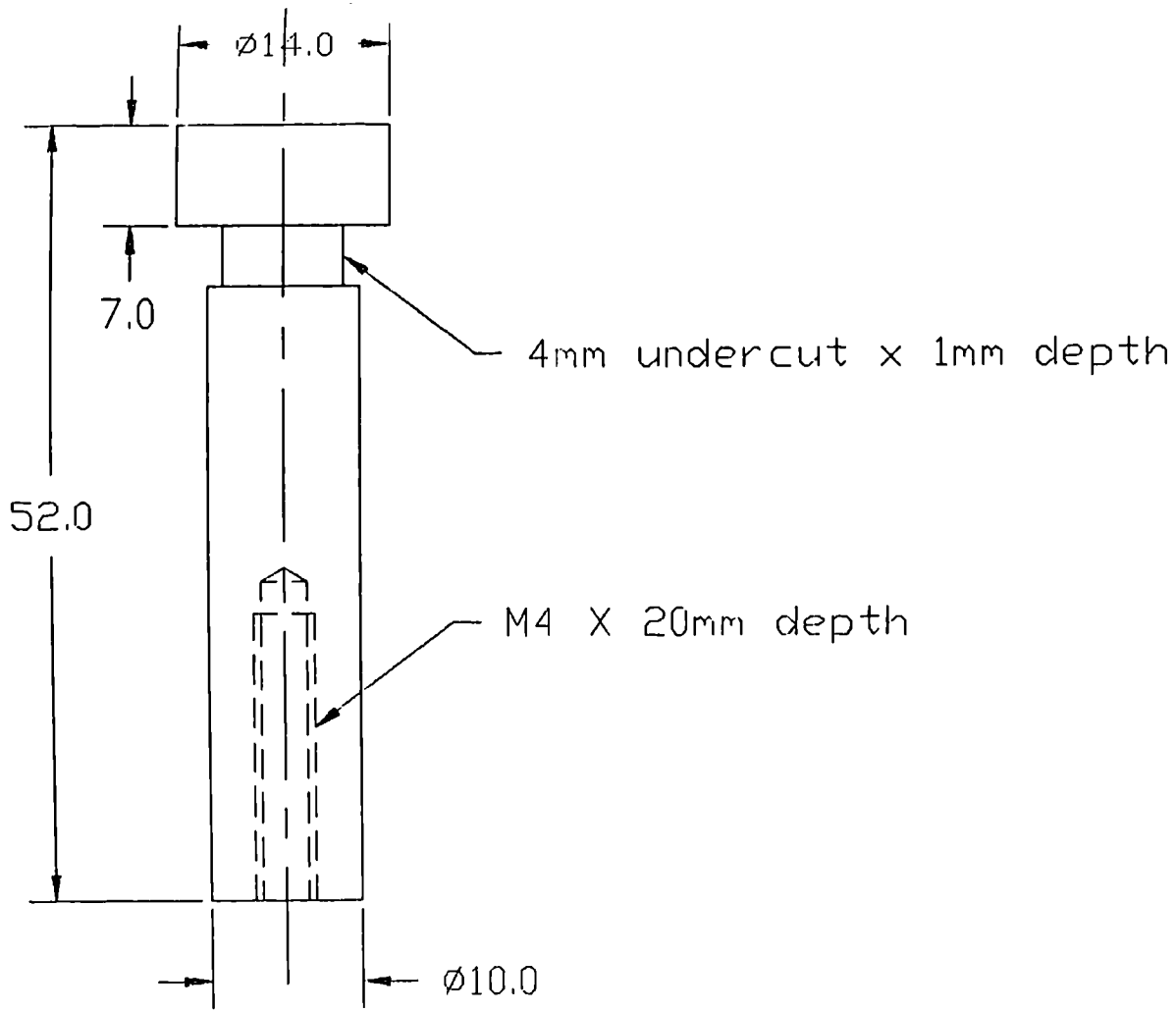


Figure B3 : Part drawing of the guide pin in clamping fixture

# Appendix C

## Representative screens available in

## "Computer Data Book"

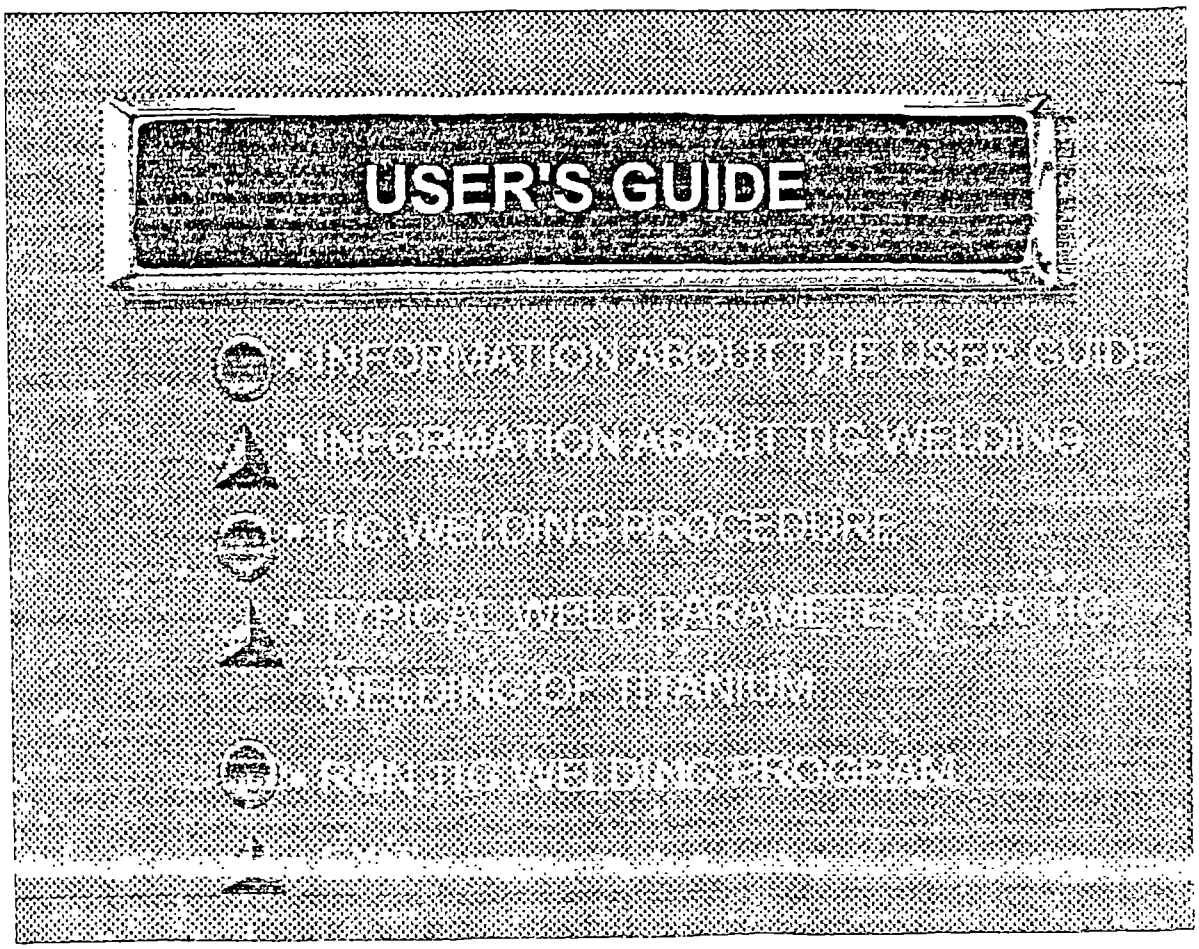


Figure C1

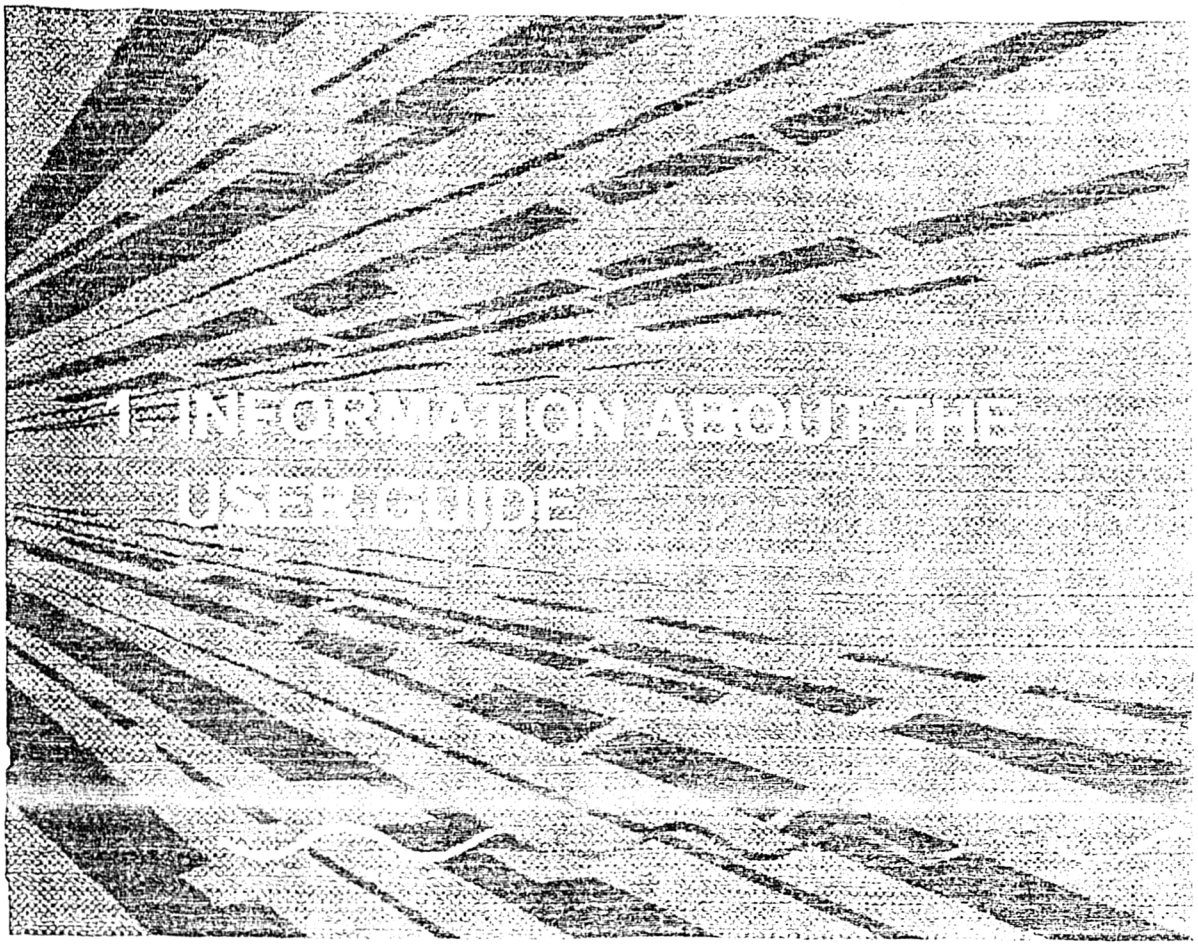


Figure C2

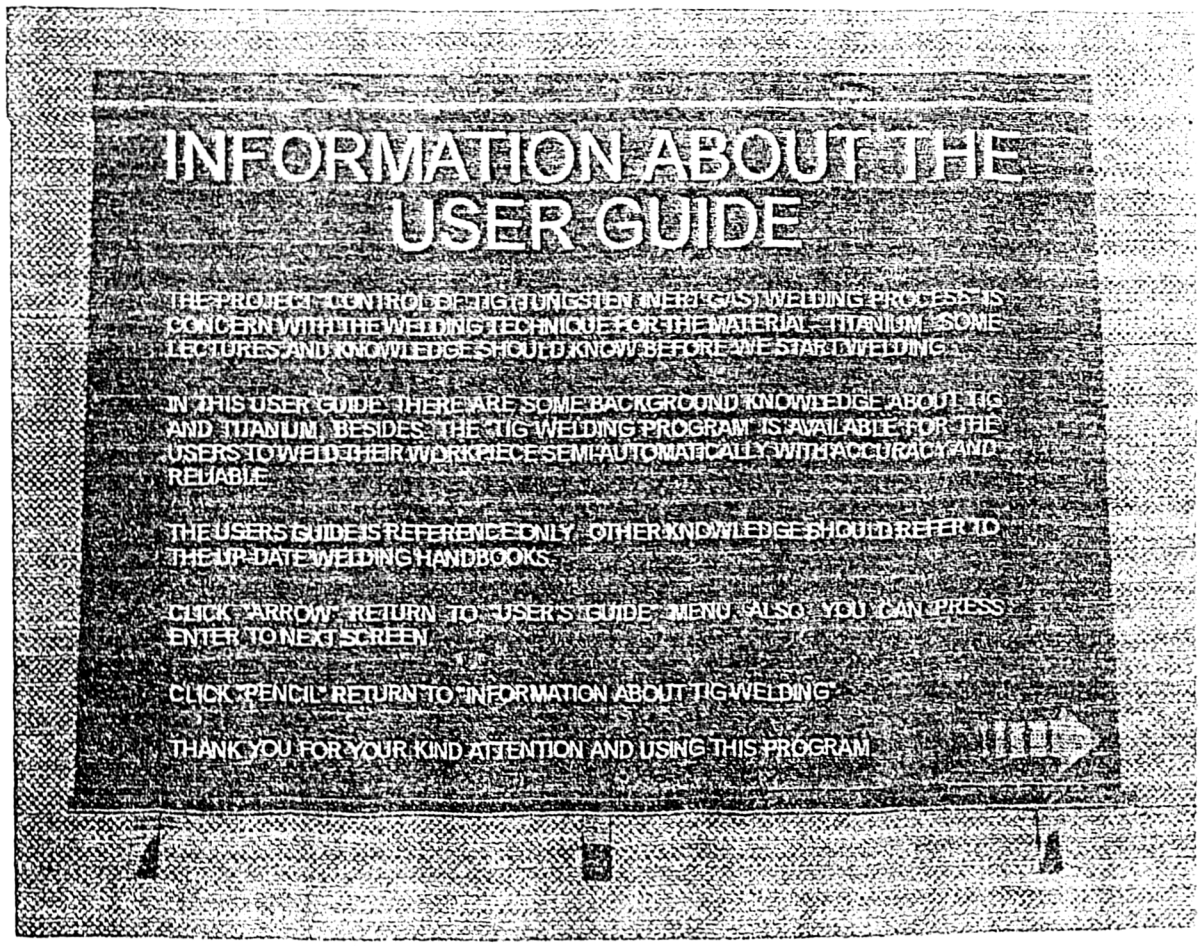


Figure C3

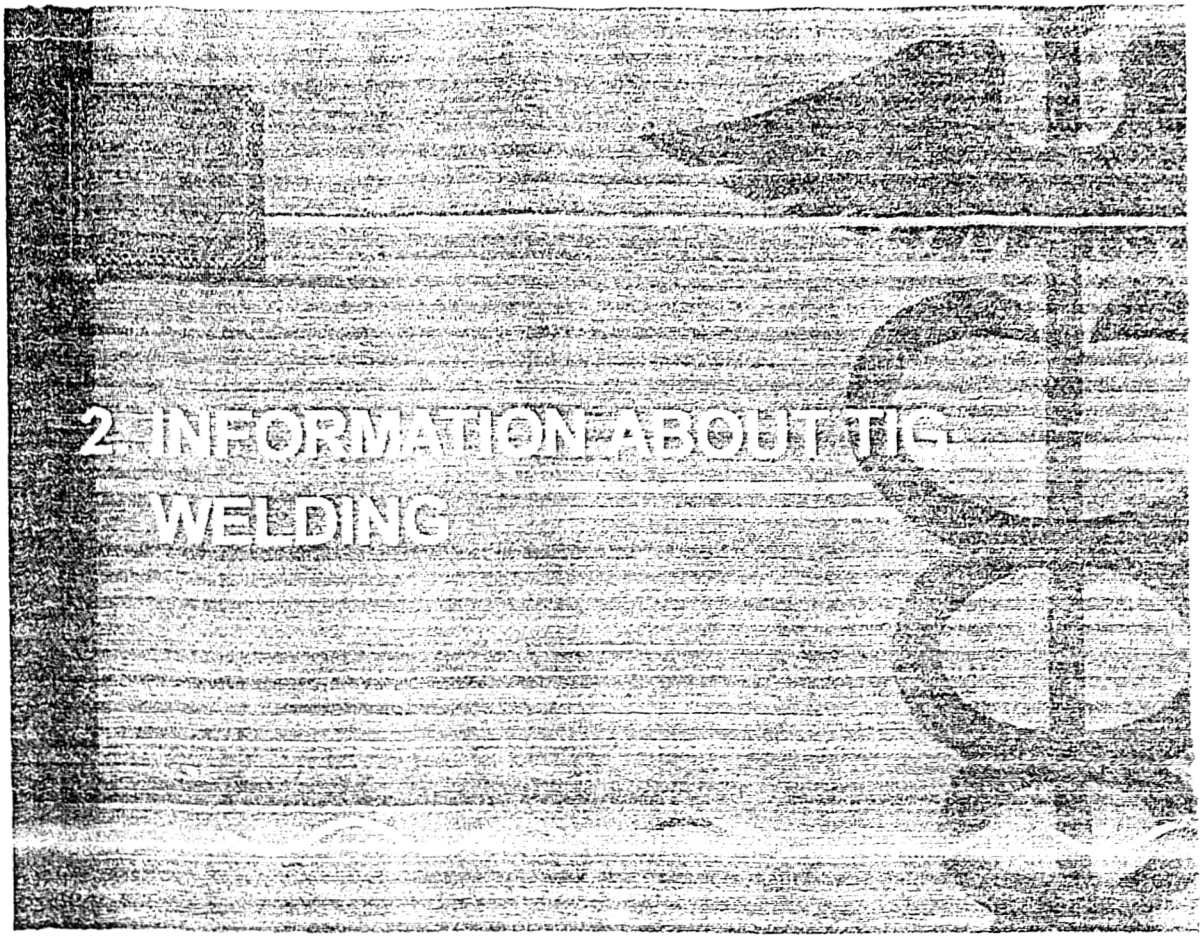


Figure C4

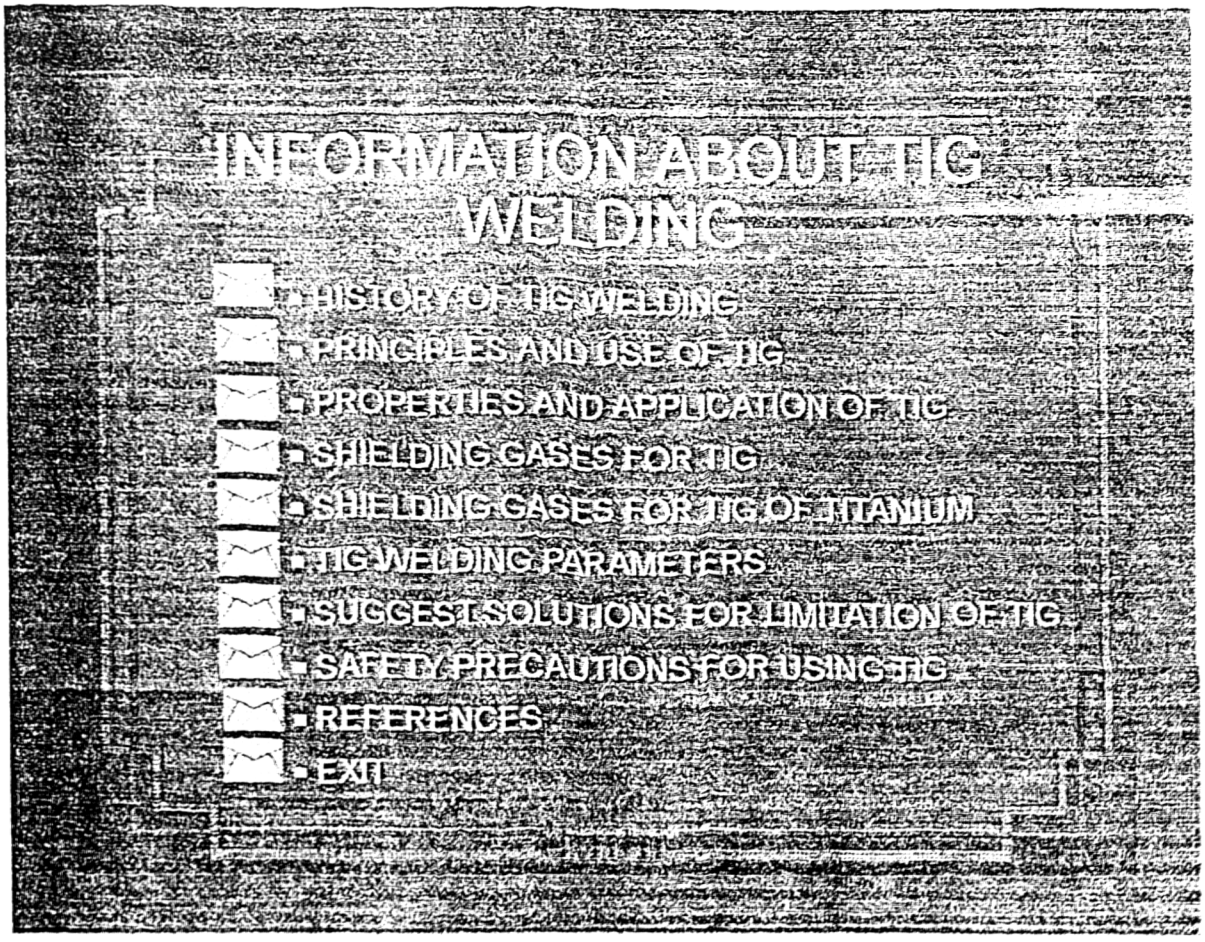


Figure C5

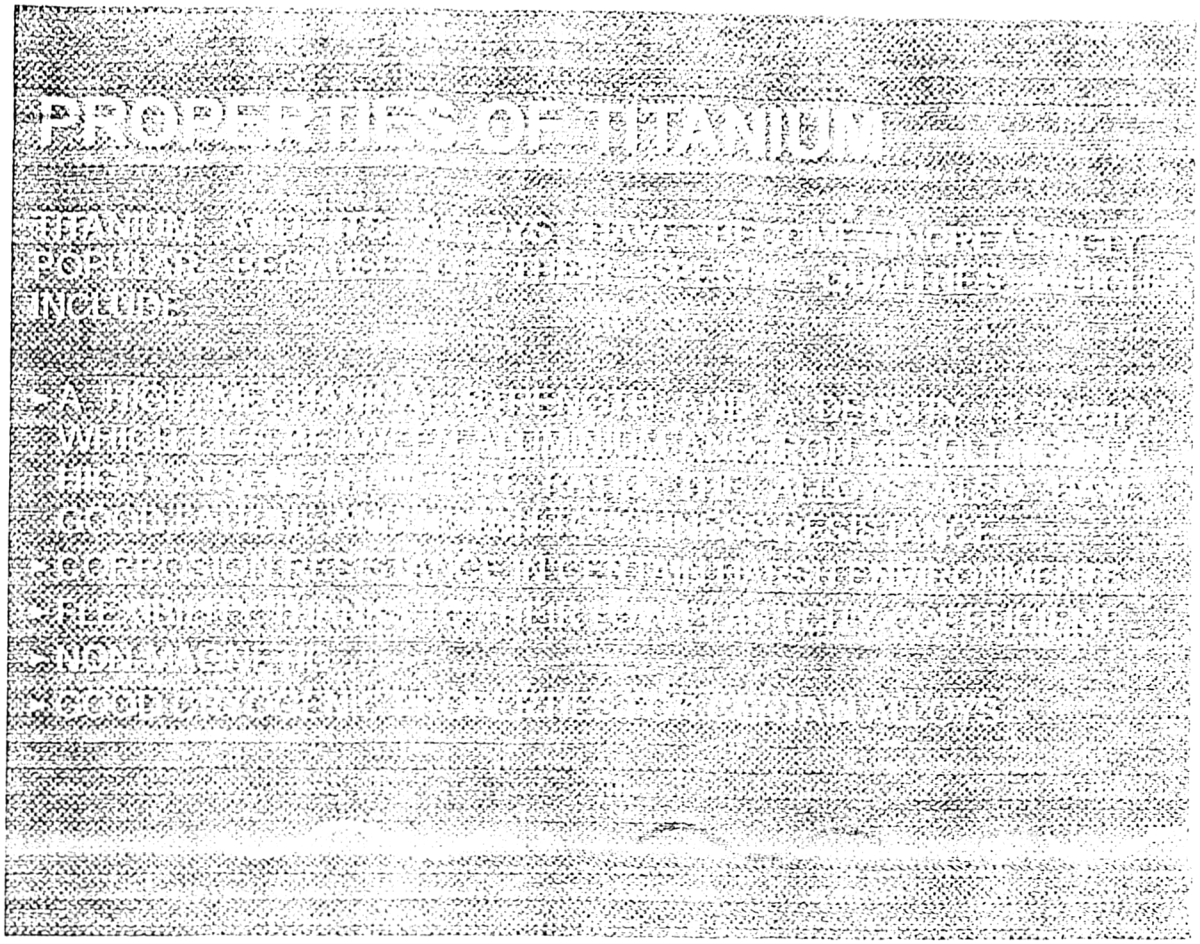

Figure C6

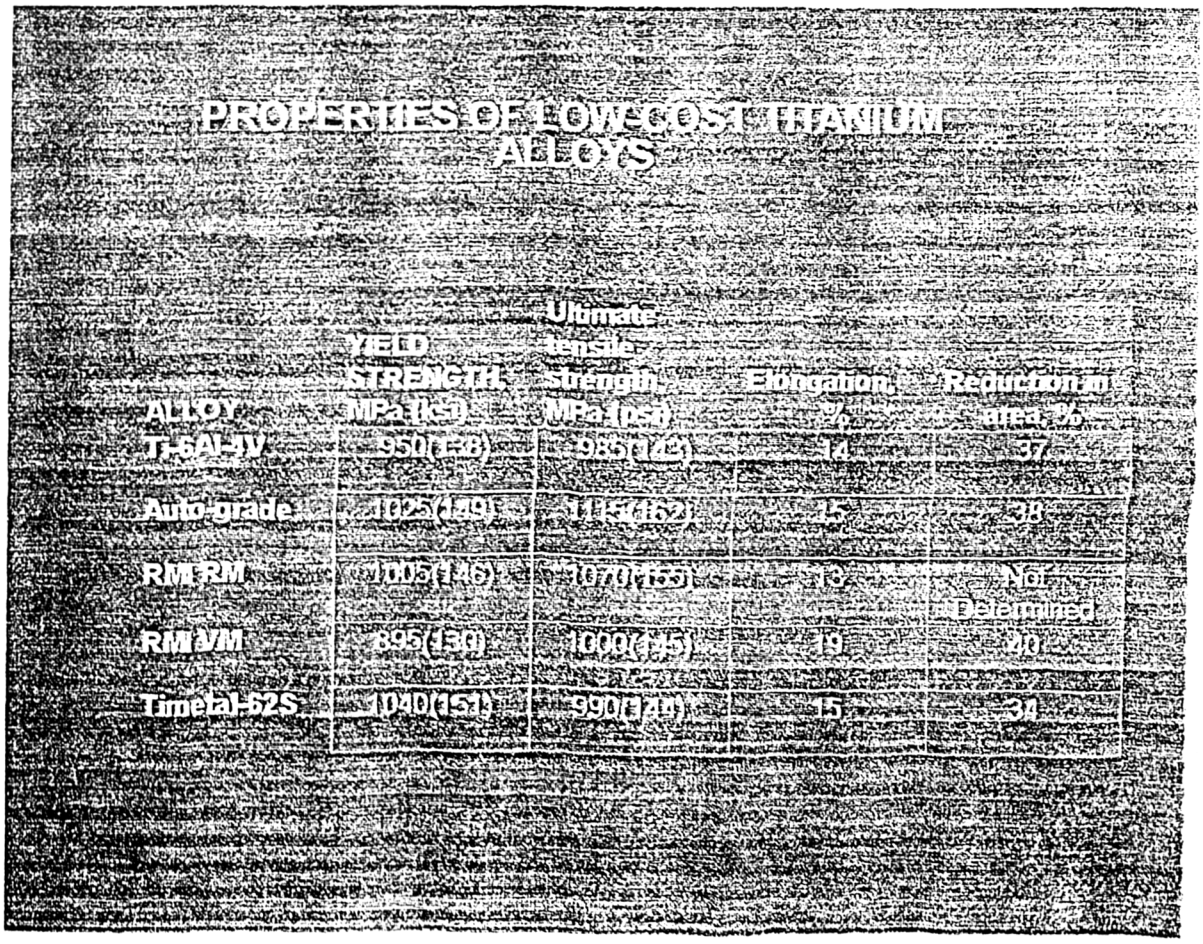

PROPERTIES OF LOW COST TITANIUM ALLOYS

| ALLOY | YIELD STRENGTH MPa (ksi) | Ultimate Tensile Strength MPa (ksi) | Elongation % | Reduction in area % |
|---|---|---|---|---|
| Ti-6Al-4V | 950 (138) | 985 (143) | 14 | 37 |
| Auto-grade | 1025 (149) | 1150 (162) | 15 | 38 |
| RMI RM | 1005 (146) | 1070 (155) | 16 | Not Determined |
| RMI VM | 895 (130) | 1000 (145) | 19 | 40 |
| Timetal-62S | 1040 (151) | 990 (144) | 15 | 34 |

Figure C7

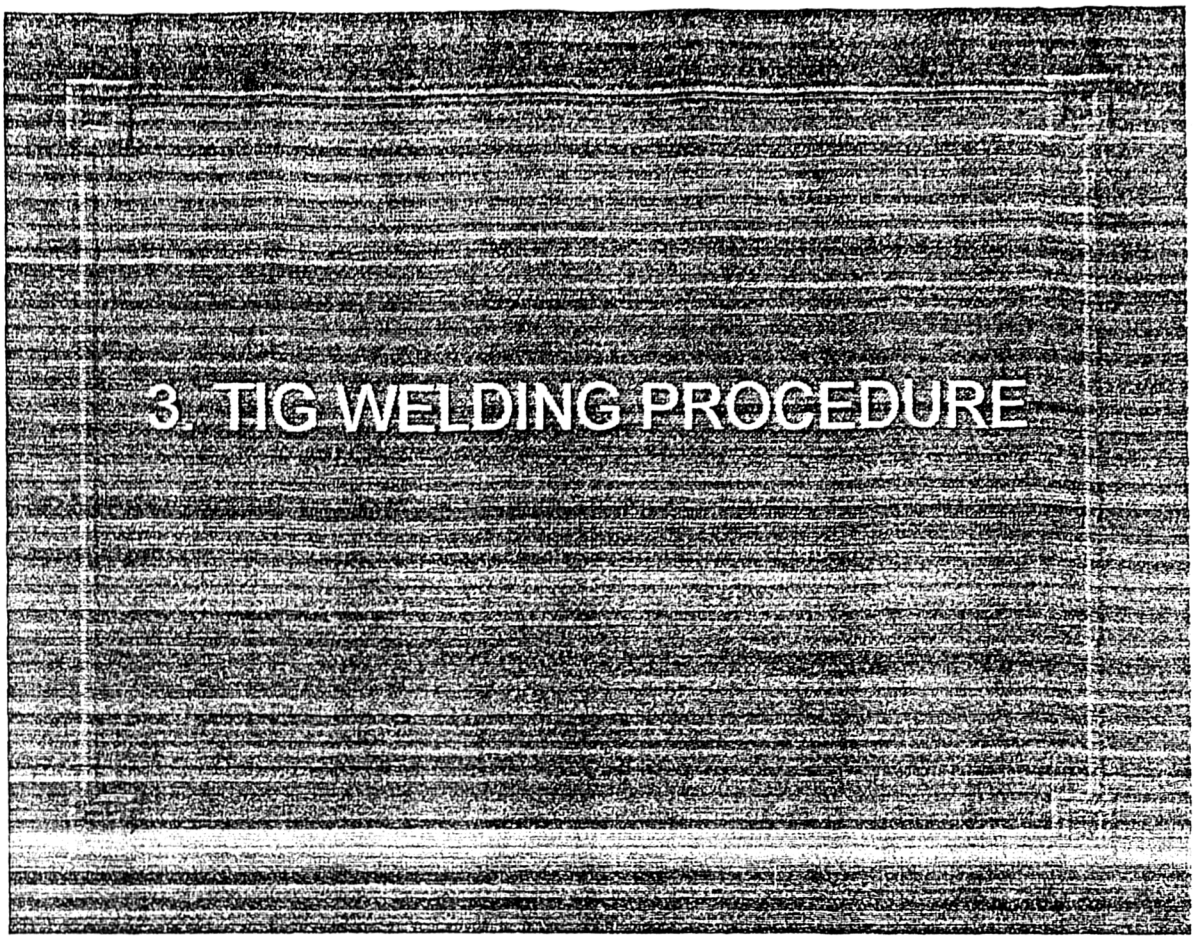


Figure C8

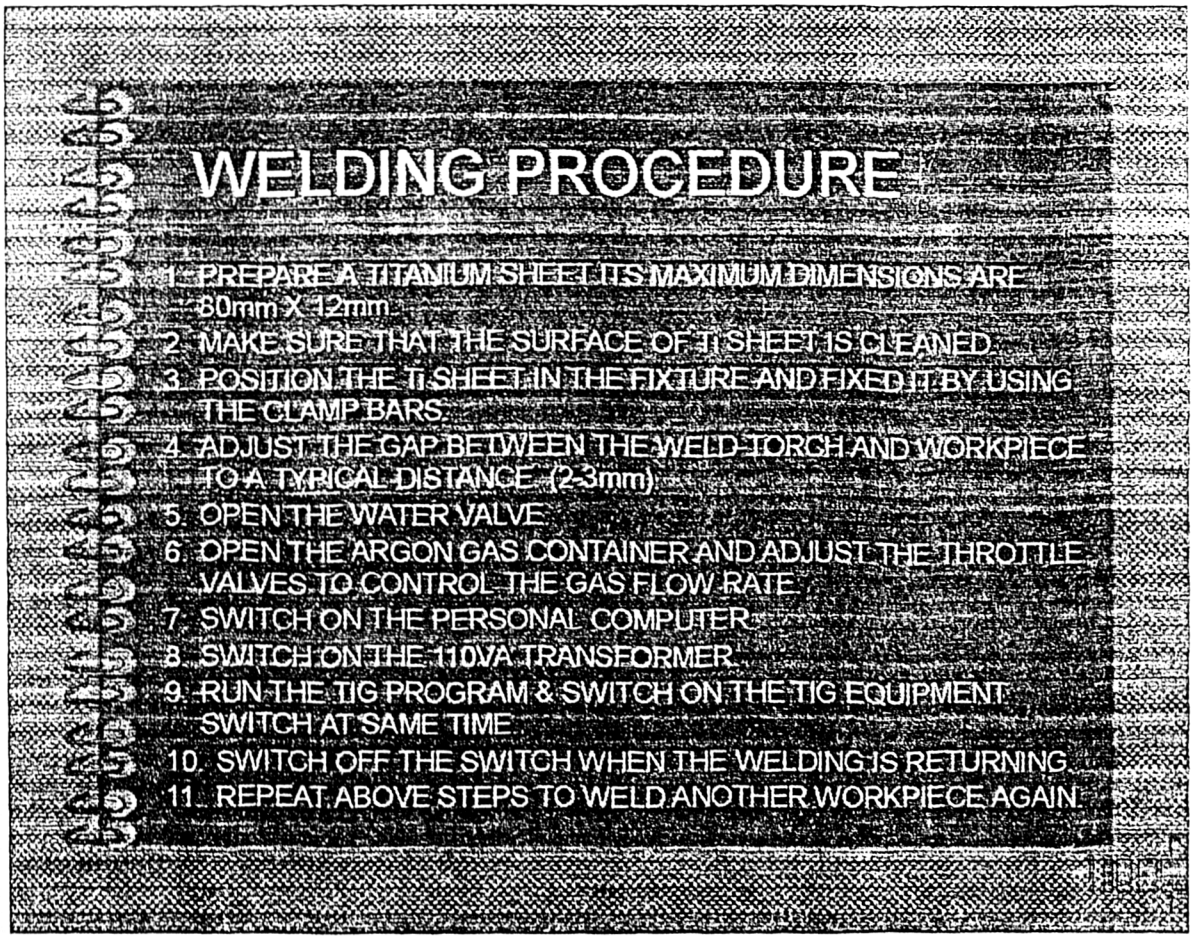


Figure C9

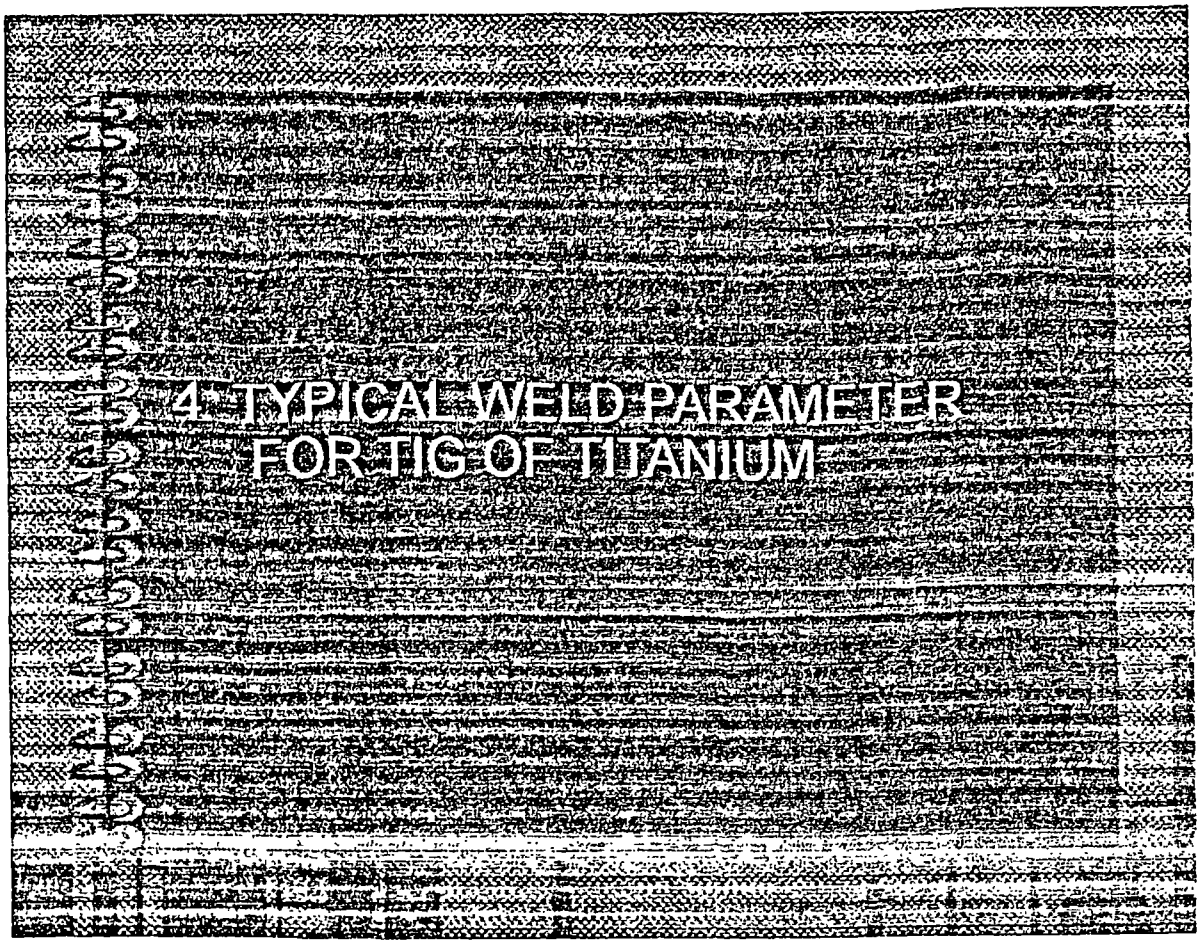


Figure C10

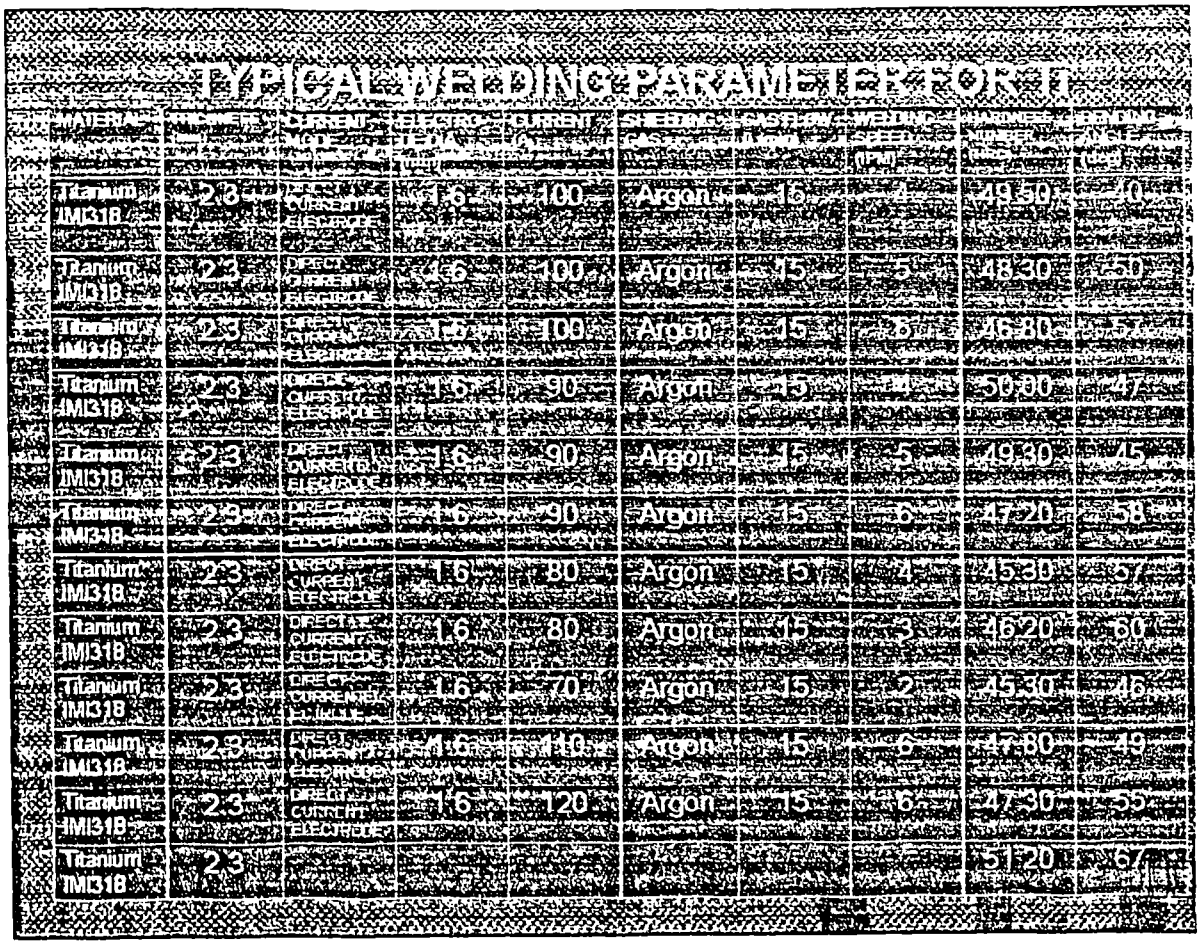


Figure C11

# Appendix D

# Program listing

# of the weld depth control program

# and its flow chart

# Program Flow Chart

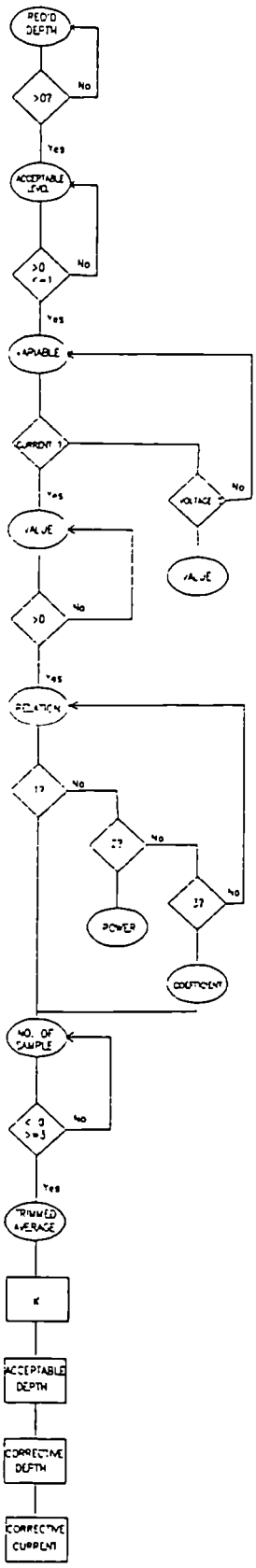


Figure D1 : Program flow chart of the weld depth control program

```
/* Program name : vcc.c ( Voltage / Current Control in
language C )

   Objective    : calculate corrective voltage or current

   Parameters   : required depth of weld, reqd_depth
   ( Legend )     acceptable level, acc_level
                  existing current, e_current
                  existing voltage, e_voltage
                  corrective depth, cor_depth
                  corrective current, cor_current
                  corrective voltage, cor_voltage
                  trimmed average, t_average
                  welding constant, k
                  maximun sample, tmpmax
                  minimun sample, tmpmin
============================================================ */

#include <stdio.h>
#include <bios.h>
#include <math.h>
#include <dos.h>

#define outport         outportb
#define inport          inportb
#define prt1            0x378
#define prt1a           0x37A
#define port            632
#define ad_delay        1
#define ad_loop         5
#define D_channel       7
#define F_channel       3


/* Find minimun */
float min( x, y )
float x, y;
{
  if ( x <= y )
     return x;
  else
     return y;
}

/* Find maximun */
float max( x, y )
float x, y;
{
  if ( x <= y )
     return y;
```

```
   else
      return x;
}


float sample;
float average, t_average, sum;
int   i, num;
float e_current, reqd_depth, acc_level, k;
float cor_current, cor_depth;
float e_voltage, cor_voltage;

void main()
{
  char  ch;
  char  kind;
  float m, n;
  float tmpmax = -1000;
  float tmpmin = 1000;
  float sum = 0;

  clrscr();

/* Input required depth */
  {
     printf(" The required depth of weld is ", reqd_depth);
     scanf("%f", &reqd_depth);
     if ( reqd_depth <= 0 )
     {
     printf("\n Error  : Required depth  <=  0 ");
     printf("\n Warning: Required depth should be  >  0
!!\n");
     return;
     }
  }

/* Input acceptable level */
  {
     printf(" The acceptable level ( <1.0 ) is ",
acc_level);
     scanf("%f", &acc_level);

     if ( acc_level <= 0  ||  acc_level > 1 )
     {
     printf("\n Error  : Acceptable level  <  0  or  >=  1
");
     printf("\n Warning: Acceptable level should be  >  0
and  <=  1  !!\n");
     return;
     }
```

```
   }

/* Choose voltage or current to be corrected */
   {
      do
      {
      printf(" Type in  v ( voltage )  or  c ( current )  to
be correct.", ch);
      scanf("%c", &ch);

      ch = getchar();

      switch( ch )
      {
         case 'c':
           printf("\n ..... Correct current
..... \n\n");

/* Input existing current */
           printf(" The current shown on welding machine is
", e_current);
           scanf("%f", &e_current);
           if ( e_current <= 0 )
           {
           printf("\n Error  : Existing current  <=  0 ");
           printf("\n Warning: Existing current should be  >
0  !!\n");
           return;
           }
           break;

        case 'v':
           printf("\n ..... Correct voltage
..... \n\n");

/* Input existing voltage */
           printf(" The voltage shown on welding machine is
", e_voltage);
           scanf("%f", &e_voltage);
           if ( e_voltage <= 0 )
           {
           printf("\n Error  : Existing voltage  <=  0 ");
           printf("\n Warning: Existing voltage should be  >
0  !!\n");
           return;
           }
           break;
     }
     }
     while ( ch!='c'  &&  ch!='v' );
```

```
  }

/* Choose the depth and current or voltage relation */
  {
     {
     if ( ch == 'c' )
     {
        printf("\n The relation between depth of weld and
current is : \n");
        printf("\n 1. Depth = k * current  ");
        printf("\n 2. Depth = k * ( current to the power n )
");
        printf("\n 3. Depth = k * ( exp( m * current ) - 1 )
\n\n");
        printf("\n If no option is exact, choose the one
approximate the relation best. \n\n");
     }
     else if ( ch == 'v' )
     {
        printf("\n The relation between depth of weld and
voltage is : \n");
        printf("\n 1. Depth = k * voltage  ");
        printf("\n 2. Depth = k * ( voltage to the power n )
");
        printf("\n 3. Depth = k * ( exp( m * voltage ) - 1 )
\n\n");
        printf("\n If no option is exact, choose the one
approximate the relation best. \n\n");
     }
     }
     {
     do
     {
        printf(" Choose option ( 1, 2, or 3 ) :  ", kind);
        scanf("%c", &kind);

        kind = getchar();

        switch( kind )
        {
           case '1':
          {
             if ( ch == 'c' )
                k = reqd_depth / e_current;

             if ( ch == 'v' )
                k = reqd_depth / e_voltage;
          }
          break;
```

```
        case '2':
        {
           if ( ch == 'c' )
           {
              printf(" The current is to the power of  ",
n);
              scanf("%f", &n);
              k = reqd_depth / pow( e_current , n );
           }
           if ( ch == 'v' )
           {
              printf(" The voltage is to the power of  ",
n);
              scanf("%f", &n);
              k = reqd_depth / pow( e_voltage , n );
           }
        }
        break;

        case '3':
        {
           if ( ch == 'c' )
           {
              printf(" The value of m is  ", m);
              scanf("%f", &m);
              k = reqd_depth / ( exp( m * e_current ) - 1
);
           }
           if ( ch == 'v' )
           {
              printf(" The value of m is  ", m );
              scanf("%f", &m);
              k = reqd_depth / ( exp( m * e_voltage ) - 1
);
           }
        }
        break;
     }
  }
  while ( kind!='1'  &&  kind!='2'  &&  kind!='3' );
  }

  if ( k <= 0 )
  {
  printf("\n Error  : Welding constant  <=  0 ");
  printf("\n Warning: Welding constant should be  >  0
!!\n");
  return;
  }
```

```
      }

      tmpmin = min( sample, tmpmin);
      tmpmax = max( sample, tmpmax);
      sum += sample;
      }

      average = sum / (float)num;
      t_average = (float)(sum - tmpmax - tmpmin) /
(float)(num-2);

      printf("\n The largest sample depth is %6.3f ",
tmpmax);
      printf("\n The least sample depth is %6.3f ", tmpmin);
      printf("\n The actual average depth is %6.3f",
average);
      printf("\n The trimmed average depth is %6.3f\n",
t_average);

      printf(" Please reminds that samples should be closely
distributed.\n");
      printf(" ( except the max. and min.)\n\n");
  }

/* Checking for unreasonable errors */
  {
      if ( t_average > 1.5 * reqd_depth )
      {
      printf("\n Error  : trimmed samples average  >>
required depth ");
      printf("\n Warning: Sample average should not be  >>
required depth  !!");
      printf("\n Check  : Number of samples should be
'integer'  !!\n");
      return;
      }

      if ( ch == 'c')
      {
      if ( cor_depth > t_average )
      {
         if ( kind == '1' )
            cor_current = e_current + ( cor_depth / k -
t_average / k );

         else if ( kind == '2' )
            cor_current = e_current + ( pow(cor_depth/k,1/n)
- pow(t_average/k,1/n) );

         else if ( kind == '3' )
```

```
        cor_current = e_current + ( log(cor_depth/k +1) -
log(t_average/k +1) )/m;
     }
     else if ( cor_depth < t_average )
     {
        if ( kind == '1' )
           cor_current = e_current - ( t_average / k -
cor_depth / k );

        else if ( kind == '2' )
           cor_current = e_current - ( pow(t_average/k,1/n)
- pow(cor_depth/k,1/n) );

        else if ( kind == '3' )
           cor_current = e_current - ( log(t_average/k +1) -
log(cor_depth/k +1) )/m;
     }
     else
     {
        printf(" The depth of weld is just acceptable.\n");
        printf(" NO futher action is needed. \n");
        return;
     }

     if ( cor_current <= 0 )
     {
        printf(" Error  : Corrective current  <= 0 \n");
        printf(" Warning: Number of samples should be
'integer'  !!\n");
        return;
     }
     }

     if ( ch == 'v' )
     {
     if ( cor_depth > t_average )
     {
        if ( kind == '1' )
           cor_voltage = e_voltage + ( cor_depth / k -
t_average / k );

        else if ( kind == '2' )
           cor_voltage = e_voltage + ( pow(cor_depth/k,1/n)
- pow(t_average/k,1/n) );

        else if ( kind == '3' )
           cor_voltage = e_voltage + ( log(cor_depth/k +1) -
log(t_average/k +1) )/m;

     }
```

```
      else if ( cor_depth < t_average )
      {
         if ( kind == '1' )
            cor_voltage = e_voltage - ( t_average / k -
cor_depth / k );

         else if ( kind == '2' )
            cor_voltage = e_voltage - ( pow(t_average/k,1/n)
- pow(cor_depth/k,1/n) );

         else if ( kind == '3' )
            cor_voltage = e_voltage - ( log(t_average/k +1) -
log(cor_depth/k +1) )/m;
      }
      else
      {
         printf(" The depth of weld is just acceptable.\n");
         printf(" NO futher action is needed. \n");
         return;
      }

      if ( cor_voltage <= 0 )
      {
         printf(" Error  : Corrective voltage  <=  0 \n");
         printf(" Warning: Number of samples should be
'integer'  !!\n");
         return;
      }
      }
  }

/* Display results */
  {
     printf(" The acceptable depth of weld is %6.3f\n\n",
cor_depth);

     if ( ch == 'c' )
     {
     printf(" The welding current should adjust to %6.3f\n",
cor_current);
     }
     if ( ch =='v' )
     {
     printf(" The welding voltage should adjust to %6.3f\n",
cor_voltage);
     }

     printf(" The new depth of weld will be %6.3f\n\n",
cor_depth);
```

```
      if ( ch == 'c' )
      {
      printf(" ( for existing current of %6.3f ,\n",
 e_current);
      }
      if ( ch == 'v' )
      {
      printf(" ( for existing voltage of %6.3f ,\n",
 e_voltage);
      }

      printf(" required depth of weld is %6.3f ,",
 reqd_depth);
      printf(" and welding constant of %6.3f )\n\n", k);

      printf(" Press  ' F3 then Enter '  for running this
 program again.\n");
   }


 /* Analog to Digital procedure */
 /* void AD() */
   {
      float b, c, d;
      int   i, m, n;

      d=0;
      for ( i= 0; i < ad_loop; i++ )
      {
      outport( port+3 , 0 );              /* Clear register
 */
      delay( ad_delay );
      outport( port+0 , D_channel );

      for ( m=0; m<5; m++ )               /* Start convert */
      {
         delay( ad_delay );
         b = inport( port + 4 );
      }
      for ( n=0; n<9; n++)
      {
         delay( ad_delay );
         b = inport( port + 5 );
      }
      delay( ad_delay );
      b = inport( port + 2 );             /* Read high byte
 */
      delay( ad_delay );
      c = inport( port+1 );               /* Read low byte */
      d = ( b - 16*( (int)( b/16 ) ) ) * 256 + c;
```

```
      }
   }

/* Write data file */
/* void writeDF()  */
   {
      int i;
      FILE  *fp;

      fp = fopen( "tmp.dat","wt" );
      if ( fp == NULL )
      {
      printf("\n File Opening Error <write Captured
data>\n");
      exit(1);
      }
      for ( i= 0; i< num; i++ )
      {
      fprintf( fp,"%6.3f%6.3f%6.3f%6.3f%6.3f%6.3f",
         t_average, &reqd_depth, k, &acc_level, cor_depth,
cor_current );
      }
      fclose( fp );
   }

/* Read data file */
/* void read_A()  */
   {
      FILE  *fp;

      fp = fopen( "control.dat","rt" );
      if ( fp == NULL )
      {
      printf("\n File Opening Error <read data from
Pascal>\n");
      exit(1);
      }
      fscanf( fp,"%f", &sample );
      fclose( fp );
   }

/* Digital to Analog procedure */
/* void DA() */
   {
      float b,c,d;
      int   m,n,low,high;

      outport( port + 7 , high );            /* Output high
byte */
```

```
      outport( port + 6 , low );              /* Output low
byte */
   }

}
```

# Appendix E

## Copy of refereed journal papers published during the PhD programme

2·3

# TRANSACTIONS

## THE HONG KONG INSTITUTION OF ENGINEERS

VOLUME 2 • NUMBER 3
MARCH 1996

# A Temperature Model For Ultrasonic Measurement of Titanium Welds

**Winco K.C. Yung***, BEng, MSc(Eng), CEng, MIEE, MHKIE, MIEEE

**Robert Fenn**†, MSc, PhD, CEng, FIQA, FWeldI, MIBF, MIM

**Brian Ralph**†, MA, PhD, ScD, CEng, CPhys, FIM, FInstP, Hon. FRMS

*Ultrasonic techniques can be used to detect and locate the edge of a molten weld pool. However, to determine the size of the weld pool correctly from transit time of echoes (ultrasonic data) returned from the pool, a correction due to the temperature gradients must be included. No such data for titanium has been reported so far. This data is a must to allow real-time control and monitoring of the weld quality. The present paper investigates how the measured ultrasonic data was affected by temperature. Both plain sheets and weld on plate of 2.3 mm titanium alloy sheet (Ti-6Al-4V) were used in this study. An attempt was then made to provide a methodology to determine the necessary correction when computing the weld pool diameter.*

*It has been shown that the traveling time of the ultrasonic shear wave changes positively and the wave velocity changes inversely with temperature. Moreover, the weld pool diameter as ultrasonically measured was found to be smaller than the actual due to changes in the microstructure in the heat-affected-zone. A compensation value has been determined and applied so as to estimate the real pool diameter. To extend this methodology to a real-time application, a fast-enough data acquisition system is suggested to compute the pool size simultaneously and instantaneously.*

*Also, using the Lagrange interpolation method, a polynomial with power of 3 has been obtained for the ultrasonic response on this titanium alloy at elevated temperatures. However, this non-linearity has no adverse impact on the result given in this paper.*

*Keywords: Ultrasonic Measurement, Titanium, Temperature Compensation Factor, Weld Pool Diameter, Mathematical Model*

## Introduction

In dynamically loaded engineering welded structures, there is always a requirement for a full-penetration weld to prevent premature failure. Thus, the monitoring of weld penetration is of prime importance in the fabrication of these titanium structures. The control and monitoring of weld penetration has to be on a real-time basis to enable a closed-loop control, or many welded structures would have to be scrapped or reworked at very high cost. The use of sensors to monitor weld penetration, combined with real-time feedback control of the welding process has proved successful in this kind of control. Among many sensors developed so far, the ultrasonic sensor is the only type of sensor that is capable both of direct measurement of penetration depth (Stroud, 1983) and also performing it at the front side of the weld. The latter is critical in a lot of cases where access to the rear side of the workpiece is not feasible.

To control the weld penetration in real-time, information about the location of the liquid/solid interface between the molten weld pool and the surrounding solid base metal is critical. Ultrasonic technique can detect and locate the edge of a molten weld pool by virtue of its unique ability of ultrasonic wave to penetrate thick metal structures and be reflected at solid/liquid interfaces due to difference in acoustic impedance. For instance, measurement of the ultrasonic wave velocity in stainless steel (grade 304) samples by Lott (1984), using timing of pulses reflected from weld-pool interface, confirmed that

* Department of Manufacturing Engineering, The Hong Kong Polytechnic University

† Department of Material Technology, Brunel University of West London

the weld-pool size can be obtained from ultrasonic data.

However, to determine the size of the weld pool correctly, correction due to the temperature gradients within the pool must be included. Fenn (1989) and Lott and coworkers (1984) commented that to control weld penetration on a real-time basis, it is necessary to take into account the temperature gradient effect since the weld will experience temperatures up to the material's melting temperature. In other words, a quantitative understanding of the propagation of ultrasonic waves near molten (i.e. at elevated temperature) weld pools is to be acquired. On this basis, Fenn & Wooten (1986) have successfully confirmed the changes of longitudinal wave velocity and attenuation in steel with temperatures up to 1374°C. Parker and coworkers (1985) also reviewed the relationship of ultrasound wave velocity with temperature for a number of common metals up to their melting points.

However, no such data and investigations on titanium have been reported. Like other metals, the ultrasound (US) velocity in titanium changes drastically with temperature; data which is of fundamental importance to the development of any ultrasonic-sensor based expert control system. Until such detailed data are available for the correction of the US traveling distance (due to change in velocity), it is very difficult to make sufficiently accurate measurements to allow real-time control and monitoring of the weld quality. Thus there is a definite and fundamental need to investigate and obtain the necessary US data for titanium at elevated temperatures.

## Experimental Set-Up

To carry out the investigation, two critical problems must be dealt with before starting the experiments. The first problem is that the transducer would be damaged if it were in contact with high temperatures. Another problem is to maintain the temperature of the titanium sheet during the tests. Also, to avoid any temperature gradient, a water-cooled arrangement near the transducer was employed. The water cooled arrangement was developed by modifying the cover of a carbolite furnace which was used to provide the heating source.

### Design of Furnace Cover

Figure 1 shows the section view of the cover. This cover allows the titanium sheet to pass through, such that part of the sheet is in the furnace environment at high temperature and part is exposed to the atmospheric environment at which the titanium sheet is maintained at the room temperature, and the ultrasonic transducer is placed here for the tests. The ultrasound is transmitted into the titanium sheet and goes into the high temperature zone to achieve the purpose of the test.

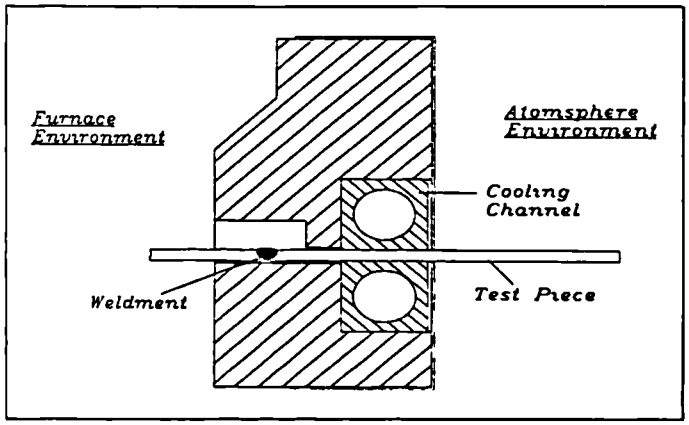


*Figure 1 – Section view of modified furnace cover*

In between the hot and cold zones, a cooling channel and brickwork were used as insulation between the zones. The high temperature inside the furnace was isolated from the outside environment by the brick insulation such that the temperature could be kept nearly constant and the cooling channel is to cool down the titanium sheet to ambient temperature.

### Material and Weld

The material used was 2.3 mm thick titanium alloy sheet (IMI 318, Ti-6Al-4V). Both plain sheet and weld bead on sheet were used as specimens. The plain sheet sample was used as a reference in the experiments. A weld bead was formed on a number of sheets using the following welding parameters:

weld mode: TIG weld on sheet without filler metal;
welding current: 120 A;
welding speed: 4.23 mm $s^{-1}$ (mm per second);
shielding gas flow rate: 3 liter/minute.

A representative specimen was carefully selected from all welded samples for subsequent measurements. The diameter of the weld pool of this specimen was measured to be 5.07 mm.

### Ultrasonic Testing

The time-base of the ultrasonicscope was first calibrated to corresponding traveling distance (D) of the US waves. Angled shear waves were used in the ultrasonic measurement since the monitoring is more easily attained. The best shear wave angle was found to be related to plate thickness (Fenn & Wooten, 1986) but generally either 45 or 60 degree transducers were used. Coupling between the 5 MHz US shear wave crystal and the specimen end was achieved by an acoustic oil. The transducer was placed at a fixed distance (80 mm) from the weld bead center line. The temperature of the furnace was then raised and the positions of the returned echo signal from the sheet edge and from the weld pool were recorded, in terms of calibrated time-base from the ultrasonicscope, and plotted for each of hundreds of temperatures.

## Results and Computation

The actual measured quantity is the traveling time t(T) of the US signal at temperature T and $V_r$, v(t) are the US velocities at room temperature (RT) and temperature T respectively. Let D(t) denote the apparent distance traveled for the plain sheet sample, $D_w(T)$ denote that for the bead on plate sample, and $D_c$ = 80 mm is constant. Figure 2 gives a graph of D(T) vs T, figure 3 gives a graph of $D_w(T)$ vs T, figure 4 gives the apparent weld pool radius Ra = $D_c$ - $D_w(T)$, Table 1 and figure 5 give D(T) - $D_w(T)$.

$$D(T) = V_r\, t(T) \qquad (1)$$

$D(T) = mT + k$ from figure 2, m is slope of graph and k is constant (2)

$\therefore \quad t(T) = (mT + k) / Vr = m' T + k'$ (3)

Since the actual distance traveled does not change as temperature increases (the small degree of linear expansion may be ignored here since the alloy sheet length is less than 180 mm), the change noted is due to the variation of velocity and time. If the temperature dependence of D(T) and Dw(T) comes solely from the temperature dependence of the US velocity, then

$$D_c = V(T)\, t(T) \quad (4)$$

$\therefore$ from (3), $V(T) = D_c / t(T) = D_c / (m' T + k')$ (5)

(4) & (1) $\Rightarrow$ $D(T) = D_c (V_c / V(T))$ (6)

Similarly, $D_w(T) = (D_c - R)(V_c / V(T))$ (7)

where R is the true weld pool radius

| Temperature (°C) | 20.5 | 44.1 | 100 | 200 | 300 | 400 | 500 | 560 | 600 |
|---|---|---|---|---|---|---|---|---|---|
| Radius of Weld Pool (mm) | 1.52 | 1.50 | 1.38 | 1.17 | 1.00 | 1.17 | 1.25 | 1.12 | 1.09 |

*Table 1 – Compensated weld pool radius at various temperatures*

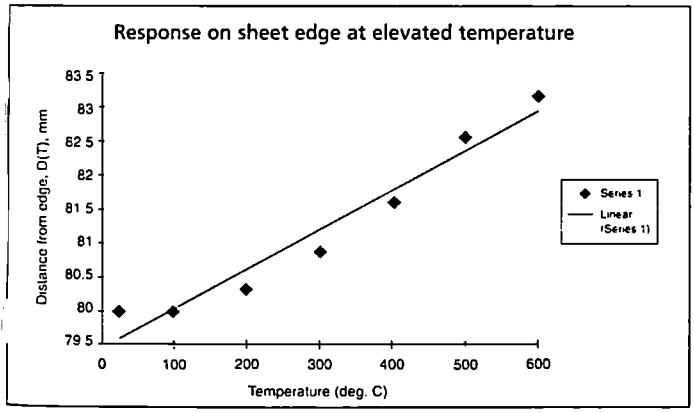


*Figure 2 – Ultrasound response on plain sheet edge at elevated temperatures*

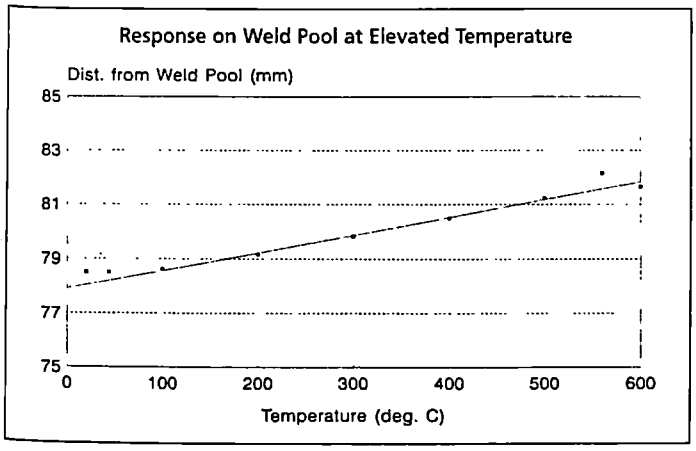


*Figure 3 – Graph of distance from weld pool, $D_w(T)$ vs temperature*

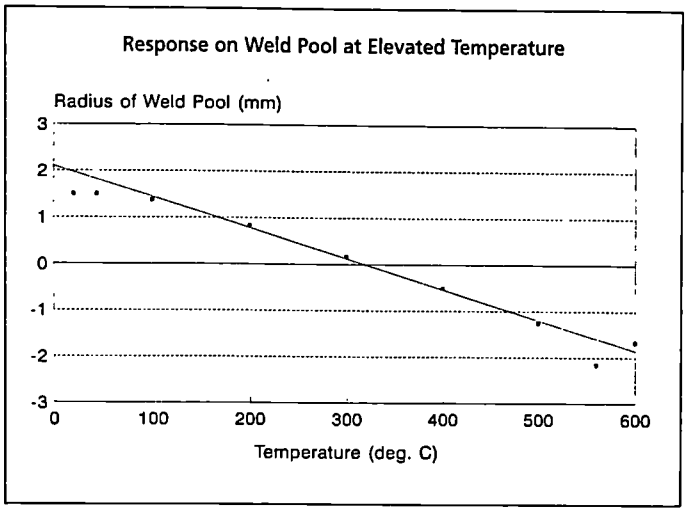


*Figure 4 – Graph of apparent radius of weld pool, $R_a$ vs temperature*

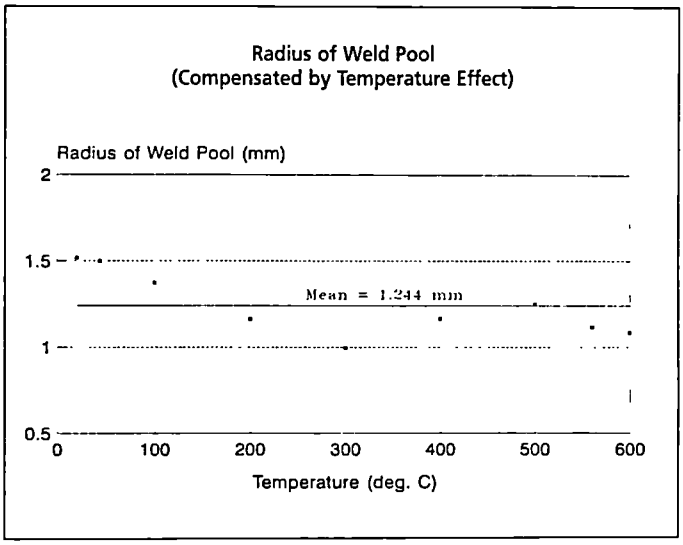


*Figure 5 – Graph of compensated weld pool radius, R vs temperature*

## Discussion

### Plain Sheet: US Response at Edge at Elevated Temperatures

From figure 2, the echoes' position relative to sheet edge is seen to change approximately linearly with temperature. The slope of this line is approximately equal to 0.00585 mm $K^{-1}$ which is a very small value. This value tells that when the temperature increases by 100°C, the apparent distance traveled by the US wave increases by 0.585 mm. Since the apparent distance actually corresponds to the time of travel, the travel time is changing approximately linearly with temperature.

From (5), it is expected that the ultrasound (US) velocity decreases as temperature increases and further, by differentiating V(T) of equation with respect to temperature T,

$$dV(T)/dT = - (D_c * m') / (m'T + k')^2 \quad (8)$$

Thus, the square of temperature affects the rate of change of ultrasound velocity.

### Bead on Plate: US Response at Weld Pool at Elevated Temperatures

The measured distance, $D_w(T)$, apparently traveled from probe to the weld pool boundary is shown in figure 3. The increase of this apparent distance is due to the reduction in velocity of the US waves at elevated temperature. As before, this increase in apparent distance is changing approximately linearly with the temperature with the increasing rate at 0.00659 mm $K^{-1}$. Since the apparent radius (not compensated) of the weld pool $R_a$ together with $D_w(T)$ equals distance between US probe to weld center line (experimentally fixed at 80 mm), the increase in $D_w(T)$ causes $R_a$ to decrease as shown in figure 4 with a slope -0.00659 mm $K^{-1}$, cutting the Y axis at 2.101 mm.

The data and graph in figure 2, which shows the additional traveling distance by US due to temperature effect, was then included to calculate the actual weld pool radius. For instance at 500°C, the additional distance traveled from figure 2 is (82.50-80.00) mm = 2.50 mm. From the data in figure 3, the apparent distance traveled, $D_w(T)$ is 81.25 mm. So the actual distance traveled is (81.25-2.50) mm = 78.75 mm. As $D_w(T)$ and weld pool radius add up to 80 mm (experimentally fixed), therefore, the weld pool radius after compensation at 500°C is (80.00-78.75) mm = 1.25 mm. Table 1 shows the weld pool radius at various temperatures after compensation.

Comparing to the actual radius (diameter) of the weld pool, 2.54 mm (5.07 mm), measured previously, all the compensated radius in table 1 are smaller. One of the major reasons is due to the presence of heat-affected-zone (HAZ) after welding. The change of the microstructure in heat-affected-zone to larger grain sizes causes a higher attenuation to the ultrasonic waves and so a longer traveling time for the ultrasound. There exists a compensation factor C in computing the actual weld pool radius in order to compensate for effects due to changes in microstructures in the HAZ. However, this factor can be dependent on many other parameters and can probably be useful if a large data base has been developed.

Also, in case real-time computation of weld pool radius is needed during welding process, the methodology used in computing the factor C can still be employed. However, since the microstructure in heat-affected-zone is then changing continuously, there is a need to use fast-enough data acquisition system to compute the pool radius simultaneously. Such data is then feedback to a control unit which in turn controls and/or varies the welding parameters, thus provides a closed-loop real-time monitoring of the welding process.

If the effect of temperature variation of the US velocity is to be eliminated, equations (6) and (7) can be re-arranged and as the factor of V(T) appears both in D(T) and $D_w(T)$, then,

$$D_w(T) / D(T) = (D_c - R) / D_c = 1 - R / D_c \quad (9)$$

$$\Rightarrow \quad R = D_c \{ 1 - D_w(T) / D(T) \} \quad (10)$$

From equation (10), the true weld pool radius can be computed for a range of temperatures as presented in table 2.

| Temperature (°C) | $D_w(T)$, mm | D(T), mm | R, mm |
|---|---|---|---|
| 100 | 78.62 | 80.00 | 1.38 |
| 200 | 79.16 | 80.33 | 1.17 |
| 300 | 79.83 | 80.83 | 0.990 |
| 400 | 80.50 | 81.67 | 1.15 |
| 500 | 81.25 | 82.50 | 1.21 |
| 600 | 81.67 | 83.17 | 1.44 |

*Table 2 – Computed true weld pool radius R at different temperatures*

It was found that the weld pool radius ranges from 0.990 mm to 1.44 mm with an average of 1.22 mm. The relationship between the true weld pool radius R and temperature, if any, may be seen from table 2 if data at temperatures beyond 600 degree Celsius are available.

After investigating the ultrasonic response at different temperatures, it is found that the data obtained is not best approximated using a straight line. A better fit to the obtained data in figure 4 requires an interpolation method. A Lagrange interpolation method was then used on these data. From these calculations, the polynomial obtained is:

$$P(T) = -1.21 \times 10^{-8} T^3 + 1.90 \times 10^{-5} T^2 - 1.67 \times 10^{-3} T + 80$$

Using this polynomial in the the computation, a different actual radius for each temperature was computed. However, only 6% deviation from the original result was observed. Thus, this nonlinearity can be tolerated.

## Future Development

Few points to be addressed in future development. The thinness of the sheet caused multiple signals such that similar amplitude signals were simultaneously display on the screen. Future investigations is recommended to employ a surface wave transducer to reduce this problem. It is also intended to use a lower frequency transducer because of its smaller attenuation which makes it more suitable for high temperature measurements. Also the temperature range will be extended above 600°C by modifications to the experimental rig. Moreover, a separate investigation is underway to study the actual temperature in the proximity of the weld pool to correlate this study to the real welding situation.

## Conclusion

(i) From these experiments, it has been shown clearly that the traveling time of ultrasonic shear waves changes linearly with the temperature and the ultrasound velocity changes inversely with the temperature. Also, the square of temperature affects the rate of change of ultrasound velocity.

(ii) The above relationship was used to determine the true weld pool radius. The radius so determined appears to be smaller than the actual due to temperature effect on ultrasound velocity and the presence of the altered microstructure within the heat-affected-zone.

(iii) The decrease in the indicated weld pool diameter can be compensated by a factor. However, this factor can be

dependent on many other parameters and can probably be useful if a large data base has been developed.

(iv) The effect of temperature variation of the ultrasound velocity on determination of true weld pool radius can be eliminated and the ratio of $D_w(T)$ / D(T) may give an indication of relationship between true weld pool radius and temperature if enough data at temperatures beyond 600°C are available.

## Acknowledgments

IMI Swansea kindly supplied the material. Part of the funding of the interaction which lead to this investigation came from a British Council LINK programme.

## References

Fenn R., Monitoring and controlling welding by ultrasonic means, *British Journal of Non-Destructive Testing*, No. 2, vol. 31, 1989, pp. 82-86.

Fenn R. & Wooton J.J, Longitudinal ultrasonic wave velocity and attenuation dependence on temperature between 20 to 1374 degree C, *Nondestructive Testing Communication*, vol. 2, 1986, pp. 115-126.

Lott L.A., Ultrasonic detection of molten/solid interfaces of weld pools, *Material evaluation*, vol. 42, 1984, pp.337-341.

Lott L.A., Johnson J.A. & Smartt H.B., Real-time ultrasonic sensing of arc welding processing, *Idaho report EGG-M-05283*, Idaho Falls, Idaho, 1984.

Parker R.L., Manning J.R. & Peterson N.C., Application of pulse-echo ultrasonic to locate the solid/liquid interface, *Journal of Applied Physics*, No. 11, vol. 58, 1985, pp. 4150-4164.

Croud R.R., *PhD Thesis*, Department of Metallurgy, Brunel University, 1983.

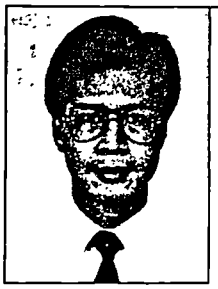

**Winco K.C. Yung**

Winco K.C. Yung receivd his bachelor degree in electrical engineering in University of Sydney of Australia and then a MSc(Eng) degree in manufacturing engineering at University of Hong Kong. He is currently an Assistant Professor in the Manufacturing Engineering Department at The Hong Kong Polytechnic University. Mr. Yung is a CEng, a full member of the IEE, HKIE and IEEE(USA). He published over 15 papers over past 3 years. Winco Yung is a PhD candidate registered at Brunel Unviersity of UK. His current research and publications include automatic penetration control in welding by ultrasonic sensor, weldability of high strength titanium alloy and laser drilling.

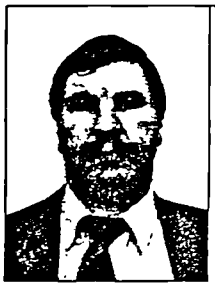

**Dr. Robert Fenn**

Dr. Robert Fenn, Senior Lecturer in the Department of Materials, Brunel University. Previous appointment was Scientific Officer at C.E.G.B. (Portishead). Previous to this he was Quality Assurance Manager at Osborn-Hadfields Steel Founders (UK).

**Prof. Brian Ralph**

Prof. Brian Ralph holds MA, PhD and DSc degrees from Cambridge where he was educated and on the academic staff from 1964 to 1983 (and fellow and sometime tutor of Jesus College, Cambridge). From 1984 to 1987 he headed the Materials Department at University College Cardiff, since then he has been at Brunel University – most recently as Dean of Technology.

Reprinted from

Journal of
Materials
Processing
Technology

Journal of Materials Processing Technology 63 (1997) 759-764

# An investigation into welding parameters affecting the tensile properties of titanium welds

Winco K.C. Yung[a], B. Ralph[b], W.B. Lee[c] and R. Fenn[d]

[a,c] Department of Manufacturing Engineering, Hong Kong Polytechnic University
[b,d] Department of Materials Technology, Brunel University of West London

ELSEVIER

ELSEVIER

Journal of Materials Processing Technology 63 (1997) 759-764

Journal of Materials Processing Technology

# An investigation into welding parameters affecting the tensile properties of titanium welds

Winco K.C. Yung[a], B. Ralph[b], W.B. Lee[c] and R. Fenn[d]

[a,c] Department of Manufacturing Engineering, Hong Kong Polytechnic University
[b,d] Department of Materials Technology, Brunel University of West London

Abstract

Grain size and amount of martensite formation affect the tensile strength of the alloy and these two factors are in turns related to the cooling rate of the welding process. There was found a trend of decreased tensile strength with the increase of welding heat input and a trend of increased tensile strength with the increase of welding cooling rate. Considering the effect of cooling rate on ductility, it was found that the higher the cooling rate, the larger is the relative elongation and hence the higher the weld's ductility.

## Nomenclature

$H_{net}$ = Net Heat input, J mm$^{-1}$
R = Cooling rate at a point on the weld center line, °C s$^{-1}$
$T_p$ = Peak temperature, °C
$T_0$ = The uniform initial temperature of the sheet, °C
$T_m$ = Melting temperature, °C
$T_c$ = The temperature of interest, °C
ρ = Density of material, g mm$^{-3}$
C = Specific heat of solid metal, J g$^{-1}$ °C$^{-1}$
k = Thermal conductivity, J mm$^{-1}$ s$^{-1}$ °C$^{-1}$
Y = Distance from the weld fusion boundary, mm
t = Thickness of sheet, mm
τ = Relative plate thickness
= Heat input, J mm$^{-1}$
η = Heat transfer efficiency
E = Volts, V
I = Amperage, A
V = Traveling speed of heat source, mm s$^{-1}$

## 1.0 Introduction

A number of studies [1-5] have shown that it can be difficult to achieve satisfactory properties when welding some high strength α β titanium alloys. It has become necessary to develop unique welding procedures and techniques to control the alpha/beta phase transformations and precipitation reactions responsible for the deleterious weld properties in these materials. For instance, it has been shown that control of weld heating and cooling rates by preheating could improve the toughness of Ti/6Al/6V/2Sn (Ti-662) welds [4]. The investigation here was conducted to gain a better understanding of the welding behavior of an advanced α/β titanium alloy, Ti/6Al/4V (Ti-64). This alloy was selected for study since it is the most commonly used titanium alloy and enhanced behavior would further extend its use. In this investigation, the microstructure and mechanical properties of Ti-64 tungsten-inert-gas (TIG) arc welds were examined in the as-welded condition.

## 2.0 Factors affecting mechanical properties of α/β alloys

### *2.1 Cooling rate*

It was found in previous studies [6,7] that the mechanical properties of alpha/beta titanium alloys are cooling-rate sensitive : high cooling rates produce more α and thinner α platelets, which lower toughness and reduce weldability, whilst low cooling rates promote the growth of α plates that enrich the β phase with β stabilizers. The enriched phase has a lower beta-transus ($M_s$) temperature and, hence, a lower tendency to transform to α, preferring to remain at room temperature as retained β. Large, tough α plates produced by low cooling rates divert crack propagation paths and possibly reduce crack propagation by blunting the crack tip. On the other hand, thin martensitic α plates will provide a poorer medium for energy absorption and limit resistance to crack propagation. These mechanisms, of course, are directly related to the strength, ductility and fracture toughness of these alloys. Therefore, once the effect of the cooling rate has been determined, control techniques for improving the mechanical properties can be explored, if needed, in a systematic manner.

In addition to the cooling rate, which is affected by the welding parameters, the mechanical properties of alpha/beta titanium alloys such as Ti-64 also strongly depend on their interstitial element content, on the prior beta grain size and on a homogeneous microstructure [8-12].


PII S0924-0136(96)02719-7

### 2.2 *Other factors affecting the mechanical properties*

i) Grain Size

It is well-established that grain boundaries affect the strength of metal material at low temperatures. Since slip cannot go directly from one grain to another, grain boundaries act as barriers during dislocation. When slip or cleavage take places, it happens only in particular crystallographic planes. Once slip or a crack propagate at the grain boundaries, it has to be nucleated and continue in the new direction in the adjacent grain. This means that the energy required for slip or a crack to propagate in metal with finer grains is higher compared to that in metal with coarser grains. Grain boundaries have been proven to be significant obstacles to the growth of crack [13]. Moreover, dislocations would pile-up at grain boundaries and hinder further dislocation. It was shown that for titanium alloy Ti/5Al/5Sn/2Zr/4Mo, the ultimate tensile strength decreased moderately and the elongation decreased significantly with increasing grain size. Therefore, grain refinement processes, which result in more grain boundaries, may improve the strength and ductility of a material.

When considering welding physics, the lower are the solidification rate and the cooling rate, the coarser are the grains. Broderick *et al.* [14], using the rapid solidification (RS) technique, showed that the microstructure of as-solidified Ti-64 was matensitic, with the martensite size decreasing with beta grain size, L, (μm), which in turn decreased with increasing cooling rate, R (K $s^{-1}$). Further, it was found that $L = 3.1 \times 10^6 R^{-0.93\pm0.12}$. This mathematical model suggests that the grain size of the beta phase and so the martensite phase, increases with decrease of the cooling rate. This is because the embryos, which are smaller than the critical size for grain growth, are easily re-dissolved into the molten metal pool when the temperature is high. As only a few embryos can grow into a nucleus successfully with a lower solidification rate, the grains are few and coarse. The results of applying RS to other alloy systems suggested that fine grain size could be produced in rapidly solidified Ti-64, leading to enhanced mechanical properties similar to those reported in a Ti/Mo/Al produced at high cooling rates [15].

Similar result suggested that a lower cooling rate resulted in significantly greater alpha plate coarseness, these resulting in lower strength. On the other hand, it was found that reducing the alpha plate thickness will increase both the tensile strength and the ductility [16]. Thus, it is believed that the strength of weld metal with high solidification rates and cooling rates may be greater than that with low rates, if the grain size effect is the only factor affecting the strength and ductility of the weld.

ii) Martensite formation

Martensite would be formed in alpha/beta titanium as carbon steel in fast cooling. When α/β titanium alloy cools fromteh α/β transformation temperature, alpha phase and beta stabilizer are precipitated, a low cooling rate promoting their precipitation. The ejected beta stabilizer enriches the untransformed beta phase, and so improve its stability. The enriched phase has a lower $M_s$ temperature and, hence, a lower tendency to transform to martensite. It was shown that for Ti-662 [17], the relative percentage of alpha phase (α) and martensite alpha phase (α'), and the fineness of α plates, all of which can be altered by different cooling rate, affected the mechanical properties of the alloy, including the tensile strength of the fusion zone of the weld.

Further, it was suggested that martensite began to age immediately after it was formed during cooling and when the martensite aged, fine alpha precipitated from it would increase its strength. It is expected that the faster the cooling rate, the finer the alpha precipitated and the higher strength it results. On the other hand, it may also be suspected that the beta stabilizing elements may distort the unit cell of titanium in room temperature if cooling rate is too fast and that it may also affect the strength of the alloy. However, this distorted structure only strengthen the metal little.

### 2.3 *Mathematical models on cooling rate and distribution of peak temperature*

The relative plate thickness, τ is given by [18]:

$$\tau = t\sqrt{\frac{\rho C(T_c - T_0)}{H_{net}}} \qquad \text{----------(1a)}$$

When $\tau > 0.75$, the plate is regarded as thick, being thin otherwise. When the plate is thin, heat flow is 2-directional [19] and the cooling rate, R, is determined by :

$$R = 2\pi k\rho C\left(\frac{t}{H_{net}}\right)^2 (T_c - T_0)^3 \qquad \text{----------(1b)}$$

Further, the peak temperature distribution during the welding process is given by [19] :

$$\frac{1}{T_p - T_0} = \frac{4.13\rho CtY}{H_{net}} + \frac{1}{T_m - T_0} \qquad \text{---------- (2)}$$

From Eqn. (2) :

$$H_{net} = \left[\frac{4.13\rho C}{\left(\frac{1}{T_p - T_0}\right) - \left(\frac{1}{T_m - T_0}\right)}\right] t\ Y \qquad \text{----------(3)}$$

Also, in terms of welding parameters :

Net heat input ($H_{net}$)=Heat input x Heat transfer efficiency

$= \mu (I \times V) / S$ ----------(4)

The theoretical net heat inputs of the welds were determined by Eqn. (3). Y is the distance from the edge of the fusion zone. In this study, the width of the heat-affected zones were used as Y. As in a study by Greenfield and Duvall [20], it was suggested that the heat-affected zone regions most distant from the fusion zone of an alloy (Ti-6246) were exposed to a temperature slightly below the beta transus. Therefore, the α/β transformation temperature was used here as the peak temperatures ($T_p$) on the boundary between the heat-affected zone and the base metal region. The other parameters were obtained from metal reference book or by direct measurement.

Since the relative plate thickness ($\tau$) ≤ 0.75 for all Ti/6Al/4V welds, the titanium plates were determined as thin. Therefore, Eqn. (1b) was used to determine the theoretical cooling rate.

## 3.0 The experiments

Titanium alloy Ti-64 welds were fabricated on 1.5 mm thin plate using a wide range of welding parameters. Acceptable welds were selected by visual inspection. The parameters of producing them were then used again to produce samples which were used to prepare transverse tensile test specimens.

Tensile tests were conducted on the weld specimens to find their strength (UTS). The load/extension curves were recorded during the test. The heat input and cooling rate were computed using previous equations and then tabled (Table 1). The fracture mode(s) of the specimens were investigated. The microstructures of the fusion zones, the heat-affected zones and base metals were also examined.

## 4.0 Results and discussion

### *4.1 Range of welding parameters producing acceptable quality welds*

Welds with acceptable visual quality were produced by pulsed TIG welding with welding currents of between 45 to 235 A, welding speeds of between 0.26 to 1.27 mm $s^{-1}$, and pulse on times of between 0.25 to 0.50 s. Within this welding parameter range, the as-welded Ti/6Al/4V had at least 1018 MPa strength (UTS) which was only 5.9% reduction as compared to that of the parent metal (1082 MPa). The "best" strength of the welds achieved (specimen C2) was 1048 MPa, which was only 3.2 % lower than that of the parent metal.

### *4.2 Factors affecting the tensile strength of weldment*

Previous study showed that the cooling rate appears to be especially critical in relation to the tensile properties for Ti/6Al/2Sn/4Zr/6Mo [20]. All of the Ti/6Al/4V welds prepared (except specimen C3), with lower cooling rates, fractured at the weld regions. The tensile strengths of the as-welded welds of Ti/6Al/4V were slightly lower than that of the base metal. This agrees with the findings of Thomas *et al.* [21] in the electron-beam welding (EBW) of Ti/6Al/4V. Specimen C3, having relative higher cooling rates, fractured at the base metal region, which agrees with the results of Wu's study on another α/β alloy [17].

Fig. 1 shows a trend of increasing tensile strength with increasing theoretical cooling rate. This indicated that within a particular range of cooling rate, there is a positive relationship between the cooling rate and the weldment strength. Also, it should be noted that C3, which was the only one sample which

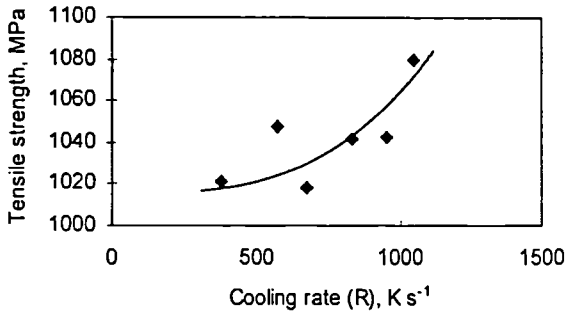


Figure 1 : Variation of the tensile strength of Ti/6Al/4V welds with the theoretical cooling rate at 1595°C.

Table 1 : Tensile strengths of welds and failure locations

| | Specimen no. | Failure location | Tensile strength (MPa) [a] at failure location ( ) shows relative extension | Heat input ($Jmm^{-1}$) | Net Heat Input ($Jmm^{-1}$) | Theoretical cooling rate, R, ($Ks^{-1}$) |
|---|---|---|---|---|---|---|
| Ti/6Al/4V | B1 | parent metal | 1082 (0.0) | | | |
| | B2 | parent metal | 1080 (0.0) | | | |
| Stage 1 | C1 | FZ | 1043 (1.020) | 345 | 32.0 | 953 |
| | C2 | FZ | 1048 (0.529) | 1130 | 39.8 | 575 |
| | C3 | BM | 1080 | 759 | 29.9 | 1050 |
| | C4 | FZ | 1042 (1.000) | 692 | 33.8 | 828 |
| | C5 | FZ | 1021 (0.412) | 828 | 51.5 | 379 |
| | C6 | FZ | 1018 (0.765) | 647 | 38.3 | 675 |

[a] Data placed at left of column means that the failure location was in the base metal.

fractured at the base metal, had the lowest theoretical net heat input (29.9J/mm) amongst the 6 welds prepared in this stage. This lowest net heat input resulted in the greatest cooling rate (1050°C/s at 1595°C, the alloy's melting temperature), which enhanced the strength of the weld. This is substantiated by C3 being found broken at the base metal region, which meant that the weld has a relatively greater strength.

The specimens C1-C6, with a lower cooling rate, still exhibit strengths comparable to that of the parent metals. The combined effect of the following factors are believed to be responsible for this :

i) The degree of coloration of the C1 to C6 welds showed that the average degree of oxidation in the specimens was obvious. This meant that a greater heat input or net heat input resulted in a greater degree of oxidation. The oxidation also implied the extent of inclusion of oxygen as a constituent element, which would increase the strength of the weld significantly if the amount of interstitial oxygen is not excessive.

ii) As the net heat inputs for specimens C1 to C6 were high, the amounts of nitrogen or other elements soluted during the welding process would also be high. (If the amount of nitrogen had been more than 0.13%, micro-cracks would have been present and caused a reduction of strength. However, no micro-cracks or other defects such as porosity was identified). This interstitial nitrogen also helps to improve the strength of the welds.

iii) The low cooling rates of specimens C1-C6 caused the former to have a more homogeneous microstructure and promoted the precipitation of alpha phase from martensite, which might have strengthened the fusion zones and the heat-affected zones.

### 4.3 *Tensile Ductility*

The fracture surfaces of the parent metal (as in control specimens B1 and B2) of Ti-64 were dull and porous, having a cup-and-cone microscopic appearance with clear macroscopic necking : these features indicated that ductile fracture had occurred. On the other hand, specimens which fractured at their welds had a faceted and shiny surface without any necking regions (Fig. 2) : these featrues showed that the fracture of the weld metal was brittle-like fracture, implying that the ductility of the alloy was deteriorated at the fusion zone upon welding. The reduction of ductility was further substantiated by making a comparison between the loading curves of control specimens (B1 and B2) with that of the weld specimens. The latter specimens exhibited elongations only 1/3 to 1/2 of that the control specimens. As these elongations may be taken as an indication of the strains of the specimens, the finding may be interpreted as a reduction of ductility. This reduction of ductility was probably due to the low ductility of martensite, a large grain size and contaminant embrittlement.

Further, although the ductility of the welds or heat-affected zones cannot be determined exactly from elongations of the specimens indicated in the load/extension curves, it is useful to study the effect of cooling rate on the ductility of Ti-64 welds by comparing the relative elongations measured from the load/extension curves of the specimens for different cooling rates. With reference to Table 1, it was found that the greater the cooling rate, the greater is the relative elongation and hence the greater is the ductility of the welds. A graph was plotted as Fig. 3 to examine the relationship between the relative elongation and the cooling rate. The graph in the figure is a third-order polynomial. In other words, the elongation is approximately related to the third power of the cooling rate. Therefore, considering the relative elongation alone, the control of cooling rate affects the ductility of the weldment quite significantly.

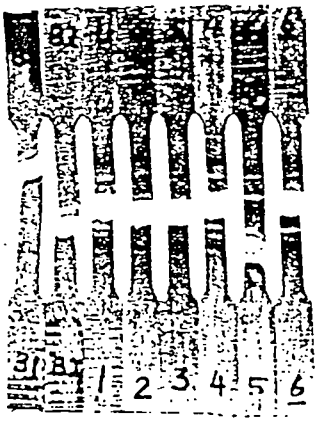


Figure 2 : Tensile test specimens of Ti/6Al/4V showing faceted and shiny surfaces

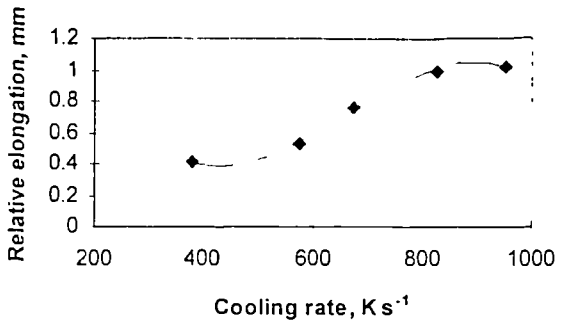


Figure 3 : Relationship between the relative elongation and the cooling rate

## 5.0 Conclusions

Based on the experimental results and discussions, conclusions were drawn as follows :

i) For Ti-64 alloy, welds with acceptable visual quality were produced by pulsed TIG welding with welding currents of between 45 to 235 A, welding speeds of between 0.26 to 1.27 mm $s^{-1}$, and pulse-on times of between 0.25 to 0.50 s. The "best" strength of the welds achieved (specimen C2) was 1048 MPa, which was only 3.2 % lower than that of parent metal.

ii) At low cooling rates, the more homogeneous microstructure and the inclusion of interstitial element such as oxygen and nitrogen were significant factors in contributing to the strength of the weld.

i) The ductility of the as-welded weld metal of Ti-64 was lower than that of the parent, metal which was revealed by the change of fracture mode from ductile fracture in the parent metal to brittle-like fracture at the weldment. The reduction of ductility was further substantiated by noting that most of the specimens exhibited elongations only 1/3 to 1/2 of that the control specimens. The reduction in ductility was due to the low ductility of martensite, a larger grain size and contaminant embrittlement.

Considering the effect of cooling rate on ductility, it was found that the higher the cooling rate, the larger is the relative elongation and hence the higher the weld's ductility.

## Acknowledgments

'I Swansea kindly supplied the material. Part of the funding of 'e interaction which lead to this investigation came from a 'r tish Council LINK programme.

## References

Mitchell, D.R. and Tucker, T.J., "The properties and transformation characteristics in welds in Ti-6Al-2Sn-4Zr-2Mo titanium alloy", Welding J., 48 (1), (Jan. 1969), Res. Supp., 23s-33s.

Schwenk, W., Kaehler, W.A. and Kennedy, J.R., "Weldability of titanium alloy sheets 6Al-6V-2Sn and 8Al-1Mo1V." Welding J., 46 (2), (Feb.1967), Res.Suppl., 64s-73s.

Simpson, R.P. and Wu, K.C., "Microstructure - property control with postweld heat treatment in Ti/6Al 6V/2Sn", Welding J., 53 (1), (Jan.1974), Res. Suppl., 13s-18s.

4. Lewis, R.E. and Wu, K.C., "A study of weld heat-affected zones in the titanium 6Al-6V-2Sn alloy", Welding J., 42 (6), (June 1963), Res. Suppl., 241s-249s.

5. Hatch, W., "Development of welding practices for titanium alloy 8Mo-8V-2Fe-3Al", Technical report to army materials and mechanics research agency, Watertown, Ma., AMMRC PTR-73-4, (March 1973).

6. Wu, K.C., "Weldability study of titanium 8Al-1Mo-1V", Rene 41, Northrop report NOR 65-250, (Oct. 1965).

7. Wu K.C., "Qualitative evaluation of the heat-affected zone in the tungsten inert gas welding of titanium alloys", Water Arsenal memorandum report, (1961).

8. Chesnutt, J.C., Rhodes, C.G. and Williams, J.C., "Relationship between mechanical properties, microstructures, and fracture topography in alpha + beta titanium alloys", Fractograph-Microscopic Cracking Processes, ASTM STP 600, (1976), 99-138.

9. Greenfield, M.A., Pierce, C.M., Hall, J.A., "The effect of microstructure on the control of mechanical properties in alpha/beta titanium alloys", Titanium Sci. and Tech., 3, (1972), 1731-1743.

10. Lin, F.S., Starke, E.A. Jr., Chakrabortty, S.B., Gysler, A., "The effect of microstructure on the deformation modes and mechanical properties of Ti-6211 : part 1, Widmanstatten structures. Met. Trans. 15A, (1984), 1229-1246.

11. Peters, M., Williams, J.C., "Microstructure and mechanical properties of a welded (alpha + beta) Ti alloy. Met. Trans. 15A, (1984), 1589-1596.

12. Enjo, T., Kuroda, T., Nishizawa, M., "Microstructure and mechanical properties in weld heat-affected zone of titanium alloy", Trans. of JWRI 17 (2), (1988), 113-118.

13. Jieping Zhang, et al., "Tensile deformation and fracture in high purity titanium: In situ observation by scanning electron microscopy", *Materials Science and Engineering A: Structural Materials: Properties, Microstructure and Processing*, A114, (2), (1989), 89-96.

14. T.F. Broderick, A.G. Jackson, H. Jones and F.H. Froes, "The effect of cooling conditions on the microstructure of rapidly solidified Ti 6Al 4V", *Met. Trans. A*, 16A, (11), (1985), 1951-1958.

15. Belov, A.F. and Polkin, I.S., "German metallurgical society workshop", University of Nuremberg, Erlangen, (July 12, 1982).

16. S.J.Chen and J.H. Devletian, "Microstructure and mechanical properties of electroslag welds in Ti/6Al/4V alloy", *Welding J.*, 69, (9), (1990), 319s-324s.

17. K.C. Wu, "Correlation of properties and microstructure in welded Ti/6Al/6V/2Sn", *Welding J.*, 60, (11), (1981), 219s-226s.

18. E.F. Nippes, *Metal Handbook, 9th Ed., Vol. 6 Welding, Brazing and Soldering*, American Society for Metals, USA, 1983.

19. Adams, C.M., Jr., "Cooling rate and peak temperatures in fusion welding." *Welding J.*, 37, (5), (1958), 210s-215s.

20. M.A. Greenfield and D.S.Duvall, "Welding of an advanced high strength titanium alloy", *Welding J.*, 54, (3), (1975), 73s - 80s.

21. G.Thomas, V. Ramachandra and R. Ganeshan, "Effect of pre- and post-weld heat treatments on the mechanical properties of electron bead welded Ti/6Al/4V alloy.", *J. of Mat. Sci.*, 28, (1993), 4892-4899.

Reprinted from

Journal of
Materials
Processing
Technology

Journal of Materials Processing Technology 63 (1997) 802-805

# The Control of The Thin-plate Welds Geometry and Microstructure

Winco K C. Yung[a], W B. Lee[b], B, Ralph[c] and R. Fenn[d]
[a,b] Department of Manufacturing Engineering. Hong Kong Polytechnic University
[c,d] Department of Materials Technology, Brunel University of West London

ELSEVIER

ELSEVIER

Journal of Materials Processing Technology 63 (1997) 802-805

Journal of Materials Processing Technology

# The Control of The Thin-plate Welds Geometry and Microstructure

Winco K.C. Yung[a], W.B. Lee[b], B, Ralph[c] and R. Fenn[d]
[a,b] Department of Manufacturing Engineering, Hong Kong Polytechnic University
[c,d] Department of Materials Technology, Brunel University of West London

Abstract

In this paper, an attempt was made to employ conventional shear waves to investigate the quality of thin-plate welds. A quantitative measure of the weld pool width was suggested, and the alignment as well as the symmetry of the pool about the weld line is indicated without micro-sectioning the weld. Also, the relative grain sizes around the weld's fusion zone could be indicated by their corresponding ultrasonic attenuation. Mathematical relationships of ultrasonic attenuation with welding current and heat input rate were established.

## 1. Introduction

Ultrasonic (US) techniques offer very useful and versatile ways of investigating the microstructure and geometry of material welds. Basically, a transducer operating in the pulse-echo mode converts electrical signals into high-frequency sound waves that travel to the area of the weld pool. When the sound wave hits the metal/molten metal interface, a portion of the energy in the wave is reflected, this ultrasonic echo providing information about the location of the interface.

There are various mechanisms by which energy can be lost from ultrasonic waves propagating through real materials, and measurement of this ultrasonic attenuation can yield valuable information about the weld geometry [1,2] and internal microstructure [3], particularly around the weld bead. Amongst the inhomogeneties which can cause ultrasonic attenuation, those at grain boundaries and interphase boundaries are of most interest as far as welding control is concerned.

### *1 Investigation of thin-plate welds geometry and microstructure*

Work into the feasibility of detecting the molten pool started in 1977 [4,5]. Since then much research effort has been put into the application of ultrasonic sensors on a real-time basis. However, most work was done on thick materials [6-8], i.e. any thickness over 10 mm, and very little on thinner materials: one of the possible reasons for which may be the need of using Surface or Lamb waves for "better" ultrasonic detection, which are more complicated to generate and interpret than are conventional ultrasonic compression and/or shear waves.

### *1.2 Various investigation techniques*

For background purposes, it will suffice here to say that Lamb waves are the type of stress wave that may be propagated in a thin sheet with stress-free surfaces and that they consist of an infinite number of modes of vibration. Surface waves, which are also named Rayleigh waves, are defined as elastic vibrations the energies of which are confined to a narrow region just below the free surface of an extended solid.

Although both of these waves offer some advantages in revealing the quality of thin plate welds[9,10], they also suffer from constraints. For example, when working with surface waves, the surface of the solid under investigation has to be very smooth [10], which cannot be achieved easily in practice. Any scratch or defect on or just below the surface will cause an acoustic reflection, and will give rise to unwanted signals.

On the other hand, when working with Lamb waves, the generation of pure mode waves requires a tight control on the bandwidth and beam spread of the signals produced from the ultrasonic transducer [11], which involves very complicated procedures and control.

### *1.3 Technique using shear waves*

In this paper, conventional shear waves were used to investigate the welding of thin plate material (6 mm 304 stainless steel) and the welds geometry and microstructure. Shear waves were chosen over compression wave because of there better reflectivity at the inhomogeneties around the weld bead interface and the advantage of allowing measurement from the welding side of the plate rather than on edge (as in the case of using compression waves).

## 2. Experimental details

All the weldments were done using a TIG (Tungsten Inert Gas) welder. The material used was 6 mm AISI 304 stainless steel plate with ER308 filler metal of 3.2 mm diameter. The arc length was maintained at 2 mm. Pure Argon gas was used as the shielding gas with a flow rate controlled at 83.3 $cm^3\ s^{-1}$ (5 l/minute). The welding parameters selected included welding currents of between 135 A and 200 A, welding speeds of from 1.7 $mms^{-1}$ to 2.1 $mms^{-1}$ (4.0 ipm to 5.0 ipm) and a welding voltage of 12.8 V. The weldments were taken for analysis by an ultrasonicscope. A 4 MHz dual angle-TR-probe was employed to generate a 60 degree shear wave, with oil as the sonic couplant. Before carry out the ultrasonic measurements, the system was calibrated using a standard A2 IIW calibration


PII S0924-0136(96)02728-8

Table 2 : Amplitude of the reflected signal and the welding parameters

| Sample no. | Amplitude A; $A^{2/3}$ (unit) | Welding parameters: Current, I (A) | Speed, v (mm $s^{-1}$) | Heat input rate, Q ($Jmm^{-1}$) |
|---|---|---|---|---|
| 1 | 4.0; 2.53 | 160 | 2.12 | 724.5 |
| 2 | 5.0; 2.94 | 135 | 1.69 | 766.9 |
| 3 | 46.1; 13.02 | 200 | 2.12 | 905.7 |
| 4 | 11.2; 5.05 | 140 | 1.69 | 795.3 |
| 5 | 14.1; 5.89 | 150 | 1.69 | 852.1 |
| 6 | 14.2; 5.92 | 153 | 2.16 | 679.3 |

Depending upon the structural and positional make-up of a single grain, the ultrasound will change velocity, consequently the ultrasound is scattered by grain boundaries. If d is the grain size, $\lambda$ is the wave length of the ultrasound and A is the reflected signal amplitude, Hecht and his co-workers [12] proved that, neglecting diffraction losses and multiple-scattering, in the Rayleigh scattering range which is characterized by :

$$0.02 \leq d/\lambda \leq 0.2 \quad (1)$$

then :

$$d = K_d A^{2/3} \quad (2)$$

where $K_d$ is a constant depending on the experimental set-up.

Hecht et al later also showed that $A^{2/3}$ changes positively with d. With this as background, graphs of amplitude data were plotted against welding current (I) and heat input rate (Q) from Table 2 and presented in Figs. 3 and 4. It can be seen that, within experimental accuracy, both the welding current and the heat input rate changed positively with amplitude (A) similar to (2) viz :

$$A^{2/3} = K_i I, \quad (K_i \text{ is a constant}) \quad (3)$$

and heat input rate :

$$A^{2/3} = K_q Q, \quad (K_q \text{ is a constant}) \quad (4)$$

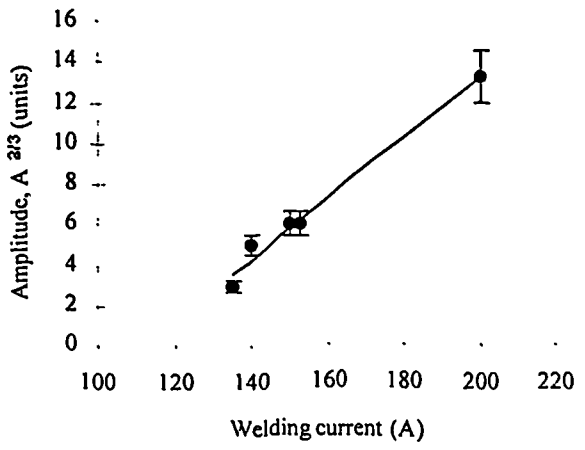


Figure 3 : Graph of amplitude of the ultrasonic signal vs the welding current

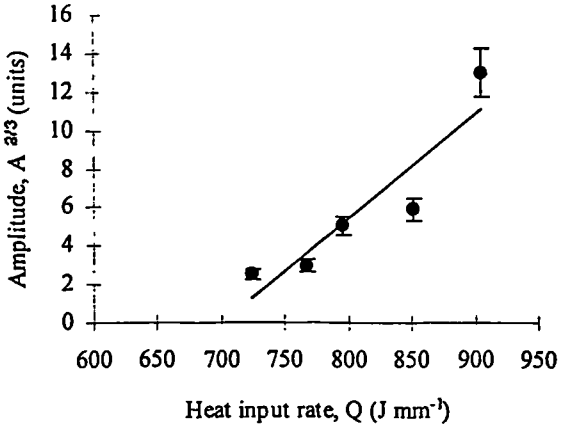


Figure 4 : Graph of amplitude of the ultrasonic signal vs the heat input rate

Comparing Eqn. (2) with Eqns (3) and (4), it can be deduced that :

$$I = K_1 d, \quad (K_1 \text{ is a constant}) \quad (5)$$

$$Q = K_2 d, \quad (K_2 \text{ is a constant}) \quad (6)$$

The above can be explained in terms of the final grain size around the fusion zone boundary increasing with increasing peak temperature and increasing residence time (time of heating and cooling). As the maximum peak temperature is related to the welding current, it justifies Eqn.(5). The residence time for three-dimensional heat flow may be obtained from the charts developed by Christensen and his co-workers [13], these charts showing that the residence time is roughly proportional to Q (the heat input rate). Thus the heat input rate affects the grain size positively, which further justifies Eqn. (6) above.

## 4. Conclusions

In this paper, an attempt was made to employ conventional shear waves to investigate the quality of thin-plate welds and obtain information related to the microstructure around the weld's fusion zone boundary and the geometry of the weld bead.

Although it was a post-weld study, it was found that it did provide some good understanding of the weld.

It is shown that by calculating the Time-of-Flight, a quantitative measure of the weld pool width was suggested, and the alignment as well as the symmetry of the pool about the weld line is indicated. This provides a means to obtain information related to the weld joint quality without micro-sectioning the weld.

Also, it was found that the relative grain sizes around the weld's fusion zone, resulting from different welding parameters and heat input rates, could be indicated by their corresponding ultrasonic attenuation. Also, mathematical relationships of ultrasonic attenuation (received signal amplitude) with welding current and heat input rate were established.

For on-line use of the technique presented in this paper, it is essential that the information on reflected US signals can be analysed efficiently, accurately and automatically, to enable any changes in the welding parameters to be carried out quickly. Since the microstructure around the weld bead is changing continuously, there is a need to use a sufficiently fast data acquisition system to determine the weld geometry and grain size from the US signals. Such data is then fed back to a control unit which in turn controls and/or varies the welding parameters, thus providing closed-loop, real-time monitoring of the weld process and of the resulting weld geometry and grain size.

## Acknowledgment

The authors wish to gratefully thank the Research Committe of the Hong Kong Polytechnic University for the support of this research project.

## References

[1] C. Duffill, G. Haywood, B. Scruby, J. Stares, "On-line Assessment of Weld Quality using Ultrasonics", *Harwell Report* AERE 13401. (1989).

[2] R.L.Parker,"Ultrasonic Measurement of Solid/Liquid interface during Solification and Melting of Metals", *Physics in the Steel Industry Conf. (New York) Proc.* No.84, (1982) pp.254-271.

[3] R.E.Green, "Effect of Metallic Microstructure on Ultrasonic Attenuation", *Nondestructive Eval.*, (1981) pp.115-132.

[4] L.A.Lott, J.A.Johnson, and H.B.Smartt, "Real-Time Ultrasonic Sensing of Arc Welding Processes", *Proc. of Symp. on Nondestructive Eval. Applications and Mat. Processing, American Society for Metals*, (1983) pp. 13-22.

[5] L.A.Lott, "Ultrasonic Detection of Molten/Solid Interfaces in Weld Pools", *Mat. Eval.*, 42, (1984) pp. 337-341.

[6] R.Fenn & R.R.Stroud, "The Measurement and Control of Penetration during Submerged-Arc Welding", Paper 5, *Int. Conf. on Offshore Structures, The Welding Institute, London*, (1982) pp. 5-1 to 5-5.

[7] J.A.Johnson, N.M.Carlson, J.O.Bolstad, H.B.Smartt, M.B.Ward, R.T.Allemeier, L.A.Lott and D.C.Kunerth, "Automated Welding Process Sensing and Control", *Proc. of Second Int. Symp. on the Nondestructive Characterisation of Materials*, 1986, pp. 409-417.

[8] Stroud R., "Problems and Observations whilst Dynamically Monitoring Molten Weld Pools using Ultrasound", *British J. of N.D.T.*, 31, (1989) pp. 29-32.

[9] E.J.Kubiak and R.R.Rowand, "Lamb Wave Inspection System for Thin-Sheet Metals", *6th Int. Conf. on Non-Destructive Testing*, Report No. K5, (1970) pp. 47-57.

[10] E.G.Cook and H.E.Valkenburg, "Surface Waves at Ultrasonic Frequencies", *American Society for Testing of Materials Bull.*, No. 198, (1954) pp. 81-84.

[11] D.N.Alleyne and P.Cawley, "Optimization of Lamb Wave Inspection Techniques", *NDT & E Int.*, 25, (1), (1992) pp. 11-22.

[12] A.Hecht, R.Thiel, Neumann and E.Mundry, "Nondestructive Determination of Grain Size in Austenitic Sheet by Ultrasonic Backscattering", *Mat. Eval.*, 39, (1981) pp. 934-938.

[13] N.Christensen, V. de L.Davies, K.Gjermundsen, "Distribution of Temperatures in Arc Welding", *British Welding J.*, 12, (1965) pp. 54-74.

TECHNICAL PAPER

MS97-192

# A Study on the Effect of Welding Parameters and Heat Input Rates on Titanium Weld's Grain Size

## authors

WINCO K.C. YUNG
Assistant Professor
Hong Kong Polytechnic University
Hong Kong

ROBERT FENN
Brunel University
of West London
United Kingdom

BRIAN RALPH
Brunel University
of West London
United Kingdom

## abstract

Fine grains help to improve the mechanical properties of the weld such as ductility and fracture toughness. In most titanium welding applications, beta grain size is determined principally by the weld energy input, with a higher energy input promoting a courser grain size. The beta grain size may be reduced somewhat by altering the welding parameters. This paper presents a study on the effect of welding parameters (current and speed) and corresponding heat input rate and cooling rate on the grain size of a titanium $\alpha/\beta$ alloy. It was found that with smaller heat input rates, the effect of welding speed in determining the grain size was found more significant than that of welding current. It was also found that with lower cooling rate, the grain size was larger. At the HAZ, there is a general decrease of grain size when moving towards the parent metal.

## conference

NAMRC XXV
May 20-23, 1997
Lincoln, Nebraska

## terms

Titanium Alloys
Cooling Rate
Welding Parameter
Heat Input Rate
TIG Welding
Grain Size

Society of
Manufacturing
Engineers
1997



Sponsored by the
North American Manufacturing Research Institution
of the Society of Manufacturing Engineers
One SME Drive • P.O. Box 930 • Dearborn, MI 48121
Phone (313) 271-1500

## ABSTRACT

Fine grains help to improve the mechanical properties of the weld such as ductility and fracture toughness. In most titanium welding applications, beta grain size is determined principally by the weld energy input, with a higher energy input promoting a coarser grain size. The beta grain size may be reduced somewhat by altering the welding parameters. This paper presents a study on the effect of welding parameters (current and speed) and corresponding heat input rate and cooling rate on the grain size of an titanium $\alpha/\beta$ alloy. It was found that with smaller heat input rates, the effect of welding speed in determining the grain size was found more significant than that of welding current. It was also found that lower the cooling rate, larger was the grain size. At the HAZ, there is a general decrease of grain size when moving towards the parent metal.


## INTRODUCTION

It is well known that the formation of fine grains in the fusion zone of a weld has many advantages. Finer grains help to reduce the susceptibility of the weld metal to solidification cracking during welding. Moreover, fine grains help to improve the mechanical properties of the weld such as ductility and fracture toughness. According to Easterling (1992), the crystal that are formed during solidification of the weld pool are nucleated by the solid crystals located at the solid-liquid interface and it is epiaxial. The primary grain size is determined by the grain size of the solid metal at the fusion boundary.

## EFFECT OF COOLING RATE ON GRAIN SIZE

The work of Watanabe et al. (1995) shows that the grain size is influenced by the welding speed. The grain size decreases when the welding speed increases. According to Kou (1987), under the same heat input, the cooling rate increases with increases the welding speed. Besides, the higher the cooling rate, the finer the cell spacing of the structure. Therefore, the subgrain structure becomes finer as the welding speed increases. In fact, it has been observed in several metals that the higher the heat input rate of the weld, the coarser the dendrite arm spacing. Furthermore, finer cell spacing has the higher ductility and yield strength of the weld and the more effective the postweld heat treatment.

For the commercial pure titanium alloy, the slow cooling rate results the size of the saw-tooth-like $\alpha$ structure or the needle-like $\alpha$ structure become larger. For the $\alpha+\beta$ system alloys, the prior $\beta$ grains is coarser and precipitates coarser needle-like $\alpha$ phase during slow cooling. For the cooling speed is high, the diameter of prior $\beta$ grains become smaller and the $\alpha$ phase of the grain boundary does not precipitate and so the grains become single martensite phase.

## GRAIN SIZE & HEAT INPUT OF TITANIUM WELDS

Fusion welds in titanium alloys are generally characterized by coarse, columnar-shaped beta grains in the fusion zone (FZ). FZ beta grains nucleate epiaxially from coarsened beta grains in the weld HAZ and grow competitively into the weld pools. The FZ beta grain structure is dependent on several factors, including : (1) the weld thermal cycle as it influences the size of the nucleating beta grains in the near-HAZ and the cooling rate during FZ solidification and (2) the shape of the weld pool due to its influences on the competitive beta grain growth process.

In most titanium welding applications, beta grain size is determined principally by the weld energy input, with a higher energy input promoting a coarser grain size. The beta

grain size may be reduced somewhat by altering the welding parameters or using alternate welding processes which provide a lower net energy input, e.g. laser of electron beam welding (Baeslack & Banas, 1981).

However, the potential for reducing the beta grain size by producing a weldment with an increased number of smaller (i.e. lower energy input) passes is generally not effective due to the successive epitaxial nucleation of beta grains as each weld layer is deposited, resulting in the formation of vertically oriented columnar beta grains. This effect was clearly demonstrated by Misra et al. (1982) for multi-pass Tungsten Inert Gas (TIG) welds in Ti-6Al-4V. It is also important to note that the higher cooling rates associated with a reduced energy input can promote the formation of a brittle martensitic transformed-beta microstructure.

This paper presents a study on the effect of welding parameters (current and speed) and corresponding heat input rate and cooling rate on the grain size of single-pass welds of an titanium $\alpha/\beta$ alloy, Ti-6Al-4V (IMI 318), using thin plates of thickness 1.0 mm and 2.7 mm. Investigation on the distribution of the grain size across the welds will also be done and discussed.

## MATERIALS AND EXPERIMENTAL SET-UP

All the titanium sheets were sheared to 85 x 50 mm pieces. The specimens were then cleaned with a steel brush, pickled in $H_2O/HNO_3/HF$ solution, and then degreased with acetone prior to welding. Different welding currents and speeds were used to fabricate autogeneous welds on plate. Other welding conditions employed in this study were presented as following :

| | |
|---|---|
| Electrode : | 1.6 mm diameter, pure tungsten |
| Polarity : | Direct current straight polarity |
| Arc length : | 2.0 mm |
| Crater current: | 30 A |
| Initial current : | 70 A |
| Welding voltage : | 12.8 volt |
| Torch inert gas: | $1.0 \times 10^5$ mm$^3$ s$^{-1}$ |
| Back shielding gas: | $1.0 \times 10^5$ mm$^3$ s$^{-1}$ |
| Arc efficiency : | Taken as 0.8 (Giedt et.al, 1989) |

All welds were studied for surface appearance and integrity of penetration. Each of the specimens was sectioned perpendicular to the weld. Cooling rate was computed using a 2-dimensional heat-flow model (Adams, 1958).

### IMI 318 Plates of 1.0 mm Thickness

To study the effect of the welding parameters on the weld size, autogeneous welds were fabricated using IMI 318 thin plates of thickness 1.0 mm with different peak pulse welding currents (group A) and welding speeds (group B). These parameters are presented in Table 1.

The samples were measured of the grain size across the weld by using the Qunatiment 500 computer software. Particular interest was drawn on the distribution of the grain size in the FZ, HAZ near to the FZ (near HAZ), HAZ near to the parent metal (far HAZ). The measurements were taken firstly from the FZ then across the weld towards the parent metal at 0.5 mm intervals. The result of the measurement was plotted against zone distance at different heat input rates (HIRs) in Figure 1.

Grain Size in HAZ. Within sample group A, at the HAZ, there is a general decrease of grain size when moving towards the parent metal (PM). At the far HAZ, the grain size was found nearly the same regardless of the welding current and HIR changes. However, at the near HAZ region (between 2.5 and 3.5 mm), the average grain size were found larger for larger welding currents (100 A, 120 A) and HIRs (20 & 24 mm s$^{-1}$).

Within sample group B, at the HAZ, most of the samples showed the expected decrease of grain size when moving towards the PM. At the whole spectrum of HAZ between 2.5 mm and 4.5 mm, all the samples had virtually the same grain size regardless of the changed welding parameters. This was more obvious than that found in group A. In other words, the change in welding speed did not result a significant change in grain size at the whole HAZ spectrum.

Grain Size in FZ. Within sample group A, at the FZ between 0.5 and 2.5 mm, it was found that the first two samples $S_{1A}$ and $S_{2A}$, with lowest welding currents and HIRs, did nut exhibit much change in grain size. In $S_{3A}$ and $S_{4A}$, a small variation in grain size could be seen between the same region whereas in $S_{5A}$ to $S_{7A}$, much larger variation was evidenced. It was worth to note that $S_{7A}$, with the highest welding current and HIR, had a grain size of 120000 μm at 0.5 mm which is the largest grain size amongst the samples in the group and had the most variation in grain size across the zone.

Within sample group B, at the FZ between 0.5 and 2.5 mm, it was found that the first two samples $S_{1B}$ and $S_{2B}$, with lowest welding speeds but highest HIRs, had the most variation in grain size and resulted the largest grain size averaged across the zone. The other samples on the contrary, with higher welding speeds, did not exhibit much change in grain size across the FZ.

Considering both sample groups A & B, it was found that the samples with highest welding current and lowest welding speed, both of the highest HIRs, had resulted the largest grain size and exhibited the most variation of grain size across the FZ in their own sample groups.

The largest grain size (marked with "•" in Figure 1) in the measurement was then plotted against the HIR for the two sample groups. All of them were found located within the FZ. It was obvious that for both sample groups, the maximum grain size was affected by and varied positively to the HIR. In terms of individual welding parameter, the maximum grain size changed positively with the increase of welding current in group A, and with the decrease of welding speed in group B.

However, when taking the results of two groups together and looking at the range of HIR between 19.5 to 24.5 J mm$^{-1}$, which are the higher ends of HIR in the two groups, it was found that the effect of the change in welding speed (group B) on the maximum grain size much more than that by the change in welding current (group A).

## IMI 318 Plates of 2.7 mm Thickness

To further the study on grain size of welds, autogeneous welds on plates were fabricated, with varying peak pulse welding currents between 80 and 140 A(group A) and welding speeds between 3.4 and 5.1 mm s$^{-1}$ (group B) on thicker IMI 318 plates which is of thickness of 2.7 mm and the grain size on both sides of HAZ was measured and compared. Details of the welding parameters used were listed out in Table 2.

The grain size at the FZ and the two adjacent HAZs were measured again by the Quantiment 500 computer software at 1 mm intervals in both directions from the centre of the FZ. For ease of reference, the center of the FZ was taken to be the zero mark. Therefore, +3 mm mark and -3mm locations represented HAZ 3mm from the right hand side and left hand side of the FZ respectively.

The grain size distribution was at large symmetrical around the center of the FZ. Also, grain size showed a decrease trend with distance away from the FZ center. In other words, the grain size was largest at the center of the FZ. This was in contrary to the findings obtained in previous section on thinner IMI 318 plates (1.0 mm).

As seen in Figure 2, within group A, the largest grain size was found in sample 4 which received highest heat input rate (132 J mm$^{-1}$) and in such case, the highest welding current (140 A), whereas in group B, the largest grain size was found in sample 5 which also received highest heat input rate (118 J mm$^{-1}$) and in such case, the lowest welding speed (3.4 mm s$^{-1}$).

Moreover, sample 5 with smaller heat input rate than sample 4, had larger grain size identified at FZ. With similar heat input rates, sample 6 also had larger grain size than that of sample 3. This showed that, with similar and relatively high HIRs, the effect of welding speed may be more significant than that of welding current in determining the grain size.

To study the effect of individual welding parameter on the grain size, the largest grain size across the weld (mostly at center of FZ) were plotted against heat input rate in Figure 2, and against the welding current and welding speed in Figure 3 respectively. At FZ, as clearly seen from Figures 2 and 3, the largest grain size varied positively with both heat input rate and welding current, and negatively with welding speed. However, there existed a "flat-out" at some welding currents where the variation of grain size was not as significant. Also, similar "flat-outs" were identified at the higher and lower end of welding speeds being used, where the grain size were found nearly the same.

## Grain Size And Cooling Rate

In order to relate the effect of cooling rate during welding with the grain size, the cooling rates on samples 1 to 9 at the transformation temperature for IMI 318 (the β transus temperature which is 1156 K) were computed and plotted against the largest grain size at FZ in Figure 4. It was found that lower the cooling rate, larger was the grain size. This substantiated Kou's ideas on the effect of cooling rate (1987) in this α/β titanium alloy - IMI 318.

## CONCLUSION

a) At the near HAZ region, the average grain size were found larger for larger welding currents (120 A, 140 A) and HIRs (24 & 25 mm s$^{-1}$). On the other hand, the change in welding speed did not result a significant change in grain size at the whole HAZ spectrum as compared to that resulted from changing welding current.

b) At FZ, welds with highest welding current and lowest welding speed, both of the highest HIRs, had resulted the largest grain size and exhibited the most variation of grain size across the FZ in their own sample groups. For both sample groups, the maximum grain size was affected by and varied positively with the HIR.

c) At FZ, with smaller heat input rates, the effect of welding speed in determining the grain size was found more significant than that of welding current.

d) It was found lower the cooling rate, larger was the grain size. At the HAZ, there is a general decrease of grain size when moving towards the parent metal.

## REFERENCES


Adams, C.M.Jr., "Cooling rate and peak temperatures in fusion welding", *Welding Journal*, V37, (5), 1958, pp. 210s-215s.

Baeslack, W.A. III and Banas, C.M., "A Comparative Evaluation of Laser and Gas Tungsten Arc Weldments in High-Temperature Titanium Alloys", *Welding Journal*, (60), 1981, 121s-130s.

Easterling, K.E. *Introduction to the Physical Metallurgy of Welding, 2nd edition.* Oxford, U.K. : Butterworth Heinemann Ltd, 1992.

Kou, S., *Welding Metallurgy.* New York, United State of America: Wiley, 1987.

Misra, M.S., Olson, D.L. and Edwards, G.R., "The Influence of Process Parameters and Specific Additions on Epiaxial Growth in Multiple Pass Ti-6Al-4V Welds", *Grain Refinement in Castings and Welds*, TMS/AIME, Warrendale, PA, 1982.

Watanabe, T., Shibata, S. & Goto, H. "Grain-Boundary Behaviour in the Heat Affected Zone of an Austenitic Stainless Steel and its Relations to Weld Metal Grain Growth". *Quarterly Journal of the Japan Welding Society*, 13 (2), 1995, pp. 262-269.

Giedt, W.H., Tallerical, L.N. and Fuerschiback, "GTA welding efficiency, calorimetric and temperauter field measurements", *Welding Journal*, 68(1), 1989, pp. 28s-32s.


TABLE 1 : WELDING PARAMETERS USED IN WELDING IMI 318 OF 1.0 mm THICKNESS

| Sample no. | Ip (A) | Heat input rate ( J $mm^{-1}$ ) | Sample no. | V ($mm\ s^{-1}$) | Net heat input rate ( J $mm^{-1}$ ) |
|---|---|---|---|---|---|
| $S_{1A}$ | 20 | 4.05 | $S_{1B}$ | 29.63 | 22.43 |
| $S_{2A}$ | 40 | 7.09 | $S_{2B}$ | 33.87 | 19.63 |
| $S_{3A}$ | 60 | 11.80 | $S_{3B}$ | 38.10 | 17.45 |
| $S_{4A}$ | 80 | 15.70 | $S_{4B}$ | 42.33 | 15.70 |
| $S_{5A}$ | 100 | 19.60 | $S_{5B}$ | 46.57 | 14.27 |
| $S_{6A}$ | 120 | 23.53 | $S_{6B}$ | 50.80 | 13.09 |
| $S_{7A}$ | 140 | 24.44 | $S_{7B}$ | 55.03 | 12.08 |

TABLE 2 : WELDING PARAMETERS USED IN WELDING IMI 318 OF 2.7 mm THICKNESS

| Parameters | $I_p$ | V | Net heat input rate | Parameters | $I_p$ | V | Net heat input rate |
|---|---|---|---|---|---|---|---|
| Sample | ( A ) | ( $mms^{-1}$ ) | ( $Jmm^{-1}$ ) | Sample | ( A ) | ( $mms^{-1}$ ) | ( $Jmm^{-1}$ ) |
| 1 | 80 | 4.23 | 75.66 | 5 | 100 | 3.39 | 118.18 |
| 2 | 100 | 4.23 | 94.54 | 6 | 100 | 3.81 | 105.05 |
| 3 | 110 | 4.23 | 103.99 | 7 | 100 | 4.23 | 94.54 |
| 4 | 140 | 4.23 | 132.32 | 8 | 100 | 4.66 | 85.95 |
| | | | | 9 | 100 | 5.08 | 78.79 |

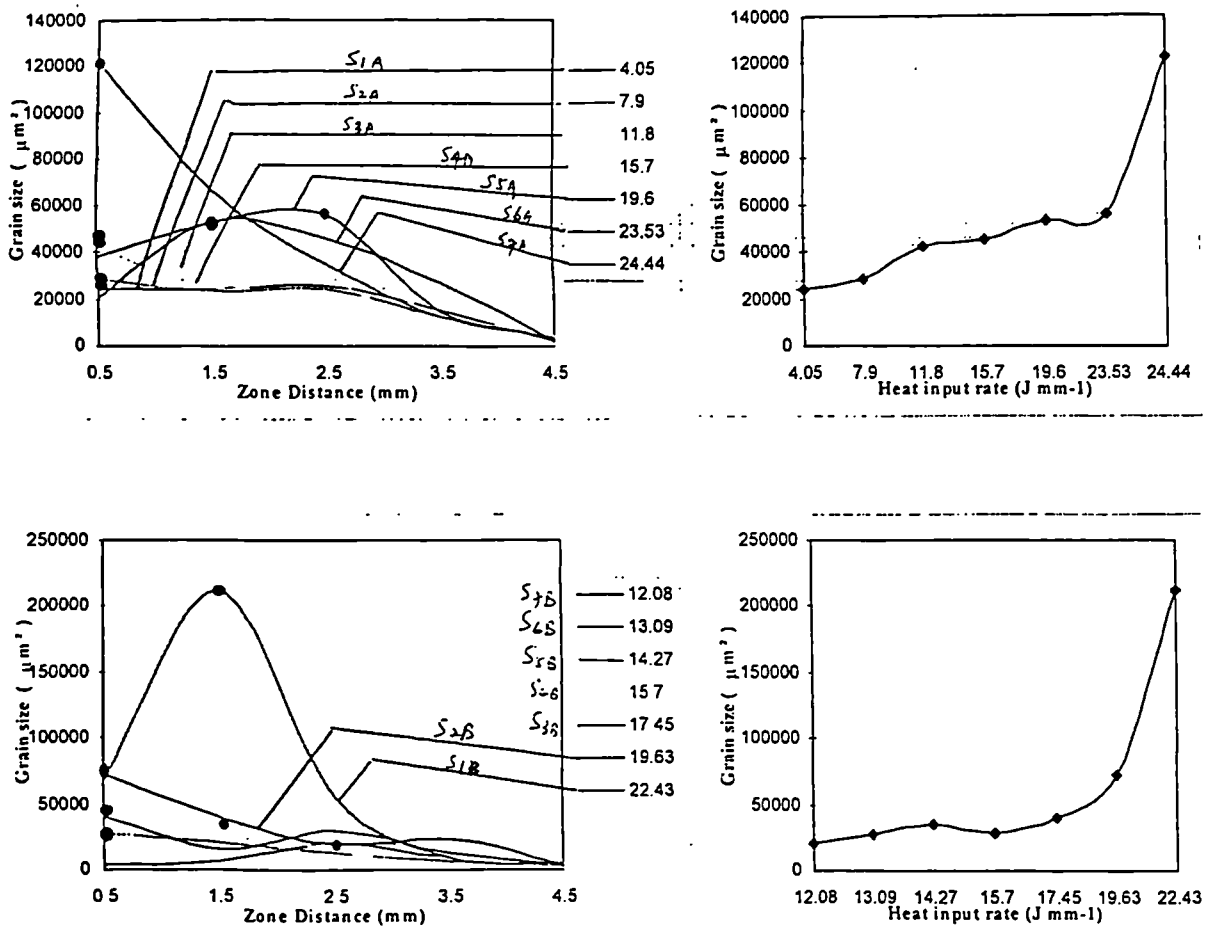


FIGURE 1 : THE RELATIONSHIP BETWEEN HEAT INPUT RATE AND MAXIMUM GRAIN SIZE FOR GROUP A SAMPLE (UPPER GRAPHS) AND GROUP B SAMPLES (LOWER GRAPHS)

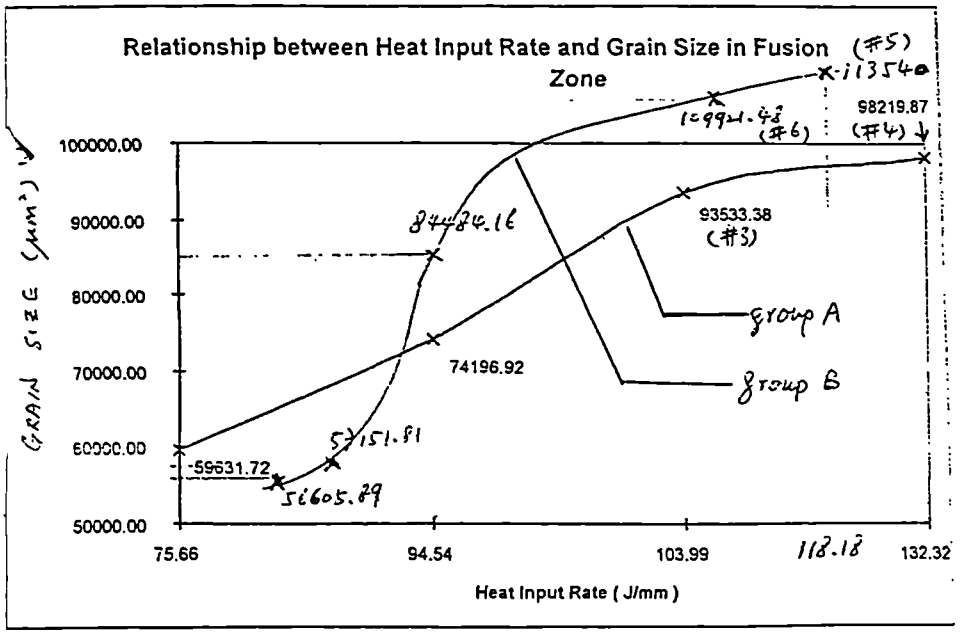


FIGURE 2 : RELATIONSHIP BETWEEN GRAIN SIZE & HEAT INPUT RATE FOR SAMPLES OF 2.7 mm IMI318

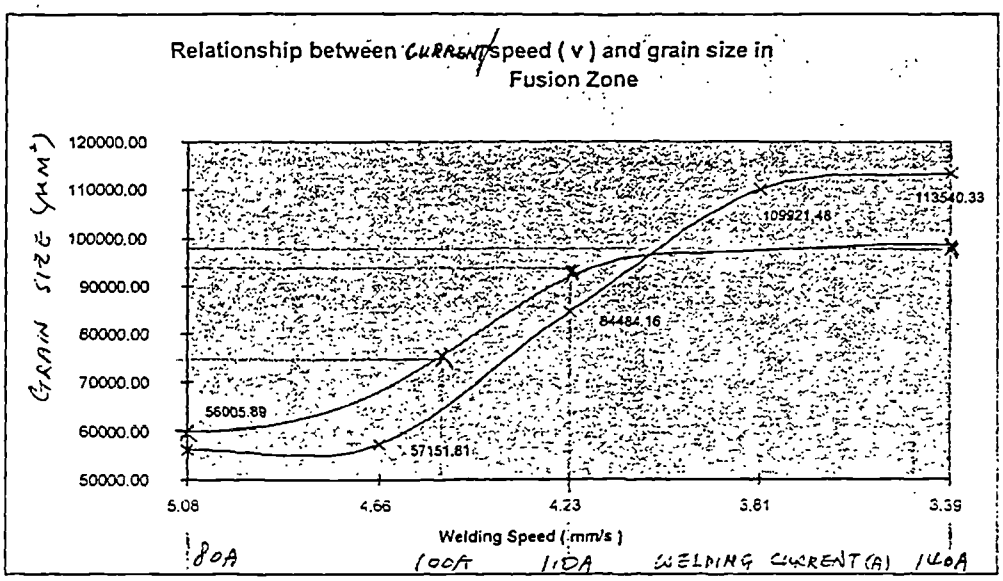


FIGURE 3 : RELATIONSHIP BETWEEN GRAIN SIZE AND WELDING CURRENT. SPEED FOR SAMPLES OF 2.7 mm IMI318

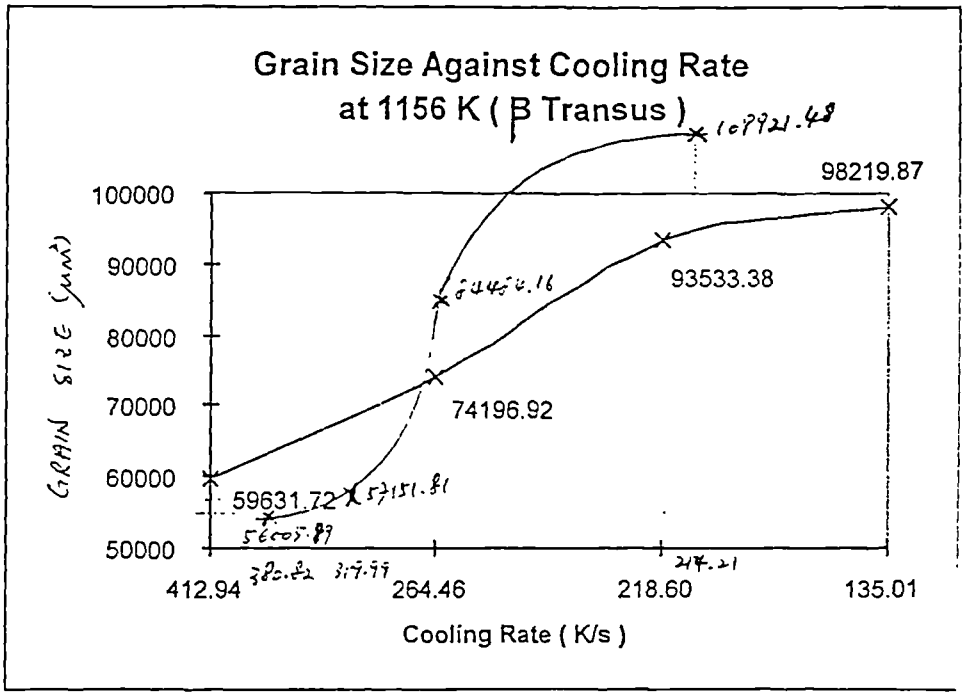


FIGURE 4 : RELATIONSHIP BETWEEN GRAIN SIZE AND COOLING RATE FOR SAMPLES OF 2.7mm IMI318